Micro-extrusion of fine ceramic latticework

Chi, Xiaopeng

Micro-Extrusion of Fine Ceramic Latticework

Xiaopeng Chi

A thesis submitted for the degree of

Doctor of Philosophy at University of London

School of Engineering and Materials Science

Queen Mary, University of London

December 2008

“I certify that this thesis, and the research to which it refers, are the product of my own work, and that any ideas or quotations from the work of other people published or otherwise, are fully acknowledged in accordance with the standard referencing practices of the discipline. I acknowledge the helpful guidance and support of Professor Julian R. G. Evans and Lecturer Shoufeng Yang.”

Xiaopeng Chi

December 2008

Acknowledgement

My deepest gratitude goes first and foremost to Prof. Julian, R. G. Evans, my supervisor, for his constant encouragement and guidance. He has walked me through all the stages of the writing of this thesis. Without his consistent and illuminating instruction, this thesis could not have reached its present form.

Second I would like to express my heartfelt gratitude Dr. Shoufeng Yang who led me into the world of RP technology and his precise attitude and method of deliberated thought to science influenced me deeply. He also helped me overcome many difficulties and suggested countless and priceless advice, especially during the work of extrusion freeforming worktable modification. Thanks for Dr. Hongyi Yang for her invaluable discussions and I have enjoyed working with her.

I am grateful to the Engineering and Physical Sciences Research Council (EPSRC) for supporting this work under grant number GR/S57068 and Ian Thompson (Kings College) and surgeons Richard James Cook and Paul Robinson of Guys and St. Thomas Hospital for their *in vivo* tests and histology analysis.

I also would like to use this opportunity to express my gratitude to my family, especially to my wife. They have been always standing behind me and ready for help.

Abstract

Microextrusion freeforming of ceramic lattices from high solids ceramic pastes is a method for forming complex multi-scale hierarchical porous structures. It has the advantages of low shrinkage stress, high sintered density and environmental compatibility. A user friendly graphical user interface (GUI) was created so that the micro-extrusion freeforming worktable could be made very easy to manipulate even for a beginner. A solvent-based approach to paste preparation for extrusion freeforming was established, involving selection of solvent, polymer and dispersant. The parameters in the process such as solid fraction in the paste, paste viscosity, extrusion rate, X, Y table velocity, filament diameter and the volatilization of the solvent were studied. A substrate material which provided sufficient adhesion to resist shrinkage efficiently and also allowed the extruded lattice to be easily detachable was selected. The extrusion pressure in the alumina paste was monitored and was found to be useful in predicting and optimizing the extrusion behaviour. Hydroxyapatite (HA)/ tricalcium phosphateTCP and alumina lattices were directly fabricated using 80-500 μm diameter filaments. This thesis reports the implementation of design and fabrication of these scaffolds for tissue engineering, band gap materials and micro-fluidic devices. Multi-scale hierarchical void structures were fabricated and tested in vivo for regenerative medical applications. A co-extrusion nozzle assemble was design to produce tubular alumina lattice.

Publications Resulting from the Thesis

1. Xiaopeng Chi, Hongyi Yang, Shoufeng Yang and Julian R.G. Evans, Direct Extrusion Freeforming of Ceramic Pastes, Solid Freeform Fabrication Proceedings, 2006, pp 304-315, The Solid Freeform Fabrication Symposium, Laboratory for Freeform Fabrication/Texas Materials Institute, Mechanical Engineering Dept, The University of Texas, Austin, USA. (Best poster awarded)
2. Shoufeng Yang, Hongyi Yang, Xiaopeng Chi, Julian R. G. Evans, Ian Thompson, Richard J. Cook, Paul Robinson, Rapid prototyping of ceramic lattices for hard tissue scaffolds, MATERIALS & DESIGN, 2008, 29(9), pp.1802-1809.
3. H.Y. Yang, S.F. Yang, X. P. Chi, J.R.G. Evans, I. Thompson, R.J. Cook, and P. Robinson, Sintering behaviour of calcium phosphate filaments for use as hard tissue scaffolds, Journal of the European Ceramic Society, 2008, 28(1), 159-167**.**
4. Hongyi Yang, Shoufeng Yang, Xiaopeng Chi, Evans Julian R. G., Fine ceramic lattices prepared by extrusion freeforming, Journal of biomedical materials research. Part B, Applied biomaterials, 2006, 79(1), 116-121.
5. Yang HY, Thompson I, Yang SF, Chi XP, Evans JR, Cook RJ, Dissolution Characteristics of Extrusion Freeformed Hydroxyapatite-tricalcium Phosphate Scaffolds, Journal of Materials Science. Materials in Medicine, 2008, 19(11), pp.3345-3353.
6. J. JONES, R. COOK, P. ROBINSON, E. ODELL, H.Y. YANG, S. YANG, X. P. CHI, J. EVANS, and I. THOMPSON, Ceramic Lattices for Bone Repair, Back to the IADR

General Session & Exhibition (June 28 – July 1, 2006), Brisbane Convention & Exhibition Centre Exhibit Hall 1.

Contents

List of Figures

List of Tables

1 Introduction

1.1 Aims and Objectives

The primary aim of this project is to build hard tissue scaffolds with multi-scale hierarchical void structures to encourage new bone formation in non-load-bearing cases. The project is funded by the Engineering and Physical Sciences Research Council (EPSRC) and involves co-operation between Queen Mary, University of London, Guy's Hospital, London and King's College London. The scaffold used as the bone substitute is fabricated by the micro-extrusion freeforming method. This technology can be also used in the fabrication of metal matrix composites, band gap materials and micro fluidic devices and these applications are also explored.

The objectives of the project are as follow:

- To establish the micro-extrusion freeforming worktable by which means the scaffolds are fabricated. A user-friendly graphical user interface (GUI) was needed so that the micro-extrusion freeforming worktable can be very easy to manipulate even for a beginner.
- To establish an approach for preparing paste for micro-extrusion freeforming. The type and volume fraction of solvent, polymer and dispersant used in the processing of paste preparation need to be selected. The dry and wet volume fractions of ceramic powders need to be chosen.

- To select safe and biocompatible HA and TCP powders and the appropriate HA/TCP ratio for the lattices.
- In a sintering studies, preliminary screening should be carried out on extruded rod to keep the same particle arrangement that will be obtained in scaffolds.
- To measured flexural strength of extruded filaments by 3 point loading to augment sintering and composition studies.
- To design the structure of scaffolds. The lattice configuration involves a large number of parameters: filament diameter, pore size, pore connectivity, pore distribution and scaffold shape etc.
- To design a co-extrusion nozzle assembly so that filaments with different inner and outer materials can be extruded.

After preparation of scaffolds for bone substitute, the clinical experiment and histology of sample slices were processed in Guy's Hospital, London. This thesis is based on the work at QM.

1.2 Processing of Ceramic Powders

Ceramics have been processed for several millennia. The ancient crafts principally involved clay-based ceramics, with the earliest development dating back to hand-formed pottery in 7000 BC and hand-thrown pottery in 3500 BC[1,2]. There is evidence of coiled clay pots to show that creating an artifact from a cylindrical strand

of deformable ceramic has its origin in Egypt in the Naqada 1 period (ca 4500-4000 BC)[3]. Many of the traditional forming methods used today, including slip casting, extrusion, filter pressing, and dry pressing, originated in the 1700s and 1800s[2,4].

Dry pressing

Dry pressing is an economical technique to mass-produce ceramics from dry powders providing relatively simple geometry. It is used widely in the ceramics, powder metallurgy (PM), and pharmaceutical industries. In this technique, pressure is applied to a mould or dies which have been filled with granulated ceramic powders. The granule is usually a free-flowing, spray-dried powder and typically contains 0-5 vol. % additives. Uniform die filling is important for the micro-scale uniformity of the pressed product. Spray dried powders are used because of their higher flowability which helps to fill the die uniformly and hence produce a homogeneous compact. Uniformity of particle packing is enhanced by using soft and deformable spray-dried granulate spherical powders in the 20-50μm region in diameter[5]. During compaction, the pressure causes fracture or deformation of granules with consequent rearrangement of particles preferably into a densely packed arrangement[6].

There are three types of dry pressing: isostatic, die pressing and a hybrid form of pressing called ramming. In isostatic pressing, the granulated ceramic powder is placed into a rubber mould and pressure is applied via a liquid medium. The pressure

is evenly distributed over all the surfaces of the powder assembly inside the rubber mould[7]. The products made by isostatic pressing can have a wider range of geometry than in die pressing because the only limitation of the geometry is the shape of the rubber mould which is quite easy to make. In die pressing, the granulated ceramic powders are placed into a hardened steel mould, and then pressed by a die. The pressing action is uniaxial and can be single or double ended. Relatively complex shapes can be achieved by using novel dies. Large production runs are almost always made with die pressing and not isostatic pressing[7]. As to ramming, it is a combination of both types of force application. The ceramic powders are placed in a thick walled rubber mould and a steel mandrel is rammed into the mould. Ramming is often used to fabricate a ceramic object with a shape like a crucible[7].

Injection moulding

In traditional injection moulding, viscous dispersions of ceramic powder are forced into intricate forms by the high pressure. In this processing, the melted binder fluidizes the powder instead of the solvent. More binder is needed here than with the other ceramic processing. To minimize warpage, it takes longer times to burn out this larger amount of organic material.

The aqueous injection moulding (AIM) technique was developed by Fanelli et al.[8]. In this method, a concentrated ceramic suspension is prepared in an agarose-based liquid

vehicle which forms low viscosity solution at temperatures near 100°C and solidifies to rigid gels upon cooling below the so-called gel point temperature, 37°C[8]. This process can be compatible with existing commercial injection-molding equipment and yields high-strength components that can be green machined. Unlike conventional injection moulding (IM), however, such components contain relatively low binder content (~10 vol. % or less)[9].

Slip casting

Slip casting is the traditional method for shaping dishes, sinks, etc., and has been used for hundreds of years with clay-based compositions[10]. In slip casting, a ceramic suspension is cast into a porous mould (usually a permeable gypsum mould), and the combination of hydrostatic pressure and capillary suction dewaters the ceramic suspension adjacent to the mould[11]. After the ceramic suspension becomes dry enough to have some self-supporting strength, the mould halves can be removed separately.

Tape casting

Tape casting is a manufacturing process for the production of thin sheets of ceramic materials. The slight difference between tape and slip casting is that the suspension in tape casting is cast on a flat surface rather than being poured into a shaped mould as in slip casting. Lower viscosity slip is used in tape casting to avoid any pits at the surface

of the freshly cast sheet. The compaction between powders is not externally driven like other ceramic process, but instead it arises from internal forces within the "gelled" binder as it shrinks during drying[10]. The thin sheets fabricated by tape casting can be cut into a near-net shape and sintered to give a useful ceramic object. In addition, these layers serve as the basic building blocks of multi-layer ceramic packages (MLCs) and capacitors (MCCs). Tape-cast layers also serve as feedstock for laminated-based solid freeform fabrication techniques, such as CAM-LEM (Computer-Aided Manufacturing of Laminated Engineering Materials)[12].

There are two methods of tape casting: in one, the blade moves over the stable flat surface and in the other, the blade is fixed and the support moves. The first method is normally used for small scale production or in the laboratory. The latter is a continuous method and is normally used for large-scale continuous production.

Pressure casting

Pressure casting (sometimes called pressure filtration) is a method in which the fluid flows through porous filter driven by an applied pressure. The pressure is usually given by a piston and the porous filter is usually a frit bottom to allow the excess liquid to leave the chamber and the ceramic powder to be caught on the frit. The highest green densities can be obtained by this method, because the water is a very

effective lubricant which allows the particles to slide against each other while moving to close-package positions[10].

The simplified illustrations of the equipments for ceramic processes are shown in Figure 1.1[10]. The method of roll compaction is a variant of extrusion and will be introduced in a section with extrusion.

The ceramic processes introduced above are not exhaustive and some methods with gaseous phase starting materials are absent. Rahaman divided the main fabrication methods into three groups, depending on whether the starting materials involve a gaseous phase, a liquid phase, or a solid phase (Table 1.1)[13].

Here, the method using gaseous phase starting materials includes three kinds of reactions which are reactions between gases, reactions between a gas and a liquid, or reactions between a gas and a solid.

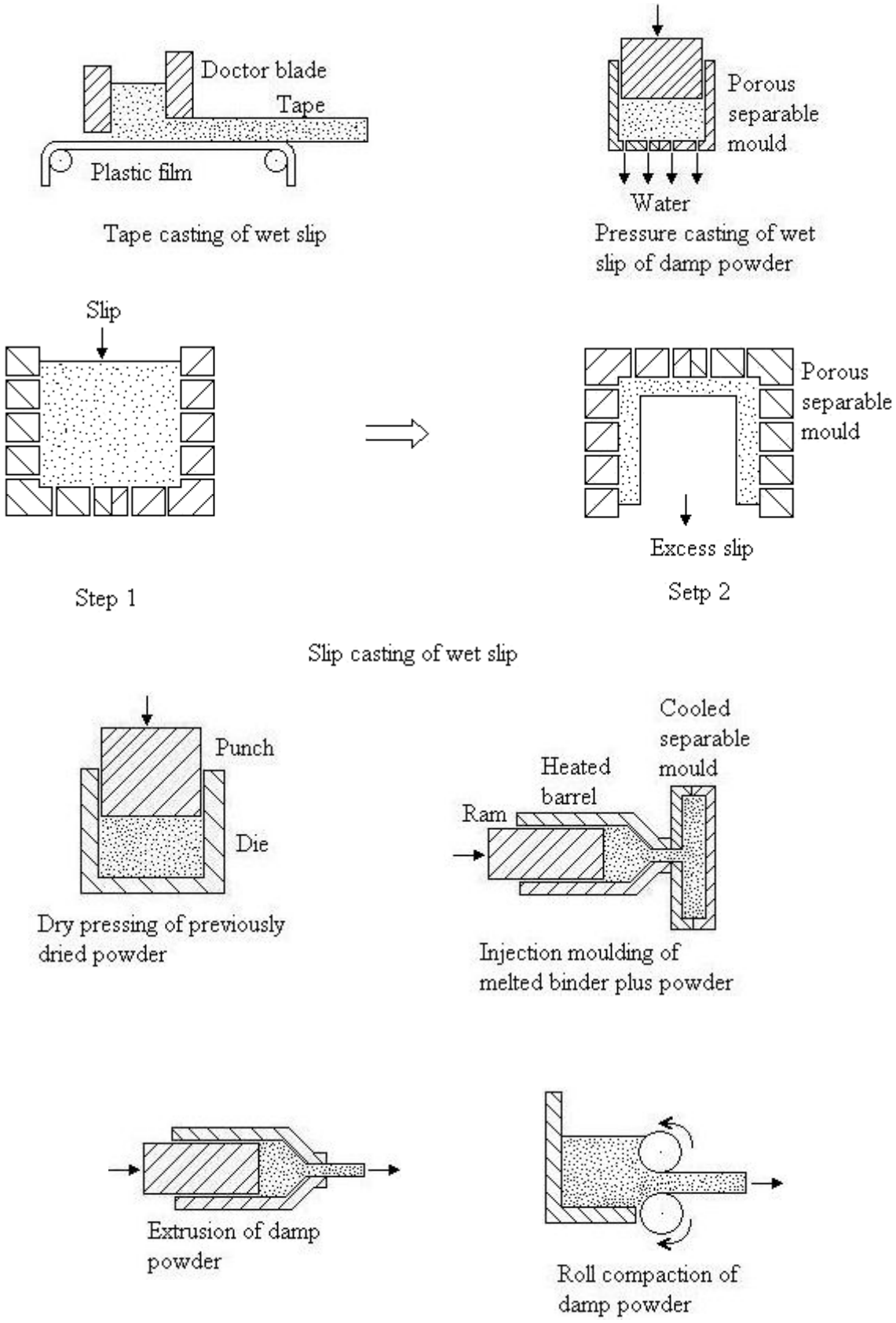

Figure 1.1. Illustration of the equipments for different ceramic processes[10].

Table 1.1. Common Ceramic Fabrication Methods[13].

Starting materials	Method	Product
Gases	Chemical vapour deposition	Films, monoliths
Gas-liquid	Directed metal oxidation	Monoliths
Gas-solid	Reaction bonding	Monoliths
Liquids	Sol-gel process	Films, fibers
	Polymerization	Films, fibers
Solids(powder)	Melt casting	Monoliths
	Sintering of powders	Films, monoliths

Chemical vapor deposition

Chemical vapor deposition (CVD) is a method widely used for the production of films and monolithic bodies. In this process, the products are obtained through the deposition of the films by the chemical reactions between gases. These reactions are mostly endothermic, so the substrate on which the ceramic deposits must be heated. So in CVD, the temperature of the substrate is a important variable which can influences the deposition rate and is the main factor controlling the structure of the deposit. Besides temperature of the substrate, there are other variables must be manipulated to form products with the desired properties. These process variables include the flow rate of the reactant gases, the nature and flow rate of any carrier gases, and the pressure in the reaction vessel[13]. The concentration of the reactant gases,

the diffusion of reactants toward the substrate, and the diffusion of the products away from the surface can be controlled by the pressure in the reaction vessel. The higher diffusivity at lower pressure leads to the formation of films with better uniformity[13].

Depending on the reaction being used, the reaction temperature, and the configuration of the substrate, different apparatuses are used for CVD. Some illustrations of reactors for the deposition of films on substrates to produce silicon wafers are shown in Figure 1.2[14].

CVD method provides a distinct advantage of fairly low fabrication temperature for ceramics and some other composites that are difficult to fabricate for their high melting point. The range of materials which are coated by CVD can be also increased for the low reaction temperature. However, for the production of monolithic bodies, CVD method is very time-consuming and expensive for its low deposition rate. Another problem that is normally encountered in the fabrication of monolithic bodies by CVD is the development of a microstructure consisting of fairly large, columnar grains, which leads to fairly low intergranular strength[13].

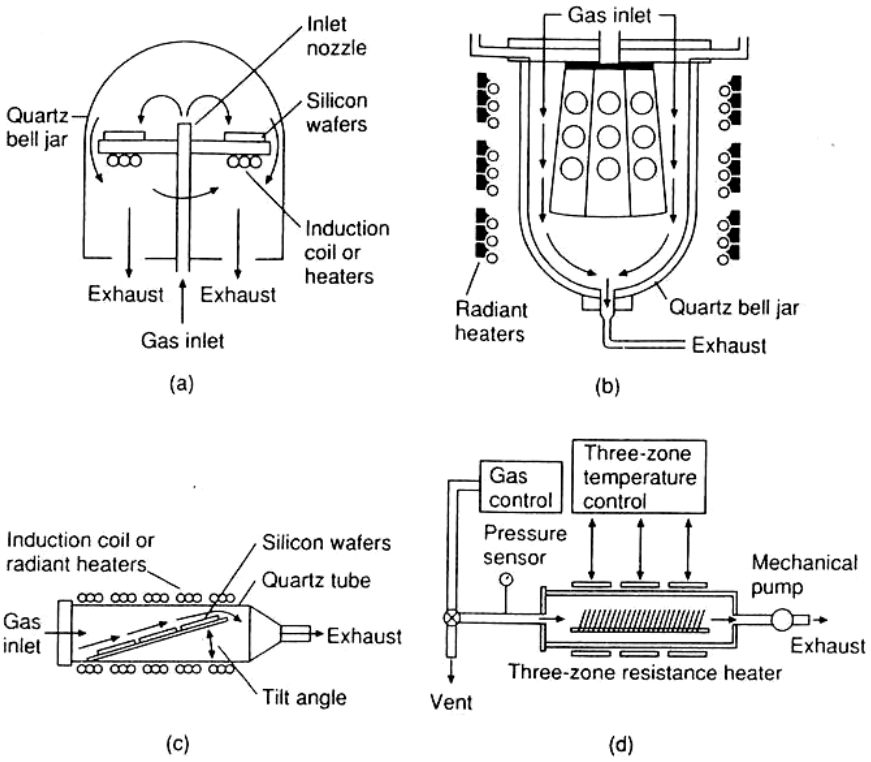

Figure 1.2. Typical reactors used in CVD: (a) pancake reactor; (b) barrel reactor; (c) horizontal reactor; (d) low-pressure (LPCVD) reactor[14].

Direct metal oxidation

Direct metal oxidation produces ceramic bodies using the reactions between a gas and a liquid but the reaction product usually forms a solid protective coating so that the reactants are separated and the reaction is stopped. To avoid the coating protection, the metal liquid is heated to keep molten state in the oxidation process[15]. The oxide coating contains small pores through which molten metal is drawn up to the top surface of the coating, thereby avoiding coating protection and continuing the oxidation process[13]. The illustrations of direct metal oxidation used by the Lanxide

Corporation for porous and dense materials as well as composites are shown in Figure 1.3[15]. Figure 1.3 (a) is the equipment used to produce the metal oxide. The molten metal can be aluminum, titanium and zirconium. The term 'direct metal oxidation' is taken to include all reactions in which the metal gives up or shares its electrons[13]. So the materials produced by this method can be not only oxides but also nitrides, carbides, borides, and titanates. In Figure 1.3 (b), a filler material shaped into the desired size and shape is put onto the surface of molten metal, and then the oxidation process occurs outward from the metal surface and into the filler materials over a range of temperature, such that the oxidation product becomes the matrix of the composite.

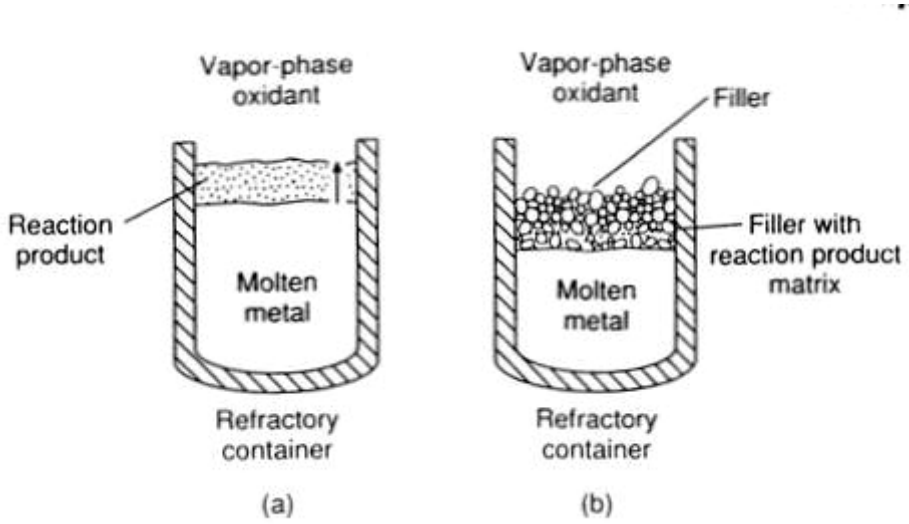

Figure 1.3. Schematic diagram of (a) the formation of a matrix of oxide and unreacted metal by directed metal oxidation of molten metal and (b) oxidation in the presence of a filler[15].

Obviously little or no change in dimensions occurs during the growth of the matrix into the filler materials, so the shrinkage during densification typical of other fabrication routes is avoided.

Reaction bonding

Reaction bonding is used to get a ceramic body depending on the chemical reactions between a gas and a solid. It is mainly used in the fabrication of Si_3N_4 and SiC bodies. In the production of Si_3N_4, before reaction bonding occurs between Si and N_2, the silicon powder is consolidated by one of a variety methods (e.g. pressing in a die, slip casting and injection molding) into a billet or a shaped body and then is preheated in argon at 1200°C. These billets after preheating can be machined to the required components with different shapes and dimensions. Finally, the components are heated in N_2 gas at a temperature in the region of 1200-1400°C[13]. Then the reaction –bonded silicon nitride (RBSN) is produced by nitridation of silicon.

Although, the strength of RBSN is inferior to that of dense Si_3N_4 produced by other methods (e.g. hot pressing) for its low porosity (almost 20%), an obvious advantage of RBSN is high degree of dimensional accuracy for very little shrinkage during the reaction bonding process.

Liquid precursor methods referred to in Table 1.1 make the ceramic product through converting a solution of solid compounds into solid body. The solution of solid compounds has to be concentrated into gel before it is fabricated into a solid body, so this method is also called colloidal processing[9]. The earliest colloidal processing of ceramics can be date back to hand-formed pottery in 7000 BC. The ancient crafts principally involved clay-based ceramics[1, 2]. Since the mid-1970s, the sol-gel process has attracted intense interest as a liquid precursor method[16]. This method is mainly used to produce chemical composites consisting of simple or complex oxides. In the past 20 years, polymer pyrolysis, another liquid precursor method, has been mainly used to produce silicon nitride (Si_3N_4) and silicon carbide (SiC)[17].

Sol-Gel Processing

According to the starting liquid, the sol-gel processing is classified into two different routes[13]. One uses a suspension of very fine particles. The gelled material from this suspension consists of colloidal particles that have been joined together by surface forces to form a network. The other uses a solution consisting of metalorganic compounds (such as metal alkoxides). In this route, the solution is converted into polymeric gel which consists of a network of polymer chains. At suitable concentration of reactants and pH, the solution is stirred constantly at temperatures slightly above room temperature (normally 50-90°C) and then the hydrolysis and

condensation reactions occur leading to the formation of polymer chains. For example, the reactions for a tetravalent metal may be expressed as follow:

$$M(OR)_4 + H_2O \rightarrow M(OR)_3OH + ROH \quad \ldots\ldots\ldots\ldots\ldots\ldots\ldots\ldots\ldots\ldots\ldots\ldots \text{(1.1)}$$

$$M(OR)_4 + M(OR)_3OH \rightarrow (RO)_3 - M - O - M - (OR)_2 + ROH \ldots\ldots\ldots\ldots \text{(1.2)}$$

where, $M(OR)_4$ is the general formula of metal alkoxides; R is an alkyl group.

Equation (1.1) is the hydrolysis reaction and equation (1.2) is the condensation reaction. The polymer chain $(RO)_3 - M - O - M - (OR)_2$ is formed. With interlinking and cross-linking of the polymer chains, the viscosity of the solution increases and the solution is polymerized into a gelled material with a continuous solid network and a finite elastic shear modulus.

As indicated above, excess water and alcohol are used in the reactions so that the remainder of the liquid in the gelled materials must be removed prior to firing. Drying of the gels is the most difficult step in the overall fabrication route. Normally, the liquid is present in fine channels, typically ≈ 10-50 nm in diameter[13]. So during the removal of the liquid, large capillary stressed are generated and the gel undergoes considerable shrinkage. If there are no precautions, severe cracking and warping of

the dried gels will occur. Two approaches are used to avoid these phenomena: one is to slow the evaporation to control the pressure gradient in the liquid. Normally, the remainder of the liquid is removed under supercritical conditions in an autoclave; another one is to speed up the drying process while avoiding cracking through adding certain chemical agents such as formamide, glycerol, or oxalic acid into the solution before gelation[13].

Although the sol-gel processing has some disadvantages such as the expensive starting materials and difficult drying step with the severe problem of cracking, warping and considerable shrinkage, the materials produced by this processing have chemical homogeneity and high purity.

Polymer Pyrolysis

In polymer pyrolysis, the ceramic is produced after pyrolysis of the polymerized materials[18]. The basic requirement in the polymer pyrolysis is the main chain of the polymers contains Si[13]. Normally, the Si atoms are present in the main chain in two different systems, polysilazanes, $(-\underset{|}{\overset{|}{Si}}-\underset{|}{\overset{|}{N}}-)$, and polycarbosilanes, $(-\underset{|}{\overset{|}{Si}}-CH_2-)_n$.

So this method is mainly used to produce silicon nitride (Si_3N_4) and silicon carbide (SiC). Si_3N_4 can be prepared from the pyrolysis of polysilazanes which contain

nitrogen already bonded to the Si in the main chain. After suitable nitridation, polycarbosilanes can also be used to produce Si_3N_4. SiC is usually prepared from pyrolysis of polycarbosilanes. First, the polysilanes are produced by the reaction of the dimethyldichlorosilane with Na in the presence of benzene. Then they are converted to silicon carbide by a two-step heating process. This route can be expressed by the equation (1.3)[13] as follows:

$$(CH_3)_2SiCl_2 \xrightarrow{Na} [-Si(CH_3)_2-]_n \xrightarrow{470^\circ C} (-\underset{\displaystyle H}{\overset{\displaystyle |}{Si}}CH_3CH_2-)_n \xrightarrow{1200^\circ C} SiC \quad \ldots (1.3)$$

Obviously, the loss in mass cannot be avoided in the process of pyrolysis and considerable shrinkage occurs. So it is difficult to use this method to produce monolithic ceramics, it is more suitable for the production of films and fibers. In fact, Yajima and Okamura[18] etc. have produced commercial SiC fibers by the method of polymer pyrolysis in 1970s.

The routes for fabricating ceramics from solid starting materials have two most widely used methods: one is melting casting used for glass forming which produces a solid finished body by heating the powder mixture to its melting point and then cooling and forming it. Another is firing of compacted powders after shaping the powders to the desirable form before sintering them. Many ceramics have a high melting point so that it is difficult to obtain a melt. This method is therefore usually

used in the fabrication of glasses. In principle, the firing of compacted powders can be used in the fabrication of glasses, but this method is more expensive than melting casting. So in practice, it is usually used to produce the polycrystalline ceramics.

To date, several colloidal routes have been developed to produce ceramic components of varying geometric shape, complexity, and microstructural control. Depending on consolidation mechanism, these colloidal routes are classified into three types as shown in Table 1.2.

Fluid Removal

In this route, particles consolidate into a dense layer or body by fluid removal, including pressure filtration[19,20], slip casting[19,11], osmotic consolidation[21,22], tape casting[23], and "robocasting"[24]. In pressure filtration, slip casting, and osmotic consolidation, a portion of the liquid vehicle is removed to yield a saturated ceramic body that must undergo subsequent drying. In tape casting and "robocasting", shaping and drying processes occur simultaneously.

In osmotic consolidation, the ceramic suspension is immersed in a polymer solution separated by a semipermeable membrane, through which fluid flows in response to an osmotic pressure. But during drying, fluid is removed via evaporative processes[22].

Table 1.2. Representative Colloidal-Forming Routes Classified by Consolidation Mechanisms[9].

Forming method	Consolidation mechanism	Component shape
	A. Fluid removal	
Slip casting	Fluid flow into porous mold driven by capillary forces	Complex, 3D, thin walled
Pressure filtration	Fluid flow through porous filter driven by an applied pressure	Simple, 3D
Osmotic consolidation	Fluid flow through a semipermeable membrane driven by osmotic pressure difference	Simple, 3D
Tape casting	Fluid removal due to evaporation	Simple, 2D, thin layers
"Robocasting"	Fluid removal due to evaporation	Complex, 3D
	B. Particle flow	
Centrifugal consolidation	Particle flow due to applied gravitational force	Complex, 3D
Electrophoretic deposition	Particle flow due to applied electric field	Simple, 2D or 3D
	C. Gelation	
Aqueous injection molding (AIM)	Physical organic gel forms in response to a temperature change	Complex, 3D
Gelcasting	Cross-linked organic network forms because of chemical reaction	Complex, 3D
Direct coagulation casting (DCC)	Colloidal gel forms because of flocculation	Complex, 3D
"Robocasting"*	Colloidal gel forms because of flocculation	Complex, 3D

*Solid freeform fabrication technique (consolidation can be induced via mechanism A or C).

Extrusion forming produces three-dimensional components in a layer-by-layer building sequence relying on robotics for computer-controlled deposition of ceramic

slurries which are mixtures of ceramic powder, water, and trace amounts of chemical modifiers, through a syringe. Extrusion forming is the only SFF technique developed to date that uses colloidal systems of low organic content to directly write three-dimensional bodies. This method has the potential of providing a tool for making ceramic parts that can't be built using existing methods. Also, it may result in cheaper and faster fabrication of complex parts. The challenge in robocasting is in the science of developing ceramic slurries that actually contain more solid than liquid but exhibit a fluid-like consistency and flow.

Particle Removal

Particle consolidation into a dense layer or body occurs via particle flow in response to an applied force in several forming routes, including sedimentation [25], centrifugation[26], and electrophoretic deposition[27, 28]. Particles flow in response to gravitational forces during sedimentation and centrifugation. In electrophoretic deposition (EPD), particles flow in response to an applied direct current (dc) electric field[28]. In sedimentation casting, a suspension of ceramic powder is placed in a vessel and allowed to settle until a cake is formed. The supernatant is decanted and the wet green body allowed drying[29].

For stable suspensions, centrifugation simply enhances the rate of particle consolidation by increasing the applied gravitational force. In centrifugal casting, the

same process occurs in a centrifugal field (as shown in Figure 1.4.) to speed up the cake formation.

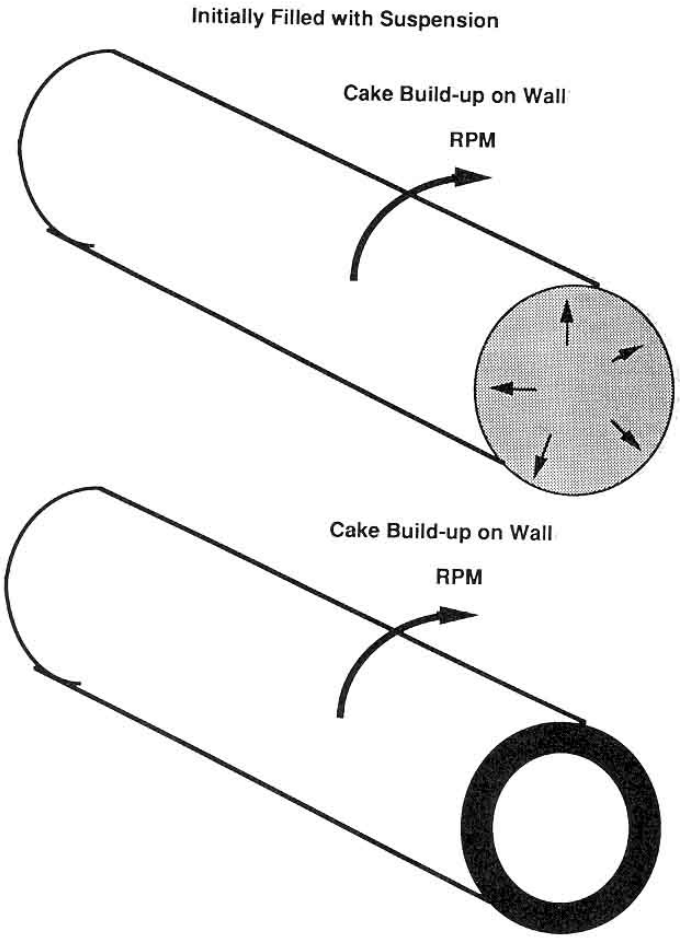

Figure 1.4. Centrifugal casting of an annular shape.

In electrophoretic deposition, the electric field makes the charged colloidal particles move toward, and, ultimately deposit on, an oppositely charged electrode to produce a consolidated layer or body. It relies on the eclectrical charge developed at solid-liquid interfaces. Electrophoretic deposition is able to make green bodies more quickly than

sedimentation casting and slip casting which, for very fine particles, require long time periods to build up a deposit. An electric field can enhance the deposition rate of ceramic particles in the cake. Recently, this technique has been used to produce unusual green body shapes or ceramic coatings for irregularly shaped electrodes.

Gelation

Consolidation via gelation relies on physical or chemical approaches to induce gelation in a concentrated colloidal suspension[9]. At the sol-gel transition, the viscoelastic properties of the system have been studied by H. H. Winter, as shown in Figure 1.5. In Figure 1.5, η is the apparent viscosity and G' is the elastic modulus. From this diagram, the viscosity of the system increased to infinity with time at the gel point. This phenomenon coincides with the formation a three dimensional product. Incomplete gelation leads to a sol phase whose apparent viscosity approaches a steady-state value with time[30]. Many techniques for the formation of a dense, solid layer or body via gelation have been developed, including aqueous injection moulding (AIM),[31,8] gelcasting,[32,33] and direct coagulation casting (DCC).[34,35]

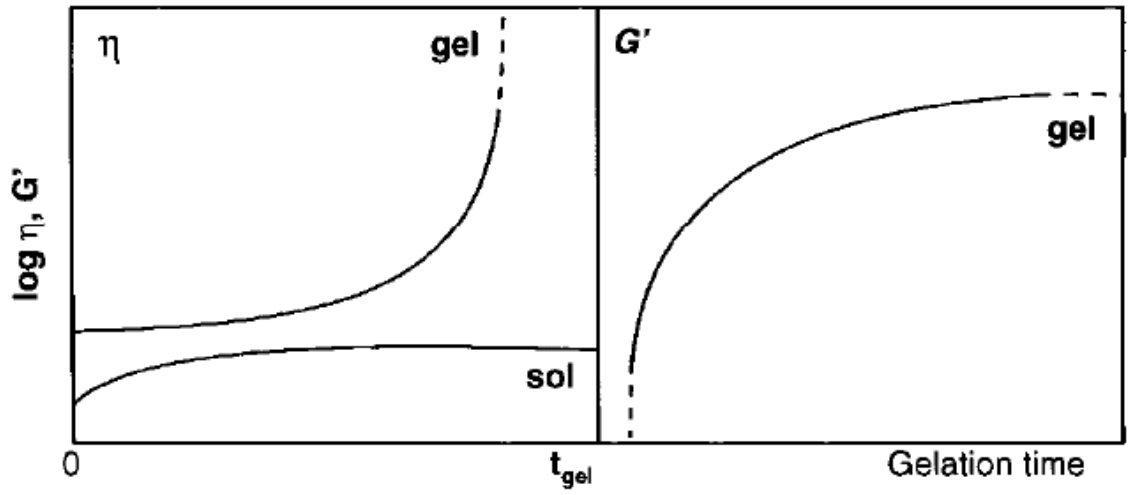

Figure 1.5. Schematic illustration of rheological property evolution as a function of gelation time for gelling systems[30].

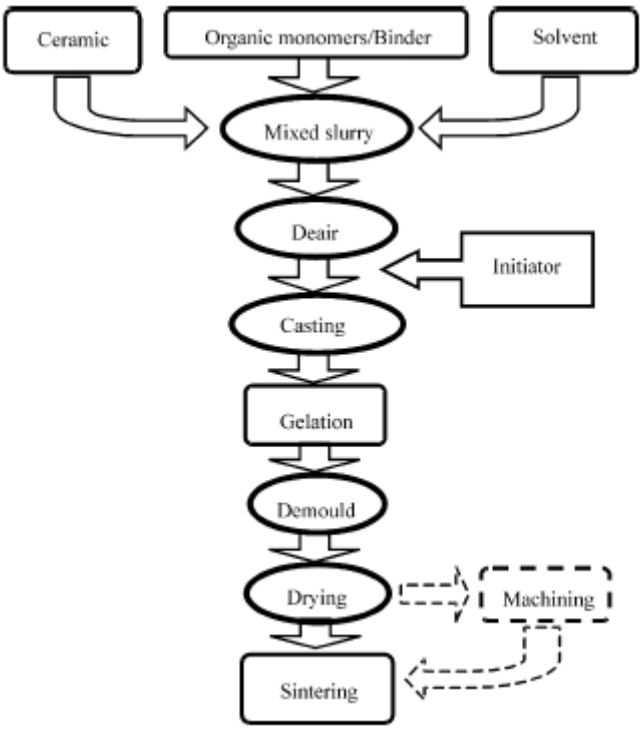

Figure 1.6. Detail flowchart of the gelcasting process.

Janney and co-workers [32, 33]developed the Gelcasting method which is a novel near-net shape forming method for fabricating complex-shaped ceramic bodies. In this process monomer, crosslinker, initiator, catalyst and ceramic powder are thoroughly mixed in water to form a homogeneous suspension with high solids loading and low viscosity, then by means of in situ polymerization, a macromolecular network is created to bind the ceramic particles together[36]. The polymerized product accounts for less than 4 wt. % of the dried solids[33]. A detailed flowchart of the gelcasting process is shown in Figure 1.6.

Gelcasting overcomes some of the major drawbacks of injection molding, e.g., long removal times and/or flaw generation during binder thermolysis. In addition, unlike slip casting, gelcasting has a quick casting rate and its green bodies are strong and machinable. Gelcasting uses high solids loading of ceramic powders in organic gels, and is distinguished from the sol--gel processes which produces ceramic powders in an inorganic gel at low solids concentration. So gelcasting is suitable for complex shape fabrication[32, 34] by offering short moulding times (on the order of several minutes), high yields, high green strength, and low-cost machining.[32, 33, 37]

Direct coagulation casting (DCC), developed by Gauckler and co-workers, [34, 35] is based on the idea of casting a high-solids-loaded stable suspension in a mould and then using a time-delayed chemical reaction in the suspension to either shift the pH toward the isoelectric point (IEP) of the suspension or increase the electrolyte

concentration in the suspension[38] to minimize double-layer repulsive forces, resulting in the destabilization illustrated schematically in Figure 1.4. This approach needs minimal binder content (≤ 1 vol. %) and can get homogeneous packing densities. However, the DCC process is limited by long coagulation times and low-strength and as-formed bodies that are not machinable in the green state[9].

1.3 Advanced Solid Freeforming Procedures

Solid freeform fabrication (SFF) is an advanced manufacturing technology which generates accurate geometrical objects directly from a three-dimensional computer image without part-specific tooling or human intervention[46]. Many SFF technologies which are superior in terms of building speed, surface finish, dimensional accuracy and material properties have been developed to date[39, 40, 41, 42].

Although there are many traditional ceramic processing methods, a high cost in machines and moulds is generally incurred for low production numbers. Fortunately the emergence of solid freeforming (SFF) in the last two decades [43] makes it possible to fabricate an individual or personalised product directly from a computer design file. The use of SFF as a rapid prototyping method enables a designer to evaluate new ceramic materials and designs under different test conditions[43]. SFF is an outgrowth of rapid prototyping (RP), in which three-dimensional shapes are created by point, line or planar addition of materials without confining surfaces such as mould or die

walls. In SFF, a CAD representation of the desired part is computationally sliced to produce a series of parallel outlines, and then a rendering process is used to serially produce thin contoured sheets that correspond to each outline. The contours are assembled and fused to produce a finished solid component. The nature of the computational representation sometimes anticipates the details of the process to be used for construction.

The details of the SFF processes vary widely. Some define geometry before fusing to the stack, some fuse first and then define the shape, others do the two simultaneously. Similarly, fusion is accomplished in varying ways, e.g. local solidification, gelation, or addition of an adhesive. The chief, and highly significant, benefit to SFF is that the contours can be made without recourse to tooling[44].

Indeed solid freeforming can be traced further back to the earliest forms of cellular life, at around 3-5 billion years[43]. Most forms in biological systems are built cell by cell, or plane by plane. So in a sense, solid freeforming provides a conceptual link between conventional volume manufacturing and so-called "biomimetic" materials processing[45].

The emergence of solid freeforming in the last two decades is attributable principally to the development of the graphics handling capability of personal computers. Solid freeform fabrication is an advanced manufacturing technology which generates

accurate geometrical objects directly from a three-dimensional computer image without part-specific tooling or human intervention[46]. These characteristics give designers the freedom to produce physical models of their drawings more frequently, checking the assembly and function of the design as well as discussing downstream manufacturing issues with an easy-to-interpret, unambiguous prototype. These characteristics also make SFF suitable for fabricating geometrically complex components, eliminating tool set up which is necessary for numerical control machining[43]. Consequently, SFF generally minimizes the errors in the processing of ceramics and in material waste. It depresses the product development costs and lead times are substantially reduced.

In the last decade, a large number of general reviews of SFF processes have emerged. Kruth[47] classified these processes by two approaches (Figure 1.7). In the first approach (a), processes are classified by the state of the building materials used in SFF; in the second approach (b), they are classified according to the dimensional order of deposition.

A review by Tay and Evans et al.[43] provided a new classification of SFF according to the method of actuation and position control. In this classification, laminated object manufacture, selective laser heating and multiple layer photocuring rely on optical deflection of laser light; fused deposition and some types of inkjet printer use the stepper motor actuation which can provide <1μm resolution associated with feedback;

in drop-on-demand printing, the ejection of a droplet can be achieved either by piezoelectric or electromagnetic actuation. The droplet position can be controlled by electrostatic deflection or by the relation between printhead and substrate which is generally controlled by stepper motor[48].

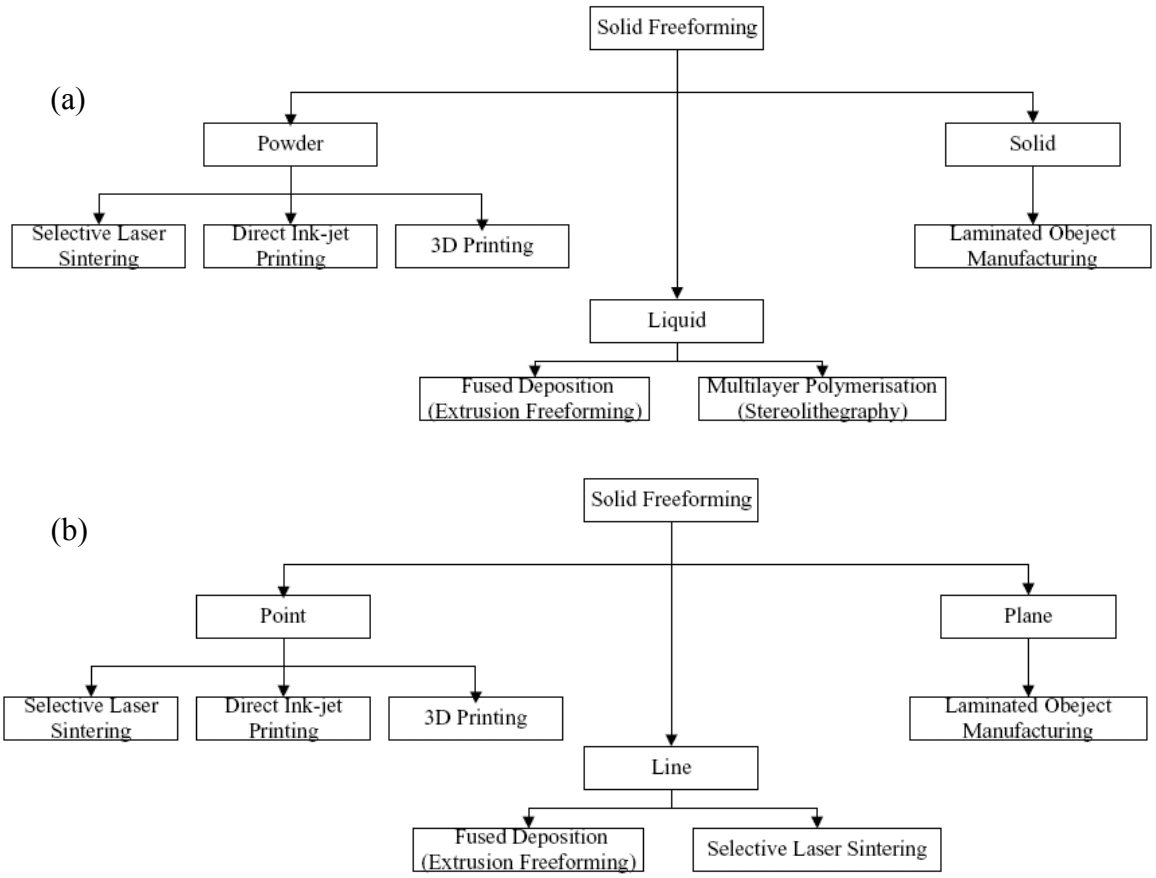

Figure 1.7. Classification of solid freeforming processes (a) by state and (b) by dimensional order.

In each method, the main quality factors in the solid freeforming of ceramics that command attention are: dimensional control, geometry of vertical walls, surface finish, microstructure, speed and integrity (e.g. porosity) [43]. All of these techniques have

been developed for different purposes. So there are no rules for process selection. Some examples of successful applications are introduced below.

Stereolithography

Stereolithography is one of the methods of giving the computer a building capability via directed movement of a focused laser beam. The term stereolithography consists of the prefix “stereo” and the word “lithography”. The prefix “stereo” means having three-dimensions or solid and “lithography” is a method of printing from a plane surface and contrasts both with letterpress in which the printing areas are raised and intaglio in which they are recessed[49]. But the stereolithography does not use lithography and it is not a printing process. Typically, it is used to create ceramic parts by polymerising a UV-curable binder filled with ceramic powder by exposure to ultra-violet radiation from a laser[50] and then the cured resin is removed. The schematic representation of stereolithography was shown in Figure 1.8. In this equipment, photopolymerisable monomer is cured by UV laser which scans the surface to fabricate the wanted layers. The recoating mechanism is used to provide a fresh layer of monomer and remove the unwanted polymerised resin at the surface which may affect accuracy and surface finish.

This problem is induced by the excess resin that is produced in the resin re-coating step and cannot be drained through the base[46]. To eliminate this problem, many

recoating mechanisms have been invented, e.g. scraper blade, inverted 'U', viscous retention and positive displacement pump[47]. But the problem is still present and it is more serious for highly viscous ceramic suspensions because a high shear stress transmitted during coating may damage the part under construction. A process in which the ceramic suspension is re-laminated into semi-solid foils and pressed into the previous cured layers has been developed to overcome re-coating problems encountered with a scraper blade[47].

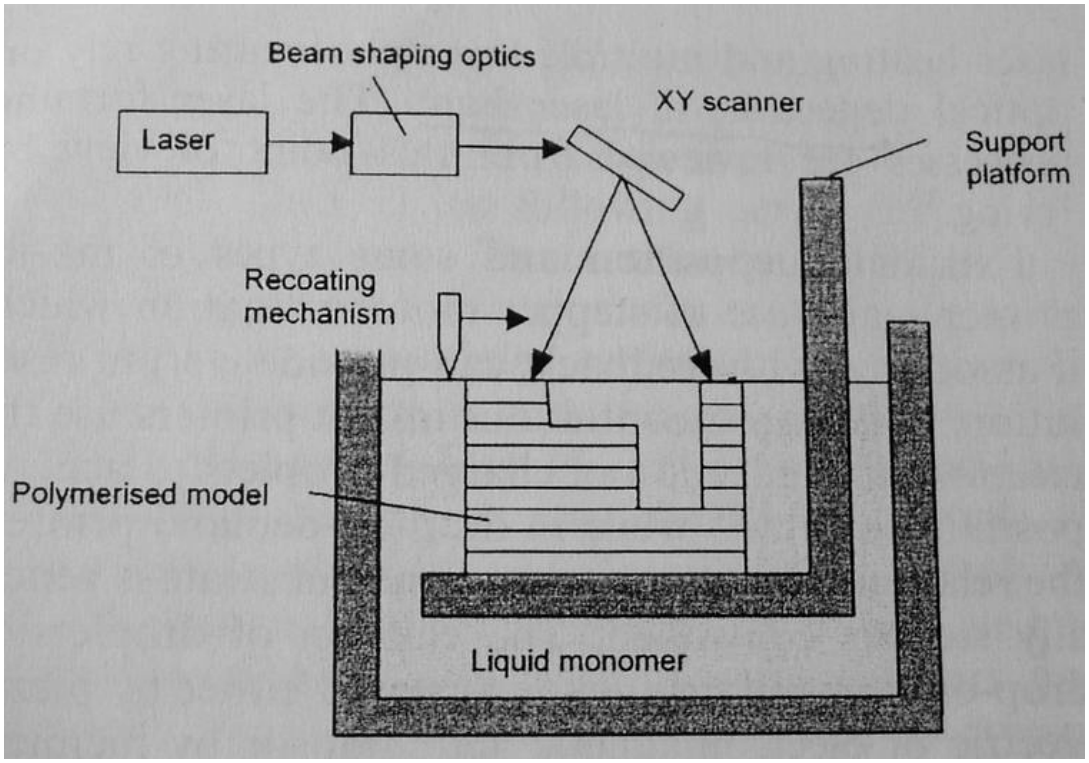

Figure 1.8. Schematic representation of stereolithography (multi-layer photopolymerisation).[50]

The property of the paste is very important in the processing of stereolithography. First, the paste has to be very homogeneous to be properly spread in thin layers. Homogeneity is also necessary for continuity of the ceramic phase of the bulk polymerized part to promote good debinding and sintering without introducing cracks[51]; second, the rheological behaviour of the paste is another important feature for stereolithgraphy. In order to achieve high density ceramic parts, high solid loading ceramic paste is needed, typically 50-65 vol. % of solid[43], on the other hand, the paste should have a low viscosity at the shear rate imposed during spreading to enable flow and allow a high speed of deposition[51]. Typical rheological behavior is shown in Figure 1.9[51].

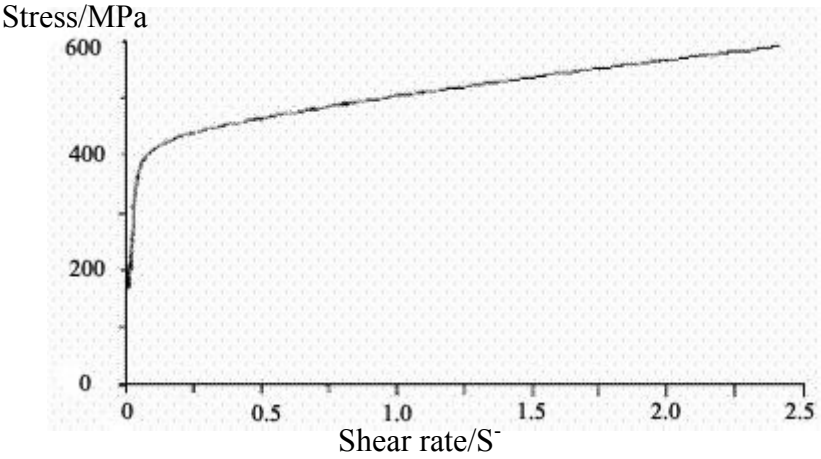

Figure 1.9. Suitable rheological behavior of ceramic paste for stereolithography.

The behaviour seen in Figure 1.9 is regarded as ideal for stereolithography because it is near-Newtonian; shear stress is almost proportional to shear rate. In fact, close

inspection shows that the fluid is slightly shear-thinning, an effect nearly always seen in particle suspensions in Newtonian liquids and in high molecular weight polymers.

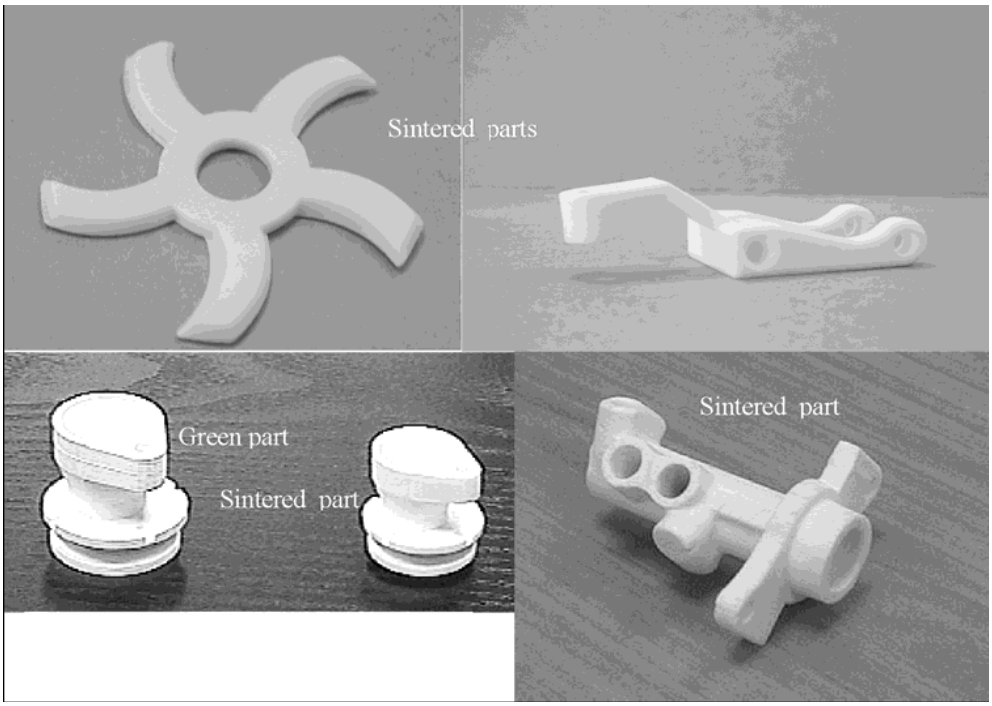

Figure 1.10. Examples of alumina parts (edited from reference 51)

Stereolithgraphy uses laser light to solidify the UV-curable resin mixed with concentrated ceramic powders, so there are at least four and sometimes five different components to be mixed together to obtain a paste: photocurable resin, photo-initiator, thickener, dispersant and ceramic powder[51]. Photocurable resins generally contain 2-5% photo-initiator that generates free radicals in the presence of UV light and then the monomer or oligomer is polymerized when attacked by these free radicals, but the reaction stops in the absence of light because free radicals react with oxygen[43]. When one layer is cured by the focused laser beam which scans the liquid surface according

to the 3D computer information, the elevator is lowered and liquid resin covers the last solidified layer. The recoating and leveling of a new layer of resin then ensures that the liquid level corresponds to the focal plane and excess resin beyond the desired layer thickness is removed[46]. In this way, the three dimensional part is fabricated layer by layer. Some alumina parts fabricated by stereolithgraphy are shown in Figure 1.10[51]. During the stereolithgraphy process, the light scattering from the particle suspension is found to significantly influence the fabrication resolution in both lateral and depth dimensions. So a UV absorber was added to the organic vehicle to reduce the scattering effect of ceramic particles[52].

Stereolithography, like most of the other SFF methods, can be used to fabricate ceramic parts which have complex geometry and fine surface quality, but this process has some disadvantages. For high viscosity ceramic suspensions, a long time is needed to drain the excess resin from the complete part and in this process, structures are required to hold the various connecting parts of the product and support the weak overhanging regions during the recoating of layers[47]. A decision-support tool which is a feature-based system produced using an object-orientated programming language and a solid modeling CAD environment has been developed to orientate the prototype correctly in the RP machine to obtain the best trade-off between time, cost, and accuracy[53]. Recently, an advanced micro stereolithography system which operates by using pinpoint solidification generated at a tightly focused spot inside a liquid photopolymer has been developed[54]. Unlike conventional micro and macro

stereolithography, this three-dimensional (3D) pinpoint exposure technique allows true 3D microstructures to be fabricated without relying on layer-by-layer processing. Moreover, the direct drawing technique inside the liquid photopolymer makes it possible to fabricate freely movable micromechanisms without support parts or sacrificial layers.

Selective Laser Sintering

Selective laser sintering builds a three dimensional object layer by layer out of a powder bed that has been selectively fused by laser radiation [55] from a three-dimensional representation. This can be a three-dimensional computer-aided-design (CAD) model, the information obtained from a computed tomography (CT) or magnetic resonance imaging (MRI) scan[56]. It originated at the University of Texas in Austin in 1986 and was commercialized in 1992[57].

A schematic diagram of the selective laser sintering process is shown in Figure 1.11. The powders are deposited onto the surface of an elevator platform to form a thin layer. A laser then selectively scans this layer to fuse the powders. The scanning route is defined by the geometry of the cross-section of a CAD model. The non-fused powders remain in place to be the support structure. After each layer is scanned by laser, the elevator platform lowers and another layer is deposited. The laser energy

also fuses consecutive layers together. So layer by layer, a three-dimension product is fabricated by selective laser sintering.

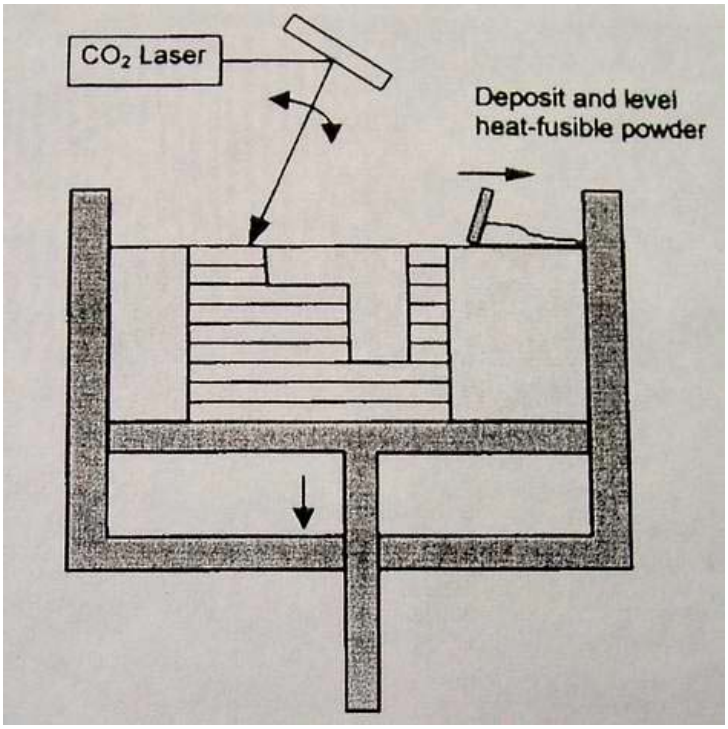

Figure 1.11. Schematic diagram of selective laser sintering process[58].

Unlike some other solid freeforming methods, selective laser sintering can fabricate powders directly without sacrificial binders[59]. But for some powders with high melting point, a binder with lower melting point is used to assemble powders. These binders can be an organic binder, an inorganic binder (e.g. ammonium dihydrogen phosphate)[60] or a metallic binder[59].

Products fabricated by selective laser sintering are often porous and have a low density. There are two routes to improve the density of products. The density of the

finished product increases with increasing density of the powder bed. So the first route is to improve the density of the powder bed. Another route is to improve the final density directly through post processing[57]. Conventional means of improving the powder bed density include the use of spherical particles, bimodal size distributions of powder, agglomeration of fine powder and optimizing the volume fraction of combustible binder[57] . Conventional sintering and hot isostatic pressing are two common post processes used to increase the final density.

The obviously advantage of selective laser sintering is no support structure needed and changing from one material to another in the same production is convenient.

Laminated object manufacturing

The first laminated object manufacturing (LOM) was developed in 1985 and commercialized by Helisys Corporation in the USA[47]. This early LOM is mainly used layers of paper or plastic to build components. At the end of 1990s, some modified LOM techniques were developed to fabricate ceramic components.[61,44] These new LOM include ceramic laminated object manufacturing (CerLOM) and Computer-aided Manufacturing of Laminated Engineering Materials (CAM-LEM). CerLOM was developed by Lone Peak Engineering Inc., USA and has been used to fabricate composites consisting of layers of different ceramic materials[40]. CAM-LEM was developed by Case Western Reserve University, USA and adopts a

'cut-then-stack' approach where the layer is cut to desirable shape before it is placed onto the stack to laminate[62]. This 'cut-then-stack' approach allows fugitive tapes, which are organic materials and can be removed by thermolysis later, to be added to the partially complete stack, and then ceramic productions with hollow structures can be fabricated.

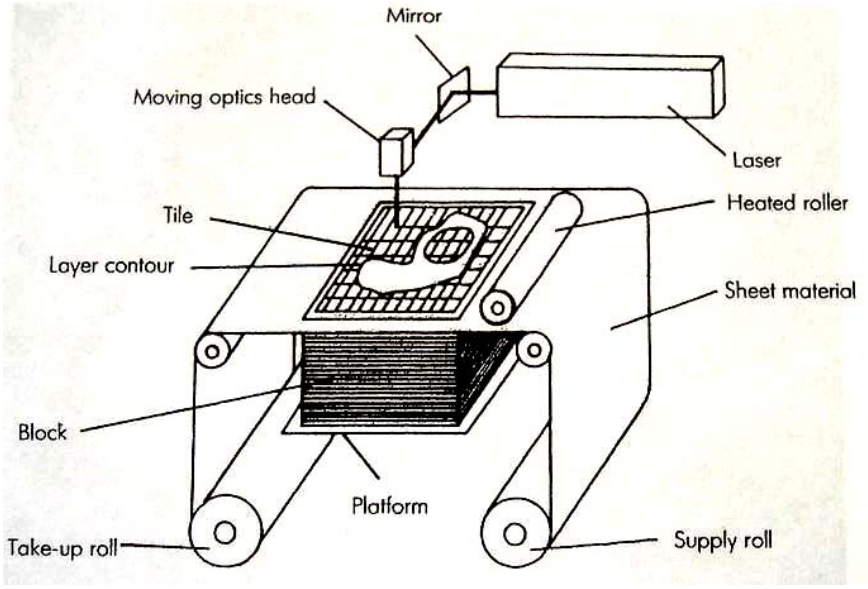

Figure 1.12. Schematic diagram of laminated object manufacturing (LOM) process[63].

A schematic diagram of LOM is shown in Figure 1.12. A sheet is cut by laser according to CAD description and then laminated with adhesive to the previous sheet. The waste materials remain to serve as a support. The process is repeated until the three-dimensional component is finished. The finished component is removed from the platform and the waste materials are separated manually. A binder removal by sintering is necessary for this method. During sintering, delamination and bloating are

induced by the relaxation of residual stresses. To counteract this problem, appropriate pressure is applied during binder burnout.

Although the interfaces between layers induce the problems of delamination and bloating, microstructural defects within each layer can be minimized if each sheet is processed separately in this method[62]. Since the shrinkage or thickness can be compensated as the thickness of the sheet materials is known beforehand[61], then LOM can be used to fabricate a highly accurate production. Another advantage of LOM is layers of different materials with different properties can be fabricated to functionally graded materials or multi-layered composites (e.g. Al_2O_3/Ce-ZrO_2)[40].

Three-dimensional printing

Three-dimensional printing (3DP) was developed at Massachusetts Institute of Technology, USA in 1992 as a method to fabricate components from the starting materials of metals and ceramics powders[64,65] . This technology was developed initially to produce ceramic moulds for metal casting and for printed parts with controlled surface texture and internal microstructure. Parts are obtained through control of the placement of droplets; this technology is also used to make casting moulds for orthopaedic implants[43].

A schematic diagram of the 3DP method is shown in Figure 1.13. In this process, dry powders are leveled to form a thin powder bed by a roller or an alternative such as mechanical, acoustic or ultrasonic vibration[66]. Binder is printed onto this loose powder bed through an ink-jet printhead which moves in raster motion. The printing routes are defined by the CAD model. The binder diffuses through the powders by capillary action and pulls neighbouring particles together[65], and then a piston lowers the platform. The processing is repeated until a three-dimensional product is finished. In the whole process, the free powder remains to support the overhanging features and is removed before sintering.

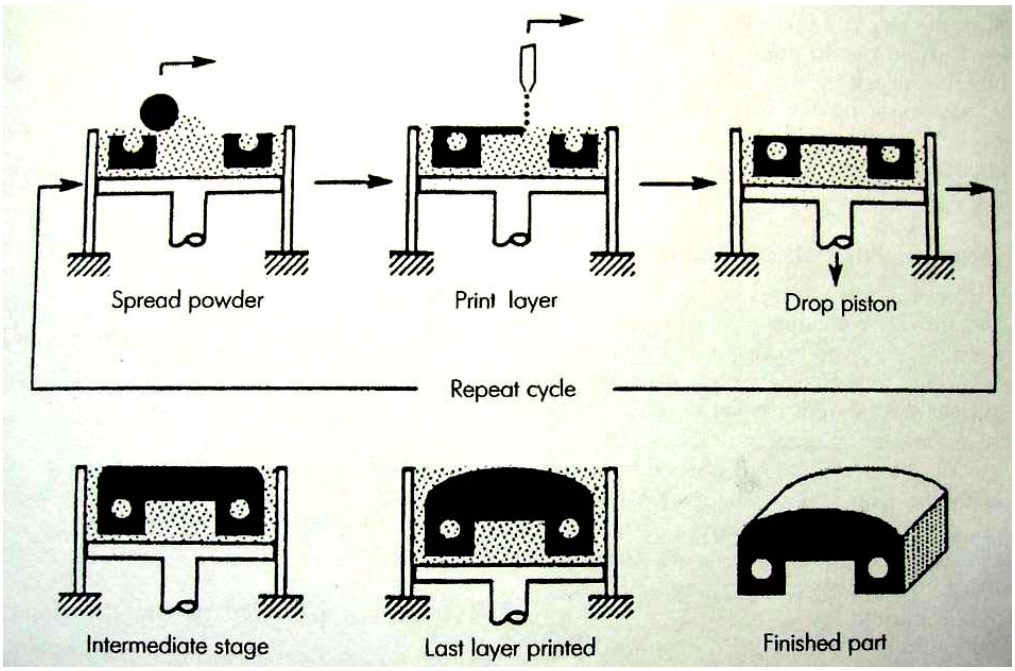

Figure 1.13. Schematic diagram of three-dimensional printing (3DP) method[64].

During spraying of binder, the powder bed is easily cut into a trench and powders are redistributed. So a moistening treatment of the powder is usually used to increase the

cohesive strength between particls[67]. Another problem of this method is the high surface area of the fine powder decreases their flowability and therefore it is difficult to obtain the defect-free layers. However, there are some distinguishing advantages of 3DP. A product with desirable pore size and shape can be obtained by this method. By using multiple printheads, additives may be deposited in a prescribed fashion to create gradients in compostion[43], e.g. in the fabrication of compositionally graded zirconia toughened alumina (ZTA) ceramic multilayers[68].

Direct ink-jet printing

Direct ink-jet printing was developed from the well-established reprographic applications of home and office printing[43]. Unlike 3DP, direct ink-jet printing creates components by dispensing ceramic powders, which are well dispersed in a colloid suspension, instead of binder through the printhead. So successful direct ink-jet printing relies on the properties of the ceramic powders suspension. To disperse the ceramic particles very well in suspension, a dispersant is usually used to stabilize the suspension by adsorption on the powder surface. Agglomerates are broken down by the use of a twin roll mill, ultrasonic apparatus, high energy bead milling or a combination of these[69,70,71] . To avoid the blocking of the nozzle, the dispersed suspension is left undisturbed to allow sedimentation and then filtered to remove flocs or debris before printing. Some defects, like ripples[72], splattering[72], undefined boundaries and 'faded' prints[73], have been often observed on the top surface of the

printed parts. To improve the smoothness on the top surface, a slow drying rate is preferred[74].

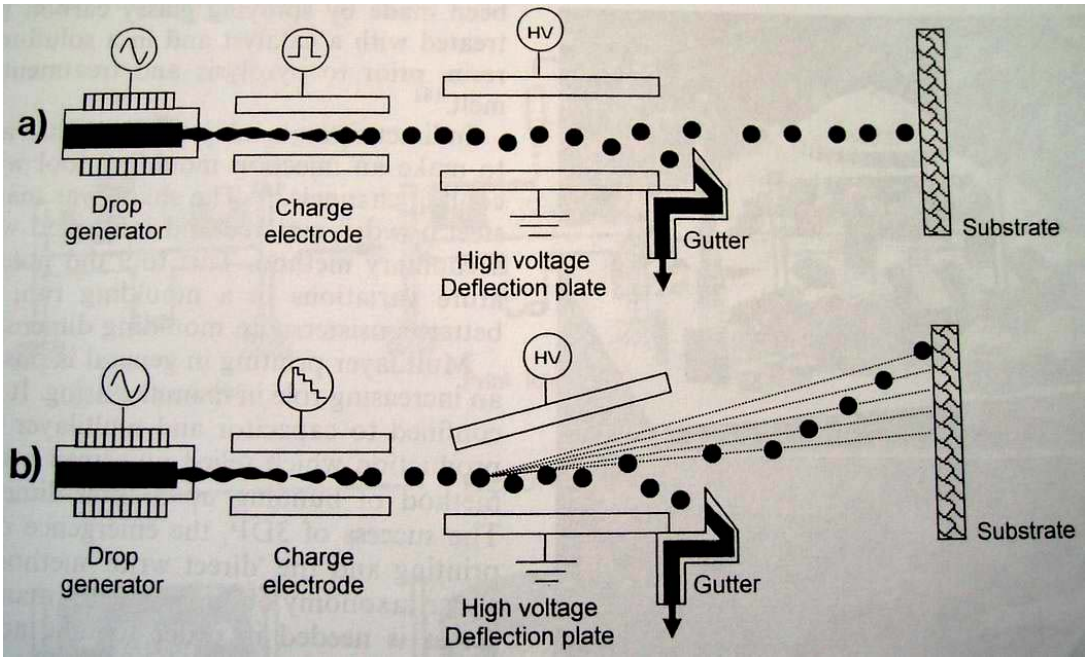

Figure 1.14. Schematic diagrams of continuous ink-jet printers a) using binary deflection and b) using multiple or analogue deflection based on Sweet's principle[75].

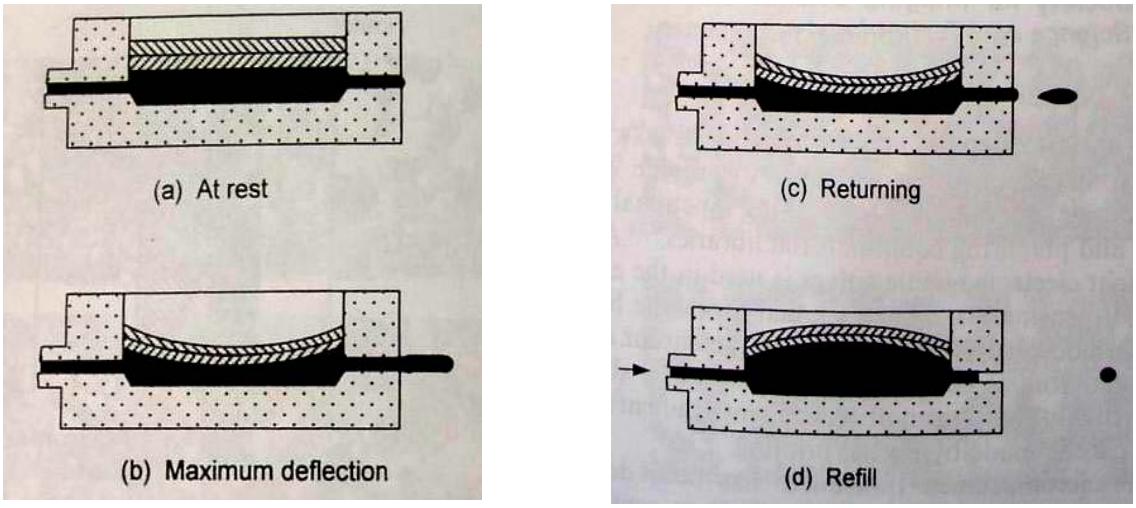

Figure 1.15. Schemantic diagram of piezoelectric drop-on-demand ink-jet printer[76].

There are two main types of ink-jet printer: continuous ink-jet printer and drop-on-demand (DoD) ink-jet printer. Their schematic diagrams are shown in Figure 1.14. and 1.15.

For a continuous ink-jet printer, a stream of droplets is formed without any print demand. That is to say, droplets through nozzle cannot be controlled to stop or start. Droplets are charged and deflected to their destination in an electric field and those not required are collected or recirculated. The DoD ink-jet printer is the most common reprographic jet printing method[43]. This method provides the control of the start-up and shut-down of the droplets through the nozzle. There are three main types printer: piezoelectric[76], thermal[75] and electromagnetic printer.

There are so many distinguishing advantage of direct ink-jet printing: high speed, no impact operation, electrical computer control, no post-printing, treatment, multi-ink capability and the capacity for rapid change of image[75]. This technology is widely used in many fields like combinatorial chemistry[77], tissue engineering[78] and hybrid microcircuits[79].

Fused deposition, or extrusion freeforming, is the main method used in this thesis, so more details are provided in the next section.

1.4 Extrusion Freeforming

Ancient civilization were well aware of the importance of pastes in making pottery, tiles and bricks[80] and extrusion as a main fabrication method of paste can be traced back to 4500-4000 BC in Egypt from where there is the evidence of coiled clay pots[3]. To date, with the development of computers, paste can be extruded into a desirable shape through a movable extrusion head which is controlled by a CAD file. This method is best described under the heading 'extrusion freeforming'.

1.4.1 The Process of Paste Extrusion Freeforming

To obtain a final extruded product, a number of unit processes are necessary in order to prepare a system by which the primal materials yield to the requirements of extrusion and the preformed extrudate is processed into a desired product.

Benbow and Bridgewater[80] described the process of flow in paste extrusion. The stages of forming a product by paste extrusion included dry mixing, wet mixing, high-shear mixing, degassing, extrusion, extrudate handling, cutting, drying and thermal processing. Drying mixing is a stage in which all of the solid components are mixed together in a dry state in order to get a uniform distribution. The solid components are not only the chemical constituents of the final product but also additives introduced to modify the paste rheology and bind the particles together in

drying and firing stages. Wet mixing is followed after the dry powders are mixed together. In this stage, liquid is added to the powders while further mixing is carried out until macroscopic uniformity is obtained. High-shear mixing is then employed to break down the agglomerates produced in the wet-mixing stage. Air entrapment could also happen in the wet-mixing stage. A degassing stage is introduced to remove entrapped gas by applying a vacuum the paste. In some extrusion approaches, a paste with high solids volume is needed so further concentration is applied to the paste. The paste is now ready for extrusion. Extrusion pressure is generated in this process and the extrusion pressure is very helpful for understanding the rheological properties of paste and deserves further discussion in the next section. The extrudate may be taken off from the substrate or die face and this handling requires more careful consideration as the extrudate is normally not strong and is deformed readily. In some applications, the preformed extrudate is cut into a desired shape and dimension so the cutting stage was introduced as the first of a number of finishing stages. Drying and thermal processing are common stages. The solvent evaporates out in the drying stage and dried extrudate is obtained. In thermal processing, the organic materials left in the extrudate are burned out and the mechanical strength of the extrudate is developed. The strength can be controlled by the firing temperature and time.

1.4.2 Extrusion Pressure Generated in the Paste Extrusion

Applied extrusion pressure is needed to press the paste into the die entry and the

die-land. Akdogan[81] pointed out that once the pressure drops along the die have been determined, estimation of the flow characteristics of the paste is possible. Understanding the nature of the flow in dies is helpful to control the extruder performance and extrudate qualities[82]. Inadequate control of the extrusion pressure causes some flaws of the extrudates like surface fracture[83,84] and lamination so extrusion pressure is an important factor for monitoring the extrusion process.

Benbow and Bridgwater demonstrated that the total extrusion pressure (P) to press particulate pastes, comprising fine particles suspended in a liquid continuous phase, through dies with circular cross section and having a square entry (shown in Figure 1.16), can be described by the followed equation[85,86].

$$p = p_e + p_1 = 2(\sigma_0 + \alpha V^n)\ln[D_0 / D] + 4(\tau_0 + \beta V^m)[L / D] \quad \text{..... (1.4)}$$

where p is total extrusion pressure of paste, p_e is die entry pressure of paste, p_1 is die land pressure of paste, α is a velocity-dependent factor for the convergent flow, β is the velocity-dependent factor for parallel flow, n and m are exponents, σ_0 is the paste bulk yield value, τ_0 is the paste characteristic initial wall shear stress, D_0 and D are the diameters of the barrel and of the die respectively, L is the die-land length and V is the extrudate velocity. In this equation, die-entry (Pe) and die-land (P_1) pressures are separated.

A coefficient of static friction for the extrudate (μ) has been demonstrated to be another relevant parameter in defining extrusion issues and the ultimate surface quality of samples[87] and can be calculated by the following relationship:

$$\mu = \frac{\tau_0}{\sigma_0} \quad \text{..... (1.5)}$$

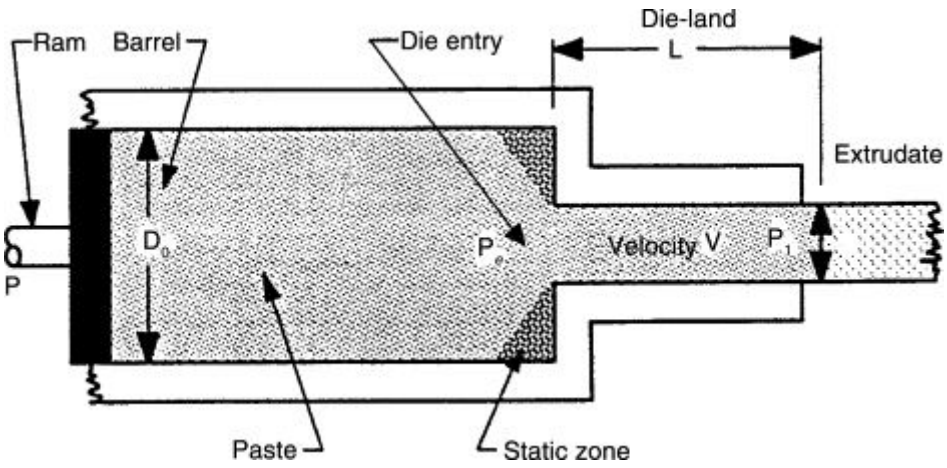

Figure 1.16. Schematic view of the extrusion through a square die in a ram extruder[87].

For highly concentrated solid-liquid suspensions or pastes, particularly as the solids volume fraction exceeds 50% and approaches the maximum packing fraction, particle-particle interactions and the use of non-Newtonian liquid phases result in these materials exhibiting non-Newtonian behaviour[7]. Extrusion features such as wall slip[88] and yield stress behaviour are frequently reported.

A typical pressure transient (shown in Figure 1.17.) during PTFE paste extrusion by means of the capillary reheometer was reported by Ochoa and Hatzikiriakos[89]. The whole pressure curve has been divided into three zones. The pressure gradually

increases and goes through a maximum in zone I and then presents a steady state in zone II. Finally, the extrusion pressure gradually increases again in zone III. In previous work, the pressure peak appeared in zone I has contributed to the initial filling and wetting of the conical zone of the die[90, 91, 92,85]. But Ariawan et al.[93, 94] demonstrated that the pressure peak still appeared when the conical zone was filled before extrusion. For the visco-elasto plastic materials, Ochoa and Hatzikiriakos attribute the pressure peak to the yield stress and to particles initial jamming[89].

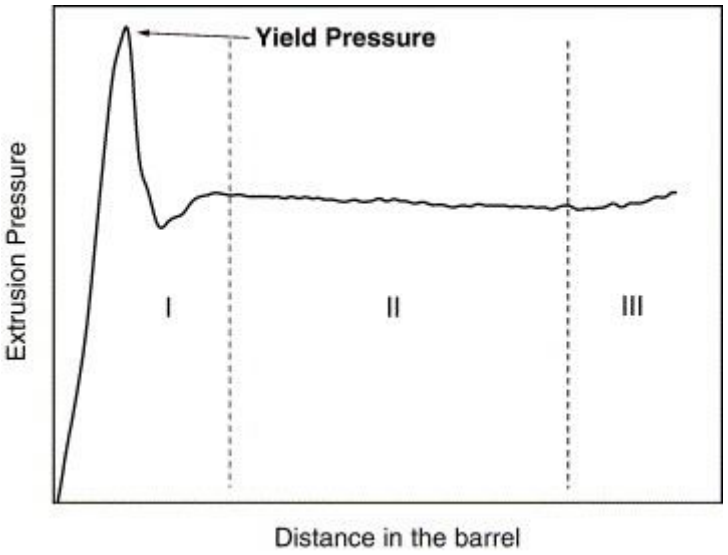

Figure 1.17. Typical behaviour of a pressure transient during PTFE paste extrusion[89].

As shown in Figure 1.18, the extrusion was stopped and restarted after different relaxation times. If the extrusion was restarted after a small relaxation period, the pressure to initiate the paste flow was very small compared to the initial maximum pressure. But after long relaxation time, the immobile clusters of particles had been reinstated completely and the maximum pressure in this case was equal to the initial

maximum pressure. The gradual increase of the extrusion pressure in zone III is because the solvent evaporation during the extrusion process caused the final part of the paste to become drier.

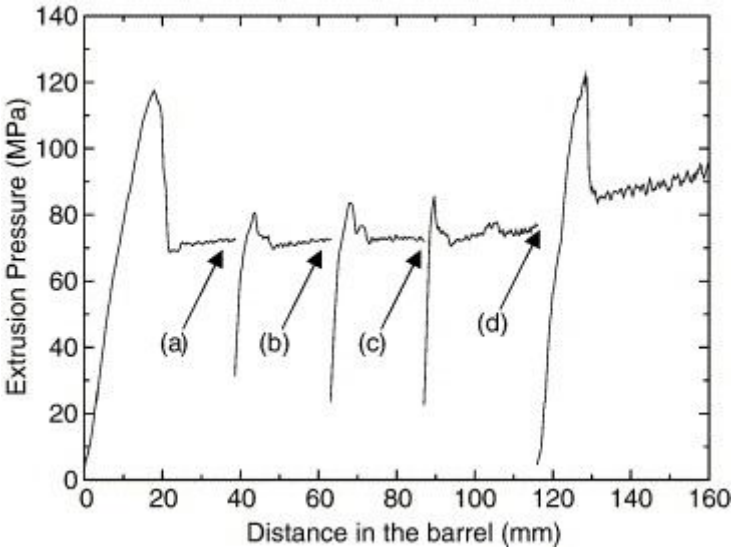

Figure 1.18. PTFE paste extrusion[89]. The extrusion was (a) stopped and restarted after 1.5 min. (b) The extrusion was stopped and restarted after 10 min. (c) The extrusion was stopped and restarted after 45 min. (d) The extrusion was stopped and restarted after 40 h.

Extrusion fluctuation can be induced by some defects of the paste like entrapped gas, agglomerates and undesired voids[95]. It has previously been reported that the incidence of extrusion defects in PTFE pastes can be reduced if the paste is subjected to a static pressure of about 2 MPa in the die at 35°C for 30s[96, 91, 94]. This is effectively a pre-extrusion compaction and it may operate by allowing rearrangement of PTFE particles.

1.4.3 Different Extrusion Methods and Comparisions

The application of the movable extrusion head controlled by computer has spawned a range of construction methods[43]. Fused deposition of ceramic (FDC), a technology developed and commercialized by Stratasys Inc. (USA)[39], is applied to the processing of polymer, wax and ceramic suspension in a polymer or wax vehicle. The schematic diagram of this method is shown in Figure 1.19. Filament is fed into a heated FDC head by rollers as a solid rod. The filament in the FDC head is heated to its molten state. The filament between rollers and heated FDC head must be stiff enough and resistant so that it can extrude the filament in the FDC head through the orifice acting as a piston. Then the filament is deposited onto a substrate by the nozzle which moves according to the patterns defined by the CAD files. The extruded filaments bond each other by contact fusion. By natural cooling, the molten filament changes its phase and solidifies rapidly. The powders must be well dispersed in the suspension and agglomerates and debris must be removed, otherwise the viscosity of the molten filament will vary and induce a fluctuating pressure.

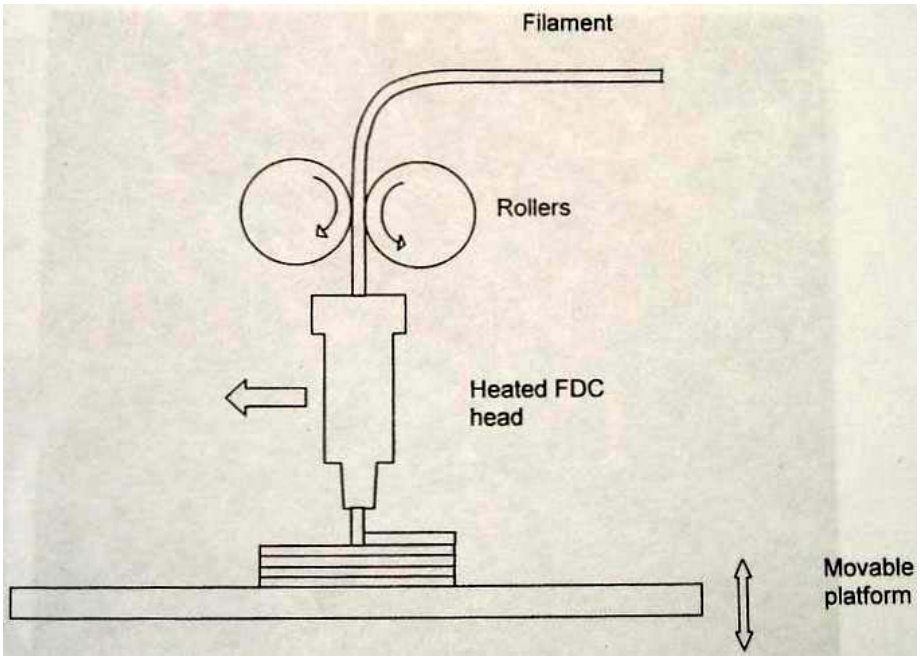

Figure 1.19. Schematic diagram of fused deposition of ceramics process[97].

Many processes similar to FDC, including fused deposition modeling (FDM)[98], fused deposition of multiphase materials (FDMM)[99] and multiphase jet solidification (MJS)[100], have been developed. Tseng and Tanaka[101] have developed a novel technique in which filaments with different diameter can be extruded by an adjustable nozzle. As shown in Figure 1.20, a conical orifice provides a variable circular cross-section of filament.

By moving a conical spindle head vertically with respect to variation of the orifice, the filament extruded through the orifice can be regulated.

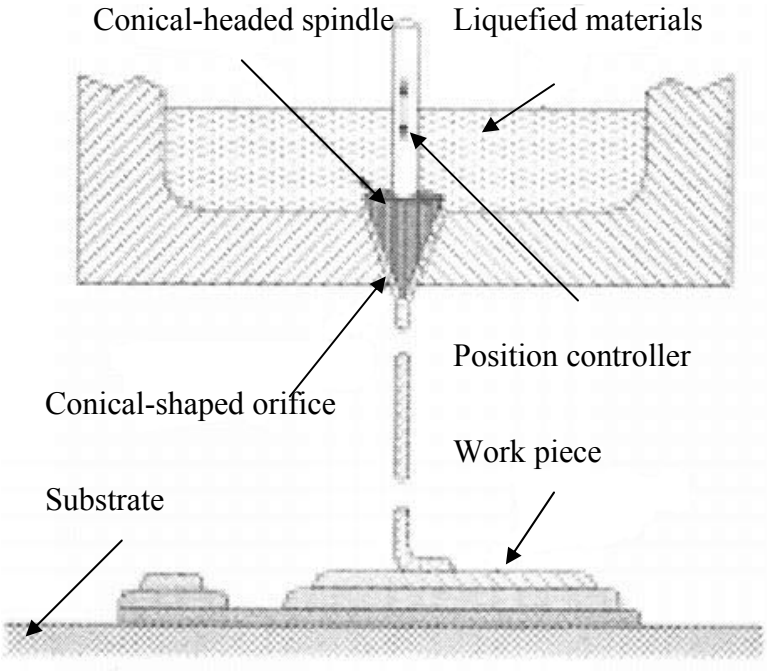

Figure 1.20. Schematic adjustable circular nozzle in extrusion freeforming[101].

Another version of extrusion freeforming, developed at Sandia National Laboratories, USA[102], is named 'robocasting'. Robocasting makes progress for its moldless and quicker fabrication time; moreover, robocasting does not require organic polymerization reactions or solidification of a polymeric melt to maintain the shape of components in contrast to gel casting and other freeform fabrication techniques[42]. Schematic illustrations of the robocasting apparatus are shown in Figure 1.21[104].

In these mouldless ceramic fabrication methods, the main difference is the method of state change. Robocasting uses temperature control on a copper substrate to transform each layer from pseudoplastic (61 vol. % powder) to dilatant (64 vol. %) [42, 102, 103]for which further deformation is prevented. To avoid this complex control of drying

kinetics, colloidal inks have been developed for robocasting and are assembled under non-wetting oil to prevent drying during assembly[104, 105].

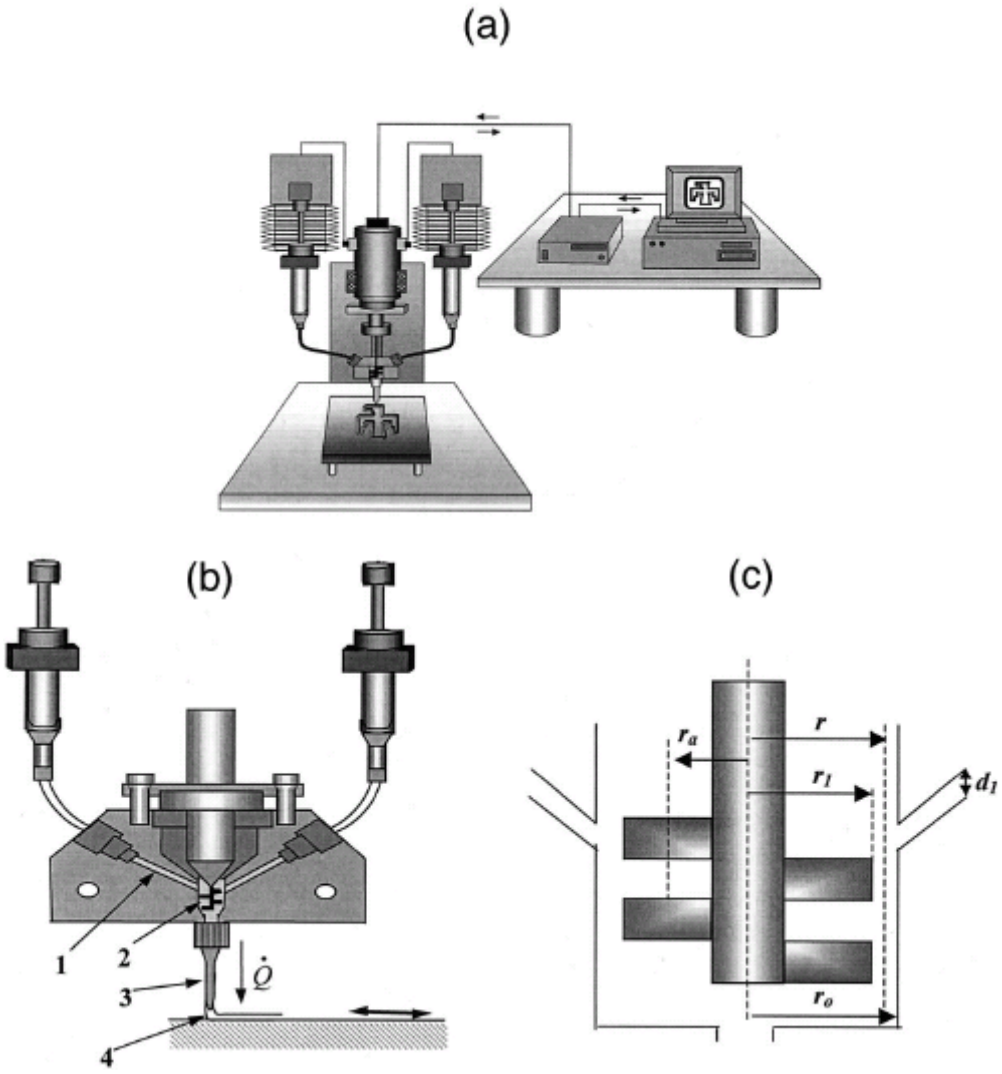

Figure 1.21. Schematic illustrations of (a) robocasting apparatus, (b) two-nozzle delivery system showing four shear zones in the mixing chamber (1) pumping from the syringe, (2) mixing via paddle mixer, (3) extrusion from the tip and (4) deposition onto the moving X–Y table, and (c) paddle design, where r=5 1.651 mm, r_a=5 0.89 mm, r_1= 5 1.59 mm, r_0=5 1.72 mm, and d_1=5 1.52 mm.[104]

As referred above, the extruded filaments in the extrusion freeforming solidify by phase change and evaporation. Another solidified mechanism, polymerization, has been used in direct writing, a propagation of extrusion freeforming[106].

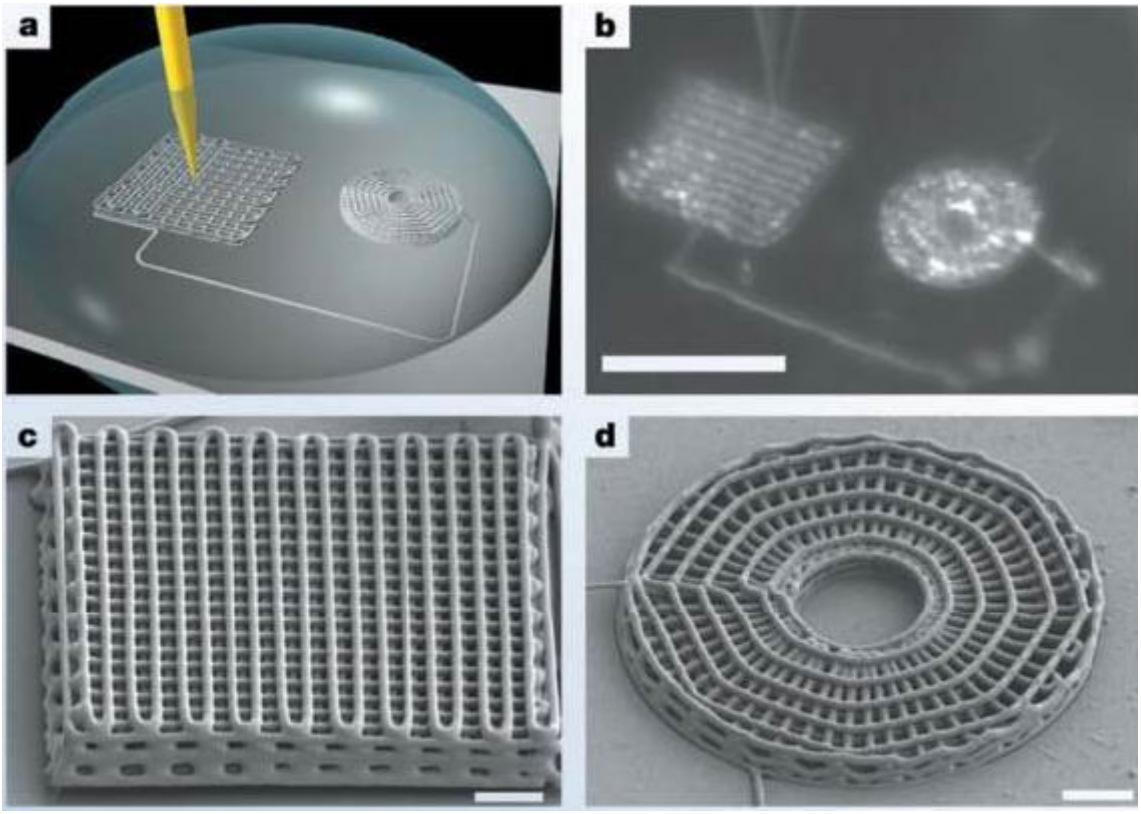

Figure 1.22. Direct-write assembly of three-dimensional microperiodic structures[106].

The inks used in this process are concentrated polyelectrolyte complexes that consist of non-stoichiometric mixtures of polyanions (polyacrylic acid, PAA) and polycations (polyethylenimine, PEI, or polyallylamine hydrochloride, PAH). By regulating the ratio of anionic (COO^-Na^+) to cationic (NH_x^+), the inks have a requisite viscosity and homogeneity. The fluid inks are extruded into a coagulation reservoir through fine deposition nozzle and then solidify rapidly (Figure 1.22 a and b.). Three-dimensional

microperiodic lattices and radial arrays assembled from the PAA/PEI ink are shown in Figure 1.22 c and d.

The freeforming method used in this project has several advantages over the use of stereolithography for ceramics a competing solid freeforming process which also uses pastes. It can produce sharply defined internal curvatures and avoids the necessity to remove uncured paste from deep recesses which would be a problem when making the fine, deep porous structures described here. The use of a solidification processes based on solvent evaporation has the advantage over the Robocasting™ process where the state change is based on a dilatant transition because it can deliver much finer filaments. It avoids the thermal management issues of Fused Deposition Modelling and the polymerisation control of monomer-based extrusion freeforming. In this project, the versatility of the method is explored not just in terms of structure and filament dimension but in terms of the capability to make use of many different powders to serve different applications.

1.4.4 Measurement of Viscosity by Capillary Viscometry

The success of extrusion freeforming partly depends on the paste viscosity and yield stress. Viscosity is defined[107] as the ratio of shear stress to shear rate which can be expressed by the equation below.

$$\sigma = \eta\dot{\gamma} \quad \text{..... (1.6)}$$

where σ is the shear stress, $\dot{\gamma}$ is the shear rate and η is the viscosity for which the SI units are Pa s.

For some suspensions, the viscosity is constant and does not vary with shear rate. Such behaviour is designated Newtonian. In the vast majority of cases, the viscosity varies with the shear rate and is non-Newtonian. For some suspensions, the viscosity decreases with increase in shear rate and this is called 'shear-thinning' behaviour. The term 'pseudoplastic' is employed to describe this kind of suspension. For some suspensions, the viscosity increases with shear rate and this behaviour is generally called 'shear-thickening'. The term 'dilatant' is used to describe this kind of suspension. Figure 1.23 shows a shear stress versus shear rate schematic diagram which represents typical behaviours of different suspensions. Notice that 'Bingham' plastics are pseudoplastic but will not flow until a yield stress is exceeded.

Several methods of measurement of viscosity, such as the cone-and-plate viscometer, the parallel-plate viscometer and capillary viscometer are described by Barnes[108] and Cogswell[109] etc.. In this experiment, the capillary viscometer is the most appropriate instrument for assessing pastes for extrusion freeforming because the flow geometry is similar.

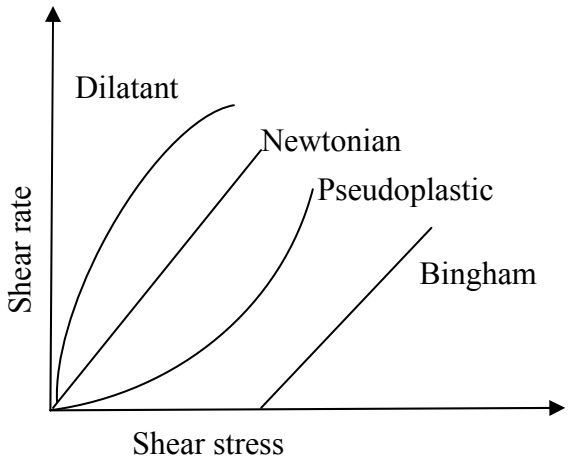

Figure 1.23. Typical shear rate/shear stress graphs of different suspension[110].

According to the Poiseuille law for capillary flow, the wall shear stress, σ_s and the wall shear rate, $\dot{\gamma}$ can be expressed by the equations below[109].

Wall shear stress, $\sigma_s = \frac{PR}{2L}(\mathrm{N/m^2})$…… (1.7)

Wall shear rate, $\dot{\gamma} = \frac{4Q}{\pi R^2}(\mathrm{s^{-1}})$…….. ..(1.8)

where P is the pressure drop (N/m^2), Q is the volume flow rate (m^3/s), R is the capillary radius (m) and L is the capillary length (m).

However, the situations which influence the variation of the viscosity with the shear rate are complex and a series of corrections are applied. These include the end effect pressure drop (Bagley correction), the Rabinowitsch correction and correction for slip

at the die wall. These are introduced to obtain the true viscosity when measuring high viscosity fluids by capillary flow[109].

When the wall shear rate is constant, the pressure drop is linearly variable with the die length-radius ratio in capillary flow[111]. So the shear stress in capillary flow can be corrected as: $\sigma_s = R/2(\frac{dP}{dL})\ \sigma_s = R/2(\frac{dP}{dL})$. In practice, the pressure gradient is determined by combining a long die (e.g. L/R=32) with an orifice (L/R=0) such that the wall shear stress can be expressed as below.

$$\sigma_s = (P_L - P_O)R/2L \quad \text{..... (1.9)}$$

where P_L is the pressure drop through a long die and P_O is the pressure drop through an orifice die (die with L/R<<1) of the same diameter at the same flow rate. A serious of dies with constant radius and different length can be used to obtain the Bagley end correction.

The Rabinowitsch correction is used to correct for the non-parabolic velocity profile of a non-Newtonian suspension and is simply expressed in the form:

true wall shear rate, $\dot{\gamma}_{true} = (\frac{3n+1}{4n})\frac{4Q}{\pi R^3}$ ..... (1.10)

where n is the flow behaviour index and is the exponent in the relationship between shear stress and (shear rate)^n as obtained from logarithmic plots. For a shear-thinning

suspension, the power law index n is less than 1. For a shear-thickening, the power law index n is bigger than 1.

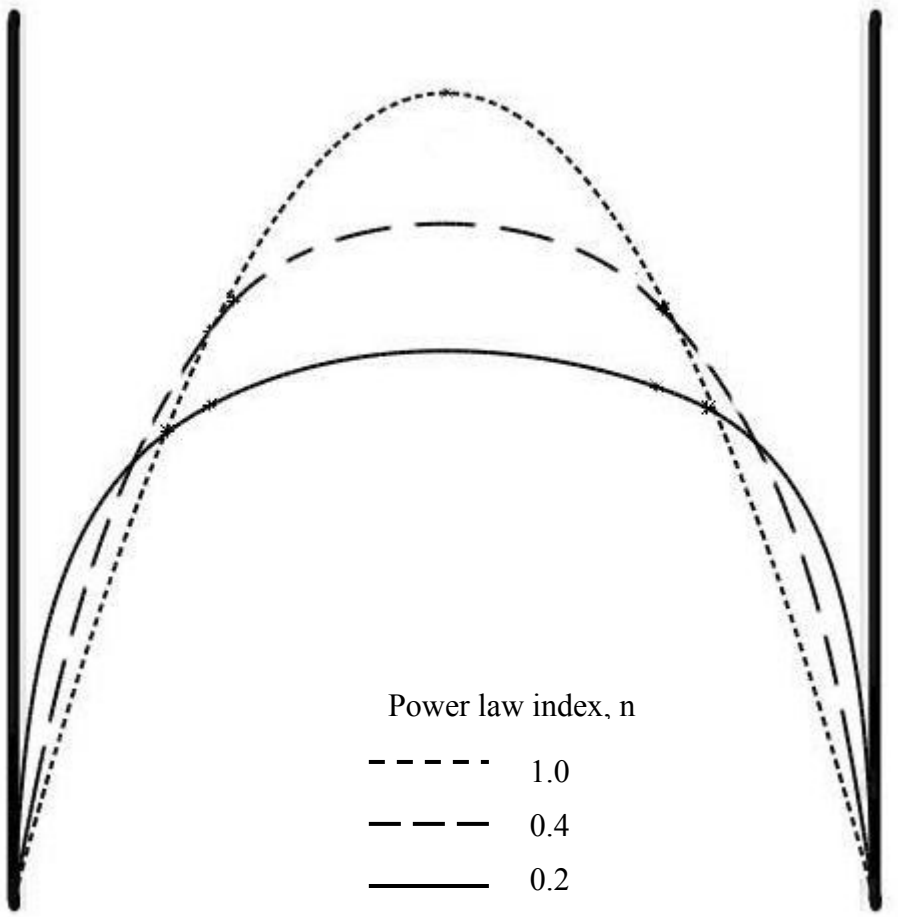

Figure 1.24. Steady state velocity profile for flow of a power-law suspension in a straight circular pipe, calculated for the same volumetric throughput.

For Newtonian suspension, the steady state velocity profile in a cylinder is parabolic. As the power law index n decreases, i.e. the degree of the shear thinning increases, the wall shear rate and the plug-like nature of the flow increases as shown in Figure 1.24.

In practice, wall slip most commonly occurs with systems which are believed to have multiphase compositions rather than molecular flow mechanism[109]. The apparent shear rate of the flow in the presence of wall slip can be measured by using the dies with different radii but the same L/R at a given pressure gradient, when

volume flow rate, $Q = \frac{\pi R^3}{4}\dot{\gamma}_{true} + \pi R^2 v$ .....(1.11)

apparent shear rate, $\dot{\gamma}_A = \frac{4Q}{\pi R^3} = \dot{\gamma}_{true} + \frac{4v}{R}$ .....(1.12)

where v is the wall slip velocity.

For general purposes, it is sufficient to measure the flow properties without considering slip at the die wall. But if slip is suspected to influence the rheology, then wall slip should be evaluated in discrete experiments.

The viscosity of suspensions is very sensitive to powder loading especially at high volume fractions[112] and can be modelled by using a range of functions of powder volume fraction if the viscosity of the suspension is expressed by relative viscosity as below[113].

$\eta_r = \eta / \eta_0$ ..... (1.13)

where η_r is the relative viscosity. η_0 is the viscosity of the unfilled organic vehicle measured under identical conditions. For an extremely dilute suspension of spherical

solid particles, Einstein's equation provides a simple theoretical expression for the relative viscosity of a suspension[114]:

$$\eta_r = 1 + 2.5V \quad \text{(1.14)}$$

One of these functions is presents by Mooney[115] and offers a good fit to experimental data at high powder loadings:

$$\eta_r = \exp\left(\frac{2.5V}{1 - kV}\right) \quad \text{(1.15)}$$

where k is $1/V_m$ and V_m is the maximum packing fraction. The following function was proposed by Eilers[116]:

$$\eta_r = \left(1 + \frac{1.25V}{1 - V/V_m}\right)^2 \quad \text{(1.16)}$$

Chong, et al.[117] present:

$$\eta_r = \left[1 + 0.75\frac{V/V_m}{(1 - V/V_m)}\right]^2 \quad \text{(1.17)}$$

From these equations, the viscosity of suspensions approaches infinity as the powder volume loading rises to V_m. A schematic which represents the typical relationship between relative viscosity and powder volume loading is shown in Figure 1.25.

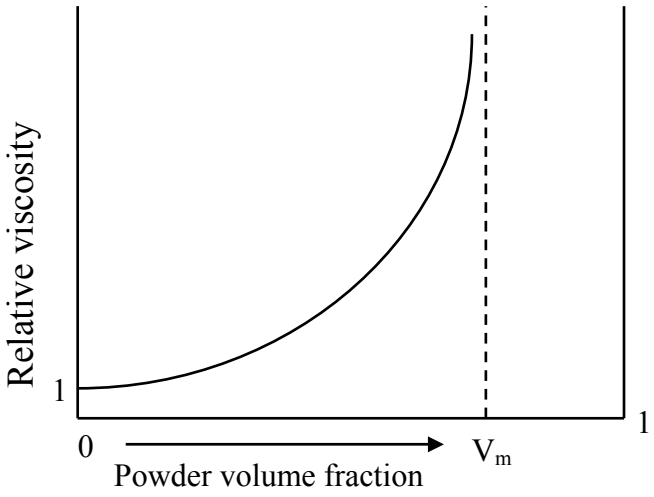

Figure 1.25. A schematic represents the typical relationship between relative viscosity and powder volume fraction.

The equations of Mooney, Eiler and Chong were compared by Zhang et al.[112] Chong's equation provided be best fit to the experimental data and was a modification of the earlier Eiler's. One of the difficulties in assessing the viscosity of suspension is that no single equation gives a good fit to the large amount of experimental data for diverse suspensions.

2 Experimental Details

2.1 Materials

The materials used in this experiment were as follows: (i) alumina powder (Al_2O_3, ex Condea Vista, Tucson Arizona), having a purity of 99.992%, surface area of 10 m^2g^{-1}, typical particle size of 0.48 μm and density of 3960 kgm^{-3}; (ii) hydroxyapatite powder (HA, $Ca_{10}(PO_4)_6(OH)_2$, Grade P221 S, Plasma Biotal Ltd. UK) with density of 3156 kgm^{-3}; (iii) β-tricalcium phosphate powder (β-TCP, $Ca_3(PO_4)_2$, Grade P228 S, Plasma Biotal Ltd. UK) with density of 3070 kgm^{-3}; (iv) poly(vinyl butyral) (PVB, Grade BN18, Whacker Chemicals, UK) with density of 1100 kgm^{-3}; (v) poly(ethylene glycol) (PEG, M_{Wt} = 600, Whacker Chemicals, UK) which is a liquid at ambient temperature and has a density of 1127 kgm^{-3}; (vi) carbon powder which is grade "Mogul L" from Cabot Carbon Limited (Cheshire, England) and has a density of 2100 kgm^{-3}; (vii) propan-2-ol (GPR, Whacker Chemicals, UK) with density of 789 kgm^{-3}.

The hydroxyapatite powder (HA, $Ca_{10}(PO_4)_6(OH)_2$) and the β-tricalcium phosphate powder (β-TCP, $Ca_3(PO_4)_2$) were calcined at 900°C and milled in water for 96 h. Manufacturer's XRD data, confirmed in our laboratory by Dr. Hongyi Yang, show that these are better than 95% phase pure. The morphology and particle size were assessed by scanning electron microscopy (SEM, JEOL JSM6300F, Japan) and SediGraph (model 5100, Micromeritics, Norcross, GA, USA) respectively. The

alumina powder (Al_2O_3) was calcined at 900°C and milled in water for 96 h.

2.2 Paste Preparation

2.2.1 Paste Formulation

Three different pastes were used in this experiment: alumina, carbon and a paste consisting of a mixture of HA powders and β-TCP powders. PVB was used as the binder in these three different pastes with additions of a grade of PEG that is liquid at ambient temperature.

The paste consisting of alumina powder was prepared as follows. The PVB and the PEG were fully dissolved in propan-2-ol in proportions 75 wt.% PVB – 25 wt.% PEG. Alumina powder was added to provide a ceramic/polymer mixture with 60 vol.% of ceramic based on the dry mass.

A mixture of HA powder and β-TCP powder was used and both powders meet the chemical purity specifications for clinical use. A powder blend with HA 75 wt. %-TCP 25 wt. %,[118] was selected and used to provide a ceramic/polymer mixture with 60 vol.% of ceramic based on the dried paste. The polymer in this paste also consisted of PVB and PEG with the proportions of 75 wt.% PVB – 25 wt.% PEG.

For the carbon paste, to get suitable fluid behaviour, a higher polymer fraction was added. Carbon powder with 50 vol.% based on the dry mass was mixed with polymer. The polymer in this paste also consisted of PVB and PEG with the proportions of 75 wt.% PVB – 25 wt.% PEG.

2.2.2 Method for Preparing Pastes

The ceramic or carbon powders were poured into a beaker with the polymer components which had been fully dissolved in propan-2-ol (GPR, VWR, UK) and the mixture was stirred and heated on a hotplate with magnetic stirrers (Barloworld Scientific Ltd., Staffordshire, UK,). Then an ultrasonic probe (IKA U200S, IKA Labortechnik Staufen, Germany), shown in Figure 2.1 (a) was used to disrupt the agglomerates and make the powders disperse evenly in propan-2-ol. To prevent the paste from sedimenting, the suspension was poured into plastic bottles and was agitated on a roller mixer SRT2 table (Barloworld Scientific Ltd., Staffordshire, UK, Figure 2.1 (b)). The suspension after dispersion by ultrasonic probe was concentrated on the hotplate with magnetic stirrers to develop a suitable paste for extrusion.

The method of state change used here results from a decrease of solvent content. The paste composed of ceramic, polymer and solvent has a high yield stress but is able to weld to the previous layer before solidifying by solvent evaporation. Sufficient polymer content (≈32vol. % based on wet paste) eliminated extrusion defects

resulting from dilatancy often found in water-based systems. High ceramic content (minimum based on wet paste ≈48vol. %) results in low sintering shrinkage. The different volume percentages based on the wet paste and on the dry paste are shown in Table 2.1. Low solvent content results in low drying shrinkage. The high yield stress of the paste minimises deformation during fabrication giving higher manufacturing precision.

Table 2.1. Composition of all pastes in volume percent based on wet and dry paste.

	Volume percent based on wet paste/vol.%	*Volume percent based on dry paste/vol.%*
polymer	32	40
Ceramic powder	48	60
solvent	20	0

This method can be used to knit any conceivable two-dimensional extruded filament pattern layer by layer. The non-volatiles (ceramic + polymer) constitute typically 70-80 vol. % of the mixture and 20-30 vol. % is volatile solvent (usually propan-2-ol). The drying-induced shrinkage after assembly was minimized to reduce distortion of the lattice.

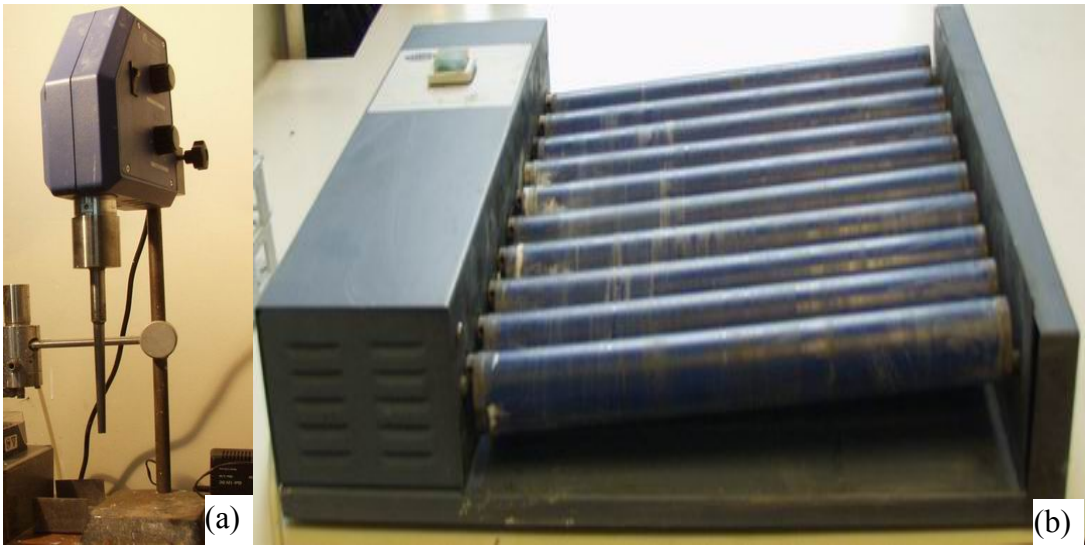

Figure 2.1. Equipment for paste preparation: (a), ultrasonic probe for suspension dispersion; (b), roller mixer table to avoid paste sedimentation.

2.3 Extrusion Freeforming worktable

2.3.1 Extrusion Freeforming Procedure

A schematic diagram of the extrusion freeforming worktable is shown in Figure 2.2. The paste was extruded into filaments from an extruder (Figure 2.2. a) by a lead screw (Figure 2.2 c) driven by a stepper motor with gear box (Figure 2.2 d). A load cell (Figure 2.2 b) was used to record the pressure and provide the over-load alarm. The filaments were drawn into different structures by moving the substrate which was controlled by the X, Y table axes, to give a series of 2D samples. To get a 3D sample, the Z axis (Figure 2.2 e) driven by a stepper motor (Figure 2.2 f) was used to control the vertical movement of the whole press axis. In this way, a 3D sample can be made layer by layer. To control the Z axis accurately, a proximately sensor (Figure 2.2 h) was used here.

Only four motion controllers were used. One was used to control the Z axis; another two were used to control the X, Y table axes separately. The last motion controller was used to control the two lead screws to extrude the paste. So a frequency divider (Figure 2.2 g) was used here. These four motion controllers were controlled by a computer through the LabVIEW software.

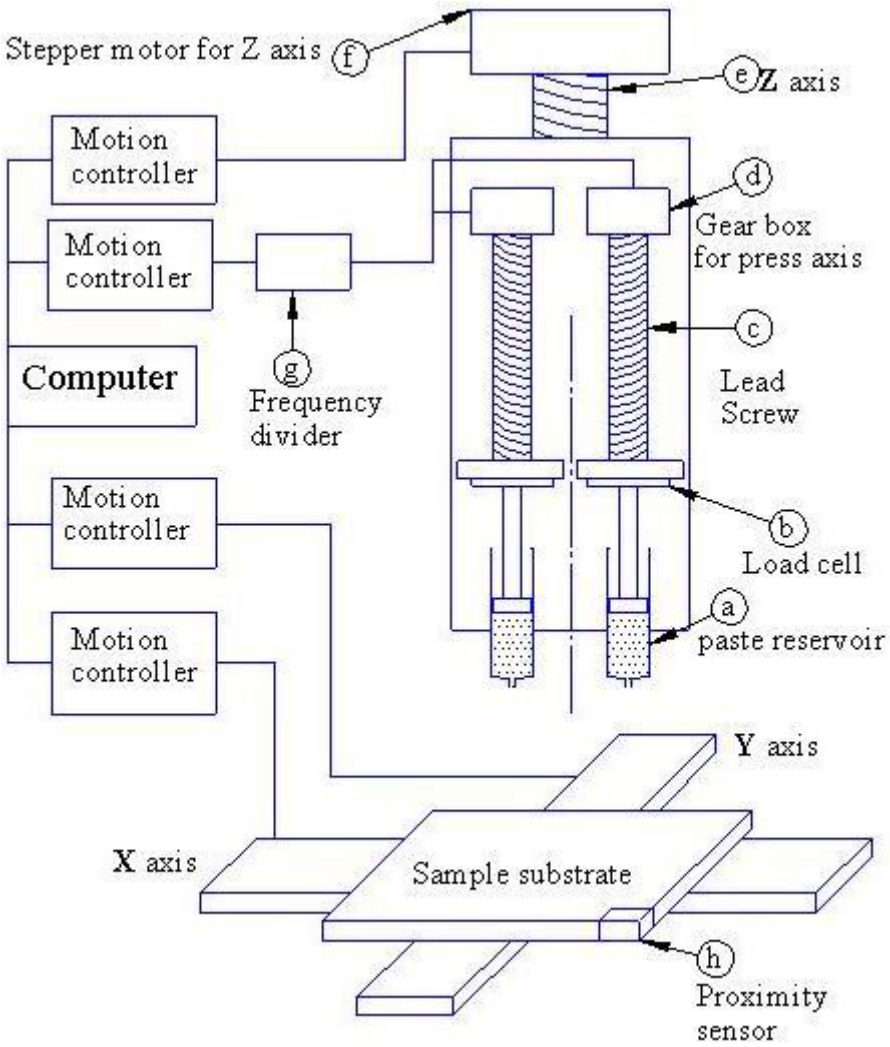

Figure 2.2. Schematic of the extrusion freeforming worktable.

2.3.2 Extrusion Freeforming Assembly

The extrusion freeforming equipment is shown in Figure 2.3. A press head driven by micro-stepper motors (50,000 steps/rev, supplied by ACP&D Ltd., Ashton-under-Lyne, U K. Figure 2.3 a) with a 64-1 reduction box driving 1mm pitch ball screws (Automation Ltd., Oldham, UK) was used to drive the extruder for the paste. The three-axis table (Parker Hannifin Automation, Poole, Dorset, UK) comprises linear servo motors driving the X, Y table axes and stepper motors driving the Z axis (Figure 2.3.). In the earlier version of the extrusion freeforminig worktable, lead screws were used as the X, Y table but they were replaced by the current high performance linear servo motor table (MX80L Miniature Stage, Parker Hannifin Automation, Poole, Dorset, UK) capable of high acceleration (49 ms^{-2}), speed (3 ms^{-1}) and encoder resolution to 0.1 μm due to the problem of locking at sharp reverse turns. A sensor (Flintec Ltd., Redditch, UK) monitored extrusion load and provided an overpressure alarm. The worktable was controlled by Labview software (National Instruments, US).

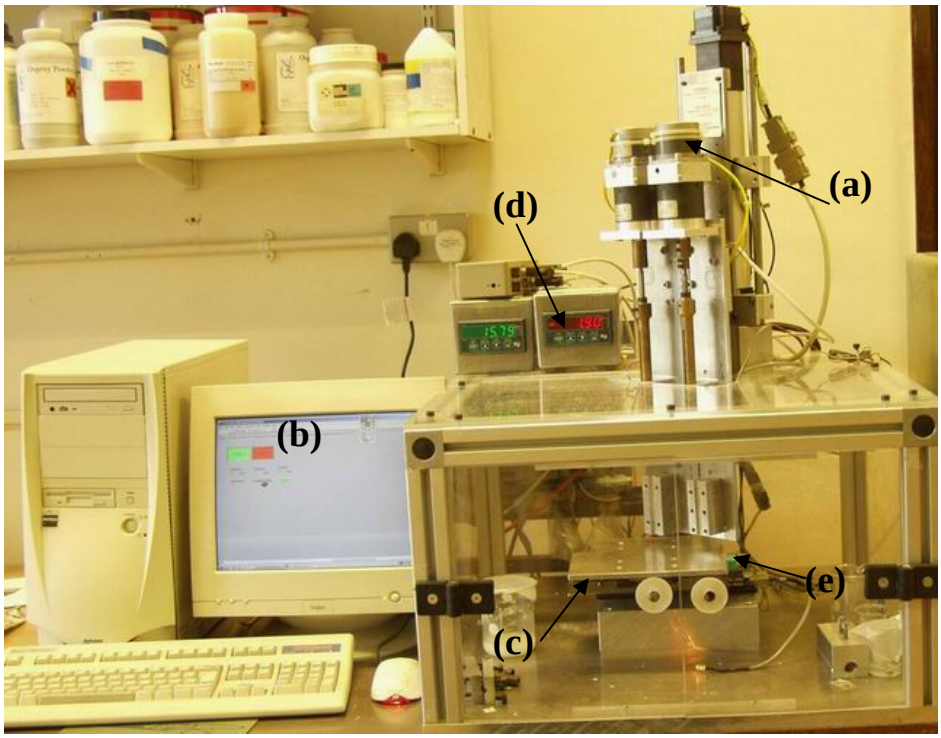

Figure 2.3. Extrusion freeforming apparatus, (a) micro-stepper motors, (b) operating system, (c) load cell meters (d) linear motor XY table, (e) the proximately sensor.

Two press axes were needed in the co-extrusion experiments, so a frequency divider (shown in Figure 2.4.) was used. In the co-extrusion experiments, the signals from the motion controller were divided and exported through ‘OUT1’ and ‘OUT2’ to control the two different press axes at different rates. Different pressure ratios of the two press axes can be obtained by changing the data on ‘A’ and ‘B’. When only one press axis was used, the frequency divider was by-passed.

Figure 2.4. Frequency divider for the press axes.

In the bone substitute scaffold extrusion experiment, hypodermic syringes (HGB81320 1ml, Hamilton GB, Ltd., Carnforth, U.K. shown in Figure 2.5. a) were used as extrusion cylinders, plungers and nozzle. In the co-extrusion and alumina extrusion experiments, the glass syringe was easily damaged and was replaced by a metal syringe. The design drawing for this is shown in Figure 2.5 b. The extrusion dies were assembled from sapphire water-jet cutting nozzles (model 1715, Quick-OHM Küpper & GmbH, Wuppertal, Ger.) supported in stainless steel and brass seals. These were inserted into hypodermic needles to suite the hypodermic syringe. For the metal syringe, a special 'insert' (shown in Figure 2.5 b) was designed to accept these nozzles.

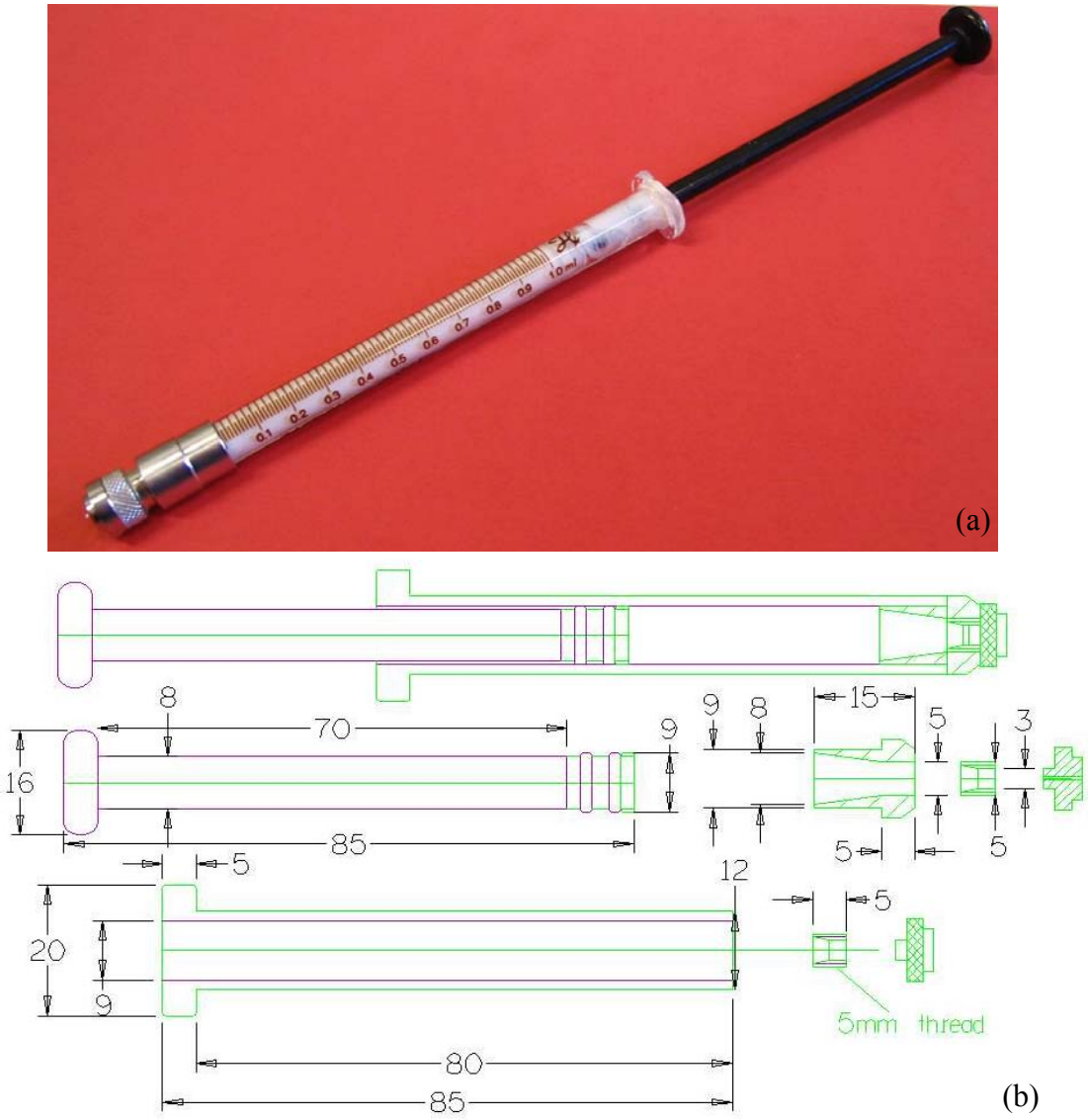

Figure 2.5. (a), Hypodermic syringe with a water-cut jet nozzle; (b), design drawing of the metal syringe and nozzle.

The earlier co-extrusion die was made of two brass parts and two hypodermic nozzles as shown in Figure 2.6. The outer paste was extruded into a channel through a hypodermic nozzle from which the needle had been removed, and then was extruded from a brass outer nozzle. The inner paste was extruded from a hypodermic needle. Figure 2.6 shows the two hypodermic syringes containing outer paste and inner paste

separately and the distance between the two syringes was fixed. However in the process of extrusion, the positions of the syringes were not absolutely vertical, so the glass syringes were dragged away and frequently broken. Although metal syringes were used in replacement, the force was so strong that the hypodermic nozzle fixed on the brass part by a screw was dragged off. So the hypodermic nozzle had to be silver soldered to the brass part and this made cleaning difficult. Another disadvantage was that the brass parts had to be disassembled to clean up after every extrusion and this meant breaking the seal. The paste leaked out through the connective edge of the two brass parts.

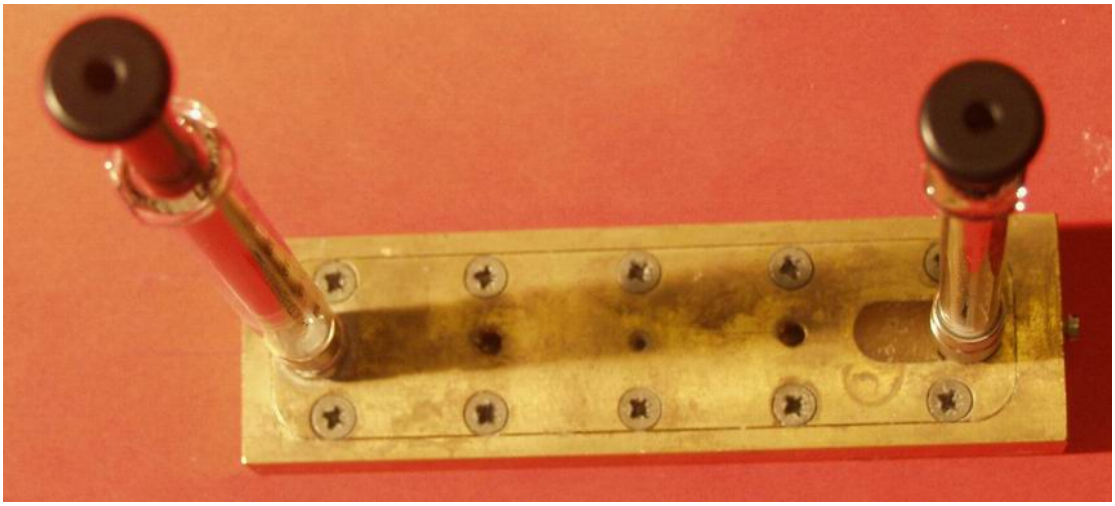

Figure 2.6. The earlier co-extrusion die with two hypodermic syringes.

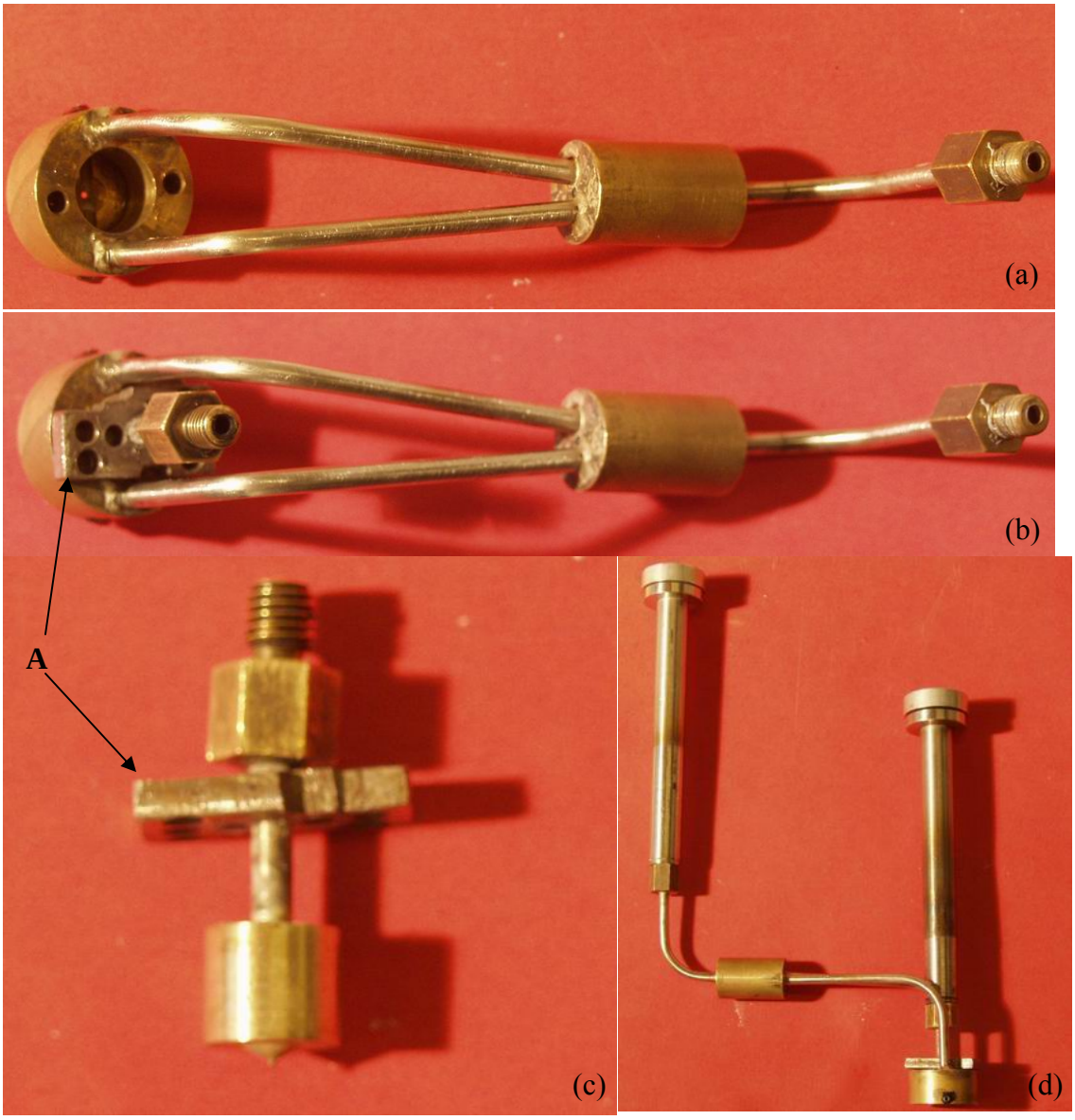

Figure 2.7. The superior co-extrusion die: (a), outer nozzle with steel tubes; (b), assembly of the inner nozzle and outer nozzle; (c), inner nozzle; (d), co-extrusion die with metal syringes.

In the superior co-extrusion die (shown in Figure 2.7.), the channel in the brass parts of the earlier co-extrusion die was replaced by steel tubes. These avoided the paste leaking from the connective edge of the two brass parts. The hypodermic nozzles were abandoned. The inner and outer nozzles were made of brass, their design

drawings are shown in Figure 2.8. From Figure 2.8, the inner diameter of the inner nozzle was 0.2 mm; the outer diameter was 0.3 mm. The die land of the inner nozzle was 1 mm. The diameter of the outer nozzle was 0.5 mm. The conical entries were used in the inner and outer nozzles to make the paste flow more easily. The inner nozzle was inserted into the outer nozzle and then the two nozzles were tightly screwed together through a metal flange (shown in Figure 2.6. A). The inner nozzle was able to be easily separated from the outer nozzle through another two screws on this metal flange. The outer paste was extruded into a steel tube by a metal syringe, and then divided into two tubes through a brass part with 'Y' channel. Through these two tubes, the outer paste was extruded into outer nozzle symmetrically and then was extruded into a filament with uniform thickness.

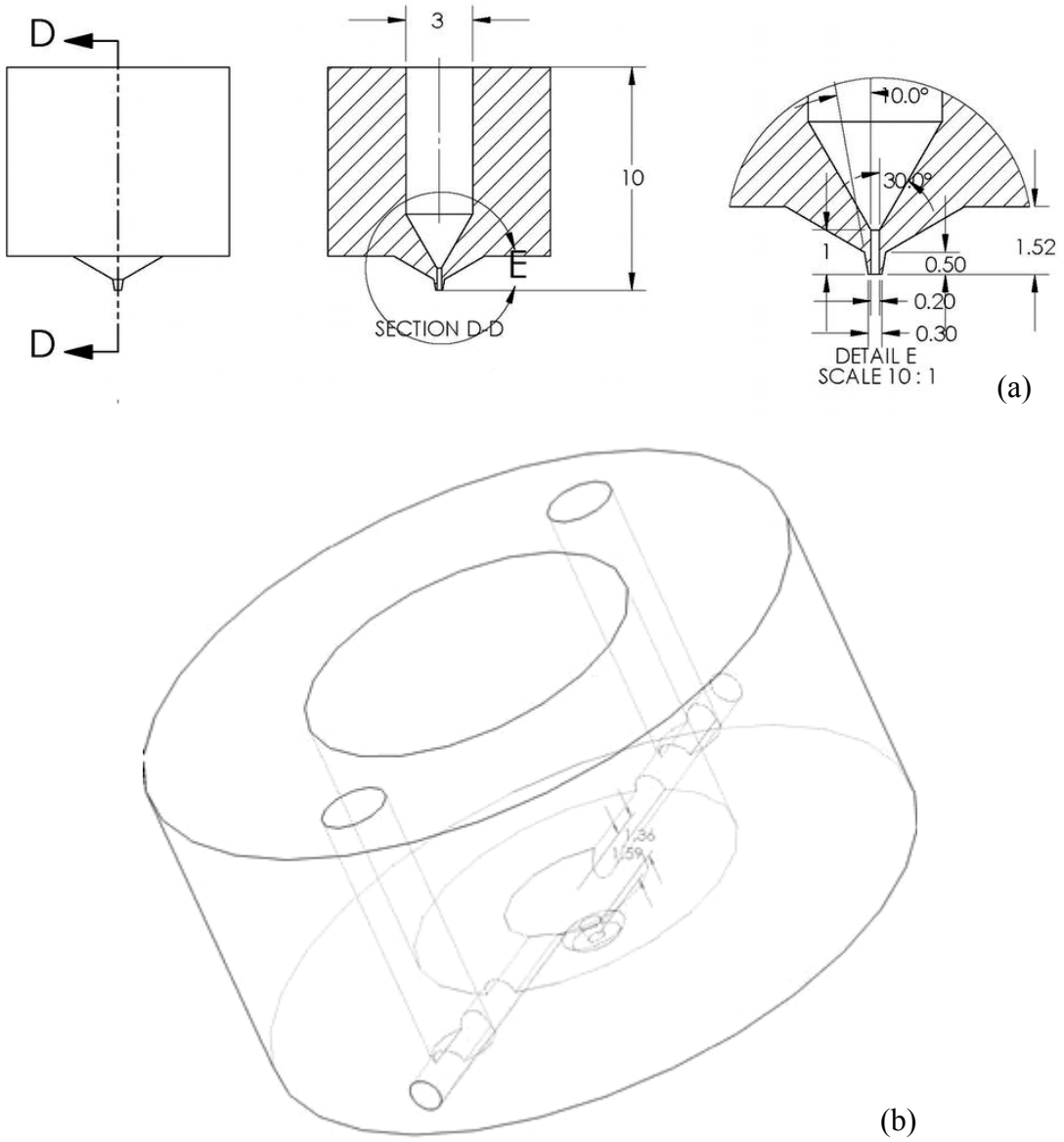

Figure 2.8. Arrangement of the co-extrusion die: (a), the drawing of the inner nozzle; (b), 3D arrangement of the outer nozzle.

2.3.3 Equipment for Three Point Loading Measurement

To estimate Weibull modulus of the ceramic filaments, flexural strength of the filaments was measured following as closely as possible the procedure of ASTM C1161-94. A schematic diagram of the equipment for three-point loading is shown in

Figure 2.9. In this schematic diagram, a press head was fixed on a metal beam and driven by the lead screw of the extrusion worktable to press the sample for testing. A strain gauge was attached to the metal beam to record the flexural strain with a Wheatstone bridge and a chart recorder. This equipment was driven by the extrusion worktable. The bottom platform to hold the sample for testing was designed to fit the syringe holder of the extrusion worktable. When the press head loads the sample for testing, deformation of the metal calibrated beam to which the strain gauge was attached occurs. This deformation changes the resistance of the strain gauge. From the circuit diagram of the strain gauge and Wheatstone bridge (shown in Figure 2.10), the strain gauge formed the variable resistor R_1 in the Wheatstone bridge, R_2, R_3 and R_4 were resistors with known resistance. As the resistance of the strain gauge changed, the voltage exported to the chart recorder was changed and recorded.

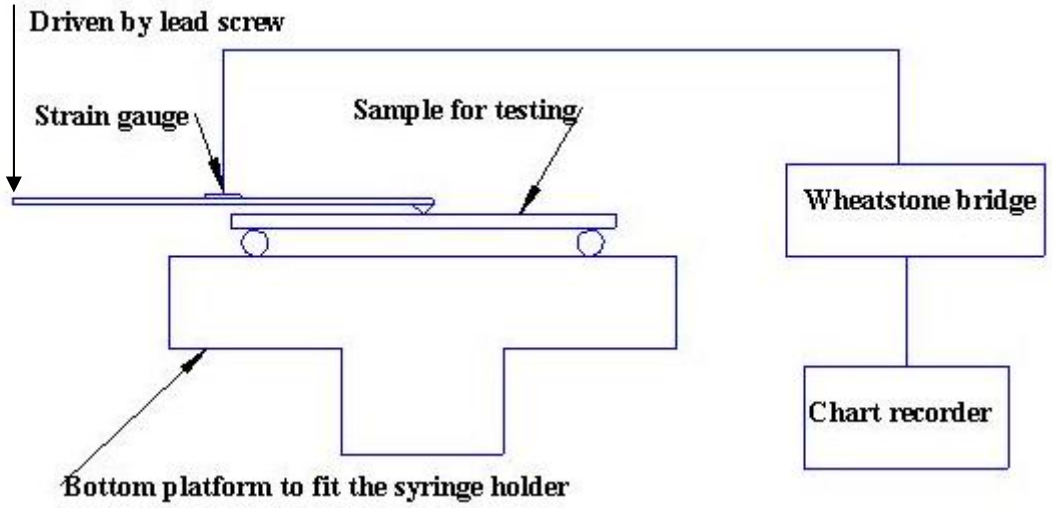

Figure 2.9. Schematic of the equipment for 3-point loading.

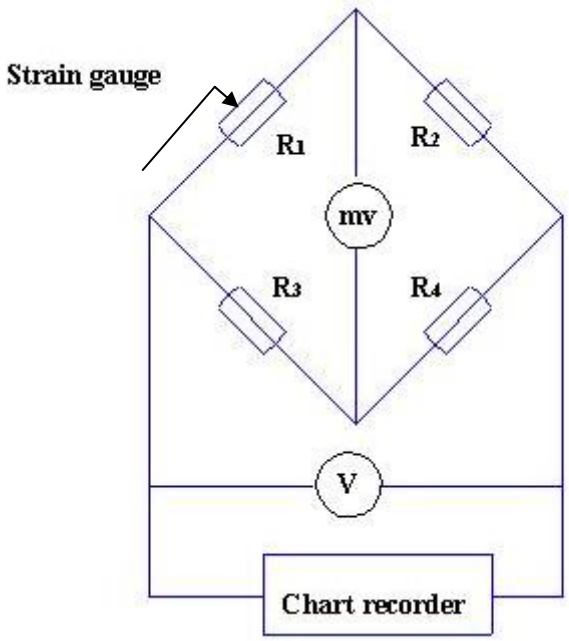

Figure 2.10. The circuit diagram of the strain gauge and Wheatstone bridge.

For the 3-point loading test，dimensions were selected according to the specimen size for the test and guided by ASTM C1161-94. The beams to support the specimen were selected and their diameters were measured. To find if the beam that was chosen was suitable for this rather unusual three-point loading test, the maximum deflection was calculated.

The size of the specimen for three-point loading was determined as follows. The filaments were extruded with a 300μm nozzle. After sintering, the diameters of the filaments were 245-270μm according to the different sintering temperatures: 1100°C, 1150°C, 1200°C, 1250°C, and 1300°C. Cross-section dimensional tolerances are ±0.05 mm. The higher the temperature, the smaller was the diameter of the filaments because of different shrinkage. Dimensions of the filament specimens are

compared with those of examples given in ASTM C 1161-94 (Table 2.2). From Table 2.2, the length decreases with the decrease of width and depth for the samples given in ASTM C 1161-94, and the length: depth ratios are 15-17. But application of this ratio results in a span of 4.6mm, deemed to be too short for precise loading. So for the samples used in this experiment, the smaller the filament diameter, the shorter sample length was selected and the final length of the filaments was chosen to be 10mm.

Table 2.2. Three point loading specimen dimensions.

Configuration	Width/mm	Depth/mm	Length/mm
O	Diameter ~0.27		10
A	2.0	1.5	25
B	4.0	3.0	45
C	8.0	6.0	90

O: cylindrical samples for this three-point loading test.

A, B and C: Samples given in ASTM C 1161-94.

According to ASTM C 1161-94, the diameter of the bearing cylinder (the beam to support the specimens) should be approximately 1.5 times the beam depth of the test specimen. So the diameter of the bearing cylinder D=0.405mm. The support spans, loading spans and the bearing diameters are given in Table 2.3.

Table2.3. Fixture spans and nominal bearing diameters

Configuration	Support Span/mm L	Loading Span/mm L/2	Nominal Bearing Diameters/mm
O	8	4	0.41
A	20	10	2.0 to 2.5
B	40	20	4.5
C	80	40	9.0

O: cylindrical samples.

A, B and C are the standard samples of ASTM C 1161-94.

The bearing cylinder consisted of a gauge 27, syringe needle tube (Hamilton Great Britain Ltd., Birmingham, UK). Its outer diameter was 0.41mm and its inner diameter was 0.21mm. The material was stainless steel.

To find the maximum measured load, the geometry and nomenclature of Figure 2.11 was used.

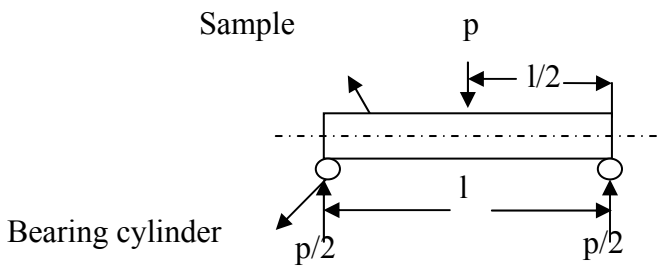

Figure 2.11. Schematic diagram for the three-point loading test.

From Figure 2.11, the maximum bending moment is:

$$m = \frac{p}{2} \cdot \frac{l}{2} \quad \text{(2.1)}$$

where l is the span length (m), p is is the force on the specimen (N),

$$\sigma = \frac{m \cdot y}{\mathrm{I}} \quad \text{(2.2)}$$

where m is the bending moment at the centre section and y is the distance from the neutral axis to the outer fibre of the beam. I is the moment of inertia.

For a cylinder, y=r.

$$I = \frac{1}{4}\pi r^4 \quad \text{(2.3)}$$

so: $$\sigma = \frac{p \cdot l}{\pi \cdot r^3} \quad \text{(2.4)}$$

When d is the diameter of the cylinder,

$$\sigma = \frac{8 \cdot p \cdot l}{\pi \cdot d^3}$$

Then:

$$p = \frac{\sigma \cdot \pi \cdot d^3}{8 \cdot l}$$

Putting l = 8 mm, d = 0.27mm and supposing $\sigma_{max} = 1.5\times10^8$ Pa, a maximum value for the ceramics of interest, then: p_{max} = 0.14 N.

From Figure 2.11, if the maximum measured load on the sample is p_{max}, then the maximum load on one bearing cylinder is $p_{max}/2$, 0.07N. To find the maximum deflection y, of the bearing cylinder (the hollow needle was chosen):

$$y = \frac{1}{48} \cdot \frac{p \cdot l^3}{E \cdot I} \quad \text{(2.5)}$$

where E is the young's modulus, for the steel, E = 200GPa[119] , p = $p_{max}/2$ = 0.07N, l = 20mm (according to the support designed in-house).

For a hollow cylinder, the moment of inertia, $I = \frac{1}{4}\pi(R^4 - R_0{}^4)$, where R is the outer radius, equal to 0.205mm and R_0 is the inner radius, equal to 0.105 mm giving I = 1.3×10^{-9} m^4.

Putting in the data above gives a maximum deflection of the hollow supporting pin (shown as 'A' in Figure 2.12) as y = 46μm. For a solid cylinder, the moment of inertia: $I = \frac{1}{4}\pi R^4$ and supposing the radius is the same as the outer radius of the hollow cylinder, so R=0.0205mm, then I=0.00139mm^4. Putting in the value of I gives a maximum deflection of the solid supporting pin as y =43μm. Thus the hollow cylinder and the solid cylinder have very similar deflections and the hollow cylinder can be selected. The ratio of the maximum deflection y and the bearing cylinder length l is 0.046/20, equal to 0.23%. The maximum deflection of the loading cylinders (46μm) is less than the maximum deflection experience by a ceramic filament during flexural testing (almost 1000μm). So the needle with an outer diameter 0.41mm and inner diameter 0.21mm can be chosen. Clearly there is too much compliance in the rig to make an assessment of Young's modulus of the filament sample.

The bottom platform with beams to support the sample in the three point loading test is shown in Figure 2.12. The sample was put into the narrow gap (shown in Figure 2.12 A.) which was helpful to locate the sample. The width of this narrow gap was designed 0.7mm to meet the condition in ASTM C 1161-94 that the cylinder bearing length shall be at least three times the specimen width. A machined aluminum block

was attached to the metal section which acted as the press head (shown in Figure 2.13.). When the press head loaded the sample, the metal section was deflected. A strain gauge was attached on the back of the metal cantilever to record this bending. The load during the three point loading test was recorded by a chart recorder (model L200E, Linseis Gmbh, Vielitzerstr., Selb, Germany).

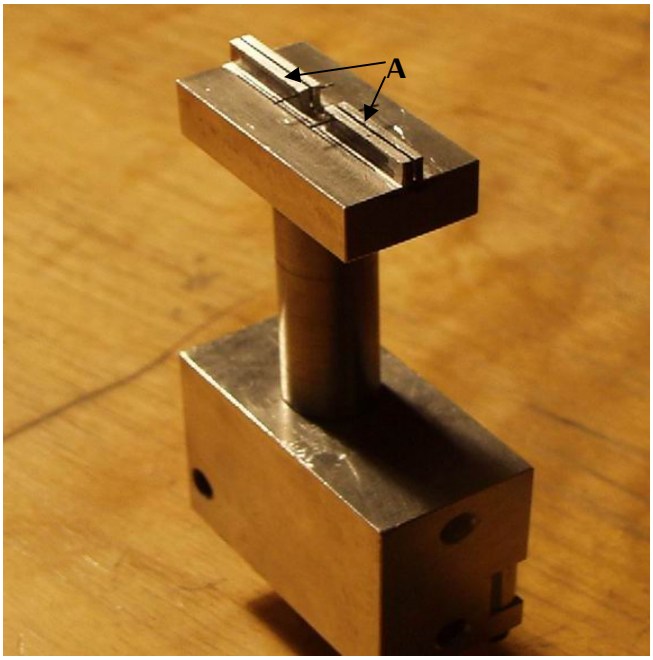

Figure 2.12. Bottom platform for the three-point loading test.

The strain gauge was calibrated by using a four place balance (TR104, DOVER, USA). The balance was calibrated first by a standard weight set (2mg, 5mg, 10mg … 500mg). The Chart Recorder (model L200E, Linseis Gmbh, Vielitzerstr., Selb, Germany.) was calibrated by a high precision power supply (model 230 made by Keithley Instruments). The load of the press head was then recorded by the calibrated balance and calibrated chart recorder.

Figure 2.13. Press head with a strain gauge attached on its back.

Balance calibration

The balance was calibrated by using standard weights. The actual mass and the reading of the balance are shown in the Table 2.4. The error was calculated from the equation:

$$E=(M_b-M_S)/M_S \quad \text{..... (2.6)}$$

where, E is the error, the M_b is the mass displayed by the balance, the M_s is the mass of the standard weight.

The relationship between the relative error and the calibration mass was given in Figure 2.14. The linear fitting equation between $-\ln E$ and $\ln M_s$ was given in the legend of Figure 2.14.; the correlation coefficient r^2 was 0.98. From Figure 2.14, the relative error decreases with increasing mass and is less than 1% when the absolute mass exceeds 100mg.

Table 2.4. Balance calibration and error

mass of standard weight/mg M_s	Display of the balance /mg M_b	Relative Error /%
2	1.6	-20%
5	5.5	10%
10	9.7	-3%
20	19.7	-1.5%
50	50.9	-1.8%
100	99.9	-0.1%
200	200.6	-0.3%
500	501.9	0.38%
500+500	1002.6	0.26%

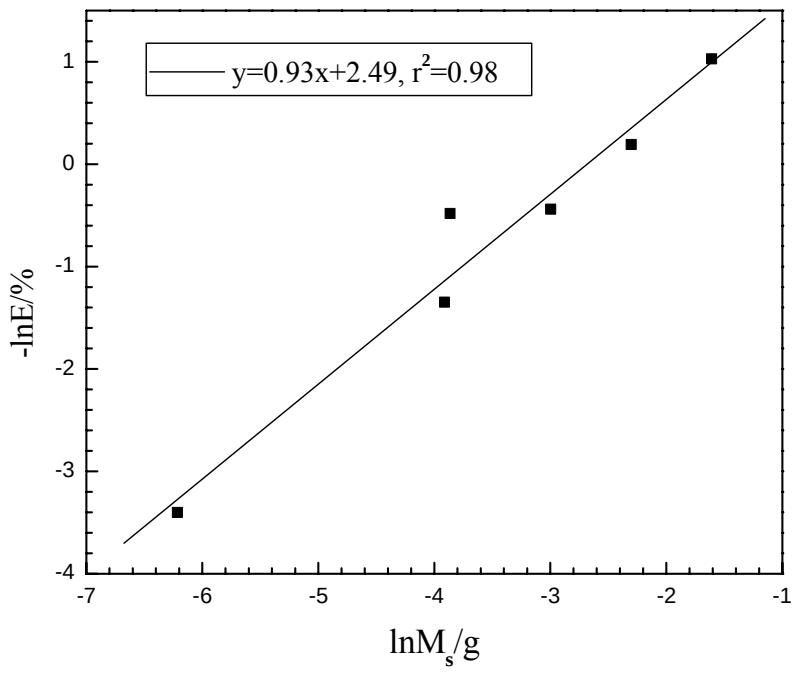

Figure 2.14. The relationship between the relative error and the calibration mass.

Chart Recorder calibration

The Chart Recorder is fitted with variable input and calibrated input. The calibrated input was checked through a high precision digital power supply (Model 230 made by Keithley Instruments). The output of the bridge amplifier is 50mV for 137 mN force. The Chart Recorder calibration was shown in the Table 2.5. The expected pen displacement was compared with the actual pen displacement obtained by the test, in order to be sure that one space of the chart which the pen moved was 0.5mV.

Table 2.5. Chart recorder calibration and error.

Voltage supplied /mV	Expected pen displacement	Actual pen displacement	Error/%
1	2.0	2.0	0
2	4.0	4.0	0
5	10.0	10.0	0
10	20.0	20.0	0
20	40.0	40.0	0
50	100.0	100.0	0

Wheatstone bridge calibration

1) Chart Recorder settings

The rotary switch was adjusted to select the input voltage range. The range of the loads measured in this experiment was 0-49mN, so the input range used was 50mV. The channel and chart speed was selected.

2) Wheatstone bridge calibration

The input signal was disconnected and the counter-voltage disabled. The zero setting button was adjusted to position the pen at the mid-point on the chart. The zero setting of the chart recorder was thus positioned. The input signal was connected. If, when the zero button on the rear panel of the bridge was being pressed, the pen was found to move then, the zero setting on the chart recorder panel was adjusted to position the pen to the mid-point on the chart while the zero button on the bridge was being pressed. The zero button on the bridge was then released. The "coarse" and the "fine" switches were adjusted so that the pen was at the mid-position on the chart. The strain gauge was then driven by the screw extruder at a speed of 0.3mm/s to load the balance, and the balance data was recorded by the computer. The strain gauge was not stopped until the force given to the balance reached 49mN.

Following the steps described above, the empirical relationship between the voltage and the force is given by linear fitting, the correlation coefficient r^2 is 0.999 (shown in Figure 2.15). The empirical equation is shown below.

$$y = 0.453x + 0.875 \quad \text{..... (2.7)}$$

where, the y is the voltage in mV, the x is the force in mN.

When running three point loading tests, the voltage data was read from the chart, and equation (2.7) was used to find the force. This empirical equation was obtained by applying force to the balance with the press head. To obtain the maximum tensile stress in the outermost fibre of the samples, the force obtained from equation (2.7) was put into equation (2.4).

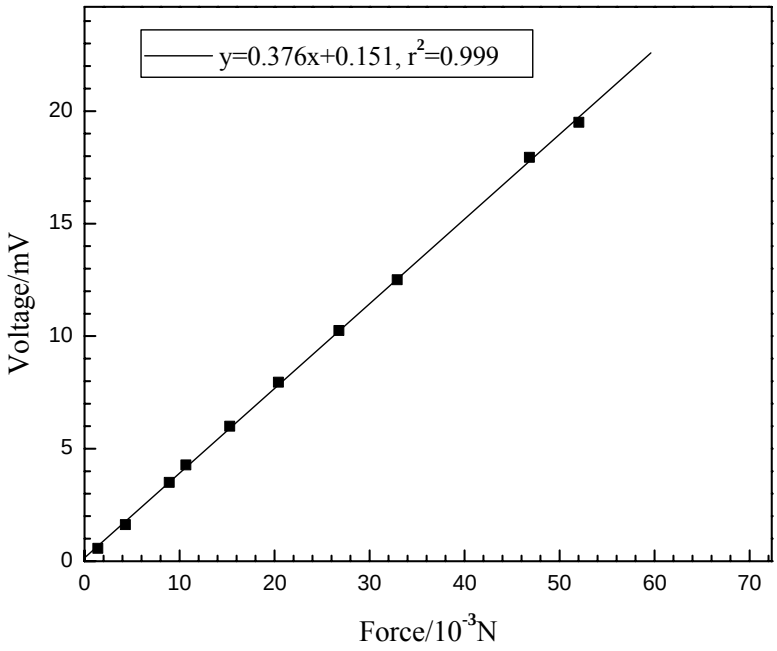

Figure 2.15. The empirical relationship between voltage and force.

2.4 Operating System to Control Extrusion Freeforming worktable

2.4.1 Tools and Methodology

In the early version operating system, Motion Planner (Parker Hannifin Corporation, Poole, Dorset, England) was used to control the extrusion freeforming worktable. But Motion Planner is text-based software, and takes a long time for the user to learn. In

this operating system, Motion Planner was still used to control extrusion freeforming worktable as “engine” and LabVIEW 8.2 (Laboratory Virtual Instrument Engineering Workbench, National Instrument, 2006) was used to develop a user friendly graphical user interface (GUI). So all standard Motion Planner features are available in this operating system as shown in Figure 2.17. Moreover the existing programs written by Motion Planner can be used in this operating system through entering the names of the programs. So this superior operating system was very easy to manipulate even for a beginner.

LabVIEW is a powerful and flexible graphic programming language and provides a platform to efficiently develop user interfaces and to display data[120]. It has been widely used by engineers and scientists in research throughout academia and industry. A labVIEW program was constructed in two parts: the Front Panel and the Block Diagram. The Front Panel was used for the user to input data through the control icons and read the data, diagram or chart, etc. from the indicator icons. The Front Panel was also used to simulate the panel of a physical instrument. The Block diagram was the source code of the labVIEW program. It defined the actual data flow between the inputs and outputs.

Another software, Compucam 1.4 (Parker Hannifin Corporation, Poole, Dorset, England), was used to translate the CAD files into the Motion Planner program. So a desired 2D structure was first drawn by the AutoCAD software and then transferred

into Motion Planner program. A Motion Planner program named p150 is shown in appendix A. The programs written by Motion Planner were then exported to LabVIEW and changed to sub-programs by entering the paths and names of the files. So the extrusion freeforming worktable was controlled by the Front Panel of the LabVIEW (shown in Figure 2.16.).

2.4.2 Main Features

For Motion Planner to be the "engine" to control whole extrusion freeforming worktable, a 'setup' file (shown in Appendix A) written by Motion Planner was firstly executed to prepare the 6K Series product for subsequent controller operations. The example shown here was the program for fabrication of the bone substitute scaffold. It can easily be adapted for other scaffold fabrications by exporting the paths and names of the desired programs written by Motion Planner to LabVIEW. This program (shown in Figure 2.16.) consisted of eight tab sheets separately named "X Y home", "Z home", "move Z axis", "move X axis", "move Y axis", "lattice", "COARSE for extrusion axis" and "FINE for extrusion axis". Each tab was developed as a separate program and had a special function. Different programs can be accessed and executed by selecting appropriate tabs at the top of the Front Panel. Specific details of these tabs were introduced below. At the right top of the main tool bar, there are three buttons,  (run),  (stop) and  (pause), to control the execution mode.

The “lattice” window.

The window named “lattice” was used to control the extrusion freeforming worktable to fabricate various lattices. To achieve this aim, this program should have some functions such as: (1) the ability to control the X and Y axes to move at the same velocity in all situations. So the Define Path Local Mode (PL) was used in the Motion Planner programs (shown in Appendix B); (2) the ability to change the velocity of the X and Y axes. Obviously the velocity of the X and Y axes are different as the extrusion velocity changed and the diameter of the filament knitted into lattices is altered; (3) the ability to change the velocity of the extrusion and at the same time keep the X and Y axes moving. This function is very important and helpful for the user to harmonize the velocity of the extrusion with the velocity of the X and Y axes to obtain the desired filaments and structures; (4) the ability to control the number of the layer and the layer height by inputting data into the control icons; (5) the ability to display the real-time layer number which has been finished and the real-time X, Y and Z positions through some indicator icons on the Front Panel so that the whole extrusion processing is under control; (6) the ability to check if the commands in the program are correct or not; if not, the operating program can give an alarm to the user and be stopped automatically; (7) the ability to record the pressure of the extrusion axis and when the pressure is too high and may exceed the limit of the load cell, the operating system can give an alarm to the user and be stopped automatically; (8) for the extrusion lag at the beginning of the filament extrusion, some time and traces are

needed to accommodate the velocity of the extrusion and match it with that of the X and Y axes.

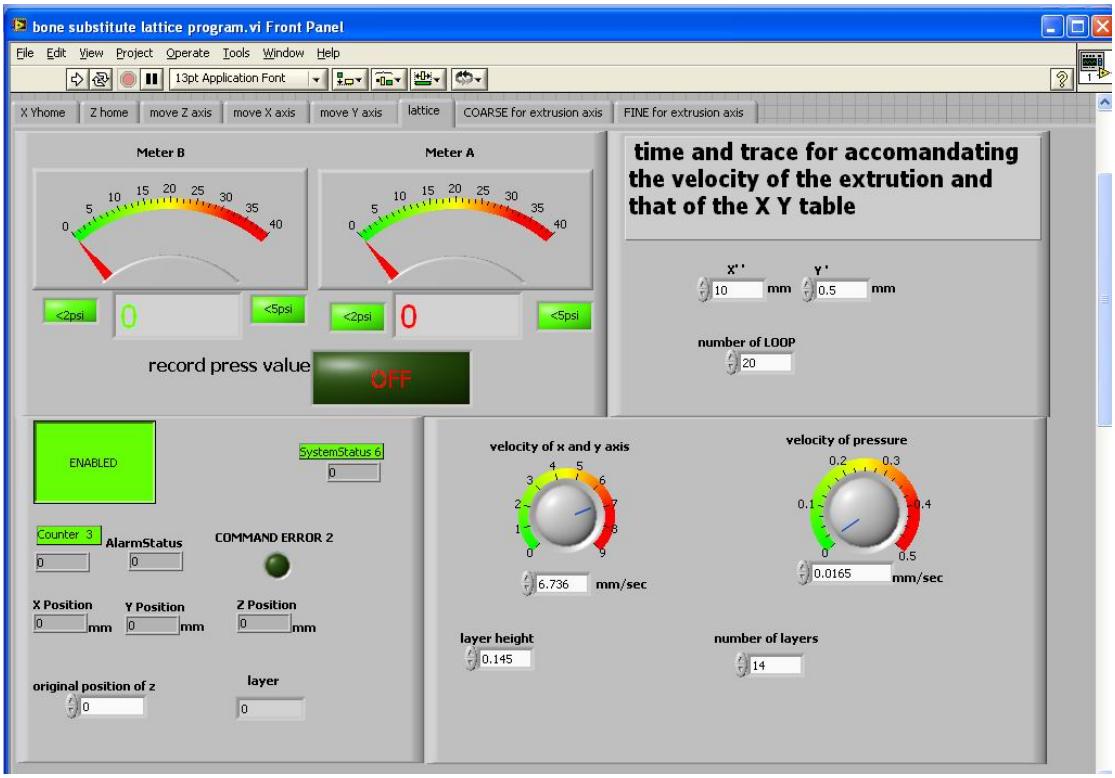

Figure 2.16. Front Panel designated “lattice” to control the fabrication of the bone substitute lattice.

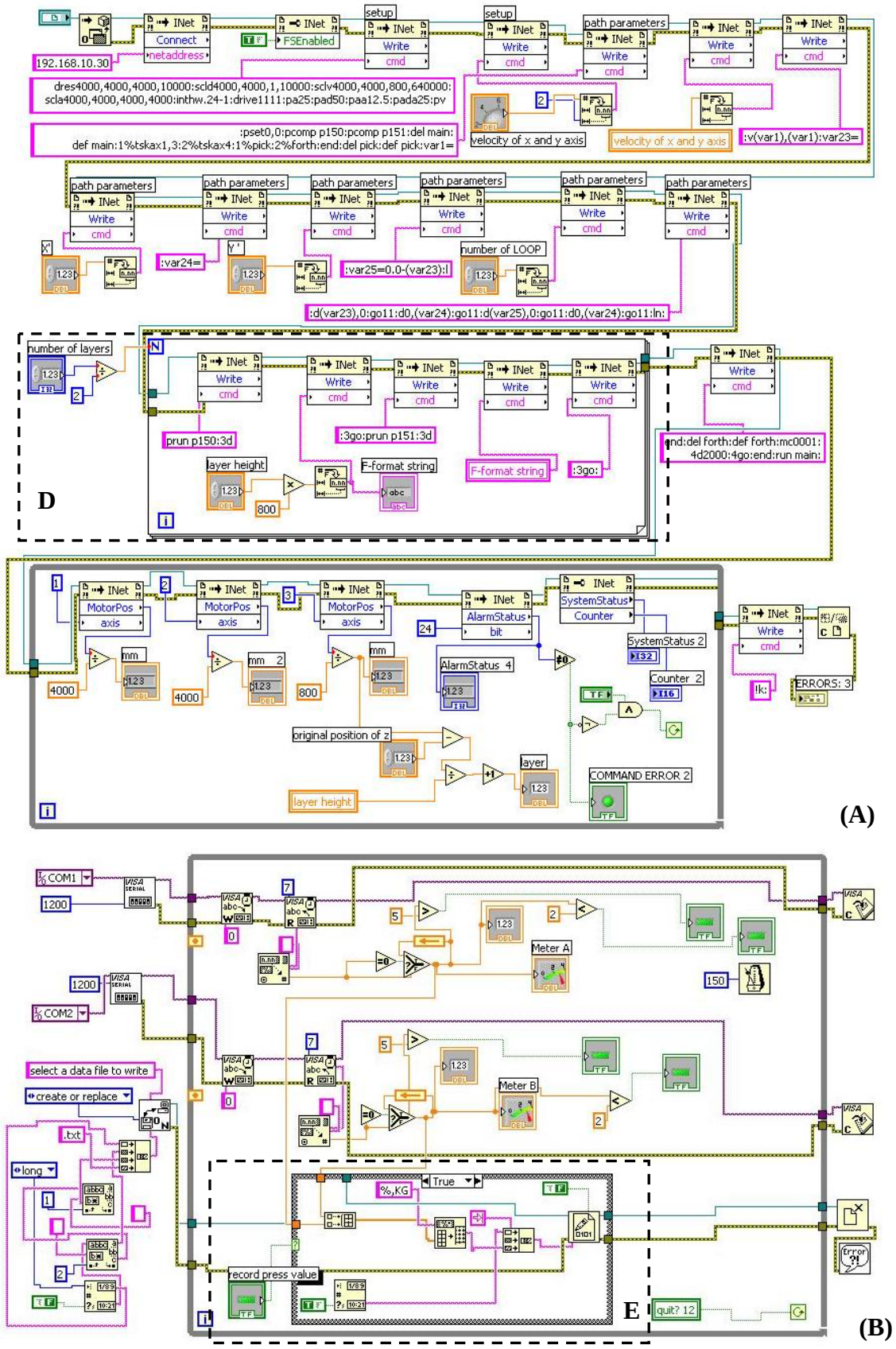

Figure 2.17. Block Diagram for the "lattice" Front Panel: part (A) and (B).

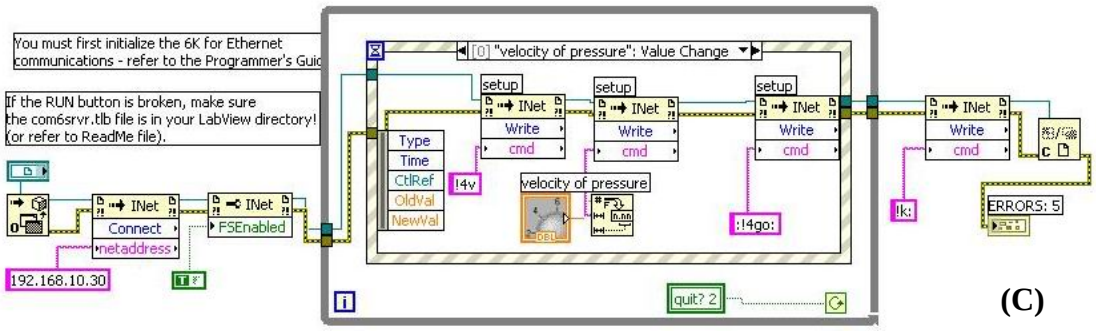

Figure 2.17. Block Diagram for the "lattice" Front Panel: part (C).

The picture shown in Figure 2.16 is the Front Panel of the program to fabricate the bone substitute scaffold. From this Front Panel, all the functions mentioned above were achieved. Moreover, the pressure value was recorded and exported to .TXT file in order to characterize the extruded paste. This function was controlled by a Boolean icon named "record pressure value". The source code of the Front Panel is in the Block Diagram (shown in Figure 2.17.). It consists of three parts: part A is to control the X, Y and Z axes movement. As shown in the dashed line rectangle D, the name of the program to control the path of each layer in one circle was inputted. When one layer was finished, the Z axis was moved up and then the program to control the path of the next layer was executed. Layer by layer, one circle was finished. The circle number was controlled by a 'count control' wired to a 'for loop'; part B is to record and export the pressure value. The Block Diagram to export the pressure value to .TXT file was shown in the dashed line rectangle E. The rest part of part B was used to record the pressure value and provide an over-pressure alarm; part C is to change the real-time velocity of the extrusion axis while the X and Y axes kept

moving. The logical relationships between them were expressed by the flow chart. In the flow chart shown in Figure 2.18., N is the real-time current number of the layer; N_0 is the desired number of the layer which is inputted by the user through a control icon on the Front Panel before starting the program. Boolean was a control icon of LabVIEW and through clicking it, 'Truth' or 'False' was inputted by the user. When the whole program was started, four processing steps were run at the same time. They were designated separately as "Multi-tasking program", "program to change the velocity of extrusion axis", "Read the pressure data from the meter" and "program to record pressure value. "Multi-tasking program" made the extrusion axis keep moving when the X, Y, Z axes moved following the routes in which filaments were knitted into a lattice.

The program to control the path of the lattice was run in the process step designated "sub-program to control the routes of the X, Y and Z axes". Through this process, different programs represented the desired lattice structure were executed only by inputting their path name. The process designated "display the real-time parameters" provided the real-time information as current layer number, current positions of the X, Y, Z axes, etc. and some local variables for the program. "Program to change the velocity of extrusion axis" made the extrusion axis move at the desired velocity which was changed at any time through an immediate command (some command settings and descriptions used in the operating system are provided in Appendix C). "Read the pressure data from the meter" provided the real-time pressure data of the load cell

through a while loop controlled by 150 ms multiple wait and gave an alarm function through a conditional represented as a diamond. The processing named “Program to record pressure value” was a selective executing program controlled by a Boolean conditional. It was used to export the pressure data to .TXT file.

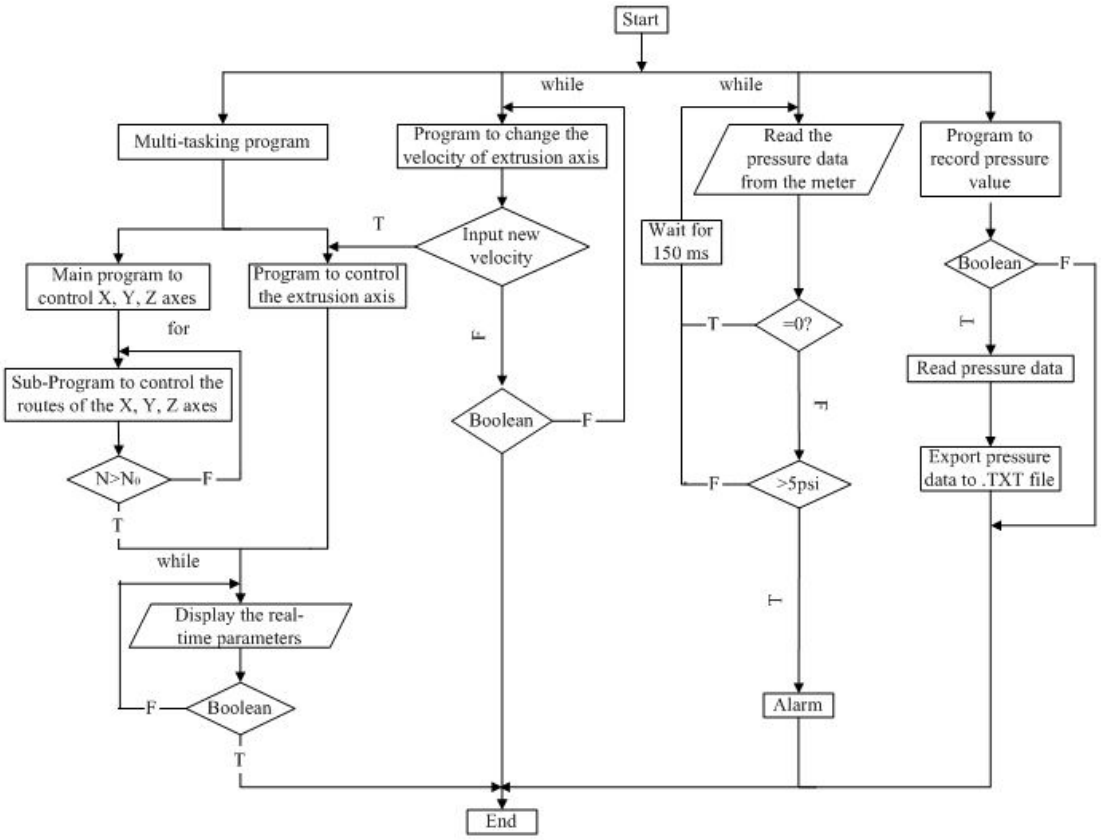

Figure 2.18. The flow chart to express the logical relationship between the programs in the Block Diagram.

The “X Y home” window.

The window named “X Y home” was a program to allow a homing operation in order to return the X, Y axes to a repeatable initial starting location. The Front Panel of this

tab was shown in Figure 2.19. From the two Boolean buttons on the Front Panel, the program was controlled to be enabled or stopped. The real-time positions of the X, Y, and Z axes were reported and the function of the alarm for command error was provided.

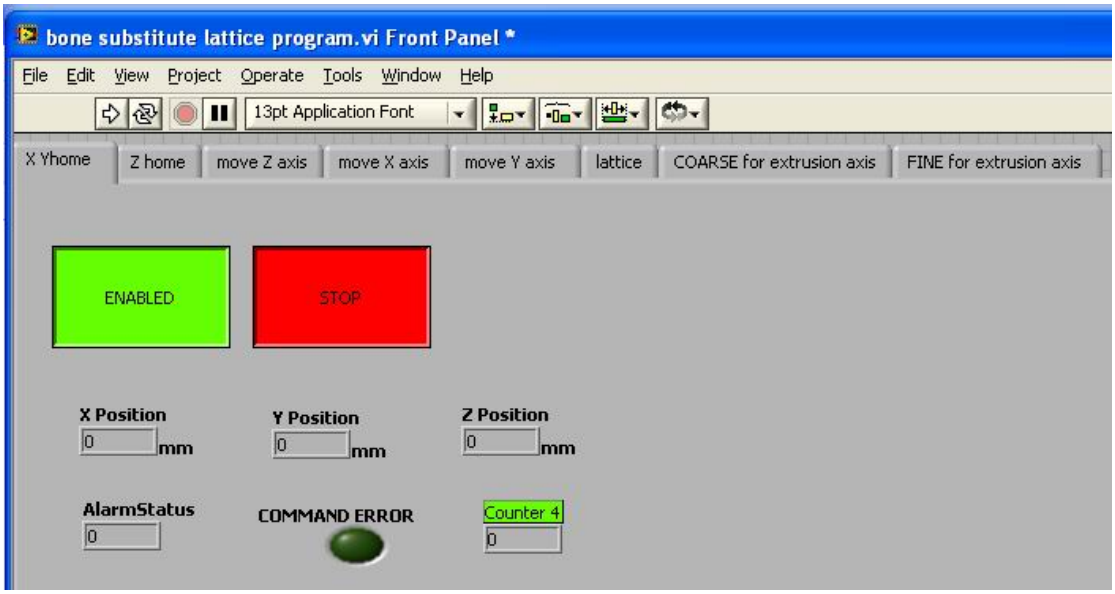

Figure 2.19. Front Panel designated "X Y home" to control the program to provide the homing operation.

The "Z home" window.

The window named "Z home" was a program provided to allow the homing operation to return the Z axis to a repeatable initial starting location. In the processing of the extrusion, the distance between the platform on which the filaments were extruded and the surface of the nozzle from which the filaments were extruded was very important. So a repeatable initial starting location that used the platform as the

reference was necessary for the Z axis on which the nozzle was loaded. A proximately sensor (RGH24, Renishaw plc, Gloucestershire, UK) was fixed on the platform (shown in Figure 2.3. e). The Front Panel of this tab was shown in Figure 2.20. The operating method and the functions of this tab were similar to those of the tab named "X Y home". But the proximity sensor was an individual device and its signal was inputted individually. The source code of this program is different from that of the program to control the tab named "X Y home". That is to say, an input function command (details seen in Appendix C) was needed to define the functions of each individual input.

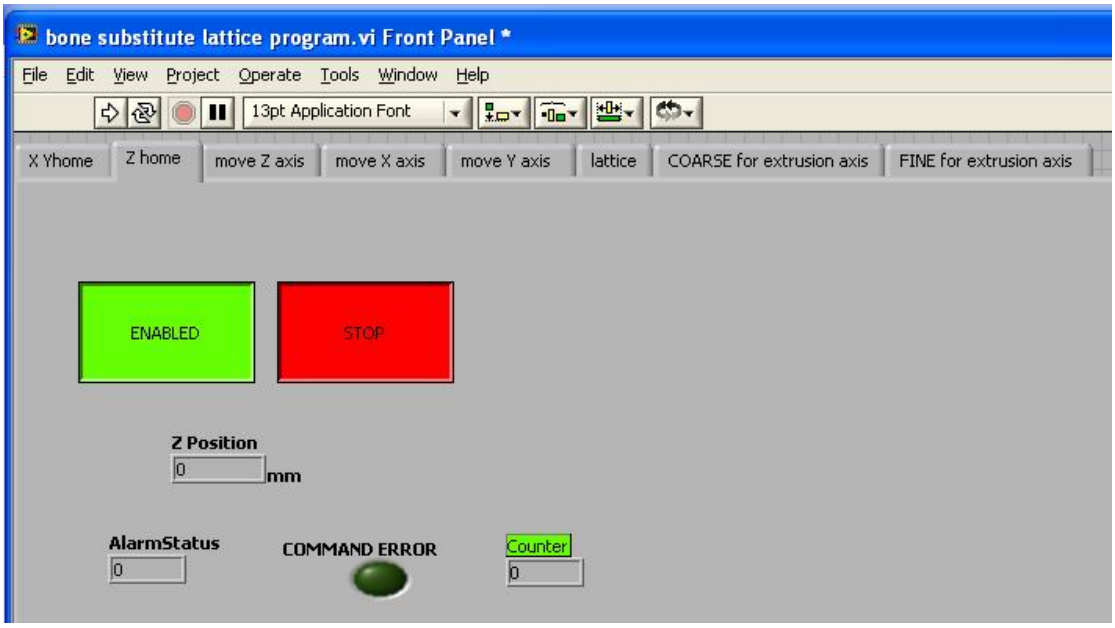

Figure 2.20. Front Panel designated "Z home" to control the program to provide a repeatable initial starting location for the Z axis.

The Block Diagram of this Front Panel was shown in Appendix D. Its core program written by Motion Planner was represented in pseudocode of the Pascle language (an influential imperative and procedural programming language) below.

D_x := X axis moved distance;

D_y := Y axis moved distance;

D_Z :=Z axis moved distance;

begin

move D_x , $D_{y;}$ (move the nozzle to the position vertical to the mark on the proximately sensor)

move –D_z; (move axis down, note that D_z should big enough to make the nozzle touch the proximately sensor)

wait for onboard input 5 to be inactive; (the signal of the proximately sensor was inputted by onboard input 5)

stop motion on Z axis;

wait for motion completed on Z axis;

move $D_{z;}$ (move Z axis up to eliminate backlash on Z axis)

wait onboard input 5 to be active;

stop motion on Z axis;

end

The "move Z axis" window.

The window designated "move Z axis" was used to control the program to move the Z axis to any desired position individually. The Front Panel for it is shown in Figure 2.21. A vertical pointer slide was used to input the desired position of the Z axis; the two Boolean buttons were used to enable or to stop the program. The operating method and functions of the tab named "move X axis" and "move Y axis" were similar to this tab.

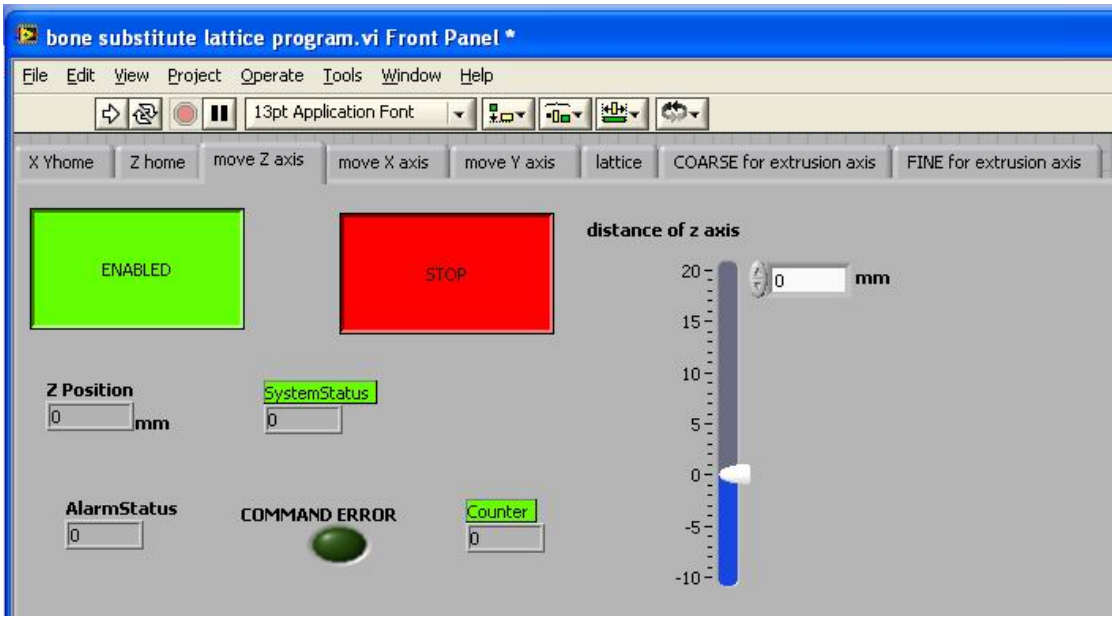

Figure 2.21. Front Panel designated "move Z axis" to control the program to move the Z axis to any desired position individually.

The "COARSE for extrusion axis" window.

The window named “COARSE for extrusion axis” was used to control the program to move to any desired position. From Figure 2.22, the desired data for the extrusion axis velocity was inputted by a knob control icon on the Front Panel. The numeric control named ‘initial position’ on the Front Panel was used to input the data for the initial position of the extrusion axis; another numeric control named ‘aim position’ was used to input the data for the desired position of the extrusion axis. This program provided a coarse control for the extrusion axis individually.

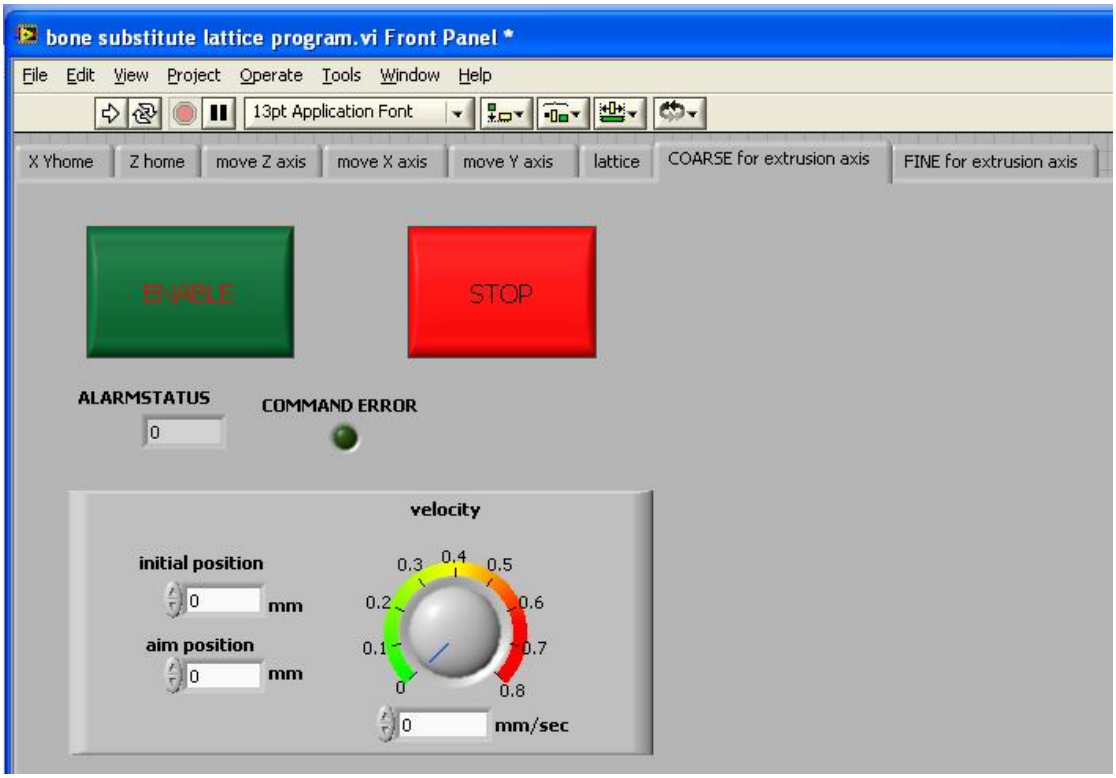

Figure 2.22. Front Panel designated “COARSE for extrusion axis”.

The "FINE for extrusion axis" window.

Although a coarse control for the extrusion axis had been provided by the through "COARSE for extrusion axis", a fine control for the extrusion axis was necessary for this experiment. Since the extrusion axis cannot be stopped automatically without a limit sensor, the screw extruder is easily damaged if the extrusion axis oversteps its limit. So when the extrusion axis was closing to its limit, it was necessary to control it carefully. Moreover when the extruder was closing to the plunger of the syringe filled with paste, the extrusion axis still needed to be moved carefully.

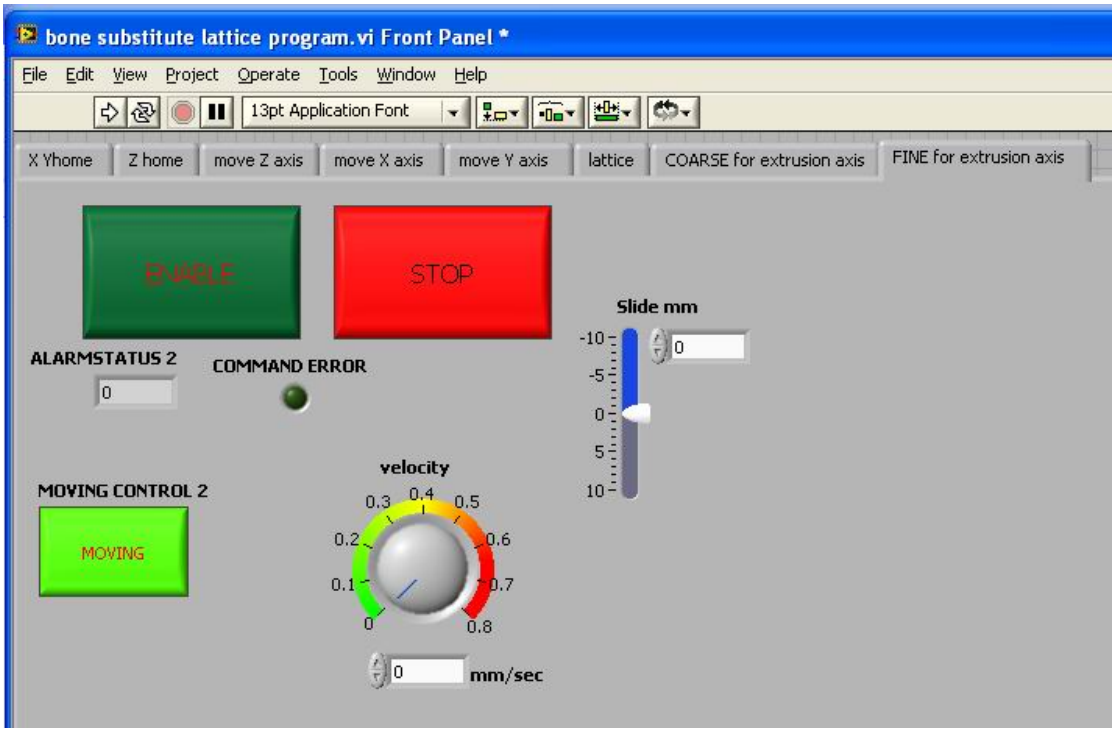

Figure 2.23. Front Panel designated "FINE for extrusion axis".

From Figure 2.23, the data for the velocity and the data for the moving distance were still inputted through the controller and the vertical position slide separately. The program was started by clicking the Boolean button for 'enable', but the extrusion axis was not moved. It was moved by keeping the Boolean button "moving control" depressed, and stopped by releasing this Boolean button. The transferring from pressing to releasing was repeatable in this program. In this way, the extrusion axis was controlled accurately by pressing and releasing the Boolean button "moving control".

2.5 Extrusion Pressure in the Fabrication of Lattices by Alumina Paste

The extrusion pressure transient in the fabrication of lattices by alumina paste was recorded and studied in this experiment. From the control of the operating system mentioned before, the extrusion pressure in any period can be recorded during the processing of lattice fabrication. The alumina pastes with different solvent volume fraction were extruded from the same nozzle at the same extrusion ram velocity, 8.25 μm/s. Because of evaporation of the solvent during loading of the paste into the syringe, the solvent volume fraction of the paste close to the die was different to that of the paste close to the ram. The solvent volume fractions in the different parts of the paste were measured by a microbalance (2100 mg ± 0.1 μg, Sartorius AG, Goettingen Germany). The syringe used to load paste was a hypodermic syringe (HGB81320 1ml,

Hamilton GB, Ltd., Carnforth, U.K) which is a gas tight syringe, the friction between the plunger and syringe wall can be different in different syringes. To account for the influence of this friction difference on the extrusion pressure, the alumina paste was loaded into two hypodermic syringes with different wall friction.

2.6 Other Equipment

The debinding experiments for the lattices prepared by alumina paste were preformed by thermogravimetric analysis (TGA) (Model: Q500, TA Instruments Ltd., Crawley UK). The microstructure of the samples was observed by a JEOL JSM 6300F field emission SEM (JEOL Ltd., Tokyo, Japan).

3 Results and Discussion

3.1 The Choice of Parameters in the Extrusion Freeforming Process

The maximum diameter of filaments prepared in this experiment was 150 μm. Using dies made from hypodermic needles, the shortened needles with this diameter and below were easily blocked partly due to the long land length (3-4 mm) although they performed well in earlier preliminary experiments on filament diameters greater than 200 μm. So sapphire water-jet cutting nozzles with an orthogonal lead-in were used to extrude different diameter filaments. These had much shorter land length (~ 500 μm).

The extrusion distance is the gap between the die exit and the substrate. If the gap is too large, the filaments are difficult to control and may drag across the substrate. A lattice extruded in this situation is shown in Figure 3.1 (a). From Figure 3.1 (a), the filaments (arrowed as B) were extruded at a velocity lower than that of the XY table and were dragged into curves. But in Figure 3.1 (a) A, the filaments were turned sharply. There are two potential reasons to induce this phenomenon: one is that the velocity of the XY table was faster than that of extrusion axis; another one is that the gap between the die exit and substrate, i.e. extrusion distance, was too high. Obviously the latter induced the filaments to turn sharply. If the extrusion distance is set too low, the nozzle smears the paste and damages the filaments. The appropriate

distance depends on the nozzle diameter and the viscosity of the paste. For the 150μm diameter nozzle, the best extrusion distance was 0.2 mm. The layer height was the distance by which the nozzle was raised on the Z axis before a new layer was started. Theoretically, the layer height for the 150μm diameter filament was 150μm, but for the extrusion distance initially set to 200μm which is greater than the filament diameter, the best layer height in practice was chosen to be 145μm. This accommodated shrinkage during drying.

Theoretically, the filament extrusion velocity V_r and the velocity of the XY table V_{XY} are related by:

$$V_{xy} = \left(\frac{R}{r}\right)^2 V_R \quad \ldots\ldots\ldots\ldots\ldots\ldots\ldots\ldots\ldots\ldots\ldots\ldots\ldots\ldots\ldots\ldots \quad (3.1)$$

where R and r are the diameter of the plunger and the nozzle respectively. If $V_r < V_{XY}$, the filament was stretched and if $V_r > V_{XY}$ it formed curves. In practice, the viscous nature of the paste also delayed the response of the extrudate to applied stress[121] so that filament extrusion speed V_r did not respond quickly to changes in the speed of the XY table V_{XY}. So many data points around the ratio $\left(\frac{R}{r}\right)^2$ were tested to discover the optimal values of V_r and V_{XY}. To increase fabrication speed, rapid XY table movement V_{XY} and extrusion velocity V_r, were needed, but this places high loads on the microextrusion press. So in this experiment, the speed of the XY table V_{XY} was set at 6.735mms^{-1} and the speed of the filament extruder V_r was 0.00825mms^{-1}. Note that the lower limit of extruder speed was 2nms^{-1}.

As the lattices fabricated by the extrusion freeforming worktable are knitted by continuous filaments, the point at which the filaments change their direction is important in fabrication of optimum lattices. If the change of direction is abrupt, jerking of the stepper X and Y axes takes place due to the abrupt acceleration or deceleration. At the speed used in this experiment, the servo motor and mechanical configurations tolerated such abrupt changes, and the jerking phenomenon was avoided. But in practice, the abrupt corner still induced some flaws in the lattice. A lattice with square corners was shown in Figure 3.1 (b). A magnified picture for a square corner (as shown in Figure 3.1 (b) labelled B) indicated that the filaments did not follow the designed routes strictly at the point where the filaments changed their direction because the distance between the nozzle and the plane on which the filaments were attached was too big. That is to say, the square corner designed in the program was changed to an irregular round corner (as shown in Figure 3.1 (b) labelled B), and as a result the filament segments on the edge needed to support the filaments of the next layer were reduced. Some displaced filaments on the edge caused by the absence of the support segments are shown in Figure 3.1 (b) labelled A.

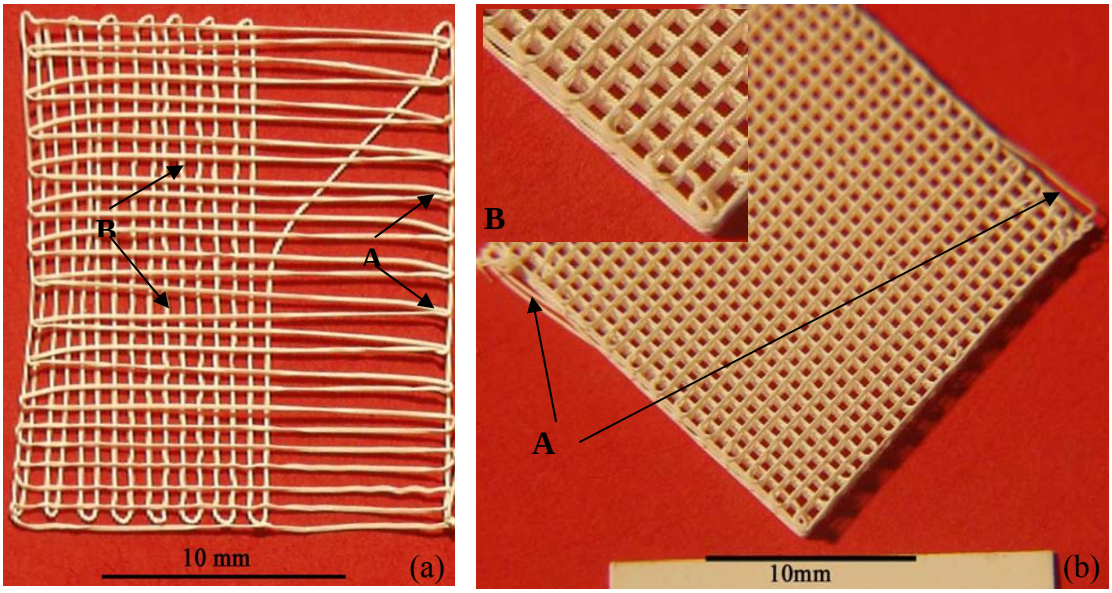

Figure 3.1. (a) Lattice extruded at exorbitant extrusion distance; (b) Lattice extruded with an abrupt corner; (c) magnified picture of the abrupt corner.

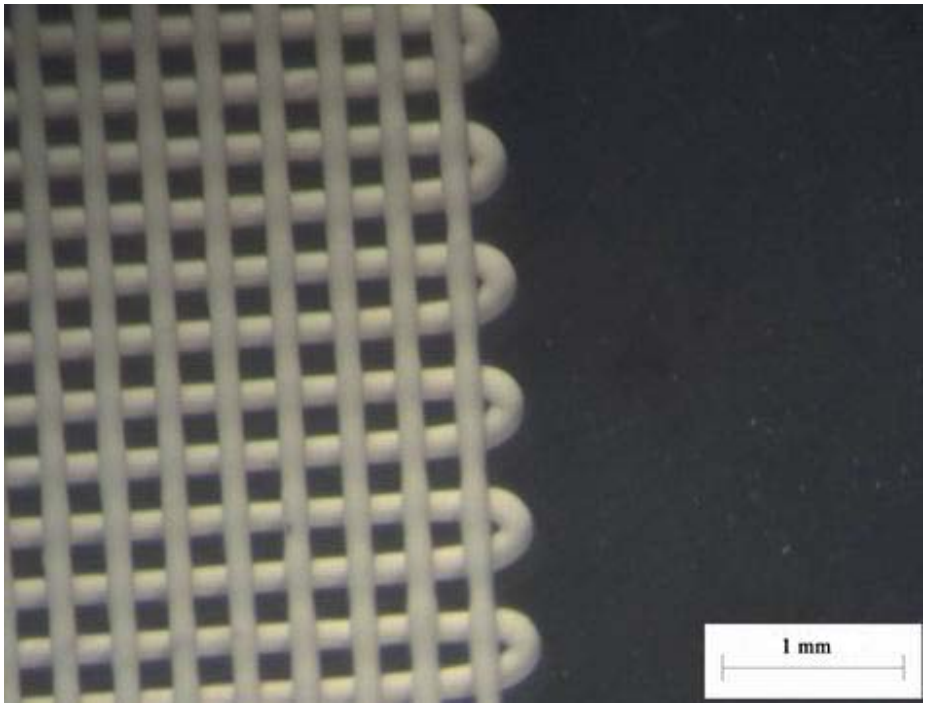

Figure 3.2. A lattice with round corners.

So in practice, the point at which the filaments changed direction was designed into round corners and elongated to support the next layer filaments as shown in Figure 3.2.

3.2 Discussion of the Non-volatile Content of the Alumina Paste for Extrusion Freeforming

The non-volatile content of the paste was found to determine the success of lattice fabrication. Each of five different pastes (30, 36, 39, 45 and 50 vol. % ceramic powder based on wet paste) were extruded to give lattices with different macro-porosity (50, 60, 70 and 80 %) in order to give different filament spacings. In the fabrication process, the 'sinking' effect, whereby filaments sag between base-layer supports, results from high solvent contents and is shown in Figure 3.3. The 'curling' effect, in which the upper layer peels away from the base layer due to drying-induced stresses, is shown in Figure 3.4. a. The schematic diagram of the 'curling' effect is shown in Figure 3.4. b. The radius of the deformation arc, R, can be obtained by the formula below:

$$R = \frac{H^2 + L^2}{2H} \qquad \text{..... (3.2)}$$

where, H is the drying deformation height; L is the drying deformation length along the filaments.

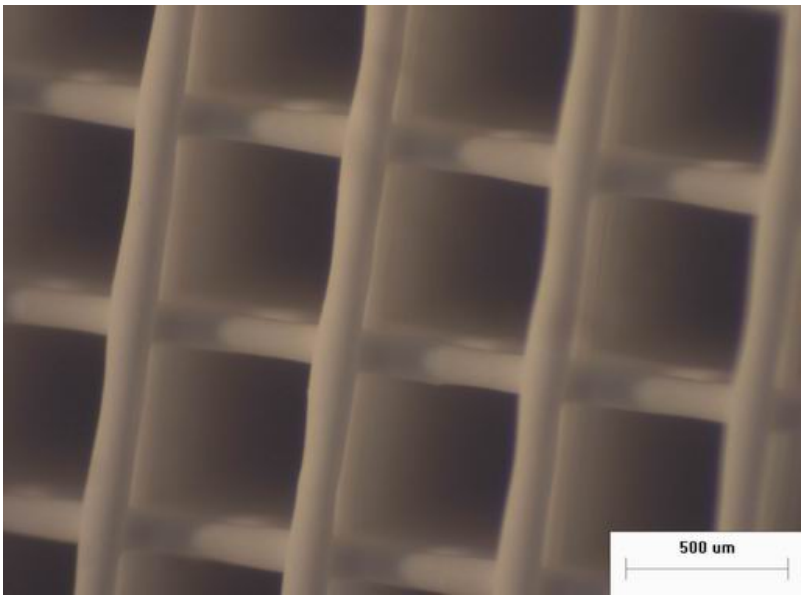

Figure 3.3. Filament 'sinking' effect resulting from high solvent content in an unsintered alumina lattice with 39 vol.% ceramic powder in the wet paste. The distance between filaments is 630μm.

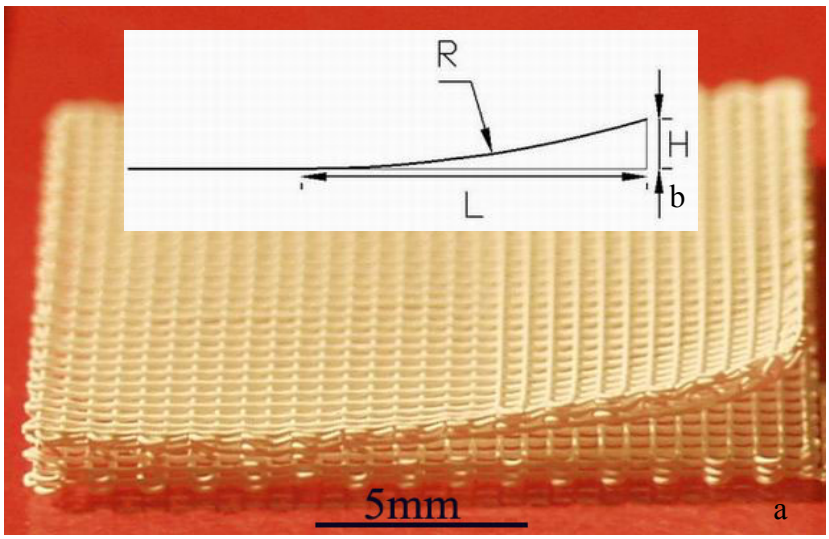

Figure 3.4. Drying defect in a 14 layer alumina lattice fabricated by the 39 vol. % ceramic powder in the wet alumina paste. The distance between filaments is 630μm.

Two factors influence the 'sinking' effect: the yield stress of the paste which is mainly influenced by solids fraction and the distance between filaments (span). Using the same paste, the span was systematically decreased which in turn decreases the macroporosity of the lattice[121,104]. Figure 3.5 shows that the largest detectable sinking distance decreases as the span decreases, i.e. as the lattice becomes less porous. Using a lattice with fixed span and hence fixed lattice porosity and systematically varying the solvent content with fixed ceramic-polymer ratio, the sinking distance decreases as the non-volatile fraction increases.

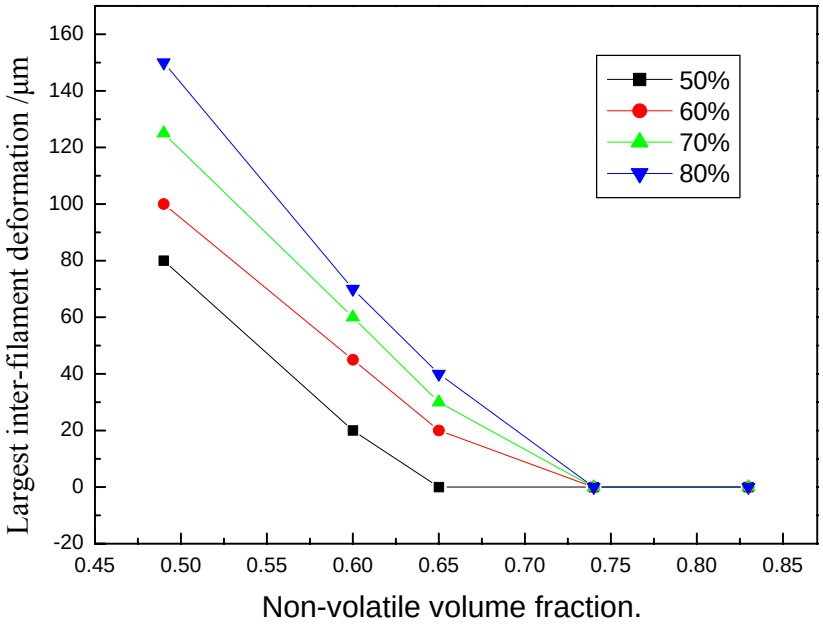

Figure 3.5. Sinking deformation as a function of the non-volatile fraction of the paste for different lattice spans; the largest observed inter-filament deformation was recorded. Note that a high lattice macroporosity (as given in the key) corresponds to a high span.

The curling effect is caused by the drying shrinkage stresses during fabrication. If the paste becomes a fully dense binary of ceramic and polymer after drying, the volume shrinkage is equal to the volume fraction of solvent. The linear shrinkage is 10% for 27 vol.% solvent. Four factors influence the extent of curling and delamination: (i) the powder fraction in the dried ink controls the elastic modulus of the 0-3 composite such that modulus typically increases steeply as the powder fraction exceeds 50 vol.%, (ii) the volatilisation of solvent influences the differential shrinkage between layers; in the worst case scenario the base layer has fully dried so that its shrinkage is complete when the next layer begins to dry, (iii) the span between filaments determines the number of welds per unit area and hence overall laminate strength, (iv) as the span decreases and the lattice becomes more densely packed, the vapour transport within the structure decreases and drying slows down, in turn reducing drying deformation.

From Figure 3.6, when the non-volatile content was less than 49 vol.%, the rendered layers remain wet while new layers are deposited. The increased weld strength between filaments counter-acts delamination. Since the first layer is strongly adherent to the substrate, deformation did not occur whatever the lattice span. That is to say the radius of the deformation arc is infinite. When the non-volatile contents were between 49 and 65 vol. %, the weld strength decreased as the solvent content increased and could not counter-act the shrinkage of filaments. Although the overall shrinkage decreased, the drying time was reduced. In this regime, drying deformation increased

with increasing non-volatile content**.** Accordingly**,** the radius of the deformation arc decreases. When the non-volatile content was between 65 and 74 vol.%, the overall shrinkage of filaments decreased and drying deformation decreased with increasing non-volatile content. As shown in Figure 3.6, the radius of the deformation arc increases in this region. When the non-volatile content was more than 74 vol. %, the solvent was correspondingly low and so the linear shrinkage was low. So the deformation arc disappeared and the filament radius was infinite.

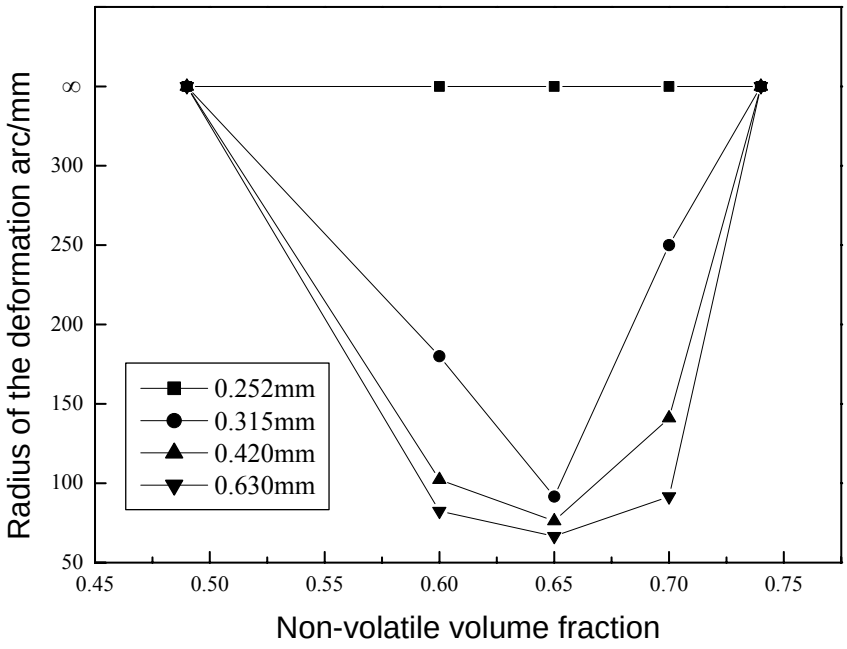

Figure 3.6. Radius of the deformation arc as a function of non-volatile fraction of the paste for different lattice spans.

The effect of lattice macroporosity is very pronounced. At high porosity, the number of welds per unit area is low and delamination is facilitated. Furthermore, the more

open structure allows faster drying of rendered layers. From Figure 3.6, in the same non-volatile volume fraction, the radius of the deformation arc increases with decreasing lattice span. When the lattice span is 0.252 mm (macroporosity 50%), the radius of the deformation arc is infinite whatever the non-volatile volume fraction. When the non-volatile content was greater than 74 vol. %, all these defect phenomena were absent as evidenced by the regular structures shown in Figures 3.7.

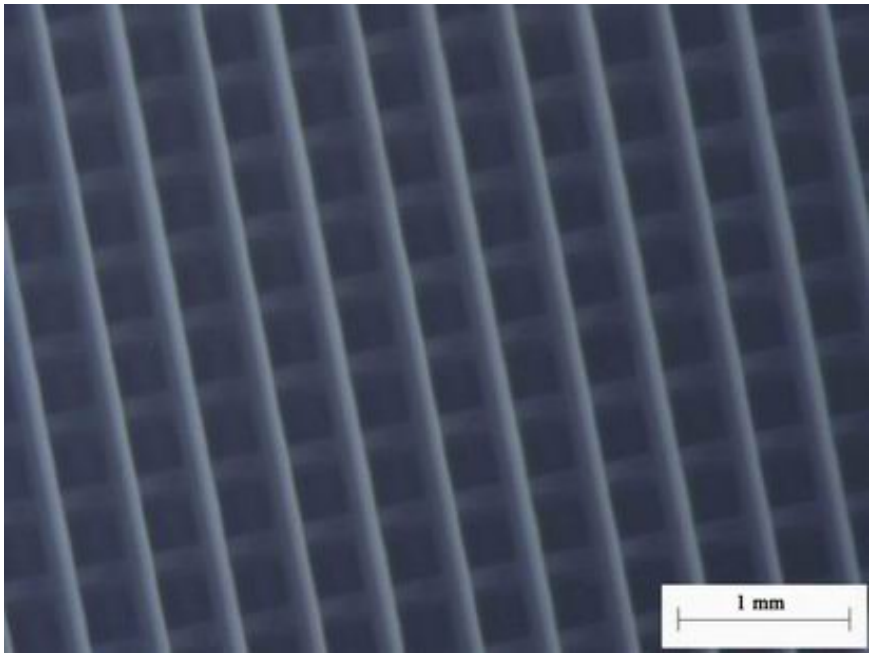

Figure 3.7. Unsintered alumina lattice with 630 μm inter-filament distance fabricated by 26 vol. % solvent paste showing no sagging or drying deformation.

The lattice with a narrow span (0.252 mm giving a gap of 0.1 mm) showed no sagging. There was no deformation due to drying when the non-volatile contents were 60 vol. % giving the appearance that these are ideal conditions. However, the distances between the filaments in this lattice became uneven in alternate layers (as shown in

Figure 3.8). Furthermore, the filaments sagged, becoming ellipsoidal in section. The variation of the filament spacing only occurred at low spans. But for the lattices with 0.252 mm span, the higher solvent content paste caused the filaments to adhere together at the point at which the filament changed its direction.

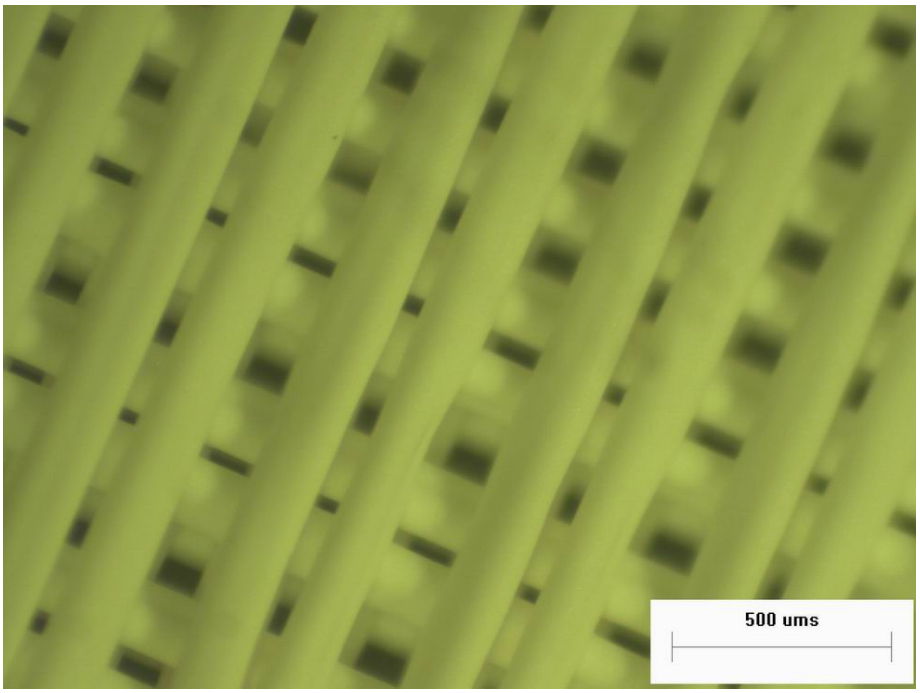

Figure 3.8. Unsintered alumina lattice with 252μm designed span fabricated by 40 vol. % solvent paste showing irregular spacing.

Thus, while the first filament was correctly placed, the second was dragged closer to the first at the turning point and this influenced its subsequent path. The third filament however, was subject to a large spacing at the turn and in this way, filaments paired up, an effect seen in Figure 3.8. When the non-volatile content was increased, the merger of adjacent filaments did not take place and the ideal lattice with 0.252 mm span was attained. Figure 3.9 shows an optical microscope picture of an unsintered

lattice with 0.252 mm span fabricated by 26 vol. % solvent paste. The filament round shape was maintained very well and the desired span was obtained.

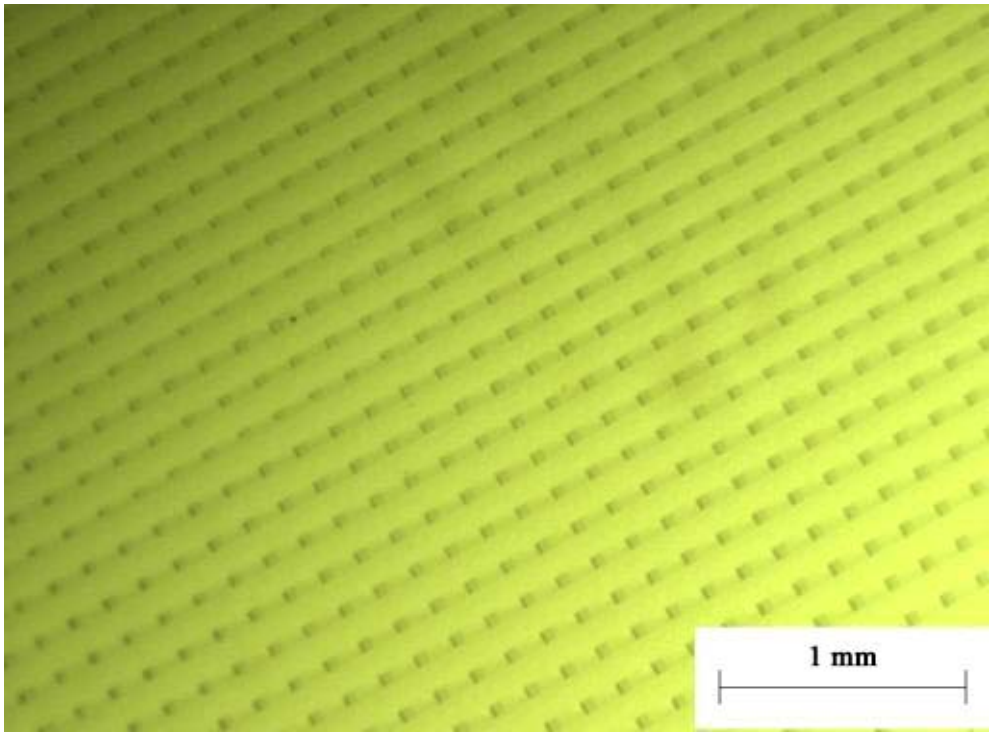

Figure 3.9. Unsintered alumina lattice with 252μm span fabricated by 26 vol. % solvent paste showing excellent uniforming.

Theoretically, the span of the lattice can be made in any size by increasing the non-volatile volume fraction. In practice, the spans between filaments cannot be increased without limit[104,105]. If the solvent content was less that 16 vol.%, the paste was too dry to weld to the base layer. The nozzle was easily blocked and the layers did not join. An ideal lattice was attained when the solvent content was approximately 26 vol.%.

Adhesion to the substrate

Since the lattice was extruded on a substrate, the solvent content also influenced the adhesion of the first layer to the substrate, which in turn, influenced the lattice quality. The filaments adherent to the substrate were subject to two forces: one is the shrinkage stress due to solvent evaporation which causes the overall shrinkage of body; and the other is a tensile stress exerted by the substrate to resist the in-plane shrinkage[122]. For the same substrate, higher solvent content means higher constrained volume shrinkage, i.e. higher shrinkage stress and induces higher constrained tensile stress as the adhesion force increases. Filaments subjected to high stress are easily cracked. For the same solvent content, the shrinkage stress within the filaments is constant.

The tensile stress imposed by the substrate is influenced by the substrate materials. If the filaments attach to the substrate strongly, shrinkage is restrained and high tensile stress is induced but it is difficult to remove the lattice from the substrate. On the other hand, low tensile stress cannot resist the in-plane shrinkage and separation may occur. To release the residual shrinkage stress, the filaments bend upwards and the lattice detaches from the substrate.

The substrate materials selected to test these effects were classified into two types according to the method for taking off samples: one type of substrate on which

samples attached was burned away in the debinding and sintering processing for the samples. Samples extruded on the other type of substrate were taken off directly before debinding and sintering. In the former, substrates including label adhesive tape and double-side tape were tested. Obviously the lattices extruded on them were attached strongly. Indeed the adhesion force between the substrate and the first layer of the lattice was far greater than the weld strength between layers of the lattice. These substrates caused the lattice to break before sintering when the substrate combusted. So this type of substrate was abandoned. In the latter, different substrates, including silicone paper, plastic film, clay slide and glass slide etc., were chosen as substrates. The lattices extruded on the silicone paper and the plastic film bent up and detached from the substrate. This phenomenon indicated that adhesion to these two materials did not resist the shrinkage stress efficiently. The lattice extruded on the clay slide was attached on the substrate strongly but difficult to remove. The glass slide provided the adhesion needed to resist the shrinkage stress efficiently and also made the lattice extruded easily detachable. It provided a flat surface that did not deform.

3.3 Discussion of the Extrusion Pressure in the Fabrication of Lattices Prepared by Alumina Paste

Although the physical properties of the polymer-solvent vehicle and the characteristics of the die geometry are the primary influences on the extrusion

pressure[89], in this experiment, the friction between the plunger and the syringe wall and the solvent volume fraction of the paste also play crucial roles because the same vehicle and die geometry were used.

Table 3.1. Solvent volume fractions of five different pastes.

	Solvent content in the paste close to the die/vol.%	Solvent content in the paste close to the extrusion ram/vol.%
Paste A	42	30
Paste B	35	30
Paste C	31	29
Paste D	32	29
Paste E	31	29

The solvent volume fractions of five different alumina-polymer based pastes were measured and shown in Table 3.1. It took 3-4 minutes to fill paste into the syringe, which resulted in the solvent volume fraction of the paste close to the die being greater than that of the paste close to the extrusion ram due to solvent evaporation. From Table 3.1, the difference between the solvent volume fraction of the paste close to the die and that of the paste close to the extrusion ram in the case of the paste A and paste B are far greater than in the case of the other pastes. Pastes A and B were loaded into the syringe and extruded separately without delay. Pastes C, D and E were loaded into syringes separately and then left in a sealed container with propan-2-ol vapour for

24 h before extrusion. This ageing process resulted in more even solvent distribution within the paste.

The pressure transient during paste A extrusion was recorded in Figure 3.10. The curve has been divided into five zones. The paste was extruded onto the substrate with a 200 μm distance between the die exit and the substrate in zones I, III and V. In zones II and IV, the extrudate flowed down freely. From Figure 3.10, the extrusion pressure was decreased in zones II and IV. When the paste was extruded onto the substrate, the extrudate provided a resistance to block the paste from extruding out. With the substrate taken away, this resistance disappeared and the extrusion pressure decreased. From Figure 3.10, a noisy pressure trace is seen in zone I but this disappeared in the other zones. This noisy pressure trace indicates that the paste loaded into the syringe was not well mixed and some defects, such as entrapped gas, inhomogeneities and undesired voids, existed in it[95]. It has been reported that the paste can be homogenized when a pressure of 2 MPa is applied to it and, at the same time, the entrapped gas and undesired voids can be removed[89]. Pressure fluctuated regularly in the extrusion for all the pastes. The mean time between the two wave peaks was 120 s. The distance traveled in a single revolution by the ball screw used to drive the extrusion ram in this experiment was 1 mm. The velocity of the extrusion was 0.00825 mm/s. So the time in which the ball screw travelled in a single revolution was almost 120 s. That is to say, the regular pressure fluctuation was induced by the pitch of the ball screw.

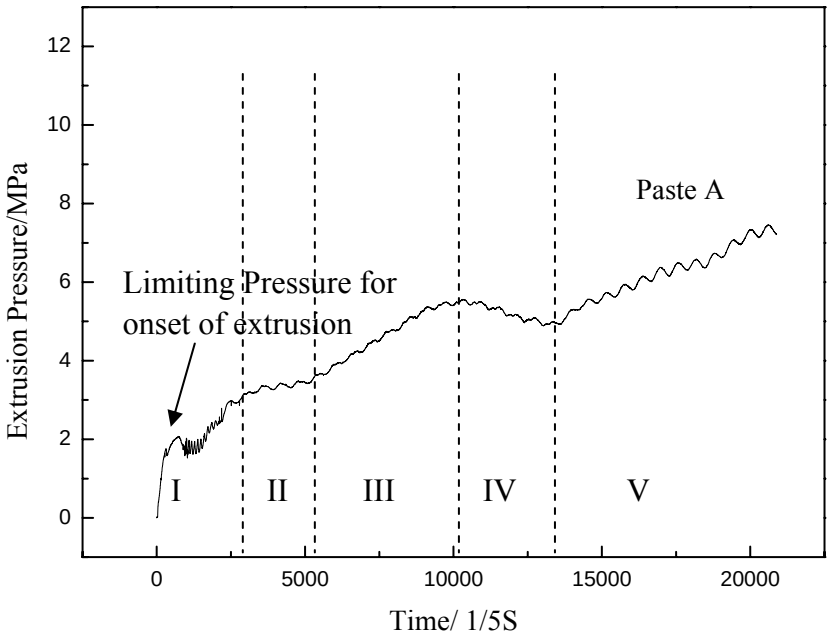

Figure 3.10. Pressure transient during the extrusion for paste A.

The pressure transients of the extrusion for pastes B and C are plotted in Figure 3.11. The noisy pressure effect did not appear in these two pressure transients for pastes B and C which were extruded at almost 2 MPa for several minutes to obtain uniform preforms. In the pressure transient for extrusion of paste B, the pressure increased slightly. Solvent volume fraction in the final part of the paste was lower due to its evaporation during filling (as shown in Table 3.1). Another reason for pressure irregularity can be that the vehicle in the paste is moving faster than the assembly of alumina particles[89], which results in lower polymer concentration in the final part of the paste. Therefore the paste becomes drier and extrudes at higher pressure.

From Figure 3.11, the slope of the pressure transient of the extrusion for paste B is greater than that of the pressure transient of the extrusion for paste C. This indicates that the solvent distribution in paste C was more even than that in paste B. Paste C had been left to age in a sealed container with propan-2-ol vapour for 24 h before extrusion. The first extrusion pressure peak (defined as limiting pressure for onset of extrusion in Figure 3.10 and 3.11) was obtained during the extrusion of Pastes A, B and C. Some papers attribute this limiting pressure for onset of extrusion to the initial filling and wetting of the conical zone of the die[90, 91, 92, 85], but in the extrusion of pastes B and C, the limiting pressure for onset of extrusion still appeared although the conical zone of the die had been filled before extrusion. So the initial filling and wetting of the conical zone of the die was not the reason for the limiting pressure for onset of extrusion. A similar result was obtained by Ariawan et al[93]. A paste with solid volume fraction exceeding 50% exhibited non-Newtonian behaviour[7]. The initial wall stress[88] and yield stress[93] develop early in the paste extrusion process. The first pressure peak was also reported to be partially induced by the finite compressibility[89]. Because the diameter of the die is smaller than that of the syringe (paste reservoir), the paste is compressed in the syringe before the limiting pressure for onset of extrusion is reached. The static pressure in the paste increases gradually. Extrusion was stopped and restarted after different periods of time by Ochoa and Hatzikiriakos[89]. When the extrusion was restarted after the small relaxation period, the limiting pressure for onset of extrusion to initiate flow was very small compared to the initial

limiting pressure for onset of extrusion providing further convincing evidence of the presence of finite compressibility.

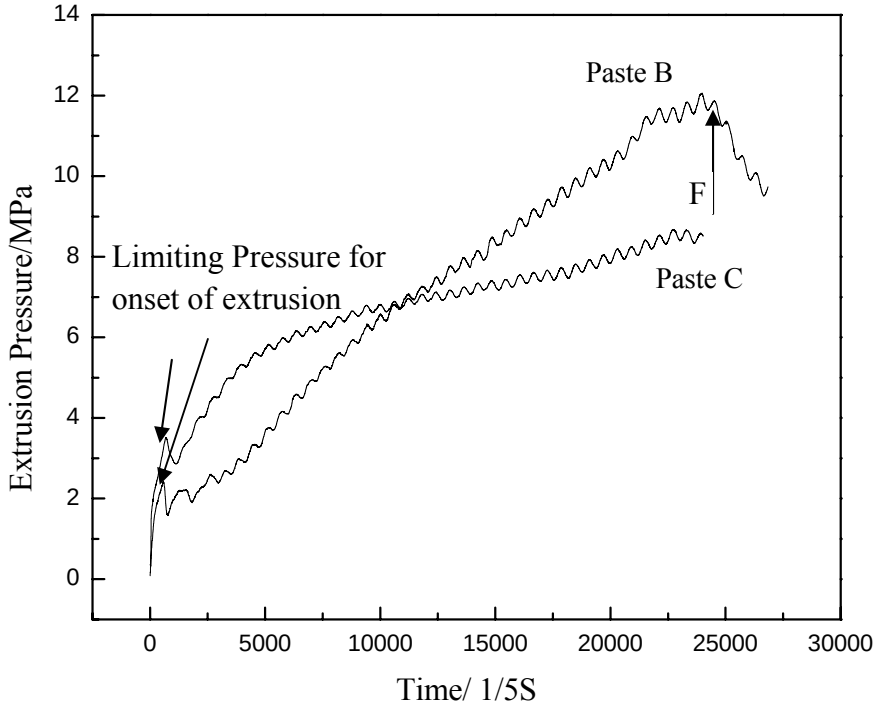

Figure 3.11. Pressure transient during the extrusion for pastes B and C. (arrow F indicated point at which substrate was removed)

A gas tight syringe was used as the ram and barrel in this experiment, so the influence of friction between the plunger and the syringe wall on the extrusion pressure was not avoided and is depicted in Figure 3.12. The extrusion pressure *P* is described by Benbow and Bridgewater[123] and expressed by the equation:

$$p = p_1 + p_2 = 2(\sigma_0 + \alpha V^m)\ln[D_0 / D] + 4(\tau_0 + \beta V^n)[L / D] \quad \text{..... (3.3)}$$

where P_1 is the pressure drop in the die entry, P_2 is the pressure drop in the die land, V is the paste velocity in the die land, σ_0 is the yield stress extrapolated to zero velocity and α is a factor characterizing the effect of velocity. τ_0 is the initial wall stress and β is the wall velocity factor which accounts for the velocity-dependence of the wall shear stress, m and n are exponents for taking account of non-linear behaviour of the paste. D_0 is the diameter of the barrel; D is the diameter of the die land and L is the length of the die land. Thus a large number of parameters for each system must be collected in order to apply equation 3.3.

In this experiment, the extrusion pressure was recorded from the load cell on the ram. Hence the extrusion pressure P_a is described by

$$p_a = p_1 + p_2 + f \quad \text{..... (3.4)}$$

where f is the friction between the plunger and the syringe wall. Figure 3.12 indicates that the friction between the plunger and the syringe used to extrude paste E is greater than that of the syringe used to extrude paste D. Before extrusion by the press head driven by a ball screw, pastes D and E were extruded by hand and kept flowing out from the die land, which resulted in the disappearance of the limiting pressure for onset of extrusion.

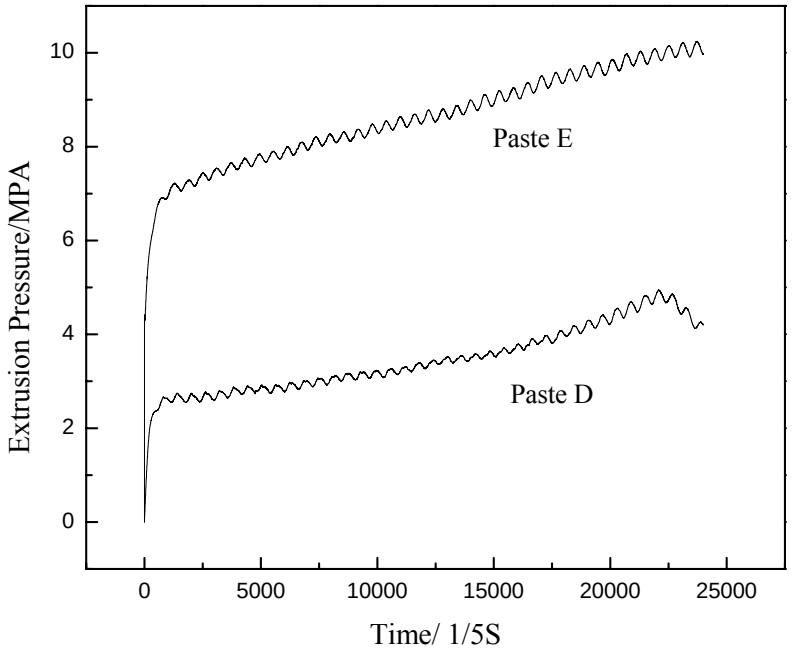

Figure 3.12. Pressure transient during extrusion of pastes D and E.

For an elastic-plastic paste, the viscosity of the paste decreases with the increase of the shear rate when the extrusion pressure exceeds the yield stress. If the velocity at which the bulk materials move to the die entry is equal to the velocity at which the extrudate exits from the die land, the extrusion pressure should be stable. But in the extrusion processing in this experiment, the extrusion pressure increased gradually after reaching the yield stress even though the ram was driven down at a constant velocity. In the paste preparation process, air bubbles and particle conglomerations occurred in the paste and induced the static pressure to increase gradually.

3.4 Design and Fabrication of the Metal Matrix Composites with Alumina Lattice and Aluminum Matrix

Four kinds of lattices with different porosity, 50%, 60%, 70% and 80%, were extruded by the extrusion freeforming method. These four different kinds of alumina lattice with different dimensions consisted of 150 μm filaments extruded from alumina paste (prepared as shown in section 2.2), and were used as preforms during fabrication of metal matrix composites.

3.4.1 Calculation of the Centre to Centre Distance Between the Filaments

To get lattices with the required porosity, the centre to centre distance between the filaments (L) was needed. To calculate the distance, a unit cell was extracted from the whole lattice as shown in Figure 3.13.

In Figure 3.13, F is a short length of the filament of the lattice; L is the centre to centre distance of the two filaments; the length of the unit extracted on the filament axes is equal to L; H is the height of the unit. From Figure 3.13, the unit extracted from the whole lattice is a rectangular plate with four quarter cylinders. Then the porosity of the unit P can be calculated by the equation below:

$$p = (1 - v/V) \times 100\% \quad \text{(3.5)}$$

where, v is the volume of all quarter cylinders and V is the volume of the rectangular plate. Then P can be expressed by the following equation:

$$p = (1 - \frac{\pi r^2}{HL}) \times 100\% \quad \text{(3.6)}$$

where, r is the radius of the cylinder, i.e. filament; H is the height of the rectangular plate; L is the centre to centre distance between the filaments.

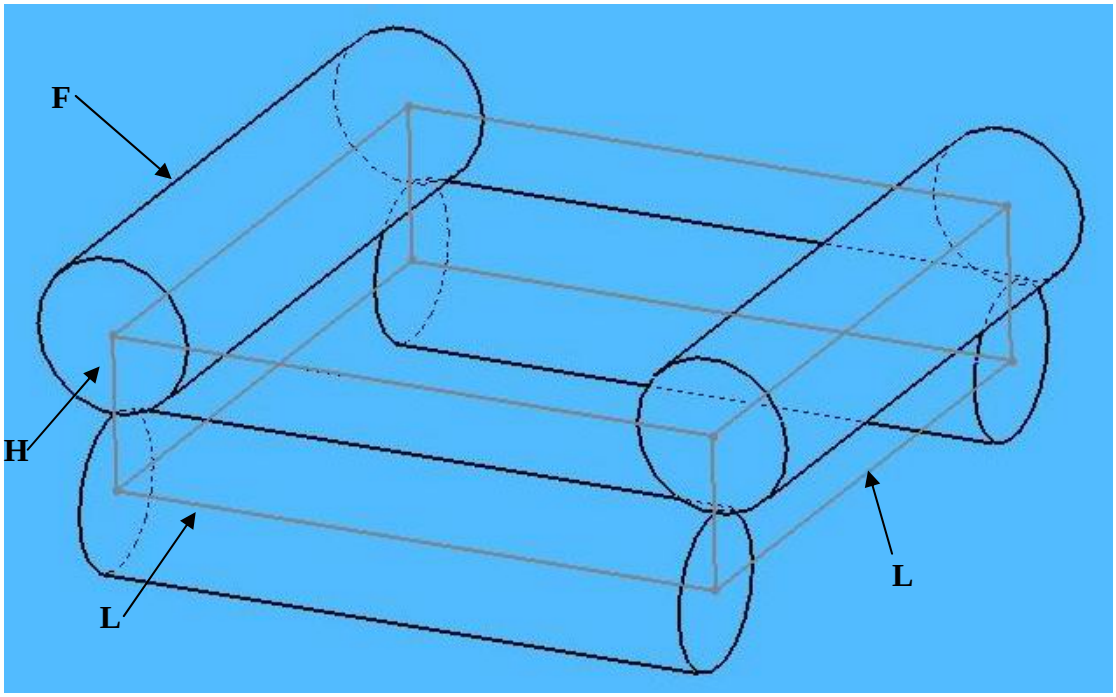

Figure 3.13. Sketch of the unit cell for calculation of the lattice porosity rate.

In Equation (3.6), H is the height of the unit and taken to be 0.15mm in theory because the diameter of the nozzle used in the extrusion is 0.15mm. The radius of the

cylinder r is 0.075mm. So for a given porosity value p, the value of the distance between the filaments L can be obtained. The value of L is in the Table 3.2 below.

Table 3.2. The value of L for different porosity lattices.

Porosity/%	L /mm
50	0.252
60	0.315
70	0.420
80	0.630

3.4.2 Fabrication of Lattices

Since the design data for the lattice have been obtained, the lattice can be fabricated through extrusion freeforming. The AUTOCAD drawings of the lattices with different porosity are shown in Figure 3.14. From the dimensions shown in Figure 3.14, the diameters of the arcs in the lattices with 50% and 60% porosity were greater than the distances between filaments in order to avoid the attachment between filaments due to deformation of the filament. For the lattices with 70% and 80% porosity, the distances between filaments were bigger enough to avoid the attachment between filaments so the diameter of the arcs were designed same to the distances between filaments. The arrows shown in Figure 3.14 indicate the travelling direction of the filament. These CAD files were put into the 'Compucam' software to get the path programs for the

lattices and then these programs were imported into the extrusion program built by Labview software. When the first layer was finished, the syringe filled with the paste was moved upward on the Z axis, and the second layer was started, to be fabricated following the path shown in Figure 3.14. Then the lattices were fabricated by the extrusion machine layer by layer. Two unsintered alumina lattices comprising 20 layers prepared from a paste with 26 vol. % solvent, having an inter-filament distance of 630 μm are shown in Figure 3.15.

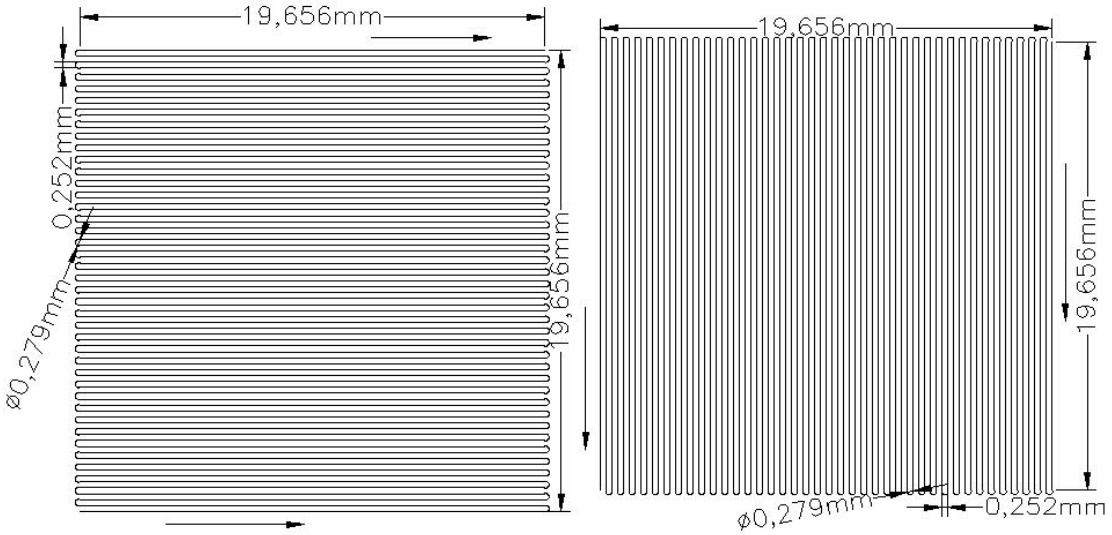

The first layer Pore size gradient (a)

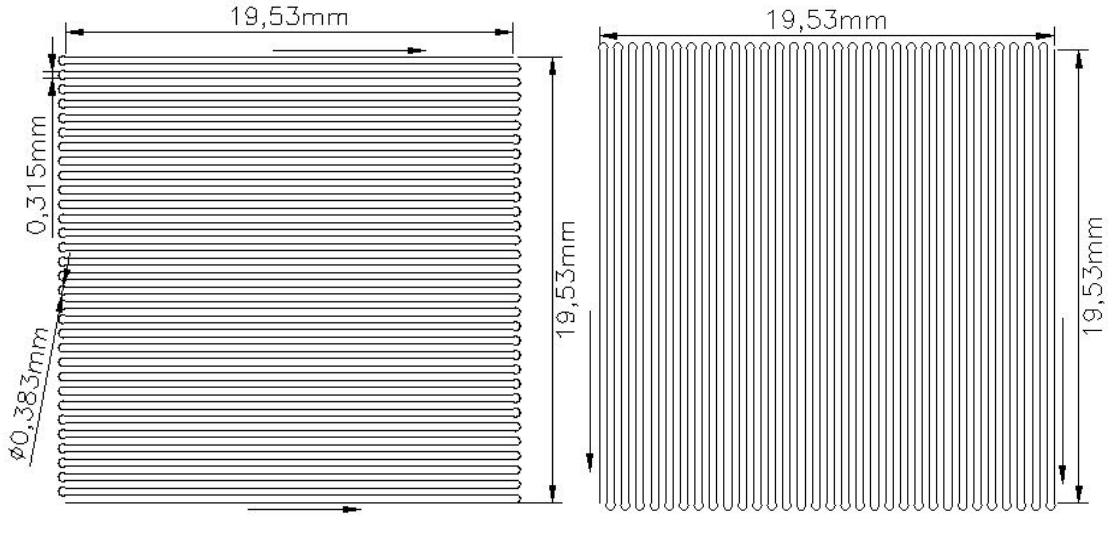

The first layer The second layer (b)

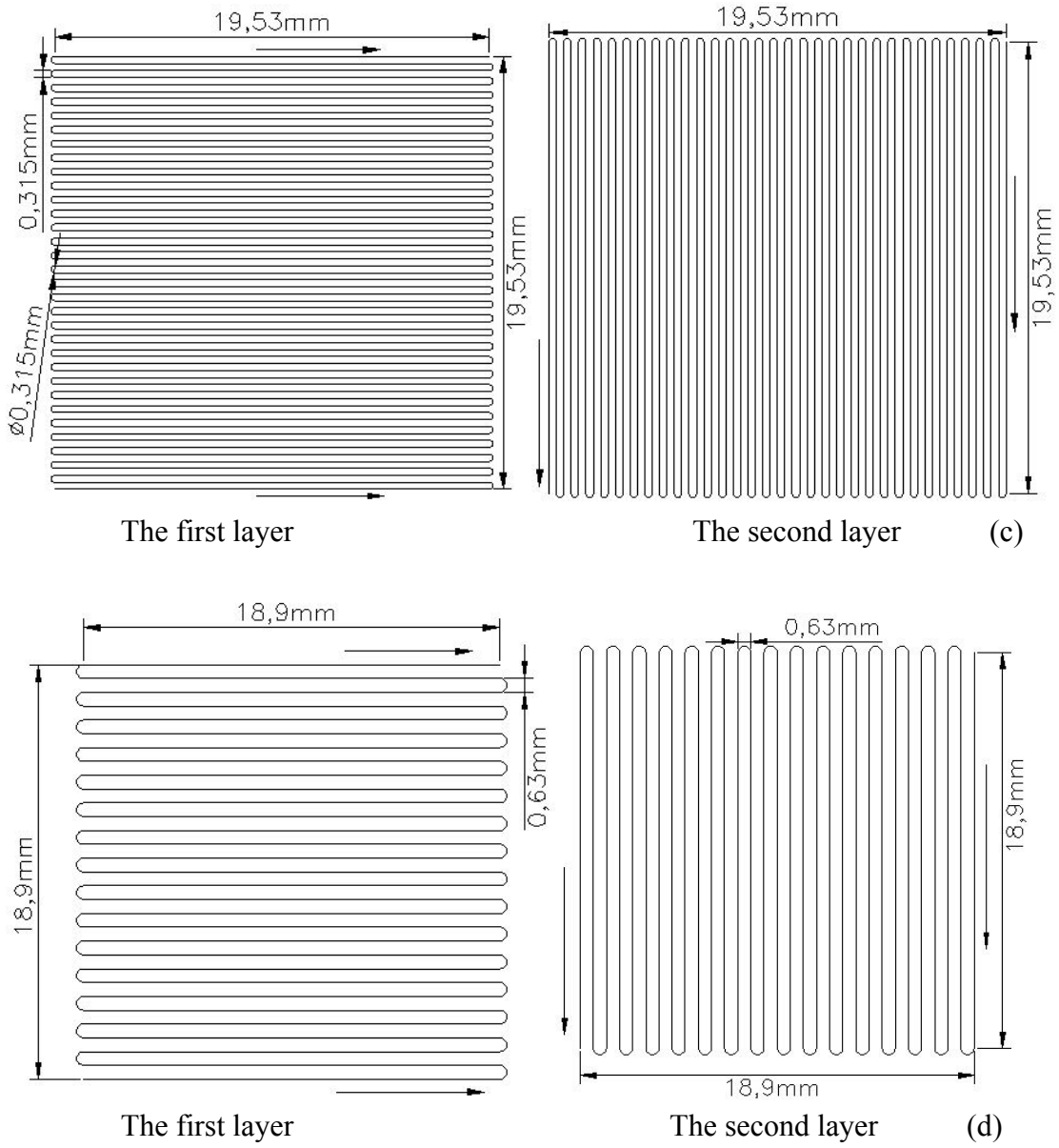

Figure 3.14. CAD drawings of the lattices with porosity (a) 50%, (b) 60%, (c) 70%, (d) 80%.

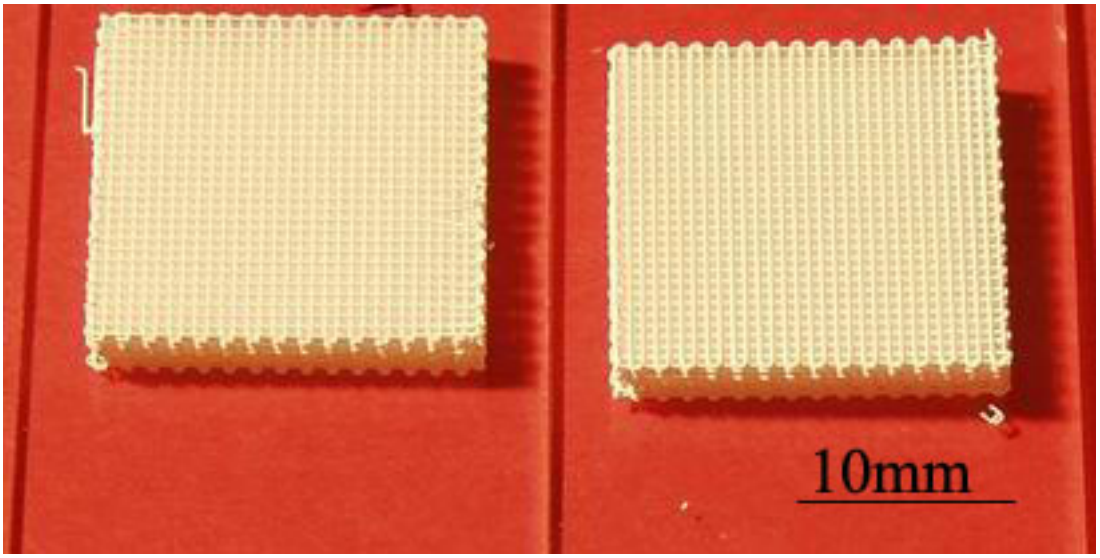

Figure 3.15. Unsintered alumina lattices comprising 20 layers prepared from a paste with 26 vol. % solvent, having an inter-filament distance of 630 μm.

3.4.3 Debinding and Sintering of the Alumina Lattices

After drying to remove the volatile solvent for 24 hours, the dried extrudates were put on the flat surface made of coarse alumina and then sintered in the furnace (Eurotherm Controller type 812, Eurotherm Limited, Worthing West Sussex, Great Britain). In the initial sintering, the furnace was controlled by a one level program. The temperature of the furnace reached 1560 °C at the rate of 5 °C per minute, and the dwell was 120 minutes. The sintered sample had distorted as shown in Figure 3.16. Two factors could induce this problem. One is the substrate surface made of 'sugar' alumina was not flat; another is the temperature of the furnace reached 1540 °C directly, and before the polymer (PVB and PEG) in the lattice was completely burned

out, the alumina began to be sintered. So a temperature dwell to burn the polymer out of the lattice was clearly needed.

In the debinding process, the polymer was softened and melted with consequent expansion[124]. Finally, the polymer was decomoposed to vapour and transported out from the pore structure of the extrudate[125]. If the degradation and the outward transportation of the polymer were unbalanced, internal stresses were produced and these could induce defects in the final product[126].

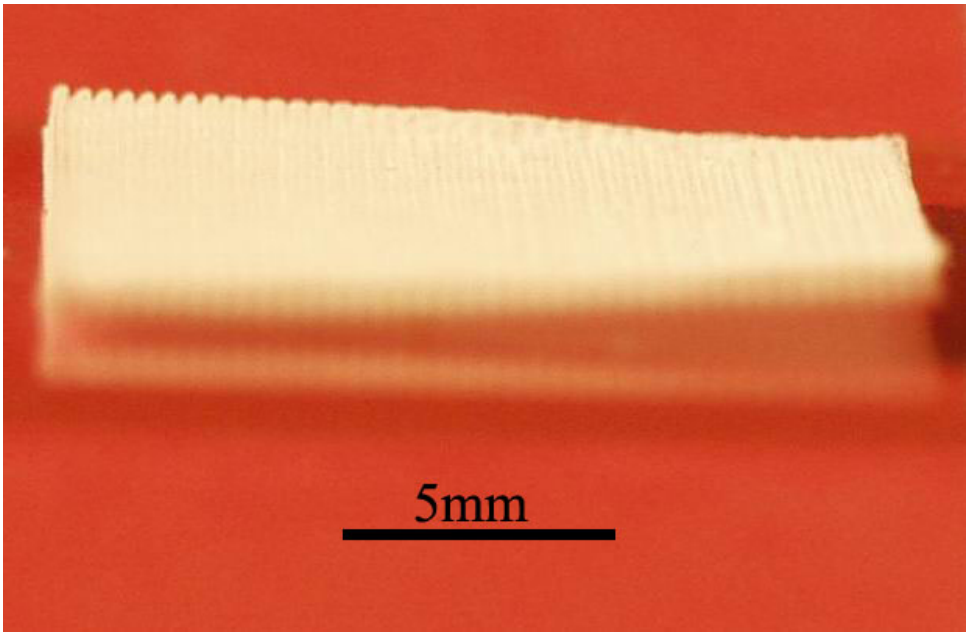

Figure 3.16. Alumina lattice sintered to 1540°C directly at the rate of 5 °C per minute on the substrate surface made of the 'sugared' alumina.

In this experiment, polymer must be transported from a small cylindrical filament with rounded surface which is a rigid structure resisting collapse and difficult for

polymer to transport out from. So a low heating rate in the debinding process was chosen. Otherwise, shrinkage in the core can result in a void or pipe at the centre of the filaments [127]. To reduce defects and get an optimal debinding process, Thermogravimetric Analysis (TGA) for the polymer-ceramic extrudate was conducted. The TGA thermograms of the PVB and PEG are presented in Figure 3.17. A low heating rate of 2 °C/min was chosen. From the graph in Figure 3.17, it was apparent that PVB and PEG were degraded and removed completely by 520 °C.

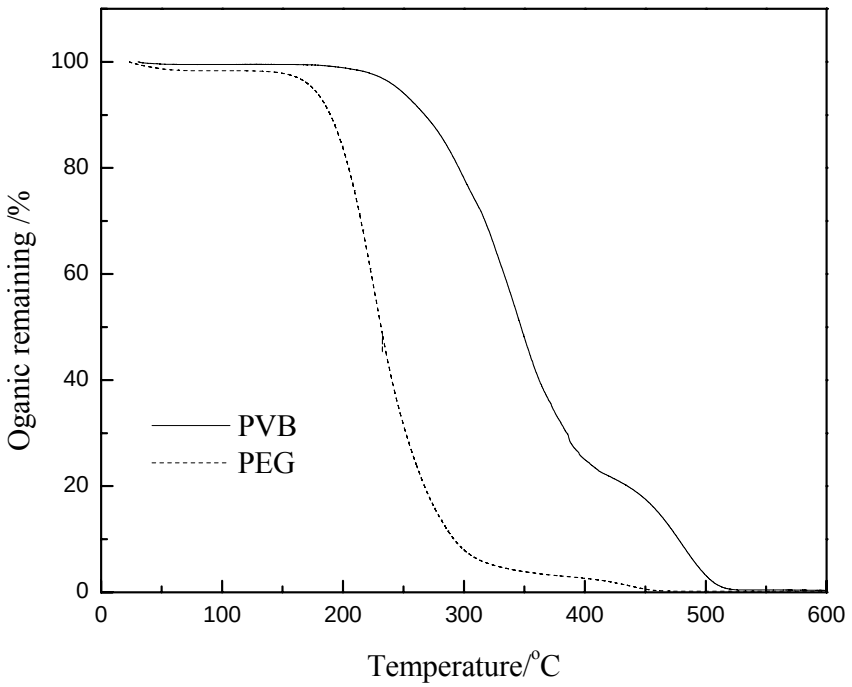

Figure 3.17. Thermogravimetric weight loss for PVB and PEG under oxygen atmosphere at a heating rate of 2 °C/min.

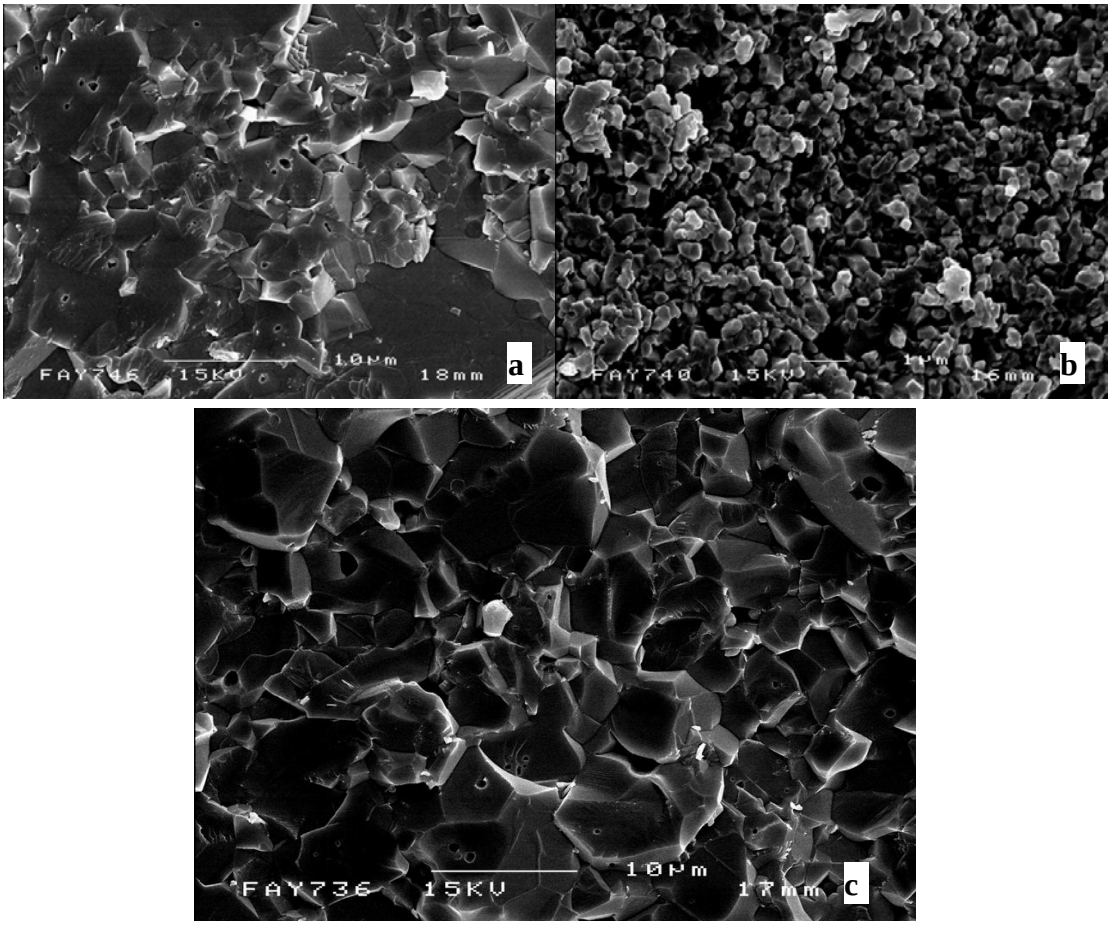

Figure 3.18. Cross sections of the filaments sintered at different temperatures: a, 1570°C; b, 1470°C; c, 1540°C.

The polymer-alumina lattices were burned to 600 °C at a heating rate 2 °C/min and then allowed to dwell for 1 hour to remove the polymer completely. After this debinding process, the samples were heated to a high temperature to attain sintered products with nearly fully dense microstructure. SEM images of the cross sections of the filaments sintered at different temperatures are shown in Figures 3.18. At 1470 °C, very little sintering has taken place and the alumina particles are remain separate. At 1570 °C, the alumina particles are extensively sintered but "large-grain growth" occurs which can reduce mechanical strength of the samples[128]. So the alumina

lattices were sintered at 1540°C for 1 hr after slow heating to 600°C at rate of 2°C/min with a 1 hour dwell so that the polymer in the samples could be removed slowly and evenly. The microstructure, observed by SEM and shown in Figure 3.18.c, is of near full density, with isolated residual porosity and average grain size in the region 2-3 μm.

Figure 3.19 shows a part of the alumina lattice assembled from 150 μm diameter filaments that had been sintered followed the selected thermal processing and then fractured. The shrinkage is almost 20%. The surface of the filament is uniform and displays an average grain size in the 2-3 μm size. The filament has a little distortion on the welding site. The degree of the distortion is decided by the weight percent of the paste which were used to extrude filaments. There are some big holes in the cross sections of the filament showed by the arrows named ‘a’ on the picture. This can be induced by air bubbles in the paste. If the air bubble is big enough, the filament may be ruptured. During the drying and concentration stage of the paste, very careful and even stirring can be helpful to alleviate air bubbles.

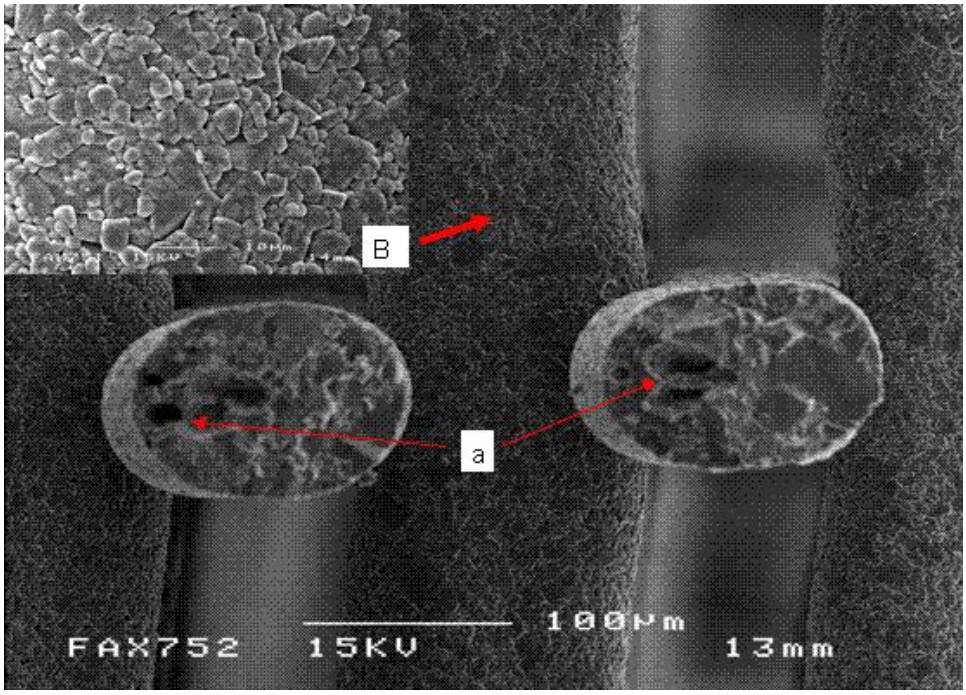

Figure 3.19. SEM images for a part of alumina lattice assembled from 150 μm diameter filaments that had been sintered followed the selected thermal cycle.

So to summary, the sequence finally selected, the samples were prepared on the surface of a alumina slide (alumina pure rate: 99%) and then sintered by the furnace controlled by a two level program: firstly, the temperature of the furnace reached 600 °C at the rate of 2 °C per minute, followed by a dwell for 60 minutes; secondly, the temperature of the furnace reached 1540 °C at the rate of 5 °C per minute, and there was a dwell of 60 minutes. The picture of the lattices with different macroporosities sintered by the furnace controlled by this two level program is shown in Figure 3.20. From this picture, the bending up phenomena shown in Figure 3.16 has disappeared.

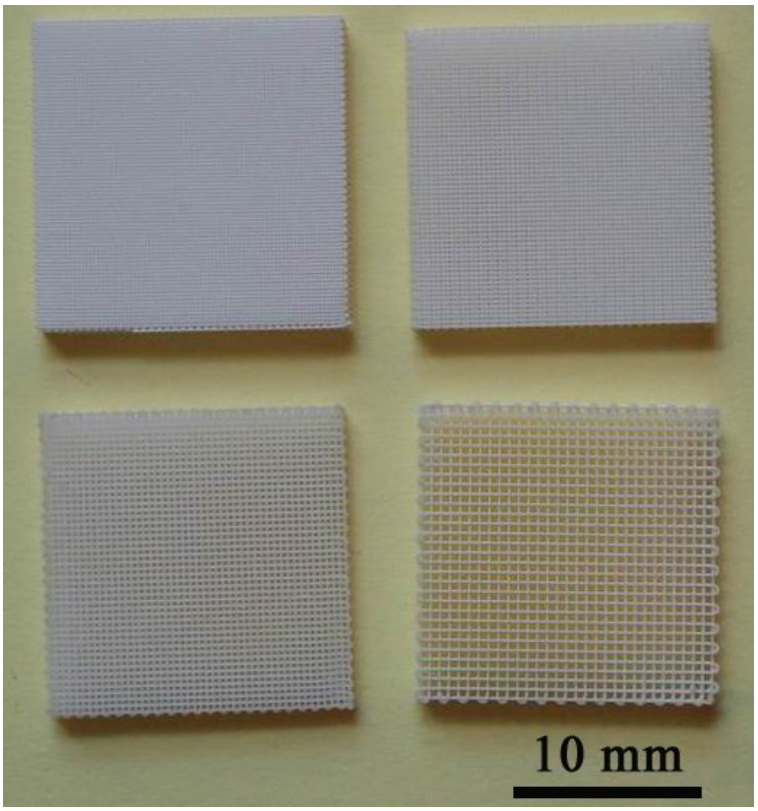

Figure 3.20. The sintered alumina lattices with different macroprorosities.

3.4.4 Measurement for the Actual Dimensions and Macroporosities of the Lattices

The actual macroporosities of the different lattices were measured according to ASTM C 1039-85[129]. The dry mass of the sintered sample m was weighed, and then the sample was immersed in water. In some cases, the macro-pores of the lattice are so small that water could not fill all of them. Vacuum was therefore applied to saturate the pore structure. After cleaning up the excess water on the surfaces and borders of the lattice with a moistened tissue or cotton cloth, the mass of the sample

filled with water m_2 was weighed. It included the dry mass of the sample and the mass of the water fill all of the macro-pores and can be expressed by the formula below:

$$m_2 = m_1 + \rho v \quad \text{..... (3.7)}$$

where, m_2 is the mass of the sample filled with water; m_1 is the dry mass of the sample; ρ is the density of the water; v is the volume of the water in the sample, its value is equal to the volume of the pores in the sample.

The porosity of the sample p is:

$$p = \frac{v}{v + v_1} \quad \text{..... (3.8)}$$

where, p is the porosity of the sample; v is the volume of the water filled the macro-pores of the samples, ; v_1 is the volume of the alumina in the sample. So according to the Equation (3.7) and (3.8), the porosity of the sample is expressed by the formula below:

$$p = \frac{(m_2 - m_1) \times \rho_1}{m_1 \times \rho + (m_2 - m_1)\rho_1} \times 100\% \quad \text{..... (3.9)}$$

where, p is the porosity of the sample; m_1 is the dry mass of the sample; m_2 is the wet mass of the sample; ρ is the density of the water; ρ_1 is the density of the alumina, 3960 kgm^{-3}. So the actual macroporosities can be obtained and were 59.3%, 64.1%, 73.8% and 82.2% separately.

The sizes of the lattices are shown in Table 3.3. From the table, the radius of the filament before sintering r, was 0.075mm and the value after sintering was 0.06mm. The height of the rectangle H before sintering was 0.15mm and the value after sintering was 0.12mm. The centre to centre distances between the filaments for the different porosity lattices L are given in the table below. According to the Equation (3.6), the theoretical macroporosities for the different lattices can be calculated and those for the lattices before sintering were 51.6%, 61.3%, 71.0% and 80.6%, those for the lattices after sintering are 51.0%, 60.8%, 71.2% and 80.4%. There was no obviously variety of the theoretical macroporosities between the lattices before sintering and after sintering.

The values of the theoretical macroporosities were lower than those of the actual macroporosities. There were two reasons for this result. One was the excess water on the surfaces and the borders of the lattices could not be perfectly removed. That would mean the apparent volume of water filling the macro-pores increased, and this induced an apparent increase of the macroporosities. Another reason is the density of the alumina. The density of the alumina used in this calculation was 3960 kgm^{-3}, which was the density of the alumina powders. The value of the density of the alumina lattice was lower than that of the density of the alumina powders. That was because of the presence of some isolated residual porosity. So the value of the actual macroporosities was higher than that of the theoretical macroporosities.

Table 3.3. Dimensions of the lattices with various porosities.

	Porosity /%	Length /mm	Width /mm	Height /mm	Filament Diameter /mm	Gap /mm	Shrinkage /%
Before sintering	50	20.06	20.06	2.90	0.15	0.25	
After sintering	50	16.00	16.00	2.30	0.12	0.20	20.2
Before sintering	60	20.00	20.00	2.90	0.15	0.32	
After sintering	60	16.00	16.00	2.30	0.12	0.25	20.0
Before sintering	70	19.89	19.89	2.90	0.15	0.42	
After sintering	70	15.90	15.90	2.30	0.12	0.34	20.1
Before sintering	80	19.68	19.68	2.90	0.15	0.63	
After sintering	80	15.70	15.70	2.30	0.12	0.50	20.2

3.4.5 Metal Matrix Composites Preparation and Microstructure Observation

The matrix material was 6061 aluminium alloy with (0.8-1.2) wt. % Mg, (0.4-0.6) wt. % Si having liquidus and solidus temperatures of 650^{o}C and 582^{o}C, respectively. The composites were fabricated by squeeze casting of the 6061 alloy into the alumina

lattices with different dimensions shown in Table 3.3. Microstructures of the alumina lattice were observed by JEOL JSM 6300F SEM and were shown in Figure 3.21. A round corner can be found at the end of each filament as a continuous writing route was used in fabrication of the ceramic lattice (Figure 3.21 b). However, some micro-voids can be normally found in the ceramic filaments under higher magnification SEM images.

The composites were fabricated by squeeze casting. The alumina lattice was placed in a steel die fitted with a vacuum system and preheated to 530 ~ 550 °C. The molten aluminium alloy at 850 °C was poured at approximately $5x10^{-5}$ m^3s^{-1} onto the preheated alumina lattice. A ram, activated by a 25 tonne hydraulic press (Dassett Engineering Corporation, UK), forced the melt into the lattice while evacuation was applied. After the infiltration process, a maximum pressure of 50 MPa was maintained until the die cooled and the aluminium phase solidified. The lattice was placed in a porous mould to facilitate the infiltration of liquid aluminium inside. (This fabrication processing was done in University of Bristol and supported by H.X.Peng and L.Yin.) To show the arrangement of the alumina lattice during squeeze casting, Schematic drawings were provided in Figure 3.22.

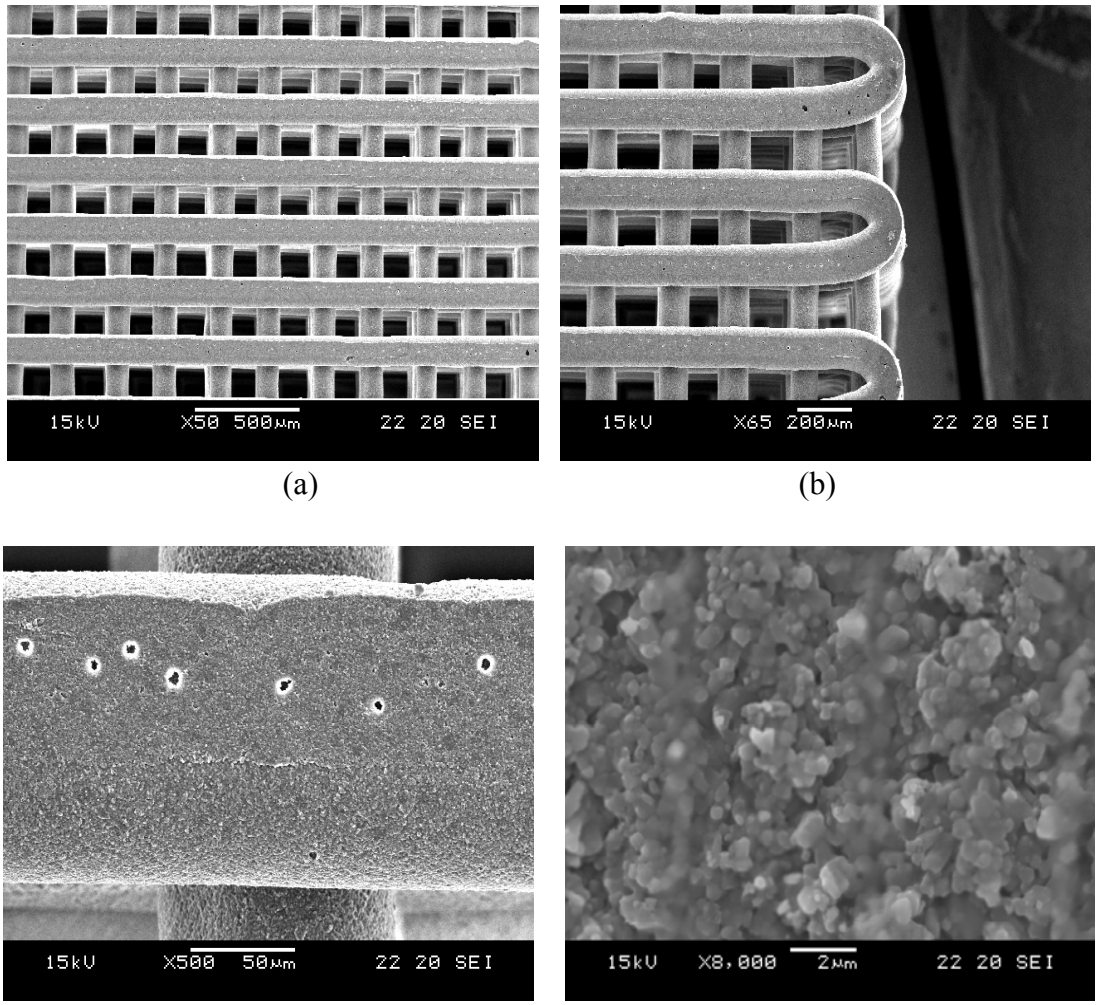

Figure 3.21. SEM images of ceramic lattices, (a) periodically 3D arranged ceramic lattice, (b)round corners can be seen at the end of filaments, (c) micro-voids can be observed in single ceramic filaments, (d) higher magnification image of the microstructure in ceramic filaments.

After squeeze casting, the alumina/aluminum composites were in an aluminum block shown in Figure 3.23. The arrow in this picture indicates the location of the porous mould with the alumina/aluminum composites in it.

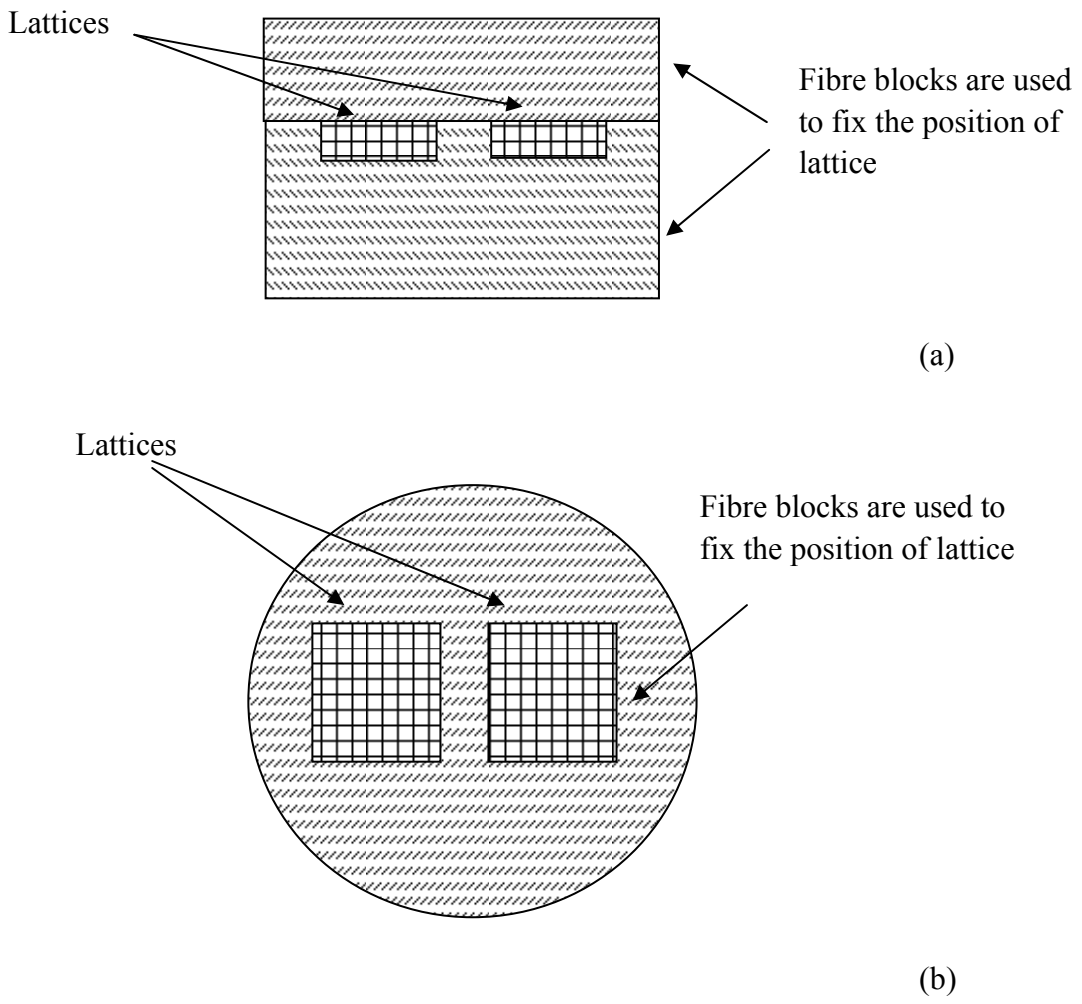

Figure 3.22. Schematic drawings show the arrangement of the alumina lattice during squeeze casting, (a) view from side; (b) view from top.

The alumina/aluminum composites were cut out from the aluminum block and polished. The optical microscope pictures of the polished composite are shown in Figure 3.24. From Figure 3.24.a, the alumina lattice was filled with aluminum and the alumina filaments by which the lattice was knitted were well maintained in the composites after a thermal shock during the metal infiltration process. The round corner filaments were also maintained very well as shown in Figure 3.24.b.

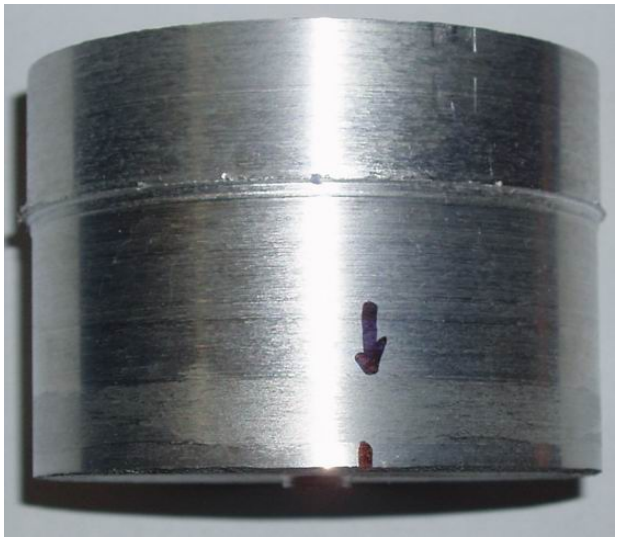

Figure 3.23. An aluminum block with the alumina/aluminum composites in it was fabricated by squeeze casting.

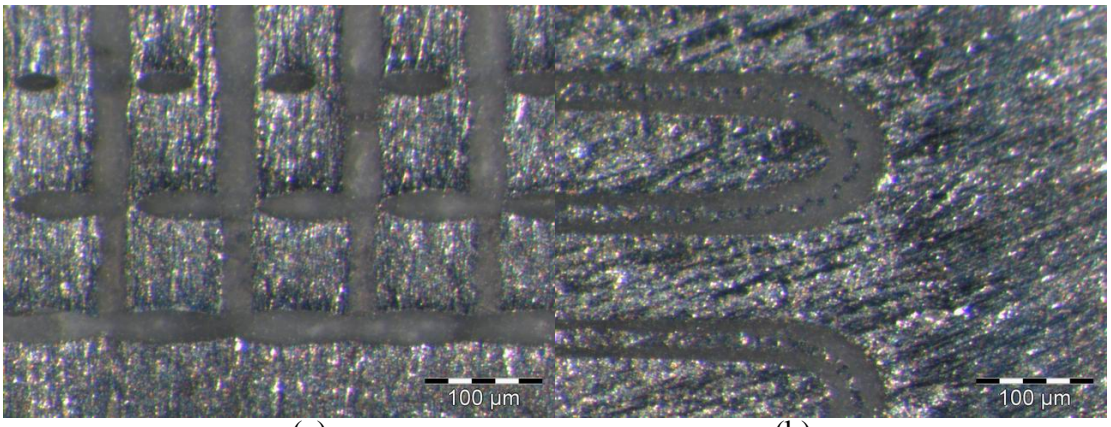

(a) (b)

Figure 3.24. Optical microscope pictures of the alumina/aluminum composites.

As seen in Figure 3.25.a, the dark phase is the alumina, while the lighter phase is the aluminum. A good interface bonding was resulted by the squeeze casting technology, even the micro-voids existed in the ceramic filaments were filled with aluminum.

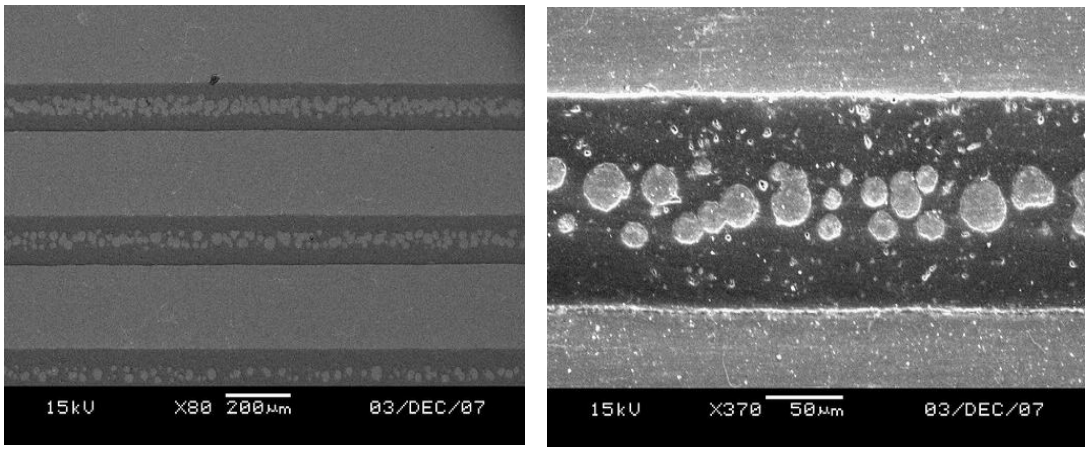

(a) (b)

Figure 3.25. SEM images of the bi-continuous composites fabricated from the alumina lattice by squeeze casting technology, (a) back scattered electron image, (b) higher magnification image shows a well bonded interface and fully filled composites.

3.5 Design and Fabrication of the Lattices for Tissue Engineering with HA and TCP

To study the shape and form of lattice for application in regenerative medicine, several types of lattices with different pore structures were designed and fabricated by the extrusion freeforming worktable. In these different types of lattices, a lattice with multi-scale hierarchical void structures was chosen and used to study the shape and form of lattice for applications in regenerative medicine. In this way, the maximum histological information can be provided from the minimum of testing.

The continuous filaments which were knitted into lattices were extruded from the two-phase calcium phosphate mixture which was made of medical grade

hydroxyapatite (HA) and β-tricalcuim phosphate (TCP) powders. HA is well known as a similar material as the carbonate apatite existing in natural bone and provides high mechanical properties[130]. But HA is also difficult to degrade in the body and is usually used in conjunction with TCP which has a good resorption in vivo[131]. The ratio of HA and TCP has been studied by H. Yang and I. Thompson et al[132]. In this experiment, the ratio of HA was 75 wt. % and that of TCP was 25 wt. % in the ceramics powders.

3.5.1 Linear Shrinkage and Mechanical Properties of the Sintered Filaments

The paste composed of 60 vol. % ceramics (75 wt. % HA and 25 wt. % TCP) and 40 vol. % polymer (75 wt. % PVB and 25 wt. % PEG) was extruded into filaments with 100 mm length and 300 μm diameter. The filaments were then cut into 80 mm length and sintered in two groups to 1150 °C and 1250 °C separately at the heating rate of 5°C/min with a one hour dwell.

The surfaces of the sintered HA/TCP ceramics filaments act as the substrates on which proteins adsorb and cells adhere and grow. To the surfaces with open porosity, the cross sectional microstructure of the sintered filaments are needed to provide the morphology of bulk porosity which is relevant to cell growth and to influence the mechanical properties of the filament. Some SEM images of the HA/TCP ceramic

filaments were shown in Figure 3.26. In Figure 3.26 (a), the filament was sintered in 1150°C. The β-TCP particle growth took place at the lower sintering temperature, while the necks between HA particles are just developing. Many open pores can be observed on the surface of the filaments sintered in 1150°C. A SEM image for the surface of the filament sintered at 1250°C is shown in Figure 3.26 (b). Both β-TCP and HA particle growth took place and open porosity disappeared. The surface of the filament is sealed and smoothed. But considerable closed porosity existed in the inner structure of the filament as shown in Figure 3.26 (c). These closed porosity indicated that the samples are not fully dense.

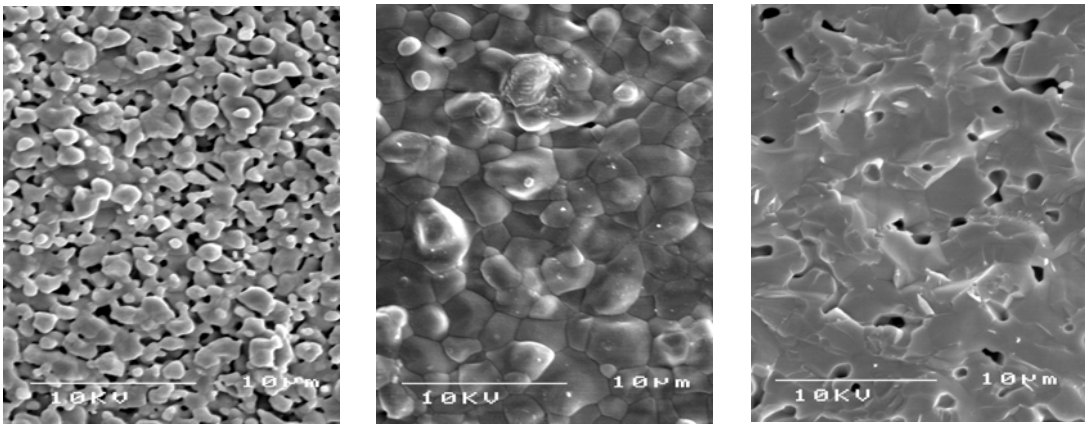

(a) (b) (c)

Figure 3.26. SEM images of the HA/TCP ceramic filaments: (a) surface of the filaments sintered at 1150°C; (b) surface of the filaments sintered at 1250°C; (c) cross section of filaments sintered at 1250°C.

`To get final samples with desirable dimensions, the overall linear shrinkage must be compensated by the design file for the lattices. The total shrinkage *S* includes two

stages, drying shrinkage S_1 and sintering shrinkage S_2, which can be represented separately by the equations below.

$$S_1 = \frac{L_0 - L_1}{L_0} \quad \text{..... (3.10)}$$

$$S_2 = \frac{L_1 - L_2}{L_1} \quad \text{..... (3.11)}$$

$$S = \frac{L_0 - L_2}{L_0} = S_1 + S_2 - S_1 S_2 \quad \text{..... (3.12)}$$

where, L_0, L_1 and L_2 are the lengths of the initial, dried and sintered filaments respectively.

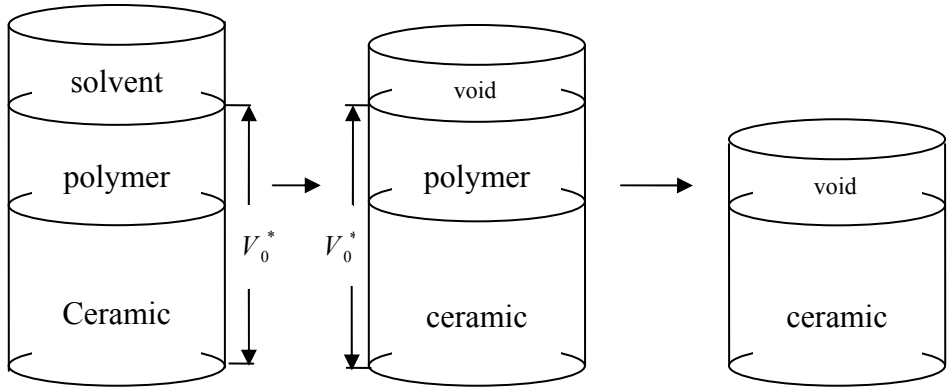

Figure 3.27. Schematic illustration of volume changes of the filament after drying and sintering.

The volume changes of the filaments after drying and sintering are shown in Figure 3.27. In the drying processing, the shrinkage occurred with the solvent evaporating from the polymer-solvent system in the pore structure. Particles congregated into a

binary polymer-ceramic system with 60 vol. % powder. As the powder volume percent is near the limit of powder loading, particles may be contacting each other before drying is completed and in that case the filaments after drying are comprised of polymer, ceramic and voids.

Since the drying shrinkage started immediately as the filament extruded from the nozzle, it was impossible to measure the initial length of the filament L_0. The drying shrinkage S_1 had to be found indirectly. If the particles used in this experiment present anisotropy, the length and diameter shrinkage may be different. The ratio of the length to diameter shrinkage can be deduced from the shrinkage of the whole lattice. In this experiment, the ratio was better than 0.95. So the particles can be taken as isotropic and the drying shrinkage S_1 can be also represented by the following equation.

$$S_1 = \frac{r_0 - r}{r_0} \quad \text{..... (3.13)}$$

where, r_0 is the radius of the initial filament, i.e. the radius of the nozzle which the filament was extruded from, r is the radius of the filament after drying.

So the drying shrinkage S_1 can be defined by the volume of extruded sample V_0 and the volume of dried sample V_1 according to the Equation (3.10) and (3.13).

$$S_1 = 1 - \sqrt[3]{\frac{V_1}{V_0}} \quad \text{..... (3.14)}$$

The volume of dried sample V_1 can be calculated from

$$V_1 = \frac{V_0^* \rho_0^*}{\rho_1} \quad \text{..... (3.15)}$$

where, V_0^* is the volume of the fully dense ceramic and polymer binary as shown in Figure 3.27, ρ_0^* is the calculated theoretical density of the ceramic and polymer composite and ρ_1 is the actual density of the dried filaments. Here, $\rho_1 \le \rho_0^*$ because full packing of the binary system may not be obtained. For the filament with length l extruded from a nozzle with radius r_0, after drying the measured mass is W_l and then ρ_1 is calculated from:

$$\rho_1 = \frac{W_l}{V_l} = \frac{W_l}{l\pi r^2} = \frac{W_l}{l\pi r_0^2 (1-S_1)^2} \quad \text{..... (3.16)}$$

According to Equation (3.14), (3.15) and (3.16), the drying shrinkage S_1 can be represented by the following equation:

$$S_1 = 1 - \frac{l\pi r_0^2 \rho_0^* V_0^*}{W_l V_0} \quad \text{..... (3.17)}$$

where, $\frac{V_0^*}{V_0}$ is the volume fraction of the polymer and ceramic in the paste which was measured before extrusion. So the drying shrinkage can be calculated through Equation (3.17) after the mass of a dried filament with fixed length was measured.

The sintering shrinkage is due to the loss of polymer in the debinding stage and the loss of porosity at the sintering temperature. Five dried samples with length L_1=80mm sintered at 1150°C and 1250°C were taken and the lengths of these sintered filaments L_2 were measured. The error due to the measurement in length was ± 0.5 mm. Inserting L_1 and L_2 into the Equation (3.11), the sintering shrinkage was obtained. The total linear shrinkage was then calculated from Equation (3.12). The results of the drying, sintering and total shrinkage of the filaments were put into Table 3.4.

Table 3.4. The drying, sintering and total shrinkage, S_1, S_2 and S, of the filaments sintered at different temperature.

Sintering temperature	S_1	S_2	S
115 0°C	0.054	0.056	0.107
1250°C	0.054	0.114	0.190

Since the particle shape was taken as isotropic, the design dimensions of the lattices can be calculated from the shrinkage results shown in Table 3.14. For example, for final dimensions of 10mm×10mm×7mm after sintering at 1150°C, the design dimension is 11mm×11mm×7.7mm, but for a final product sintered at 1250°C with the same dimension, the design dimension is 12.3mm×12.3mm×8.6mm.

The diameters of the filaments sintered at 1150°C and 1250°C respectively were measured by SEM images (n=3) and the dimensional tolerances was ±5 μm for the measured samples. The diameter of the filament sintered at 1150°C is 264 μm and that of the filament sintered at 1250°C is 236 μm. Following the method mentioned in Section 2.3.3, the three point bending strengths of the filaments were obtained. The three point bending strength of the filaments sintered at 1150°C was 33.2±2.6 MPa, and that of the filaments sintered at 1250°C was 102.7±11.7 MPa.

In this experiment, the Weibull modulus was calculated by the linear regression (LR) method due to its simplicity and more safety than the ML method in reliability prediction[133,134].

The probability of failure P can be described by Weibull's two-parameter distribution[135,136,137].

$$P = 1 - \exp\left[-\left(\frac{\sigma}{\sigma_0} \right)^m \right] \quad \text{..... (3.18)}$$

where, P is the probability of failure; σ is the stress at failure; σ_0 is the scale parameter, equal to the mean stress of the distribution, $\overline{\sigma}$, for technical ceramics[137]; m is the Weibull modulus, also called the shape parameter to represents the scatter of the fracture strength. Taking logarithms twice in Equation (3.18), Equation (3.19) is obtained below.

$$\ln \ln\left(\frac{1}{1-P} \right) = m \ln\left(\frac{\sigma}{\sigma_0} \right) \quad \text{..... (3.19)}$$

obviously, the Weibull modulus is the slope of the Equation (3.19). Since the probability of failure P is unknown, four expressions are used as prescribed estimators to define the probability of failure in the LR method[138,133,137]. In this experiment, one expression as shown below was selected to be the probability estimator due to its simplicity.

$$P_i = \frac{i}{n+1} \quad \text{..... (3.20)}$$

In the LR method, the measured fracture stresses are arranged in ascending order, *i* is the number of samples in ascending order; P_i is the probability failure for the *i*th sample, and n is the number of the samples to be measured.

The strength distributions of the filaments sintered at 1150°C and 1250°C are shown in Figures 3.28 and 3.29 respectively. The Weibull modulus was given by the slope of a graph with axes $\ln\ln[1/(1-p_i)]$ and lnσ. The Weibull modulus of the filaments sintered at 1150°C was 13.3 and that of the filaments sintered at 1250°C was 8.89.

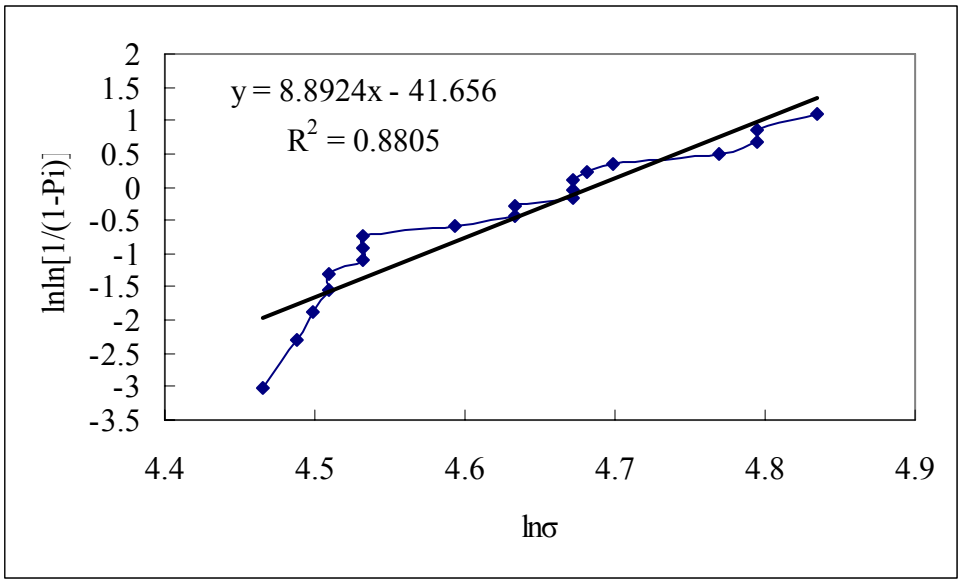

Figure 3.28. Strength distribution of the filaments sintered at 1250°C, Weibull modulus, M=8.89, n=20.

Although the samples sintered at 1250°C have a higher strength than the samples sintered at 1150°C, their Weibull modulus is lower than the samples sintered at 1150°C. The particles of the filaments sintered at 1150°C have more uniform size and

spatial distribution. The low Weibull modulus indicates that flaws in the samples tend to congregate at the sintering temperature 1250°C and decrease the reliability of the samples.

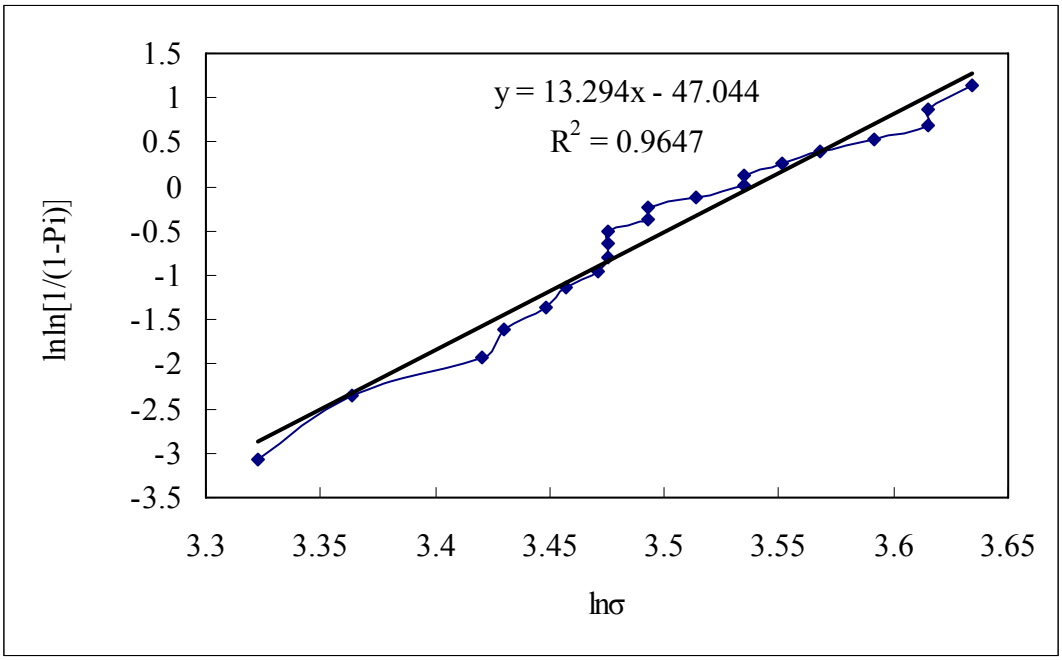

Figure 3.29. Strength distribution of the filaments sintered at 1150°C, Weibull modulus, M=13.3, n=20.

3.5.2 Design and Fabrication of Multi-scale Hierarchical Lattices for Bone Repair

Scaffolds used in the first round in-vivo testing

Multi-scale hierarchical void structures were fabricated using HA/TCP paste for bone repair and were tested *in vivo*. The whole sample was divided into four parallel zones (shown in Figure 3.30. b). A control zone without lattices served as an internal control

area to compare the function of the lattice under the same *in vivo* test conditions. The other three zones were lattices with pores of 50μm, 100μm and 150μm. All zones were interlinked by the transverse filament so the strength of the whole scaffold was improved. Vertical growth of tissue from the bottom of the scaffold to the top was investigated by in-vivo testing[139]. To define the voids distinctly in the vertical direction, the normal direction of the scaffold layers should be the same as the sample height direction (as shown by *N* in Figure 3.30.a).

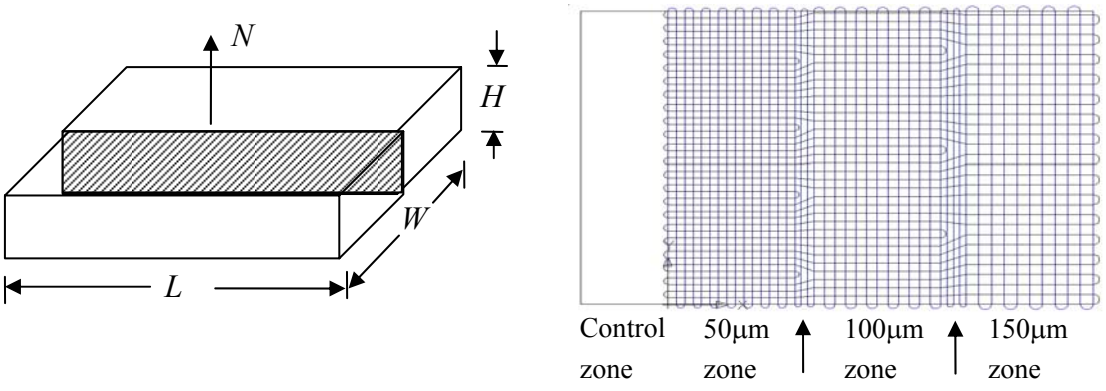

(a) (b)

Figure 3.30. (a) Sample designed for in vivo tests (L=12mm, W=8mm, H=3mm). The shadowed cross section is the direction of slicing for histological analysis. All the slicing is parallel with this section. N is the normal direction for the lattice layers; (b) Four zones with different pore size were integrated into one sample. The arrows show the location of walls between zones.

From Figure 3.30 b, the extrusion route was carefully designed to keep the filament within the whole sample throughout the rendering. To increase the effect of the interlinking, the horizontal lines were designed with minimum shift in the vertical

direction. To adjust the different line densities in different zones in order to form different void sizes, some 'U' turn lines were inserted between horizontal lines. To reduce transverse penetration of cells between adjacent zones, denser zones were designed between zones in the transverse direction (indicated by arrows in Figure 3.30 b).

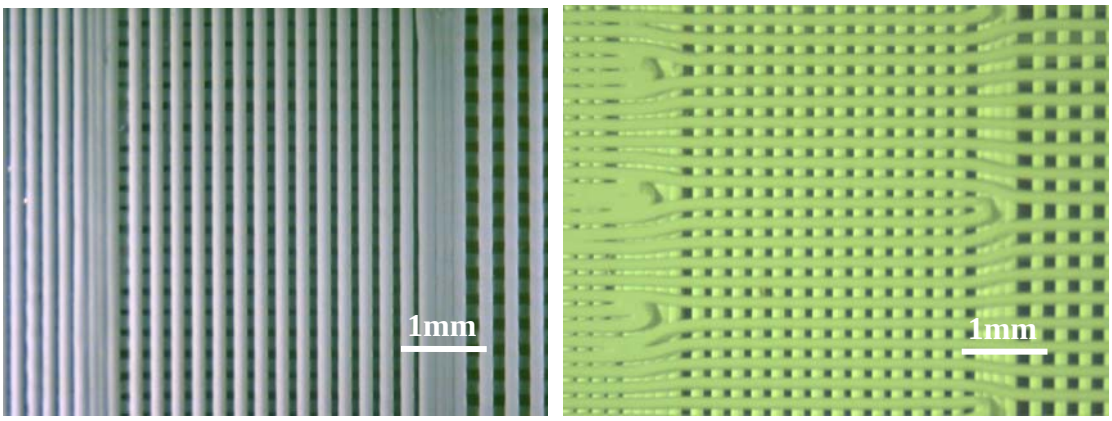

Figure 3.31. Optical images of unsintered lattice with multi-scale hierarchical void structures (cf. Figure 3.30 b): (a) vertical line structure; (b) horizontal line structure showing interlinked and 'U' turn filaments.

Optical images of unsintered lattice with multi-scale hierarchical void structures were shown in Figure 3.31. The lattices are divided into three zones with different pore sizes of 50, 100 and 150 μm from left to right by two denser filaments walls. The pores are uniform and interconnected in each zone. Some horizontal lines with minimum shift in the vertical direction and 'U' turn lines are observed in Figure 3.31 b. It can also be observed that the 'bending up' phenomena happened on the 'U' turn lines. The drag on the filament at the bending point as it is laid down is caused by the

finite yield stress of the material and causes it to follow a slightly shorter path resulting in accumulation of material.

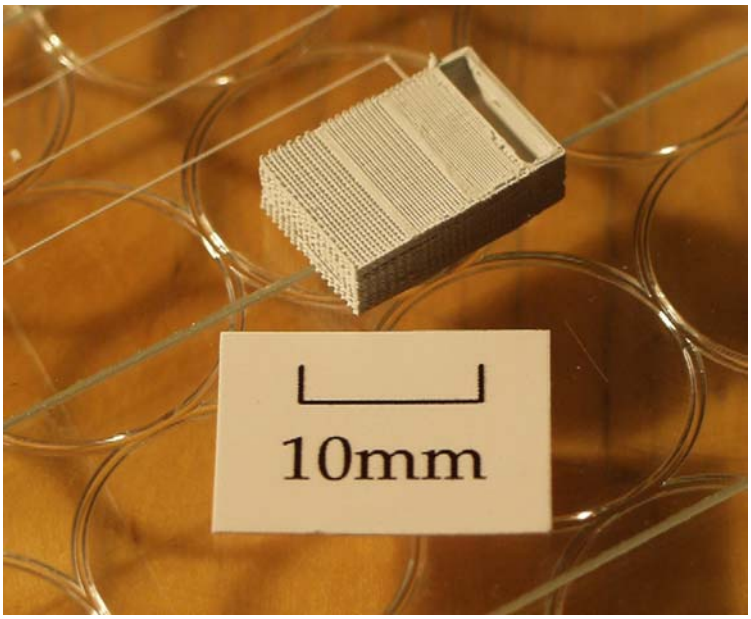

Figure 3.32. Final sintered multi structured block placed on a 15mm diameter well plate.

The samples were sintered to 1150 and 1250 °C respectively at the heating rate of 5 °C/min with one hour dwell. One sintered multi-scale hierarchical void structure is shown in Figure 3.32. These samples were placed sub-periosteally on rabbit calvarium under aseptic conditions. After 2, 4, 8 or 12 weeks, the experiments were terminated and the specimens were harvested (as shown in Figure 3.33, this *in vivo* test was conducted at Guys and St. Thomas Hospital).

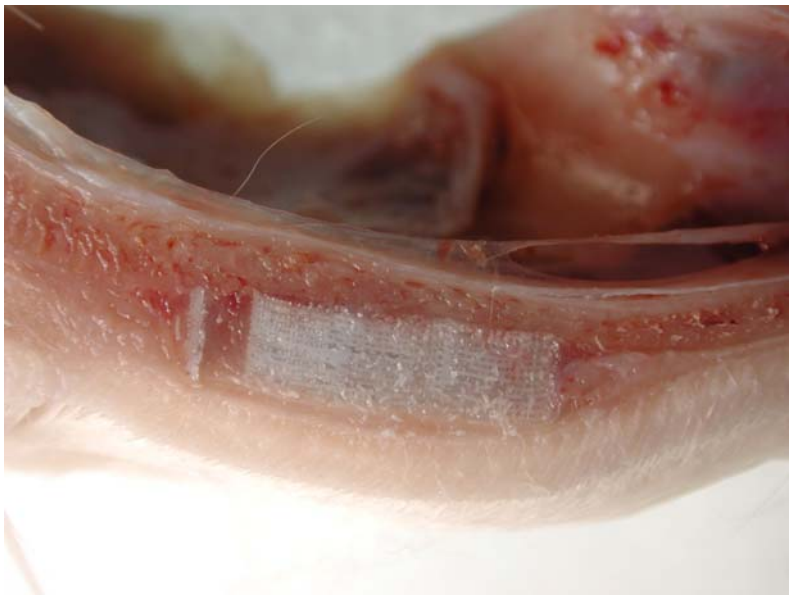

Figure 3.33. Specimen of the scaffold placed sub-periosteally on rabbit calvarium.

In this *in vivo* test, no macroscopic signs of infection or inflammation were detected. The good interface between the new bone and the materials of the first layer imply that the materials have good biocompatibility. The materials have no obvious absorption after 3 months and keep the structure well. The low absorption means that it is possible to investigate the effects of pore size on bone growth without considering the influence of degradation of the materials.

Although the implant sintered to 1150°C is more porous and has higher rate of dissolution than the implant sintered to 1250°C, the effects of the micro or nano pores on the bone growth is not obvious. More bone growth was observed in the 1250°C sintered implant than in the 1150°C sintered implant.

In the previous experimental studies, the newly formed bone, which is osteoid or woven bone, disappears gradually and was replaced by lamellar bone at 8 weeks[140,141,142]. The histological features of tissue between new bone and graft materials change to adipose tissues which resemble the host bone marrow[143]. In this experiment, the periosteum offered enough blood for the control area which contributed to blood clot and has been demonstrated to promote new bone formation in clinical and experimental studies[140,144]. The analyses of the histology of the implant slice at different time point were provided by Guys and St. Thomas Hospital. Woven bones with partial lamella were formed around the grooved cortical bone and fibrous connective tissue and blood clots filled in the control area and the spaces between filaments after 2 weeks. After 8 weeks, adipose tissue and loose fibrous connective tissue were found between the bone trabecula. Although newly formed bone changed to lamella bone, less new bone formation was observed than that of the previous experimental studies at the same time point. After 12 weeks, more adipose tissue was found.

The graft material accelerates newly formed bone generation by promoting a more stable environment[145,146], but their presence retards bone formation by occupying the space to be regenerated[145,147]. Another reason for the lower amount of new bone formation is the competition for populating the lattice between soft tissue and osteoblasts. More spaces are needed for the osteoblasts to form bone tissue. The

50-100 μm sized pore is reported to be enough for osteoconduction, but the optimal pore size for osteoconducntion and new bone formation is 300-500 μm[148,149].

Scaffolds used in the second round in-vivo testing

Lots of previous studies on implants have revealed that pore size, shape, interconnection and arrangement of pores are important to osteoconduction[149, 150, 130]. The lower amount of bone formation within the first round design implant block can be induced by the limit of pore size or the distribution of pores. So large 'corridors' with 600 μm were introduced in the second round design scaffold. These large 'corridors' were used for the vascularisation which was very important to the application and mass transport of oxygen and nutrients, and remove waste metabolites from the cells. The small 'rooms' with 30 μm were also built for the cells in the second round design scaffold (a 3D top view of second round design lattice was shown in Figure 3.34 e).

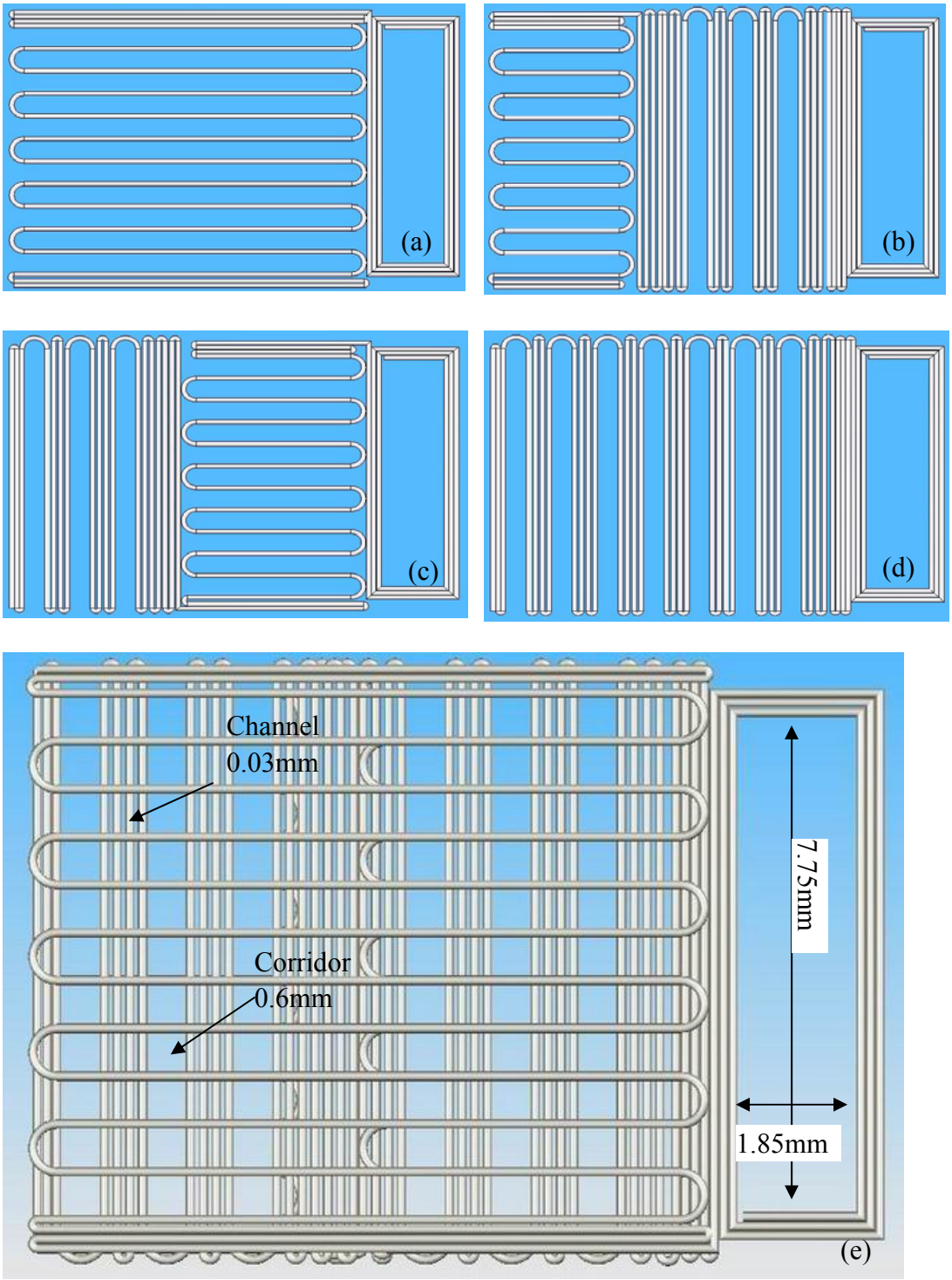

Figure 3.34. Schematic images for the second round design lattice: (a) the first layer, (b) the second layer, (c) the third layer, (d) the forth layer, (e) 3 Dimensional top view of the second round lattice with some dimensions.

The second round design implant block was constructed by units of four layers (shown in Figure 3.34 a, b, c, and d). From the 3D top view of the second round design lattice (shown in Figure 3.34 e), the lattice was divided into three parts by several adjacent filaments. A control zone which was filament-free zone was still kept to compare the function of the other zones under the same *in vivo* test conditions. The other two parts were constructed by different units. The first and third layers of the units adjacent to the control zone were constructed by horizontal filaments and the second and forth layers were constructed by vertical filaments. But in the other part, the first and second layers were constructed by horizontal filaments and the third and forth layers were constructed by vertical filaments. That is to say, the height of pores in the part adjacent to the control zone was the diameter of the filaments, i.e. 150 μm. The height of pores in the other part was two times as the diameter of the filaments, i.e. 300 μm. Many previous studies have revealed that the vertical height also influences the bone vertical regeneration in animals[146,147,151,152] and humans[153].

The size of the second round design lattice before sintering was 9.2x13.2 mm. After sintering at 1150°C, the size was 8.4x12 mm and the shrinkage was 10%; after sintering at 1250°C, the size was 7.5x10.7 mm and the shrinkage is 12%. The samples sintered at 1150°C and 1250°C respectively are shown in Figure 3.35 (a) and (b).

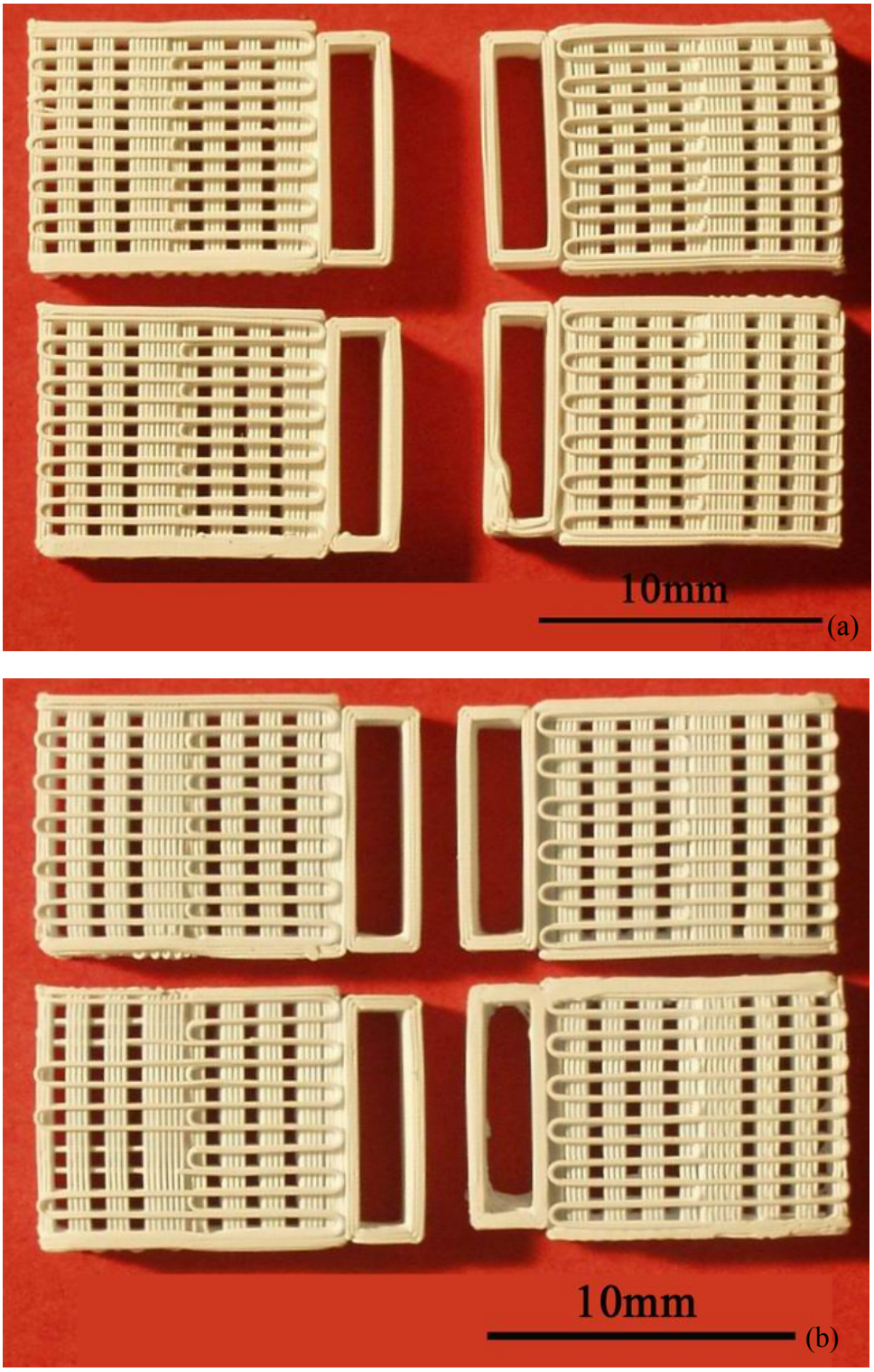

Figure 3.35. Pictures for the second round design implant block sintered at different temperatures.

Another two designs and fabrication of lattices for tissue engineering

As mentioned above, the pore size and shape are important to bone formation. Another two lattices with continuous and smooth gradients in pore size and different pore shape to the former structures were designed.

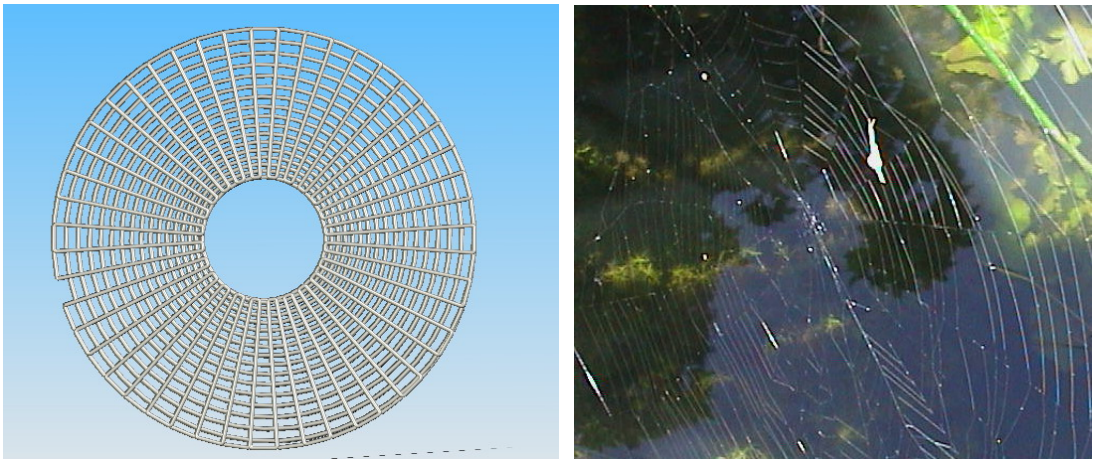

(a) (b)

Figure 3.36. "Whole web" design (a) and a real spider web (b).

The idea of this design is from a real spider web (shown in Figure 3.36. b). T. Krink has built a mathematical model describing the stages a spider uses to develop a web, which involves interesting morphogenic questions[154]. A 3D diagram of this design is shown in Figure 3.36 a. The pore shape was trapezoid with arc hemlines and the pore sizes varied following the radial lines. From Figure 3.36 a, the 'whole web' design lattice is composed of alternating spiral and spoke layers. The spiral pitch gradually increased from the inside to the outside. The pitches are an arithmetic series. There must be a hole in the middle, which forms a natural open control zone. One important

restriction in this design is that because the filament diameter is not infinitely small, to avoid a pile up of filament near the hole, the hole size and minimum/maximum pore size have to be carefully selected.

The parameters should satisfy the following equation

$$\frac{D_i}{D_o} = \frac{D_f + d_1}{D_f + d_2} \quad \text{(3.21)}$$

where D_i is the diameter of the inside hole, D_o is the diameter of the whole sample, D_f is the filament diameter, d_1 is the minimum pore size at the inside and d_2 is the maximum pore size at the outside.

The minimum hole size D_{mi} can be calculated as

$$D_{mi} \geq \frac{D_f}{D_f + d_2} D_o \quad \text{(3.22)}$$

the arithmetic series of the pitches can be found from (cf. Figure 3.38. c)

$$d_1 + n\delta x = d_2 \quad \text{(3.23)}$$

$$(D_f + d_1) + (D_f + d_1 + \delta x) + \cdots + (D_f + d_1 + n\delta x) = \frac{D_o - D_i}{2} \quad \text{(3.24)}$$

and the angle α between the adjacent spokes is

$$\alpha = 360 \times \frac{D_f + d_2}{\pi D_o} \quad \text{(3.25)}$$

A sample of the spider web design prepared with 150 μm diameter filament is shown in Figure 3.37. The trapezoid pores were presented through the overlay of a spiral on a system of spokes. The main purpose of the structure design was to investigate the

optimized pore size for tissue growth, the design is entirely pertinent for tissue engineering scaffold design with the specific requirement of larger peripheral voids and interconnections, to encourage fast initial tissue ingrowth and while retaining a higher implant core density to enhance the total strength.

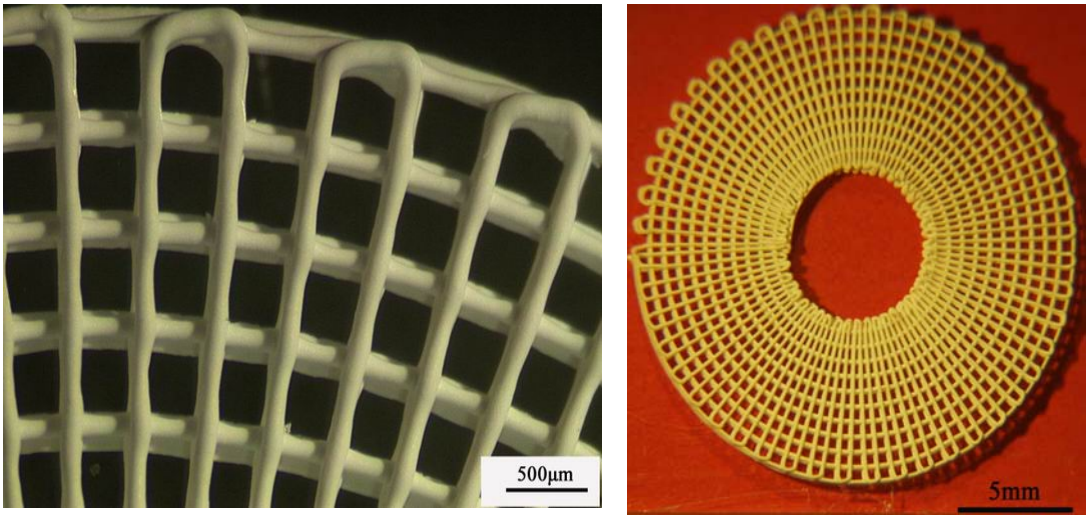

(a) (b)

Figure 3.37. A region of the spider web design prepared with 150 μm diameter filament.

To get more pore sizes in one implant block, another design was provided. A schematic diagram of this design is shown in Figure 3.38. Obviously, this design was a part of spider web design and in this sample, from left to right, the pore size increases from 50μm to 200μm (the filament diameter is 80μm so the centre-line spacing is 130μm to 280μm).

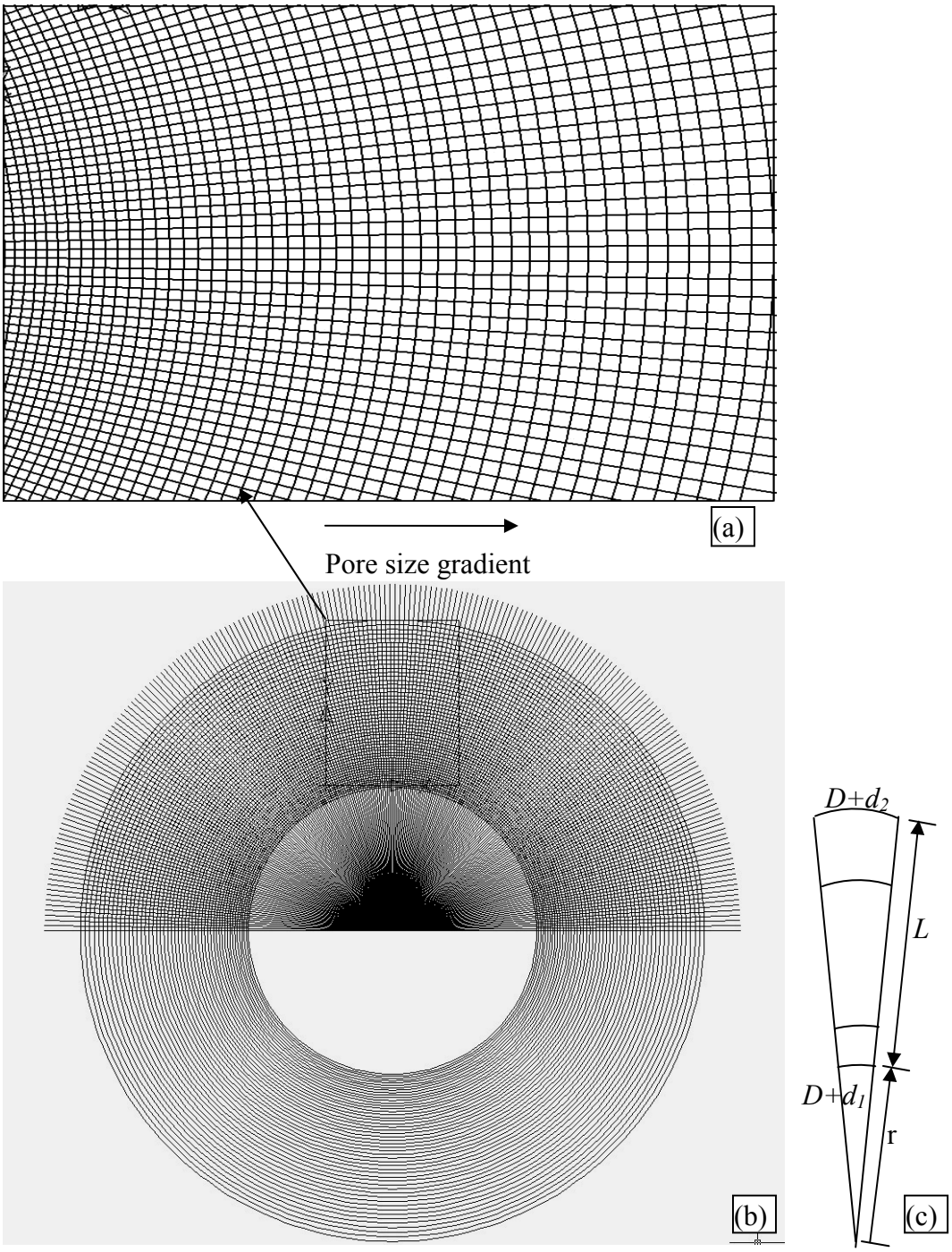

Figure 3.38. Schematic diagram of this design: (a) top view of continuous graded pore structure (c) the origin of the spider web design, (c) geometry of the arcs.

The effective pore size is an arithmetic series: 50, 50+δx, 50+2δx, … , 150, where δx is the difference between adjacent pore sizes and can be calculated by equations 3.23 and 3.24. If d_1=50μm, d_2=200μm, D_f =80μm, L=10mm (leaving 2mm as the control zone), then n=48 and δx =3.125μm. This means that almost 50 different pore sizes can be investigated in one sample and the resolution of the investigation can be as small as 3μm.

To maintain a pore size gradient by constructing radial vertical lines, the angle of the radial direction can be found from:

$$\tan\alpha = \frac{D_f + d_1}{r} = \frac{D_f + d_2}{r + L} \quad \text{……(3.26)}$$

where α is the angle between adjacent two radical lines and r is the radius of the arc for the minimum pore. Thus if d_1=50μm, d_2=200μm, D_f =80μm, L=10mm, then r=8.67mm, α =0.86°.

A sample of the graded lattice with radial spokes and arced crossovers is shown in Figure 3.39. The lattice has a graded pore structure from left to right. The diameter of the filaments is 150 μm, and the pore size is varied from 50 μm to 150 μm. Since the lattice was comprised of continuous filaments, the route of the filaments was designed carefully to finish the whole lattice. From Figure 3.39 a, the route of the filament is precisely controlled.

Obviously, to be effective as an implant block in an *in vivo* test, these two kinds of lattice need to be sectioned radially rather than in parallel planes so that all the sample slices would be distinct and unambiguous. Unfortunately such facility was not available and technically almost impossible on retrieved, mineralised resin embedded or decalcified wax sections.

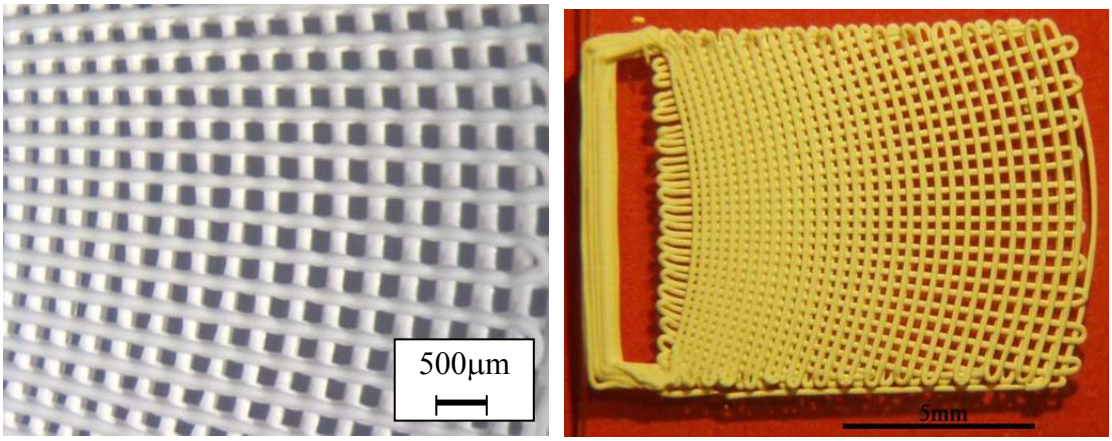

(a) (b)

Figure 3.39. A region of the graded pore structure with radial spokes and arced crossovers prepared with 150 µm diameter filament.

3.6 Design and Fabrication of Lattices for Electromagnetic Bandgap Materials

Design of a Rhomboid lattice

It is well known that periodic dielectric structures can block propagation of electromagnetic waves and one such class of structures is the 'woodpile[155, 156, 157] as discussed in the last section. Here, a new structure, the rhomboid lattice was designed

and fabricated as a potential EBG material. The trimetric view of the rhomboid lattice is shown in Figure 3.40.

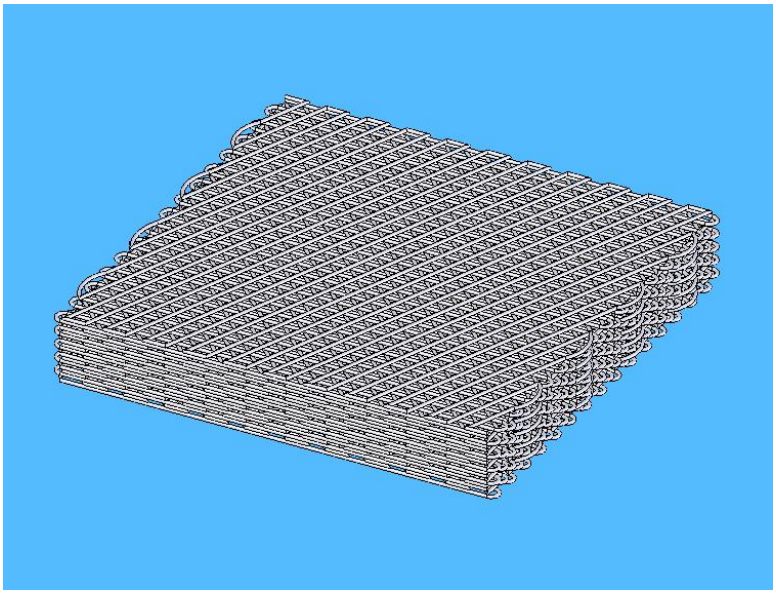

Figure 3.40. Trimetric view of a rhomboid lattice.

This lattice is made up of many units in which every unit includes four layers: the first layer is made up of a set of 0°filaments; the second layer is made up of a set of 120°filaments; the third one is made up of a set of 0°filaments; the forth one is made up of a set of 60°filaments. These four layers were assembled together to be one unit of the whole lattice. The sample (shown in Figure 3.41) was a rhomboid lattice made of 4 units, that is to say, this sample had 16 layers. The dimensions of the rhombus lattice are shown in Table 3.5.

Table 3.5. Dimensions of rhomboid lattice.

	Length /mm	Width /mm	Height /mm	Filament Diameter/mm	First layer gap/mm	Shrinkage /%
Before sintering	18.9	18.9	2.30	0.15	0.48	
After sintering	15.48	15.48	1.94	0.12	0.38	20.7

From the optical picture for the amplified region of the rhomboid lattice (shown in Figure 3.41. a, the route of the filaments was controlled very well and the rhomboid structures were present.

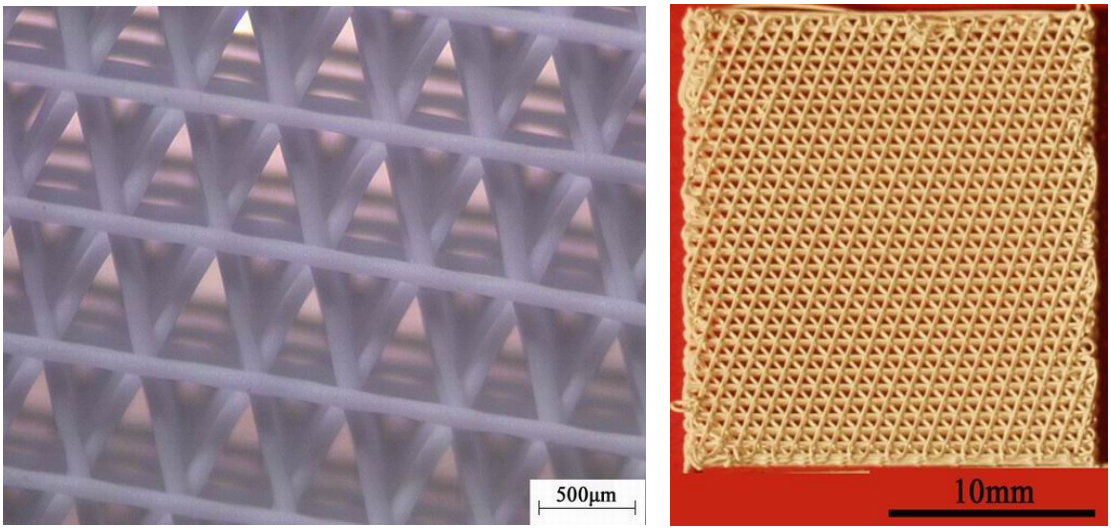

(a) (b)

Figure 3.41. Pictures of a rhomboid lattice sample.

Design of a lattice with lacuna

When defects are made periodically in an electromagnetic band gap (EBG) structure, defect mode resonance can be created[158, 159]. So a lattice with square lacuna was designed and fabricated as shown in Figure 3.42. The amplified square area was shown in Figure 3.43. It was obvious that the width of the square was limited by the distance between filaments. However the distance between filaments cannot be made too big, typically it must be below 1mm to avoid the filaments sinking. So to get a specified size lacuna in the lattice, another method was used to design a lattice with a circular lacuna (shown in Figures 3.44. and 3.45.).

From Figure 3.45, it can be seen that the size of the defect is not limited by the distance between filaments and in this method, any shape, such as a circle, square or rectangle etc. with a specific size can be fabricated. But a cross channel appears in the lattice that can influence the conduction of electromagnetic waves. Samples with square and circular defect periodic structures were fabricated by extrusion freeforming (shown in Figures 3.46. and 3.47.). The size of the sample and the shrinkage is given in Tables 3.6 and 3.7.

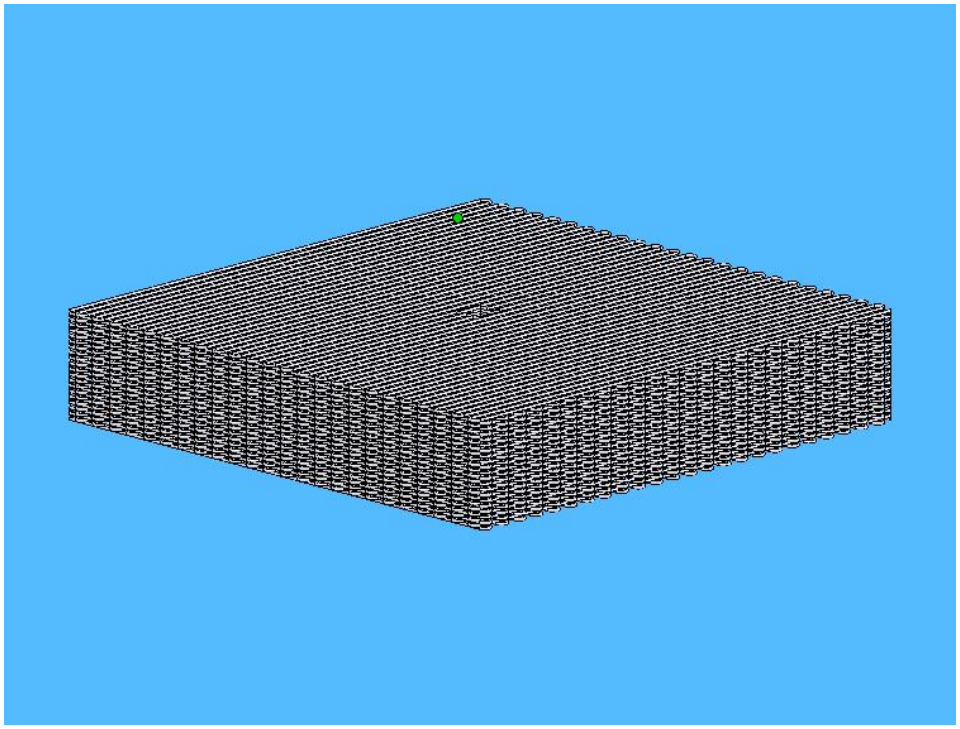

Figure 3.42. Trimetric view of the lattice with a square lacuna.

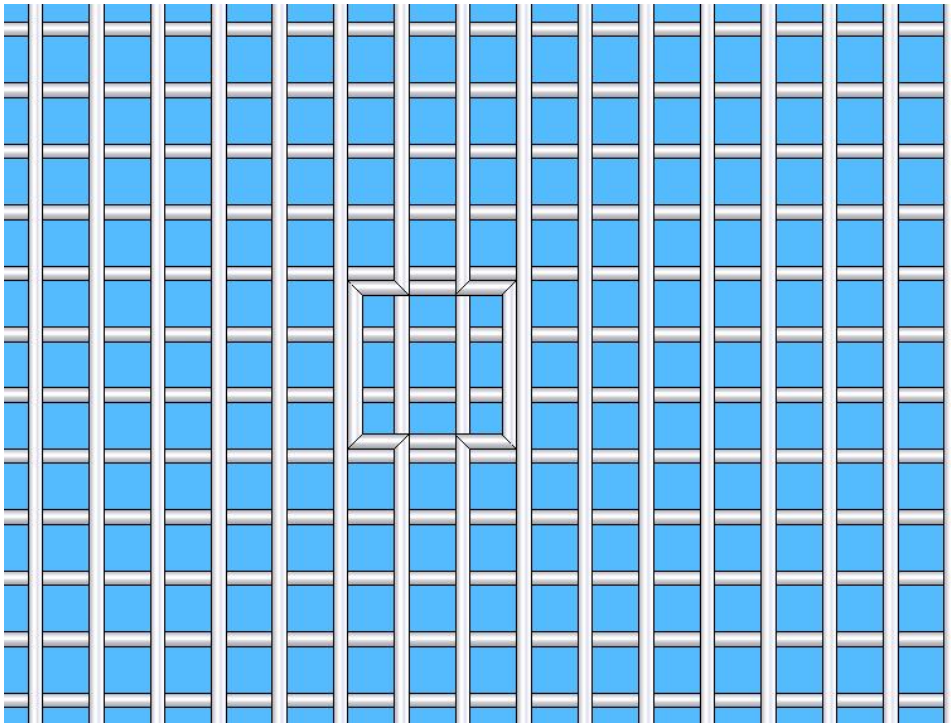

Figure 3.43. Amplified square lacuna region of the lattice.

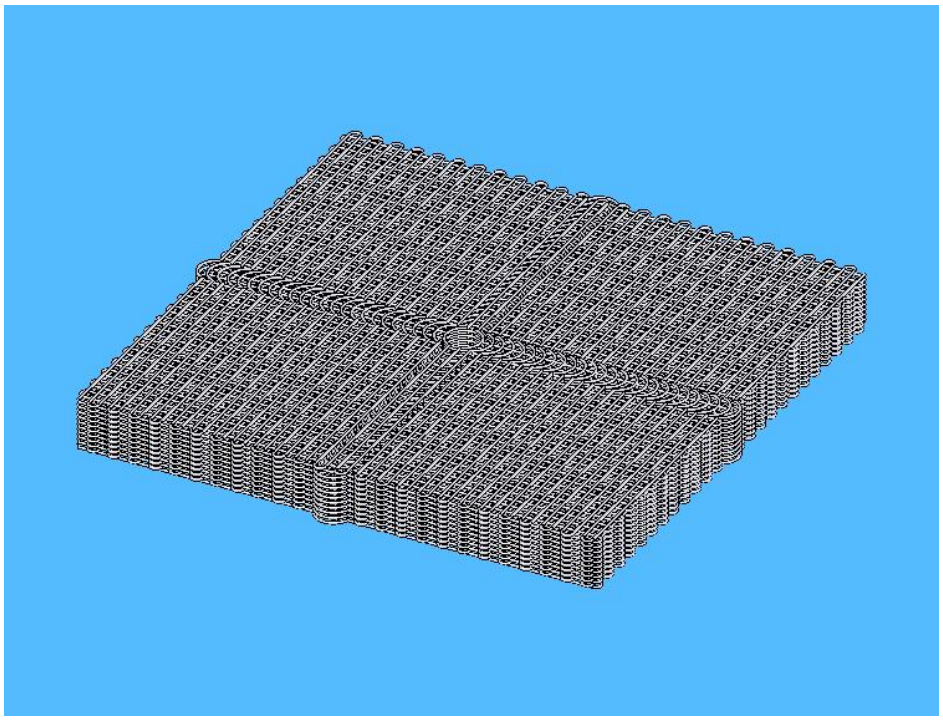

Figure 3.44. Trimetric view of the lattice with circular lacuna.

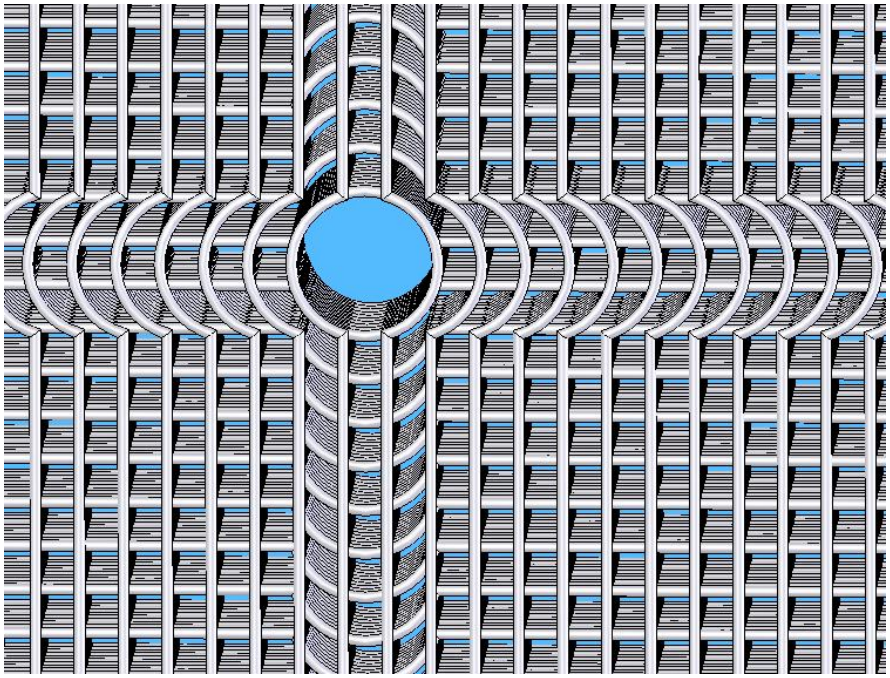

Figure 3.45. Amplified circular lacuna region of the lattice.

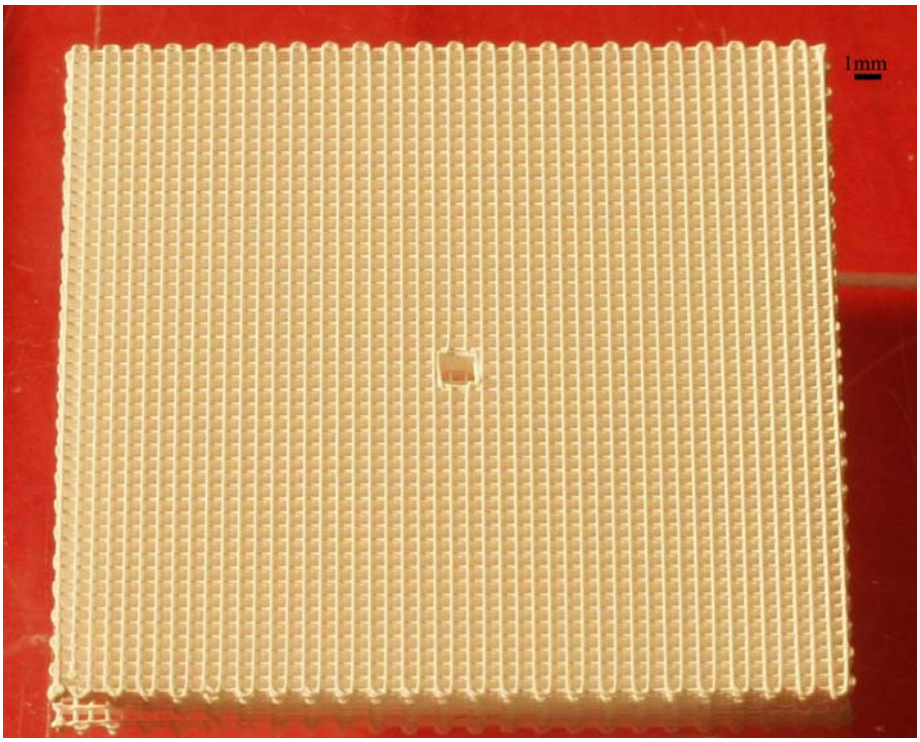

Figure 3.46. Picture of a lattice with square lacuna.

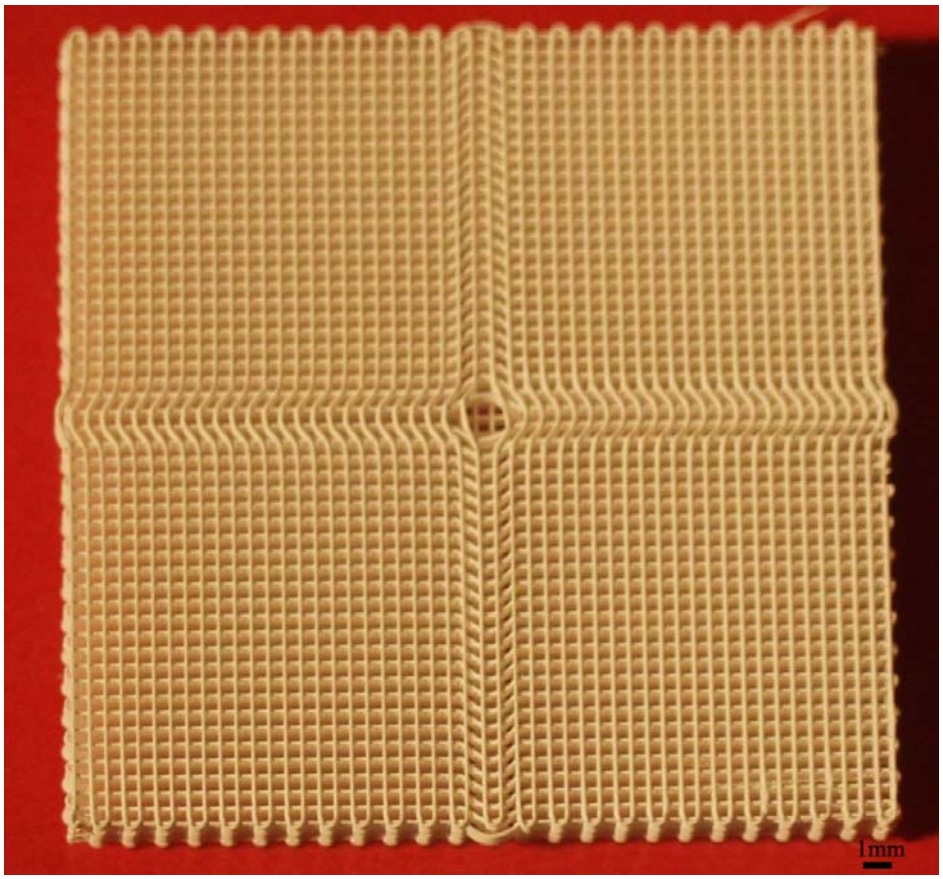

Figure 3.47. Picture of the lattice with circular lacuna.

Table 3.6. Dimensions of lattice with square lacuna.

	Length/ mm	Width/ mm	Height /mm	Filament diameter/mm	Gap/ mm	Lacuna size/mm	Shrinkage/ %
Before sintering	30.64	30.64	2.90	0.15	0.48	1.59x1.59	
After sintering	24.62	24.62	2.30	0.12	0.38	1.26x1.26	20.7

Table 3.7. Dimensions of lattice with circular lacuna.

	Length/ mm	Width/ mm	Height /mm	Filament diameter/mm	Gap/ mm	Lacuna size/mm	Shrinkage/ %
Before sintering	30.00	30.00	2.90	0.15	0.45	1.00x1.00	
After sintering	24.50	24.50	2.30	0.12	0.36	0.79x0.79	20.7

3.7 Design and Fabrication of a Lattice for Microfluidic Reactor

As applications for microfluidic reactors broaden, materials with higher temperature capability and chemical resistance are necessary to fabricate microfluidic reactors[160]. Ceramic microchannel devices have been fabricated by a prototyping process chain combining stereolithography, low-pressure injection molding[161] and lamination[160] etc. An alumina microfluidic reactor was fabricated by extrusion freeforming. The reactor was made up of five parts (shown in Figure 3.48. a). The upper and lower covers were separately made up each of two layers assembled from alumina filaments attached to each other tightly. The flow channels were made up of four layers assembled by alumina filaments with two large channels (2.55 mm) to facilitate gas flow and 20

smaller channels (0.45 mm) for the gas to disperse well. The mixing chamber was made up of four layers assembled by alumina filaments with 20 small channels (0.45 mm) for gas mixing. The outflow was made up of four layers assembled by alumina filaments with one large channel (0.9 mm) for the gas to exit. A schematic diagram of the two gas flows is shown in Figure 3.48. b. The overall size of the reactor was 15.48 x 10.68 x 1.92 mm after sintering and the small channel for the gas mixing was 0.36 mm after sintering. An alumina microfluidic reactor without the lower cover is shown in Figure 3.49.

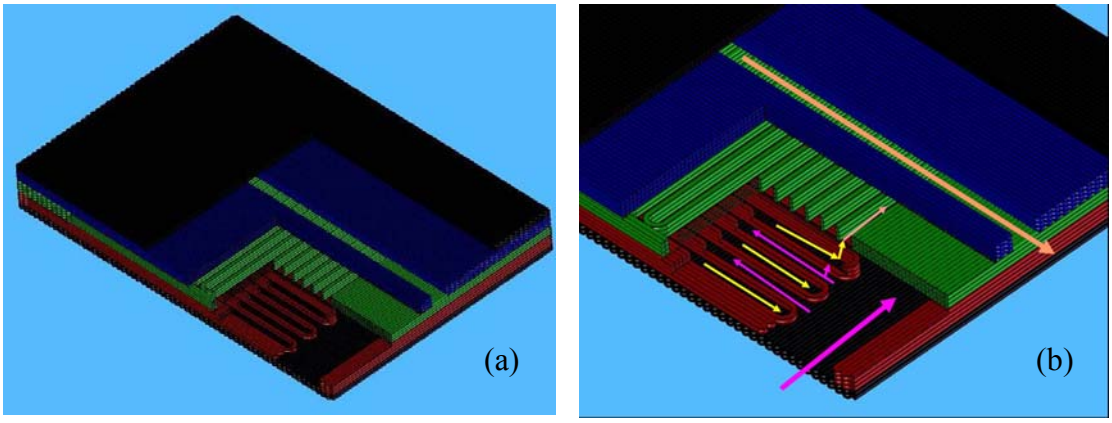

Figure 3.48. (a) Cutaway view of the alumina microfluidic reactor; (b) schematic diagram of the two types of gas flow through the reactor.

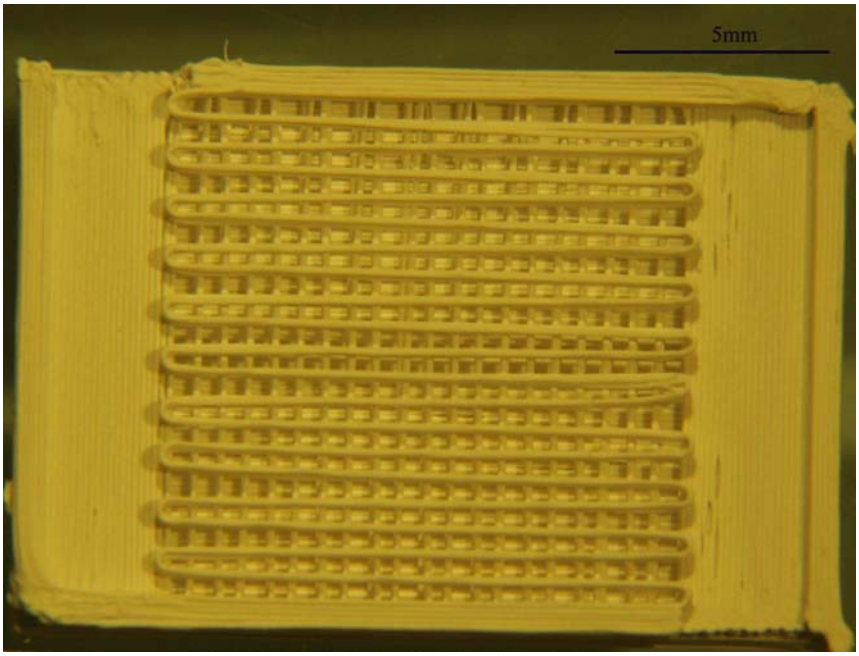

Figure 3.49. The alumina microfluidic reactor without the bottom cover.

3.8 Fabrication of Alumina Tube by Co-extrusion of Alumina Paste and Carbon Paste

In the co-extrusion processing, two different pastes were extruded from the nozzle discussed in section 2.3.2 (refer to Figure 2.7). In this experiment, the alumina paste was used as the outer material and the carbon paste was used as the inner paste. After drying, the inner carbon material was burned out and the alumina tube was obtained.

In the same period of co-extrusion processing, the volume of the inner carbon paste should be equal to the volume of the outer alumina paste. So the relation between the extrusion velocity of the inner paste and that of the outer paste can be described by the followed equation:

$$\frac{V_o}{v_i} = \frac{D_o^2 - d_o^2}{d_i^2} \quad \text{..... (3.27)}$$

where, V_o is the extrusion velocity of the outer paste; v_i is the extrusion velocity of the inner paste; D_0 is the inner diameter of the outer nozzle, here is 500 μm; d_o is the outer diameter of the inner nozzle, here is 300 μm and d_i is the inner diameter of the inner nozzle, here is 200 μm. So the ratio of the extrusion velocity of the outer paste V_o and the extrusion velocity of the inner paste v_i is 4:1. It can be achieve through adjusting the frequency divider mentioned in section 2.3.2.

Although higher extrusion velocity saves the time of sample fabrication, it also induces exorbitant extrusion pressure. Furthermore, the extrusion velocity has to match the equation 3.1. In this experiment, the velocity of the XY table was 6.7 mm/s, the extrusion velocity of the inner paste was 0.00875 mm/s and that of the outer paste was 0.035 mm/s.

An unsintered lattice knitted by the filaments comprised of carbon paste and alumina paste is shown in Figure 3.50. The inner paste, i.e. black carbon paste, was not surrounded completely by the outer alumina paste. The outer paste was extruded into the outer nozzle by two stainless steel tubes through a brass part with 'Y' channel. But the resistances to the alumina paste in the two tubes are different. The alumina paste preferred to be extruded out following the tube with less resistance. Moreover, another disadvantage of this co-extrusion nozzle was that the two tubes used to transport alumina paste were very difficult to clean. The remains of alumina paste in

the two tubes induced different resistances in the two tubes so that the tube with more resistance was blocked completely.

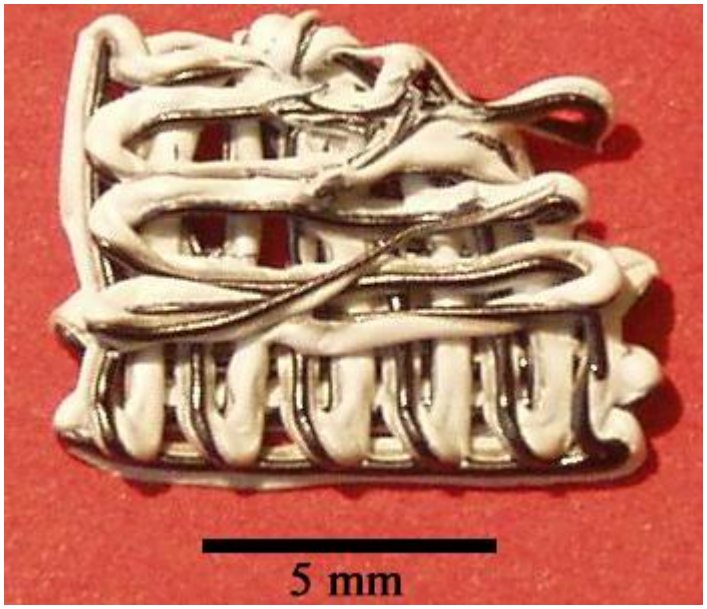

Figure 3.50. An unsintered lattice knitted by the filaments comprised of carbon paste and alumina paste.

A new co-extrusion nozzle was designed and its design drawing is shown in Figures 3.51 and 3.52. Compared to the previously designed co-extrusion nozzle, the outer nozzle block had a bigger inner base so that two arc channels could be machined on it to transport alumina paste into the outer nozzle. A 3D model drawing by Solidworks of the outer nozzle block and pictures of the inner and outer nozzle block are shown in Figure 3.53.

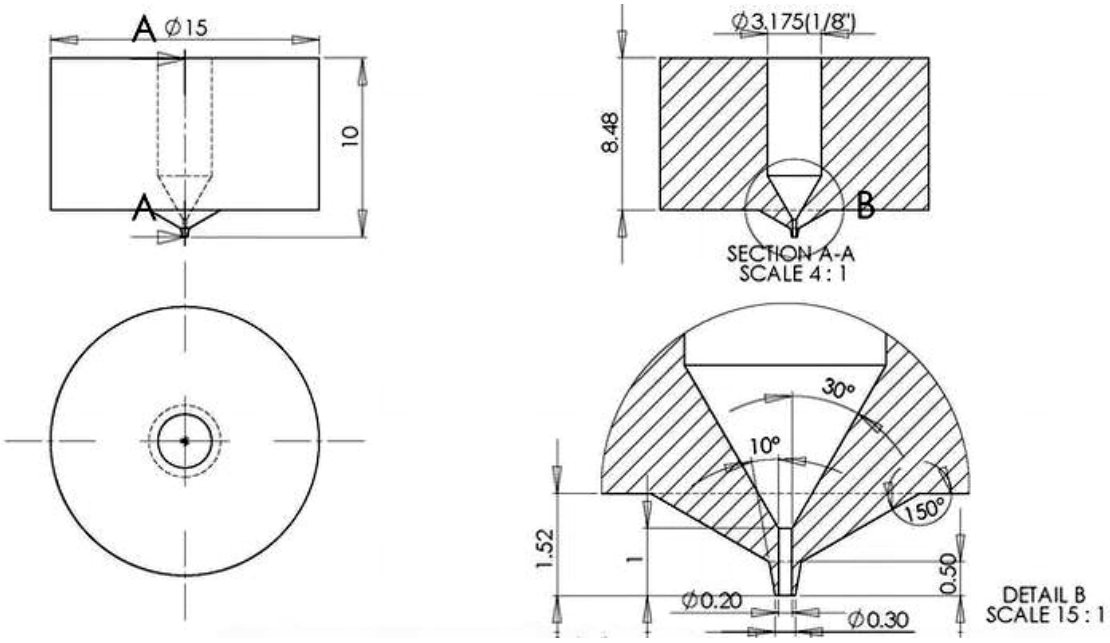

Figure 3.51. The drawing of the last design inner nozzle (cf. Figure 2.8).

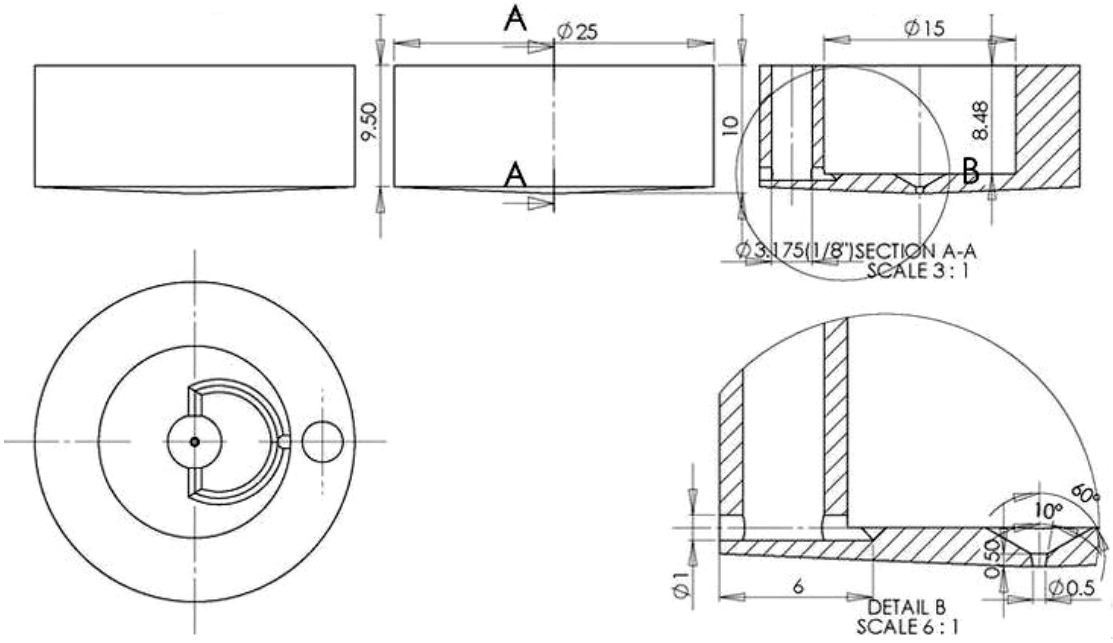

Figure 3.52. The drawing of the last design outer nozzle (cf. Figure 2.8).

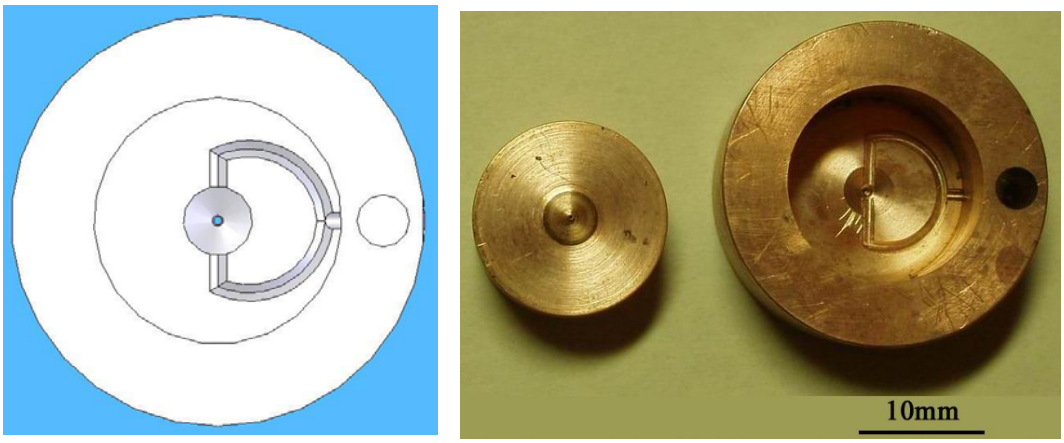

Figure 3.53. Top view of a 3D model for the outer nozzle block and pictures for the inner and outer nozzle block.

From Figure 3.53, the alumina paste was extruded into the outer nozzle through two arc channels replacing two stainless steel tubes in the previously designed co-extrusion nozzle, and this avoided the different resistance to alumina paste in two channels. To resolve the 'clean' problem of the tubes to transport paste, the whole curved tubes in the ante designed co-extrusion nozzle was replaced by some stainless steel tube segments and these tube segments were connected by the bulkhead unions with ferrules (SGE Europe Ltd. Kiln Farm Milton Keynes, UK) to eliminate leaks. A co-extrusion nozzle assembly is shown in Figure 3.54. a. The tube segments connected by the bulkhead unions can be disassembled easily (shown in Figure 3.54. b) and were easy to clean.

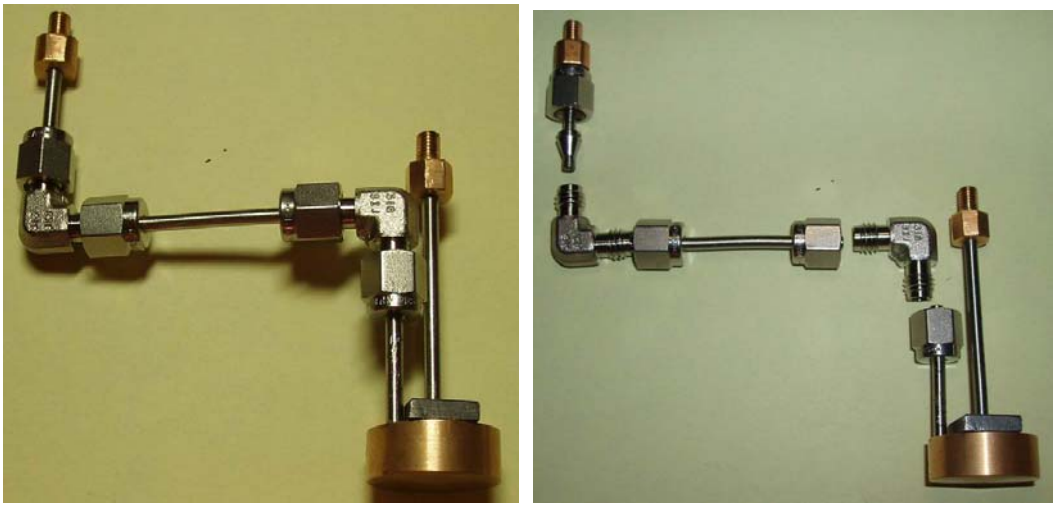

(a) (b)

Figure 3.54. Pictures for an assembled co-extrusion nozzle block and a disassembled co-extrusion nozzle block (dimensions re. Figure 3.53).

A three layer lattice knitted by the filaments made of alumina paste outside and carbon paste inside is shown in Figure 3.55. Some filaments were dirtied by the carbon paste on the nozzle (shown in label A) and can be cleaned when the lattice was sintered.

The cross section of an unsintered filament with carbon still in the middle was shown in Figure 3.56. After drying, the inner carbon still kept its shape. But the outer alumina shape was changed. The reason can be that the solvent in the inner carbon paste has to be transported to the outer alumina paste firstly before evaporating so that the alumina shape was changed. From Figure 3.56, some pores can be observed in the interface between carbon and alumina. It can be induced by the air in the co-extrusion nozzle assemble.

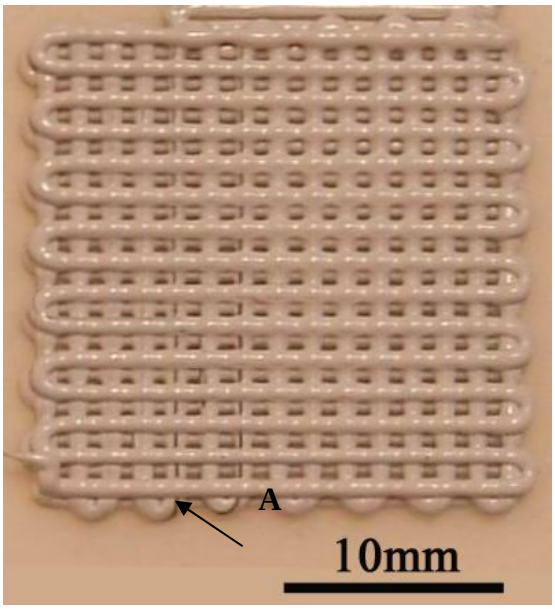

Figure 3.55. A three layer lattice knitted by the filaments made of alumina paste outside and carbon paste inside was fabricated by the co-extrusion nozzle assemble.

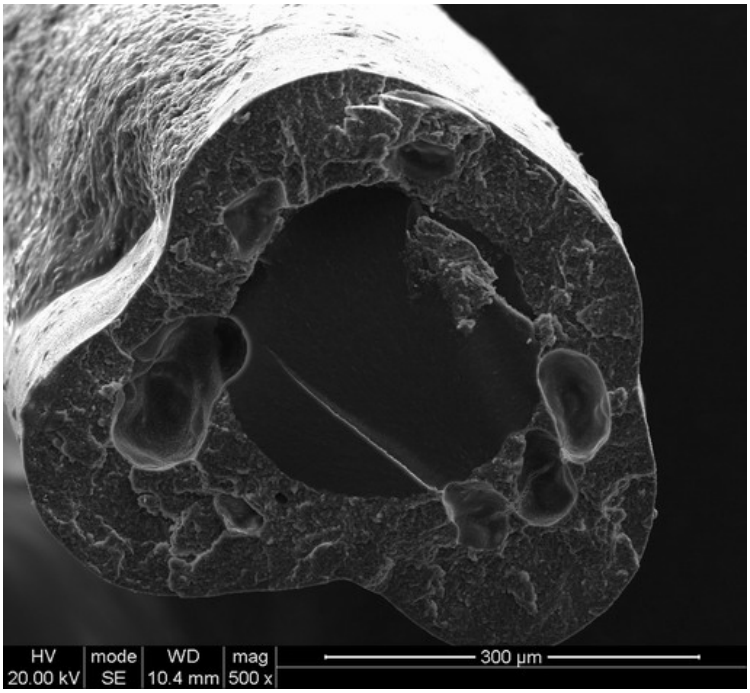

Figure 3.56. Image for the cross section of an unsintered filament with carbon still in the middle and cracks can be seen inside the pore.

SEM images for the sintered samples were shown in Figure 3.57. From Figure 3.57.a, some pores can be also observed inner wall of the alumina tube. From Figure 3.57.b, the alumina tube has a round inner shape and an anomalous outer shape. The microstructure image (shown in Figure 3.58) for the cross section of the alumina tube sintered by 10°C/min to 600°C then 20°C/min to 1300°C dwell for 3 hour shows that the sample was still not fully sintered at 1300°C.

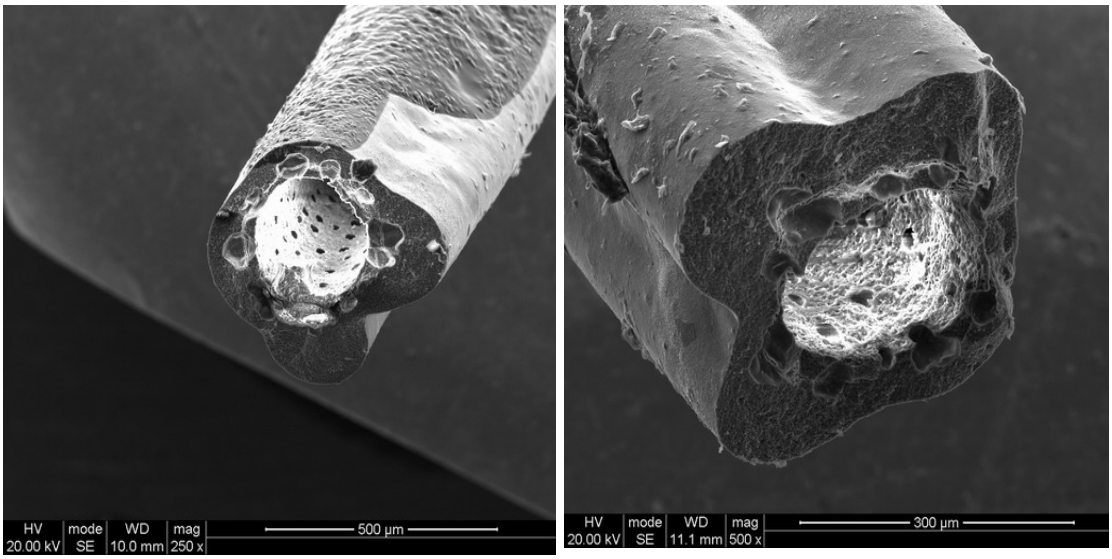

(a) (b)

Figure 3.57. SEM images for the sintered samples: (a) sample sintered by 10°C/min to 600°C then 20°C/min to 1250°C dwell for 1 hour, (b) sample sintered by 10°C/min to 600°C then 20°C/min to 1300°C dwell for 3 hour.

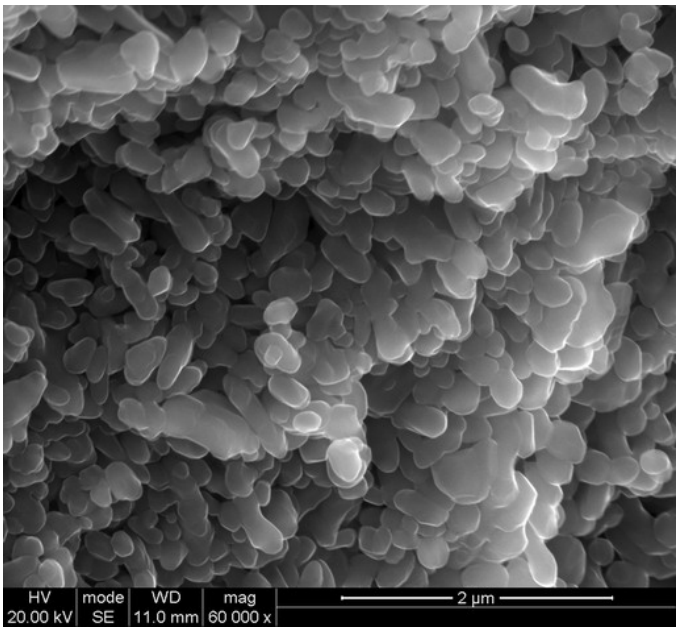

Figure 3.58. Cross section of the alumina tube sintered by 10°C/min to 600°C then 20°C/min to 1300°C dwell for 3 hour.

4 Conclusions

4.1 Equipment Establishment

An extrusion freeforming worktable was established in these experiments. A user friendly graphical user interface (GUI) was developed by LabVIEW 8.2 with Motion planner as 'engine'. In this operating system, all standard Motion Planner features are available and the existing programs written by Motion Planner can be used in this operating system through entering the names of the programs. So the extrusion freeforming worktable was very easy to manipulate even for a beginner.

4.2 Paste Preparation

An approach to preparing pastes for extrusion freeforming was developed. Three different pastes were prepared in this experiment: alumina paste, carbon paste and a paste consisting of a mixture of HA powders and β-TCP powders. It has been demonstrated that near-perfect ceramic lattices can be fabricated by extrusion freeforming through increasing the solid loading of paste. Typically the volume percent of the non-volatile content is 74%. Successful extrusion freeforming depended on the controlled interaction among the solid loading of the paste, the paste viscosity, the extrusion rate, the X, Y table velocity, the filament diameter, and the volatilization of the solvent.

4.3 Substrate Selection

The substrate materials were found to influence the adhesion of the first layer to the substrate, which in turn, influenced the lattice quality. Several substrate materials, such as silicone paper, plastic film, clay slide and glass slide etc., were tested as substrates and the glass slide provided the adhesion needed to resist shrinkage stress efficiently and also made the extruded lattice easily detachable. It provided a flat surface that did not deform.

4.4 Extrusion Pressure in the Alumina Paste Extrusion

The extrusion pressure in the alumina paste extrusion was studied and was found to be useful in predicting and optimizing the extrusion behaviour. In extrusion processing, the friction between the plunger and the syringe wall and the solvent volume fraction of the paste play crucial roles because the same vehicle and die geometry were used. It was demonstrated that in paste preparation, the air bubbles and particle conglomerations occurred in the paste and induced the static pressure to increase gradually. The regular pressure fluctuation was induced by the pitch of the ball screw. The ageing process resulted in more even solvent distribution within the paste and the existence of the substrate also influenced the extrusion pressure.

4.5 Fabrication of Alumina Lattices for Metal Matrix Composites

Four kinds of alumina lattice with different porosity, 50%, 60%, 70% and 80%, were knitted by 150 μm filaments extruded by the extrusion freeforming method and were used as preforms during fabrication of metal matrix composites. The alumina lattices were sintered at 1540°C for 1 hr after slow heating to 600°C at rate of 2°C/min with a 1 hour dwell. Upon drying under ambient conditions, the consolidated densities of alumina lattices were approximately 55%. Upon sintering, the alumina lattices have sintered densities greater than 95% with isolated residual porosity and average grain size in the region 2-3 μm.and the sintering shrinkage was 20%.

The metal matrix composites were fabricated by squeeze casting. After a thermal shock during the metal infiltration process, the alumina lattice was filled with aluminum and even the micro-voids existing in the ceramic filaments were filled with aluminum. The alumina filaments by which the lattice was knitted were well maintained in the composites and the round corner filaments were also maintained very well. A good interfacial bonding resulted from the squeeze casting technology,

4.6 Fabrication of HA/TCP Scaffolds for Tissue Engineering

The HA/TCP scaffolds with customized external shape and hierarchical levels of internal structure for tissue engineering can be fabricated on the micro-extrusion

freeforming worktable. The pore size, pore connectivity and pore size distribution in the scaffold can be controlled in this fabrication process.

Equipment for the three point loading measurement was developed according to ASTM C1161-94. The three point bending strength of the filaments sintered at 1150°C was 33.2±2.6 MPa, and that of the filaments sintered at 1250°C was 102.7±11.7 MPa and the Weibull modulus of the filaments sintered at 1150°C was 13.3 and that of the filaments sintered at 1250°C was 8.89. Although the samples sintered at 1250°C have a higher strength than the samples sintered at 1150°C, its Weibull modulus is lower than the samples sintered at 1150°C. The low Weibull modulus indicates that flaws in the samples tend to congregate at the sintering temperature 1250°C and decrease the reliability of the samples.

From *in vivo* testing, the materials used in this experiment are safe for implanting and have good biocompatibility. There are good interfaces between the new bone and the materials of the first layer. The materials have no obvious absorption after 3 months and keep the structure well. But less amount of new bone formation were observed than that of the previous experimental studies at the same time point. Although the implant sintered to 1150°C is more porous and has higher rate of dissolution than the implant sintered to 1250°C, the effects of micro or nano pores on bone growth is not obvious. More bone growth was observed in the 1250°C sintered implant than in the 1150°C sintered implant.

Other scaffolds with different pore size and pore distribution have been fabricated by the micro-extrusion freeforming method. This procedure is also ideally suited to prototyping of electromagnetic bandgap structures and microreactors. Three types of electromagnetic bandgap lattice with different structures and one microfluidic reactor with higher temperature capability and chemical resistance were fabricated through this method.

4.7 Tubular Alumina Lattice Fabrication

A new co-extrusion nozzle assemble was developed for extruding two different materials at same time. A tubular alumina lattice can be obtained by burning out the inner carbon paste. This approach can be used to fabricate lattices knitted by the filaments comprised of different inner and outer materials.

5 Suggestions for Future Work

In the future, the mechanical properties of the alumina filaments need to be measured. The high pressure developed during processing with the glass syringe needs to be resolved and the dependence of the extrusion pressure on the viscosity of the paste and the friction between the plunge and the wall of syringe should be established. At present viscosity measurements are very difficult because the volatility of a small amount of solvent during testing causes a big change in viscosity. So the extrusion pressure on the paste with different viscosities and with different syringes should be recorded and analyzed.

The weld strength between the filaments is very important for the elimination of delamination in the build-up of a ceramic lattice. The solvent (propan-2-ol) used in this paste evaporates readily, so different paste with different non-volatile content could influence the weld strength dramatically. The weld strength between unsintered filaments extruded from the paste with different non volatile content needs to be measured. The weld strength will increase when the filaments are sintered. So the weld strength between sintered filaments is measured and is compared with that between unsintered filaments.

The filament can support itself over a range of span. With the increase of span, the bending of the filaments occurs. In order to find the largest span that filaments

extruded from a paste with constant non-volatile content through a 150 μm nozzle can support itself successful without bending, a lattice with different spans from 300-1000 μm should be designed (Figure 5.1.) and fabricated.

The alumina metal matrix properties need to be measured. The micirofluidic reactor needs to be assessed for leakage when used at high temperature.

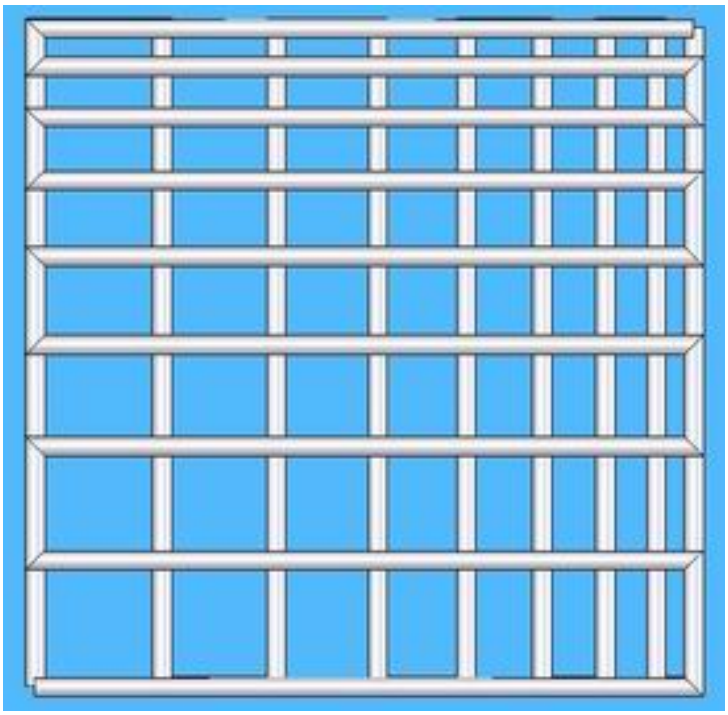

Figure 5.1. Schematic diagram of the lattice with different spans.

In the future, the HA and TCP paste could be extruded through a purpose-built co-extrusion die. In this procedure, the scaffold knitted by the filaments would consist of HA inside and TCP outside, thus opening the way for a range of composite structures.

6 References

1. F. H. Norton, Elements of Ceramics, Addison-Wesley, Reading, MA, 2nd edn.; 1974, pp. 1–5.
2. F. H. Norton, Fine Ceramics: Technology and Applications; McGraw-Hill, New York, 1970, pp. 8–19.
3. J. Bourriau, Pottery from the Nile Valley before the Arab Conquest, Cambridge University Press, 1981, pp.15-18.
4. J. S. Reed, Introduction to the Principles of Ceramic Processing; Wiley, New York, 1988, pp. 3–15.
5. S. J. Glass, K.G. Ewsuk, Ceramic Powder Compaction, MRS Bull., Vol. 22(12), 1997, pp.24-28.
6. W. E. Lee, W. M. Rainforth, Ceramic Microstructures Property Control by Processing, London, Chapman & Hall, 1994, pp. 31-32.
7. T. A. Ring, Fundamentals of Ceramic Powder Processing and Synthesis, San. Diego., Academic Press Inc., 1996, pp. 653-654.
8. A. J. Fanelli, R. D. Silvers, W. S., Frei, J. V. Burlew, G. B. Marsh, New Aqueous Injection Molding Process for Ceramic Powders, J. Am. Ceram. Soc., Vol. 72 [10], 1989, pp. 1833–1836.
9. J. A. Lewis, Colloidal Processing of Ceramics, J. Am. Ceram. Soc., Vol. 83, 2000, pp. 2341-59.

10. D. J. Shanefield, Organic Additives and Ceramic Processing second edition: with Applications in Powder Metallurgy, Ink, and Paint, Kluwer Academic Publishers, London, pp.95-100.

11. R. R. Rowlands, A Review of the Slip Casting Process, Am. Ceram. Soc. Bull., Vol. 45 [1], 1966, pp. 16–19.

12. J. Cawley, Computer-Aided Manufacturing of Laminated Engineering Materials (CAM–LEM) and Its Applications to the Fabrication of Ceramic Components without Tooling, in Proceedings of the 1997 International Gas Turbine and Aeroengine Congress and Exposition, American Society of Mechanical Engineers, New York, 1997, pp. 1–5.

13. M. N. Rahaman, Ceramic Processing and Sintering, Marcel Dekker Inc., New York, 2nd edn., 1995, pp.5-11.

14. D. W. Hess, K.F. Jensen, and T.J. Anderson, Chemical Vapor Deposition: a Chemical Engineering Perspective, Rev. Chem. Eng., Vol. 3 [2], 1985, p.130.

15. M. S. Newkirk, H. D. Lesher, D.R. White, C.R. Kennedy, A.W. Urquhart and T. D. Claar, Preparation of Lanxide Ceramic Matrix Composites: Matrix Formation by the Directed Oxidation of Molten Metals, Ceramic. Eng. Sci. Proc., Vol. 8(7-8), 1987, pp. 879-885.

16. C. J. Brinker and G.W. Scherer, Sol-Gel Science, Academic Press, New York, 1990, pp. 15-36.

17. D. Segal, Chemical Synthesis of Advanced Materials, Cambridge University Press, United Kingdom, 1989, pp. 54-76.

18. S. Yajima, K. Okamura, J. Hayashi, M. Omori, Synthesis of Continuous SiC Fibers With High Tensile Strength, J. Am. Ceram. Soc., Vol. 59, 1976, p. 324.

19. T. J. Fennelly, J. S. Reed, Mechanics of Pressure Casting, J. Am. Ceram. Soc., Vol. 55 [5], 1972, pp. 264–68.

20. D. S. Adcock, I. C. McDowall, the Mechanism of Filter Pressing and Slip Casting, J. Am. Ceram. Soc., Vol. 40 [10], 1957, pp. 355–60.

21. K. T. Miller, R. M. Melant, and C. F. Zukoski, Comparison of the Compressive Yield Response of Aggregated Suspensions: Pressure Filtration, Centrifugation, and Osmotic Consolidation, J. Am. Ceram. Soc., Vol. 79[10], 1996, pp. 2545–56.

22. K. T. Miller, C. F. Zukoski, Osmotic Consolidation of Suspensions and Gels, J. Am. Ceram. Soc., Vol. 77[9], 1994, pp. 2473–78.

23. R. E. Mistler, Tape Casting: The Basic Process for Meeting the Needs of the Electronic Industry, Am. Ceram. Soc. Bull., Vol. 69 [6], 1990, pp.1022–26.

24. J. Cesarano, R. Segalman, and P. Calvert, Robocasting Provides Moldless Fabrication from Slurry Deposition, Ceram. Ind., Vol. 148, 1998, pp. 94–102.

25. A. P. Philipse, B. C. Bonekamp, and H. J. Veringa, Colloidal Filtration and (Simultaneous) Sedimentation of Alumina and Silica Suspensions: Influence of Aggregates, J. Am. Ceram. Soc., Vol. 73 [9], 1990, pp. 2720–27.

26. J. C. Chang, F. F. Lange, and D. S. Pearson, Centrifugal Consolidation of Al_2O_3 and Al_2O_3/ZrO_2 Composite Slurries vs Interparticle Potentials: Particle Packing and Mass Segregation, J. Am. Ceram. Soc., Vol. 74 [9], 1991, pp. 2201–204.

27. P. Sarkar, X. Huang, and P. S. Nicholson, Zirconia/Alumina Functionally Graded Composites by Electrophoretic Deposition, J. Am. Ceram. Soc., Vol.76, 1993, pp.1055–1056.

28. P. Sarkar and P. S. Nicholson, Electrophoretic Deposition (EPD): Mechanisms, Kinetics, and Application to Ceramics, J. Am. Ceram. Soc., Vol. 79 [8], 1996, pp. 1987–2002.

29. T. A. Ring, Fundamentals of Ceramic Powder Processing and Synthesis, San. Diego., Academic Press Inc., 1996, p. 629.

30. H. H. Winter, Polymeric Gels, Materials that Combine Liquid and Solid Properties, MRS. Bull., Vol. 16, 1991, pp. 44–48.

31. R. D. Rivers, Method of Injection Molding Powder Metal Parts,U.S. Pat. No. 41 134 180, 1978.

32. O. Omatete, M. A. Janney and R. A. Strehlow, Gelcasting—a New Ceramic Forming Process, Am. Ceram. Soc. Bull., Vol. 70, 1991, pp. 1641–49.

33. A. C. Young, O. O. Omatete, M. A. Janney, and P. A. Menchhofer, Gelcasting of Alumina, J. Am. Ceram. Soc., Vol. 74 [3], 1991, pp. 612–18.

34. T. J. Graule, W. Si, F. H. Baader, and L. J. Gauckler, Direct Coagulation Casting (DCC): Fundamentals of a New Forming Process for Ceramics, Ceramics Transactions, Vol. 51, 1995, pp. 457–61.

35. L. J. Gaukler, T. Graule, and F. Baader, Ceramic Forming Using Enzyme Catalyzed Reactions, Mater. Chem. Phys., Vol. 61, 1999, pp. 78–102.

36. K. Cai, D. Guo, Y. Huang, J. Yang, Solid freeform fabrication of alumina ceramic parts through a lost mould method, J. Eur. Ceram. Soc., Vol. 23, 2003, pp. 921–925.

37. O. Omatete, R. A. Strehlow, and C. A. Walls, Gelcasting of Submicron Alumina, SiAlON, and Silicon Nitride Powders, Proceedings of the 37th Sagamore Army Materials Research Conference (Plymouth, MA), 1990, pp.201-12.

38. W. Si, T. J. Graule, F. H. Baader, and L. J. Gauckler, Direct Coagulation Casting of Silicon Carbide Components, J. Am. Ceram. Soc., Vol. 82 [5], 1999, pp. 1129–36.

39. M. K. Agarwala, A. Bandyopadhyay, R. V. Weeren, A. Safari, S. C. Danforth, N. A. Langrana, V. R. Jamalabad, P. J. Whalen, FDC, Rapid Fabrication of Structural Components, American Ceramic Society Bulletin, Vol.75, 1996, pp.60-65.

40. E. A. Griffin, D. R. Mumm, and D. B. Marshall, Rapid Prototyping of Functional Ceramic Composites, American Ceramic Society Bulletin, Vol.75, 1996, pp.65-68.

41. M. L. Griffith and J. W. Halloran, Freeform Fabrication of Ceramics via Stereolithography, J. Am. Ceram. Soc., Vol.79, 1996, pp. 2601-8.

42. J. Cesarano III and A. Thomas, Recent Developments in Freeform Fabrication of Dense Ceramics from Slurry Deposition, Proceedings Solid Freeform Fabrication Symposium, University of Texas at Austin, 1997, pp. 25-32.

43. B. Y. Tay, J. R. G. Evans, and M. J. Edirisinghe, Solid Freeform Fabrication of Ceramics, Int. Mater. Rev., Vol. 48, 2003, pp. 341-370.

44. J. D. Cawley, Solid Freeform Fabrication of Ceramics, Curr. Opinion in Sol. State and Mater. Sci., Vol. 4, 1999, pp. 483–489.

45. P. Calvert, Biomimetic Processing, Materials Science and Technology, VCH Pubs, Weinheim, Vol. 17B, 1996, pp.51-82.

46. D. T. Pham, R.S. Gault, A Comparison of Rapid Prototyping Technologies, Int. J. Mach. Tool Manuf., Vol. 38,1998, , pp. 1257–1287.

47. J. P. Kruth, Material Incress Manufacturing by Rapid Prototyping Techniques, Annals of the CIRP, Vol. 40, 1991, pp. 603-614.

48. J. Heinzl, C. H. Hertz, Ink-jet printing, Adv. Electron. Phys., Vol. 65, 1985, pp. 91-171.

49. R. H. Leach, R. J. Pierce, E. P. Hickman, M. J. Mackenzie and H. G. Smith, the Printing Ink Manual, Dordrecht, Kluwer Academic, 5th edn., 1999, pp. 14-85.

50. M. L. Griffith, J. W. Halloran, Freeform Fabrication of Ceramics via Stereolithography, J. Am. Ceram. Soc., Vol.79, 1996, pp. 2601-2608.

51. F. Doreau, C. Chaput and T. Chartier, Stereolithography for Manufacturing Ceramic Parts, Adv. Eng. Mater., Vol. 2, 2000, pp. 493-496.

52. C. Sun and X. Zhang, Experimental and Numerical Investigation on Microstereolighgraphy of Ceramics, J. Appl. Phys., Vol. 92, 2002, pp. 4796-4802.

53. D. T. Pham, S. S. Dimov and R. S. Gault, Part Orientation in Stereolithography, Int. J. Adv. Manuf. Technol., Vol. 15, 1999, pp. 674-682.

54. S. Maruo and K. Ikuta., Submicron Stereolithography for the Production of Freely Movable Mechanisms by Using Single-photon Polymerization, Sensors and Actuators A: Physical, Vol. 100, 2002, pp. 70-76.

55. S. Kolossov, E. Boillat, R. Glardon, P. Fischer and M. Locher, 3D FE Simulation for Temperature Evolution in the Selective Laser Sintering Process, International Journal of Machine Tools & Manufacture, Vol. 44, 2004, pp. 117-123.

56. L. Hao, M. M. Savalani, Y. Zhang, K. E. Tanner and R. A. Harris, Selective Laser Sintering of Hydroxyapatite Reinforced Polyethylene Composites for Bioactive Implants and Tissue Scaffold Development, Proceedings of the Institution of Mechanical Engineers, Part H: J. Engineering in Medicine, Vol.220, 2006, pp.521-531.

57. J. J. Beaman, J. W. Barlow, D. L. Bourell, R. H. Crawford, H. L. Marcuse and K.P. Mcalea, Solid Freeform Fabrication: a New Direction in Manufacturing, Dordrecht, Kluwer Academic, 1997, pp. 1-49 and 121-165.

58. R. Glardon, N. Karapatis and V. Romano, Influence of Nd: YAG Parameters on the Selective Laser Sintering of Metallic Powders, CRIP Ann., Manuf. Technol., Vol. 50, 2001, pp. 133-136.

59. K. McAlea, P. Forderhase, U. Hejmadi and C. Nelson, Materials and Applications for the SLS Selective Laser Sintering Process, Proceedings of the 7th

International Conference on 'Rapid Prototyping', Dayton, OH, University of Dayton, 1997, pp.23-33.

60. P. K. Subramanian, G. Zong, H. L. Marcus, Selective Laser Sintering and Reaction Sintering of Ceramic Composites, Solid Freeform Fabrication Symposium, Austin, Texas, US, 1992, pp. 63-71.
61. J. D. Cawley, Computer-aided Manufacturing of Laminated Engineering Materials (CAM-LEM) and its Application to the Fabrication of Ceramic Components Without Tooling, Proc. Int. Gas Turbine and Aeroengine Congress and Exhibition, Orlando, 1997, pp.1-6.
62. J. D. Cawley, A. H. Heuer, W. S. Newman and B. B. Mathewson, Computer-aided Manufacturing of Laminated Engineering Materials, Am. Ceram. Soc. Bull., Vol. 75, 1996, pp.75-79.
63. M. L. Griffith, M. E. Schlienger, L.D. Harwell, M. S. Oliver, M. D. Baldwin, M.T. Ensz, M. Essien, J. Brooks, C.V. Robino, J. E. Smugeresky, W.H. Hofmeister, M. J. Wert and D.V. Nelson, Understanding Thermal Behavior in the LENS Process, Materials and Design, Vol. 20, No. 2, 1999, pp.107-113.
64. E. Sachs, M. Cima, P. Williams, D. Brancazio and J. Cornie, Three-Dimensional Printing: Rapid Tooling and Prototypes Directly from a CAD Model, Journal of Engineering for Industry, Vol. 114, 1992, pp.481-488.
65. E. Sachs, M. Cima, P. Williams, J. Cornie, D. Brancazio, A. Curodeau, T. Fan, S. Khanuja, A. Lauder, J. Lee, S. Michaels, Three-dimensional Printing: the

Physics and Implications of Additive Manufacturing, CIRP annals, Vol. 42, 1993, pp. 257-260.

66. E. M. Sachs, Powder Dispensing Apparatus Using Vibration, US Patent 6036777, 14 March 2000.
67. S. Michaels, E. M. Sachs, M. J. Cima, Metal Parts Generation by Three Dimensional Printing, Solid Freeform Fabrication Symposium, Austin, TX, University of Texas at Austin, 1992, pp. 244-250.
68. J. Yoo, K. Cho, W. S. Bae, M. Cima and S. Suresh, Transformation-Toughened Ceramic Multilayers with Compositional Gradients, Journal of the American Ceramic Society, Vol. 81, 1998, pp. 21-32.
69. A. R. Bhatti, M. Mott, J. R. G. Evans and M. J. Edirisinghe, PZT Pillars for 1-3 Composites Prepared by Ink-jet Printing, Journal of Materials Science Letters, Vol. 20, 2001, pp.1245-1248.
70. H. Rashid, B. Y. Tay and M. J. Edirisinghe, Dispersion of Ceramic Ink Using an Ultrasonic Disruptor, Journal of Materials Science Letters, Vol. 19, 2000. pp. 799-801.
71. B. Y. Tay, H. Rashid and M. J. Edirisinghe, On the Preparation of Ceramic Ink for Continuous Jet Printing, Journal of Materials Science Letters, Vol. 19, 2000. pp. 1151-1154.
72. B. Y. Tay, and M. J. Edirisinghe, Investigation of Some Phenomena Occurring during Continuous Ink-jet Printing of Ceramics, Journal of Materials Research, Vol. 16, 2001, pp. 373-384.

73. J. Windle, B. Derby, Ink Jet Printing of PZT Aqueous Ceramic Suspensions, Journal of Materials Science Letters, Vol. 18, 1999, pp. 87-90.

74. C. E. Slade and J. R. G. Evans, Freeforming Ceramics Using a Thermal Jet Printer, Journal of Materials Science Letters, Vol. 17, 1998, pp. 1669-1671.

75. H. P. Le, Porgress and Trends in ink-jet Printing Technology, Society for Imaging Science and Technology, Vol. 42, 1998, pp. 49-62.

76. W. J. Lloyd and H. H.Taub, Output Hardcopy Devices, Academic Press Professional, Inc. San Diego, CA, USA, 1998, pp. 311-370.

77. A. V. Lemmo, D. J. Rose and T. C. Tisone, Inkjet Dispensing Technology: Applications in Drug Discovery, Current Opinion in Biotechnology, Vol. 9, 1998, pp. 615-617.

78. R. J. Klebe, Cytoscribing: a Method for Micropositioning Cells and the Construction of Two- and Three-dimensional Synthetic Tissues, Experimental Cell Research, Vol. 179, 1988, pp. 362-373.

79. K. F. Teng and R. W. Vest, Liquid Ink Jet Printing with MOD Inks for Hybrid Microcircuits, IEEE Transactions on Components, Hybrids and Manufactory Technology, Vol. 10, 1987, pp. 291-297.

80. J. Benbow and J. Bridgwater, Paste Flow and Extrusion, Clarendon Press, Oxford, 1993, pp. 3-24.

81. H. Akdogan, Pressure, Torque, and Energy Responses of a Twin Screw Extruder at High Moisture Contents, Food Research International, Vol. 29, 1996, pp. 423-429.

82. M. Padmanabhan, M. Bhattacharya, Analysis of Pressure Drop in Extruder Dies, Journal of Food Science, Vol. 54, 1989, pp. 709–713.

83. J. J. Benbow, S. H. Jazayeri and J. Bridgwater, The Flow of Pastes Through Dies of Complicated Geometry, Powder Technology, Vol. 65, 1991, pp. 393–401.

84. T. J. Person and M. M. Denn, The Effect of Die Materials and Pressure-dependent Slip on the Extrusion of Linear Low-density Polyethylene, Journal of Rheology, Vol. 41, 1997, pp. 249–265.

85. J. J. Benbow, E. W. Oxley and J. Bridgwater, The Extrusion Mechanics of Pastes - the Influence of Pastes Formulation on Extrusion Parameters, Chem. Eng. Sci., Vol. 42, 1987, pp. 2151–2162.

86. J. J. Benbow, T. A. Lawson, E. W. Oxley, and J. Bridgwater, Prediction of Paste Extrusion Pressure, Ceram. Bull., Vol. 68, 1989, pp. 1821–1824.

87. M. J. Ribeiro, S. Blackburn, J. M. Ferreira, J. A. Labrincha, Extrusion of Alumina and Cordierite-based Tubes Containing Al-rich Anodising Sludge, Journal of the European Ceramic Society, Vol. 26, 2006, pp. 817-823.

88. A. U. Khan, B. J. Briscoe, B. J. and P. F. Luckham, Evaluation of Wall Slip in Capillary Extrusion of Ceramic Pastes, J. Eur. Ceram. Soc., Vol. 21, 2001, pp. 483–491.

89. I. Ochoa and S. G. Hatzikiriakos, Paste Extrusion of Polytetrafluoroethylene (PTFE): Surface Tension and Viscosity Effects, Powder Technology, Vol. 153, 2005, pp. 108-118.

90. S. Mazur, Paste Extrusion of Poly (tetrafluoroethylene) Fine Powders, Polymer

Powder Technology, John Wiley and Sons, New York, 1995, pp. 441–481.

91. A. B. Ariawan, S. Ebnesajjad and S. G. Hatzikiriakos, Preforming Behaviour of Polytetrafluoroethylene Paste, Powder Technol., Vol. 121, 2001, pp. 249-258.
92. A. B. Ariawan, S. Ebnesajjad, S.G. Hatzikiriakos, Paste Extrusion of Polytetrafluoroethylene(PTFE) Fine Powder Resins, Canadian Journal of Chemical Engineering, Vol. 80, 2002, pp.1153-1165.
93. A. B. Arianwan, S. Ebnesajjad and S. G. Hatzikiriakos, Properties of Polytetrafluoroethylene (PTFE) Paste Extrudates, Polym. Eng. Sci., Vol. 42, 2002, pp. 1247-1259.
94. A. B. Arianwan, Paste extrusion of Polytetrafluoroethylene Fine Powder Resins, the University of British Columbia, Department of Chemical and Biological Engineering, PhD Thesis, 2002, pp. 101-120.
95. B. D. Russell, J. Lasenby, S. Blackburn and D. I. Wilson, Characterizing Paste Extrusion Behaviour by Signal Processing of Pressure Sensor Data, Powder Technology, Vol. 132, 2003, pp. 233-248.
96. I. Ochoa and S. G. Hatzikiriakos, Polytetrafluoroethylene (PTFE) Paste Performing: Viscosity and Surface Tension Effects, Powder Technology, Vol. 146, 2004, pp. 73-83.
97. I. Shishkovsky, Synthesis of Functional Gradient Parts via RP Methods, Rapid Prototyping Journal, Vol. 7, 2001, pp. 207-211.
98. S. S. Crump, Fused Deposition Modeling (FDM): Putting Rapid Back into Prototyping, The Second International Conference on Rapid Prototyping, Dayton, University of Dayton, 1991, pp. 354-357.

99. Y. Chen, D. Bartzos, Y. Lu, E. Niver, M. E. Pilleux, M. Allahverdi, S. C. Danforth and A. Safari, Simulation, Fabrication, and Characterization of 3-D Alumina Photonic Bandgap Structures, Microwave and Optical Technology Letters, Vol.30, 2001, pp. 305-307.

100. M. Greul and R. Lenk, Near-Net-Shape Ceramic and Composite Parts by Multiphase Jet Solidification (MJS), Ind. Ceram., Vol. 20, 2000, pp. 115-117.

101. A. A. Tseng and M. Tanaka, Advanced Deposition Techniques for Freeforming Fabrication of Metal and Ceramics Parts, Rapid Prototyping Journal, Vol. 7, 2001, pp.6-17.

102. J. Cesarano III, P. Calvert, Freeforming Objects with Low-Binder Slurry, US Patent 6,027,326, Feb., 22, 2000.

103. J. Cesarano III, Solid Freeform and Additive Fabrication, Mater. Res. Soc. Symp. Proc., Vol. 542, 1998, pp.133-139.

104. E. S. James, J. Cesarano III, and J.A. Lewis, Colloidal Inks for Directed Assembly of 3-D Periodic Structures, American Chemical Society, Vol. 18, 2002, pp.5429-5437.

105. M. Sarah, W. Willie, J. A. Lewis, Concentrated Hydroxyapatite Inks for Direct-write Assembly of 3-D Periodic Scaffolds, Biomaterials, Vol. 26, 2005, pp.5632–5639.

106. G. M. Gratson, M. Xu and J. A. Lewis, Microperiodic Structures: Direct Writing of Three-dimensional Webs, Nature, Vol. 428, 2004, p 386.

107.H. A. Barnes, J. F. Hutton and K. Walters, An Introduction to Rheology, Elsevier Science B.V., The Netherlands, 1989, pp.11-25.

108.H. A. Barnes, J .F. Hutton and K. Walters, An Introduction to Rheology, Elsevier Science B.V., The Netherlands, 1989, pp. 25-35.

109.F. N. Cogswell, Polymer Melt Rheology: A Guide for Industrial Practice, George Godwin Limited, Great Britain, 1981, pp.15-33.

110.R. L. Earle, Unit Operations in Food Processing, Pergamon Press, United Kingdom, 1966, pp.50-55.

111.E. B. Bagley, End Correction in Capillary Flow of Polyethylene, Journal of Applied Physics, 1957, Vol. 28, pp. 624-627.

112.T. Zhang and J. R. G. Evans, Predicting the Viscosity of Ceramic Injection Moulding Suspensions, Journal of the European Ceramic Society, 1989, Vol. 5, pp. 165-172.

113.M. J. Edirisinghe and J. R. G. Evans, Review: Fabrication of Engineering Ceramics by Injection Moulding, I: Materials Selection. Int. J. High Tech. Ceram., 1986, Vol. 2, pp. 1-31.

114.B. K. Hur, C. B. Kim and C. Lee, Functional Relationship Between Volume Concentration of Dispersed Phase and Relative Viscosity in a Liquid-Liquid Dispersion and Emulsion, Journal of Industrial and Engineering Chemistry, 2000, Vol. 6, pp. 318-324.

115.M. Mooney, the Viscosity of a Concentrated Suspension of Spherical Particles, J. Colloid Sci., 1951, Vol.6, pp.162-170.

116.H. Eilers, the Viscosity of Emulations Made of Highly Viscous Materials as a Function of the Concentration, Kolloid Z., 1941, Vol.15, pp.313-321.

117.J. S. Chong, E. B. Christiansen and A. D. Baer, Rheology of Concentrated Suspensions, J. Appl. Polym. Sci., 1971, Vol.15, pp. 2007-2021.

118.H. Yang, S. Yang, X. Chi, J.R.G. Evans, Fine Ceramic Lattices Prepared by Extrusion Freeforming, J. Biomedical Materials Research, Vol. 79B, 2006, pp. 116-121.

119.J. R. Davis, ASM Specialty Handbook: Stainless Steels, ASM International, 1994, p. 489.

120.K. D. Kim, Rizwan-uddin, A web-based nuclear simulator using RELAP5 and LabVIEW, Nuclear Engineering and Design, Vol. 237, 2007, pp. 1185–1194.

121.F. N. Cogswell, Polymer Melt Rheoogy, a Guide for Industrial Practice, John Wiley and Sons, New York and Toronto, 1981, p.17.

122.W. Lan, P. Xiao, Constrained Drying of Aqueous Yttria-Stabilized Zirconia Slurry on a Substrate. I: Drying Mechanism, J. Am. Ceram. Soc. Vol. 89, 2006, pp. 1518-1522.

123.J. J. Benbow and J. Bridgwater, Paste Flow and Extrusion, Oxford University Press, USA, 1993, pp. 28-32.

124.A. Bandyopadhyay, S.C. Danforth, A. Safari, Effect of Processing History on Thermal Debinding, J. Mater. Sci., Vol. 35, 2000, pp.3983-3988.

125.J. H. Song, J. R. G. Evans, M. J. Edirisinghe, E. H. Twizell, Determination of Gas Transport in Ceramic Bodies During Thermolysis of Organic Additives, Int. Mater. Rev., Vol. 41, 1996, pp. 116-128.

126.S. Ying, Y. C. Lam, J. C. Chai, K. C. Tam, Similation of Thermal Debinding: Effect of Mass Transport on Equivalent Stress, Comp. Mater. Sci., Vol. 30, 2004, pp. 496-550.

127.S. A. Matar, M. J. Edirisinghe, J. R. G. Evans, E. H. Twizell, The Effect of Porosity Developmnet on the Removal of Organic Vehicle from Ceramic or Metal Mouldings, J. Mater. Rev., Vol. 8, 1993, pp. 617-625.

128.T. Ota, J. Takahashi, I. Yamai, Effect of Microstructure on the Dielectric Property of Ceremaics, Key Eng. Mater., Vol. 66/67, 1992, pp. 185-146.

129.ASTM C 1039-85, Standard Test Methods for Apparent Porosity, Apparent Specific Gravity, and Bulk Density of Graphite Electrodes, 1995, pp. 279-281.

130.T. M. G. Chu, D. G. Orton, S. J. Hollister, S. E. Feinberg and J. W. Halloran, Mechanical and in Vivo Performance of Hydroxyapatite Implants with Controlled Architectures, Biomaterials, Vol. 23, 2002, pp.1283-1293.

131.K. Kurashina, H. Kurita, Q. Wu, A. Ohtsuka and H. Kobayashi, Ectopic Osteogenesis with Biphasic Ceramics of Hydroxyapatite and Tricalcium Phosphate in Rabbits. Biomaterials, Vol. 23, 2002, pp. 407-416.

132.H. Y. Yang, I. Thompson, S. F. Yang, X. P. Chi, J. R. Evans, R. J. Cook, Dissolution Characteristics of Extrusion Freeformed Hydroxyapatite-tricalcium

Phosphate Scaffolds, Journal of Materials Science. Materials in Medicine, Vol. 19[11], 2008, pp. 3345-3353.

133. D. F. Wu, G. Z. Lu, H. Jiang and Y. D. Li, Improved Estimation of Weibull Parameters with the Linear Regression Method, J. Am. Ceram. Soc., Vol. 87, 2004, pp. 1799–1802.

134. D. F. Wu, Y. D. Li, J. P. Zhang, L. Chang, D. H. Wu, Z. P. Fang and Y. Shi., Effects of the Number of Testing Specimens and the Estimation Methods on the Weibull Parameters of Solid Catalysts, Chem. Eng. Sci., Vol. 56, 2001, pp. 7035–7044.

135. A. Khalili, and K. Kromp, Statistical Properties of Weibull Estimators, J. Mater. Sci., Vol. 26, 1991, pp. 6741–6752.

136. ASTM standard, C1239-00 Standard Practice for Reporting Uniaxial Strength Data and Estimating Weibull Distribution Parameters for Advanced Ceramics, American Society for Testing and Materials, Philadelphia, PA, 2003.

137. D. Wu, J. Zhou, Y. Li, Unbiased Estimation of Weibull Parameters with the Linear Regression Method, J. Eur. Ceram. Soc. Vol. 26, 2006, pp. 1099-1105.

138. L. Y. Song, D. F. Wu and Y. D. Li, Optimal Probability Estimators for Determining Weibull Parameters, J. Mater. Sci. Lett., Vol. 22, 2003, pp. 1651-1653.

139. R. J. Cook, I. Thompson, J. Jones, H. Yang, S. Yang, X. Chi, J. R. G. Evans, P. Robinson, the Effects of Open Void Dimension on Histological Ingrowth of New

Bone into Extrusion Freeformed Hydroxyapatite/tricalcuim phosphate Lattices, to be published.

140. R. K. Schenk, D. Buser, W. R. Hardwick, C. Dahlin, Healing Pattern of Bone Regeneration in Membrane-protected Defects: a Histological Study in the Canine Mandible, International Journal of Oral & Maxillofacial Implants, Vol. 9, 1994, pp. 13–29.

141. D. Buser, B. Hoffmann, J. P. Bernard, A. Lussi, D. Mettler, R. K. Schenk, Evaluation of Filling Materials in Membrane-protected Bone Defects-A Comparative Histomorphometric Study in the Mandible of Miniature Pigs, Clinical Oral Implants Research, Vol. 9, 1998, pp. 137–150.

142. U. Stucki, J. Schmid, C. F. Hämmerle, N. P. Lang, Temporal and Local Appearance of Alkaline Phosphatase Activity in Early Stages of Guided Bone Regeneration-a Descriptive Histochemical Study in Humans, Clinical Oral Implants Research, Vol. 12, 2001, pp. 121–127.

143. K. Okazaki, Y. Shimizu, H. Xu, K. Ooya, Blood-filled Spaces With and Without Deproteinized Bone Grafts in Guided Bone Regeneration-a Histomorphometric Study of the Rabbit Skull Using Non-resorbable Membrane, Clinical Oral Implants Research, Vol. 16, 2005, pp. 236–243.

144. S. A. Jovanovic, R. K. Schenk, M. Orsini, E. B. Kenney, Supracrestal Bone Formation around Dental Implants: an Experimental Dog Study, International Journal of Oral & Maxillofacial Implants, Vol. 10, 1995, pp. 23–31.

145. C. H. F. Hämmerle, A. J. Olah, J. Schmid, L. Flückiger, S. Gogolewski, J. R.

Winkler and N. P. Lang, the Biological Effect of Natural Bone Mineral on Bone Neoformation on the Rabbit Skull, Clinical Oral Implants Research, Vol. 8, 1997, pp. 198–207.

146.J. Schmid, C. H. F. Hämmerle, L. Flückiger, J. R. Winkler, A. J. Olah, S. Gogolewski and N. P. Lang, Blood-filled Spaces With and Without Filler Materials in Guided Bone Regeneration-a Comparative Experimental Study in the Rabbit Using Bioresorbable Membranes, Clinical Oral Implants Research, Vol. 8, 1997, pp. 75–81.

147.L. Kostopoulos, N. Lioubavina, T. Karring, R. Uraguchi, Role of Chitin Beads in the Formation of Jaw Bone by Guided Tissue Regeneration-an Experiment in the Rat, Clinical Oral Implants Research, Vol. 12, 2001, pp. 325–331.

148.T. J. Flatley, K. L. Lynch and M. Benson, Tissue Response to Implants of Calcium Phosphate Ceramic in the Rabbit Spine, Clin. Orthop., Vol. 179, 1983, pp.246-252.

149.B. Chang, C. Lee, K. Hong, H. Youn, H. Ryu, S. Chung and K. Park, Osteoconduction at Porous Hydroxyapatite with Various Pore Configurations, Biomaterials, Vol. 21, 2000, pp.1291-1298.

150.M. Doernberg, B. Rechenberg, M. Bohner, S. Grünenfelder, G. H. Lenthe, R. Müller, B. Gasser, R. Mathys, G. Baroud, J. Auer, In Vivo Behavior of Calcium Phosphate Scaffolds with Four Different Pore Sizes, Biomaterials, Vol. 27, 2006, pp. 5186-5198.

151.N. Caplanis, T. J. Sigurdsson, M. D. Rohrer and U. M. E. Wikesjö, Effect of

Allogeneic, Freeze-dried, Demineralized Bonematrix on Guided Bone Regeneration in Supra-alveolar Peri-implant Defects in Dogs, International Journal of Oral & Maxillofacial Implants, Vol. 12, 1997, pp. 634–642.

152. D. Weng, M. B. Hürzeler, C. R. Quiñones, A. Ohlms, and R. G. Caffesse, Contribution of the Periosteum to Bone Formation in Guided Bone Regeneration-a Study in Monkeys, Clinical Oral Implants Research, Vol. 11, 2000, pp. 546–554.

153. C. H. F. Hämmerle, J. Schmid, A. J. Olah, and N. P. Lang, a Novel Model System for the Study of Experimental Guided Bone Formation in Humans, Clinical Oral Implants Research, Vol. 7, 1996, pp.38–47.

154. T. Krink, F. Vollrath, Analysing Spider Web-building Behaviour with Rule-based Simulations and Genetic Algorithms, J. Theor. Biol., Vol. 185, 1997, pp. 321-331.

155. E. Ozbay, A. Abeyta, G. Tuttle, M. Tringides, R. Biswas, C. T. Chan, C. M. Soukoulis, and K. M. Ho, Measurement of a Three-Dimensional Photonic Band Gap in a Crystal Structure Made of Dielectric Rods, Phys. Rev. B, Vol.50[3], 1994, pp.1945–48.

156. E. Ozbay, E. Michel, G. Tuttle, R. Biswas, M. Sigalis, and K. M. Ho, Micromachined Millimeter-Wave Photonic Band-Gap Crystals, Appl. Phys. Lett., Vol.64[16], 1994, pp.2059–61.

157. S. Y. Lin, J. G. Fleming, D. L. Hetherington, B. K. Smith, R. Biswas, K. M. Ho, M. M. Sigalis, W. Zubrzycki, and S. R. Kurtz, A Three Dimensional Photonic

Crystal Operating at Infrared Wavelengths, Nature (London), Vol. 394, 1998, pp. 251–53.

158.C. J. Reilly, W. J. Chappell, J. W. Halloran and L. P. B. Katehi, High-Frequency Electromagnetic Bandgap Structures via Indirect Solid Freeform Fabrication, J. Am. Ceram. Soc., Vol. 87[8], 2004, pp. 1446-1453.

159.E. Yablonovitch, T. J. Gmitter, R. D. Meade, A. M. Rappe, K. D. Brommer, and J. D. Joannopoulous, Donor and Acceptor Modes in Photonic Band Structure, Phys. Rev. Lett., Vol. 67, 1991, pp.3380-3383.

160.P. M. Martin, D.W. Matson, W.D. Bennett, D.C. Stewart and C.C. Bonham, Laminated Ceramic Microfluidic Components for Microreactor Applications, in Proc. of the 4th Int. Conf. on Microreaction Technology, IMRET 4, March 5-9, 2000, Atlanta, USA, 410.

161.K. Regina, B. Werner, G. Dieter and H. Jürgen, Manufacturing of Ceramic Microcomponents by a Rapid Prototyping Process Chain, Adv. Eng. Mater., Vol. 3[1-2], 2001, pp. 49-54.

Appendixes

Appendix A：Set-up parameters and their descriptions.

Description	Parameter setting
Drive Setup	AXSDEF 1100
Axis 1, Servo Control, Linearserv Drive	DRFLVL 1111
Axis 2, Servo Control, Linearserv Drive	DRFEN 1110
Axis 3, Stepper Control, No Drive	KDRIVE 00XX
Axis 4, Stepper Control, No Drive	DRES ,,4000,10000
	PULSE ,, 1.0, 1.0
	DSTALL XX00
Scaling Setup	SCLD 10000,10000,800,640
Distance Units - counts, counts, counts, counts	SCLV 10000,10000,800,640
Velocity Units - rev/s, rev/s, rev/s, rev/s	SCLA 10000,10000,800,640
Acceleration Units - rev/s/s, rev/s/s, rev/s/s, rev/s/s	SCALE1
Feedback Setup	SFB 1,1,,
	ERES 8000,8000,8000,
	SMPER 0,0,0,
	EFAIL 111X
	ENCPOL 001X
	ENCSND 000X
	ESTALL XX0X
	ESK XXXX
	ENCCNT XX1X
Hardware Limit Setup	LH 3,3,3,0
	LHAD 100,100,20,100
	LHADA 50,50,10,100
Software Limit Setup	LS 0,0,0,0
	LSAD 100,100,100,100
	LSADA 100,100,100,100
	LSNEG 0,0,0,0
	LSPOS 0,0,0,0
Home Limit Setup	HOMA 100,100,10,10
	HOMAA 50,50,5,10
	HOMV 10,10,5,1
	HOMAD 100,100,10,10
	HOMADA 50,50,5,10
	HOMBAC 1110
	HOMZ 0001
	HOMDF 0000

	HOMVF 1,1,1,0
	HOMEDG 0000
	LIMLVL 001001110000

Description	Parameters setting
;Native Code module	CMDDIR 0010
	V5,5,5
Servo Tuner Setup	SGP 5,2,,
	SGI 0,0,,
	SGILIM 0,0,,
	SGV 0.6,0.3878,,
	SGVF 0,0,,
	SGAF 0,0,,

Appendix B： An example Motion Planner program for the fabrication of bone substitute scaffold.

The program shown below is an example of a Motion Planner program for the fabrication of bone substitute scaffold. Some executing conditions like ‘dres’, ‘scale’, ‘scald’, ‘scalv’, etc. had been deleted because they had been defined in the LabVIEW program. The structure represented by the program as drawn by the AutoCAD software is shown in Figure A-1. The arrows with X and Y are the user coordinate system (UCS) and the arrow with A indicates the filament path direction. The AutoCAD files were saved as R12/LT2 DXF format so that the Compucam version1.4 transferred it to the Motion Planer program.

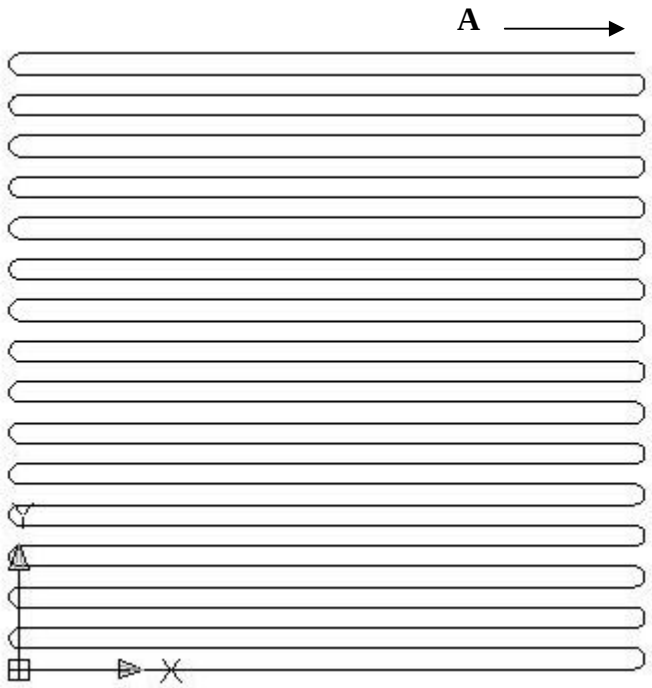

Figure A-1. The structure which the Motion Planer program represented.

```
DEL P0
DEF P0
PAXES 1, 2
PAB 1
PRTOL 0.1000
PWC 0.0000, 0.0000
PLIN 18.9000, 0.0000
PARCOM 18.9000, 0.6300, -0.0000, 0.3150
PLIN 0.0000, 0.6300
PARCOP -0.0000, 1.2600, 0.0000, 0.3150
PLIN 18.9000, 1.2600
PARCOM 18.9000, 1.8900, -0.0000, 0.3150
PLIN 0.0000, 1.8900
PARCOP -0.0000, 2.5200, 0.0000, 0.3150
PLIN 18.9000, 2.5200
PARCOM 18.9000, 3.1500, -0.0000, 0.3150
PLIN 0.0000, 3.1500
PARCOP -0.0000, 3.7800, 0.0000, 0.3150
PLIN 18.9000, 3.7800
PARCOM 18.9000, 4.4100, -0.0000, 0.3150
PLIN 0.0000, 4.4100
PARCOP -0.0000, 5.0400, 0.0000, 0.3150
PLIN 18.9000, 5.0400
PARCOM 18.9000, 5.6700, -0.0000, 0.3150
PLIN 0.0000, 5.6700
PARCOP -0.0000, 6.3000, 0.0000, 0.3150
PLIN 18.9000, 6.3000
PARCOM 18.9000, 6.9300, -0.0000, 0.3150
PLIN 0.0000, 6.9300
PARCOP -0.0000, 7.5600, 0.0000, 0.3150
PLIN 18.9000, 7.5600
PARCOM 18.9000, 8.1900, -0.0000, 0.3150
PLIN 0.0000, 8.1900
PARCOP -0.0000, 8.8200, 0.0000, 0.3150
PLIN 18.9000, 8.8200
PARCOM 18.9000, 9.4500, -0.0000, 0.3150
PLIN 0.0000, 9.4500
PARCOP -0.0000, 10.0800, 0.0000, 0.3150
PLIN 18.9000, 10.0800
PARCOM 18.9000, 10.7100, -0.0000, 0.3150
PLIN 0.0000, 10.7100
PARCOP -0.0000, 11.3400, 0.0000, 0.3150
PLIN 18.9000, 11.3400
PARCOM 18.9000, 11.9700, -0.0000, 0.3150
PLIN 0.0000, 11.9700
PARCOP -0.0000, 12.6000, 0.0000, 0.3150
PLIN 18.9000, 12.6000
PARCOM 18.9000, 13.2300, -0.0000, 0.3150
PLIN 0.0000, 13.2300
PARCOP -0.0000, 13.8600, 0.0000, 0.3150
PLIN 18.9000, 13.8600
PARCOM 18.9000, 14.4900, -0.0000, 0.3150
PLIN 0.0000, 14.4900
PARCOP -0.0000, 15.1200, 0.0000, 0.3150
PLIN 18.9000, 15.1200
PARCOM 18.9000, 15.7500, -0.0000, 0.3150
PLIN 0.0000, 15.7500
PARCOP -0.0000, 16.3800, 0.0000, 0.3150
PLIN 18.9000, 16.3800
PARCOM 18.9000, 17.0100, -0.0000, 0.3150
PLIN 0.0000, 17.0100
PARCOP -0.0000, 17.6400, 0.0000, 0.3150
PLIN 18.9000, 17.6400
PARCOM 18.9000, 18.2700, -0.0000, 0.3150
PLIN 0.0000, 18.2700
PARCOP -0.0000, 18.9000, 0.0000, 0.3150
PLIN 18.9000, 18.9000
END
```

Appendix C: Command settings and their descriptions.

Command	Description
%(task identifier)	The % prefix is used to specify that the associated task number is only used in the multi-tasking.
!(immediate command identifier)	Changes a buffered command into an immediate command. All immediate commands are processed immediately, even before previously-entered buffered commands.
COMEXC1	Enables the continuous command processing mode. Command processing continues while motion is taking place in this mode.
COMEXS1	Saves the command buffer upon a stop input or stop command.
HOMEDG111	The home reference edge command specifies the homing operation will consider negative-direction edge of the home switch as its final destination.
INTHW.24-1	The check for alarm events command determines which conditions will cause an alarm event in the program. Here it enables the command error alarm.
INFNC 5-h	The input function command defines the functions of each individual input. Here, the input bit number is 5; the function inputted is a trigger interrupt.
LH 3,3,3,0	The hardware end-of-travel limit-enable checking (LH) command is used to enable or disable the inputs defined as end-of-travel limit inputs. Here it means limits on axes X, Y, Z are enabled; limit on the fourth axis is disabled.
MC0010	The preset/continuous mode enable command was set at 0010 to enable preset mode on X, Y and the fourth axes and enable continuous mode on Z axis.
PSET 0,0	The established absolute position command was set 0, 0 to set absolute position on axes X, Y to zero.
SFB 1,1	Selects encoder feedback for axes X, Y.
WAIT (in.5=b0)	The wait for a specific condition command was used to wait for a specific expression to evaluate true. Here means waiting for onboard input 5 to be completed.

Appendix D: Block Diagrams of the Front Panels for bone substitute lattice fabrication.

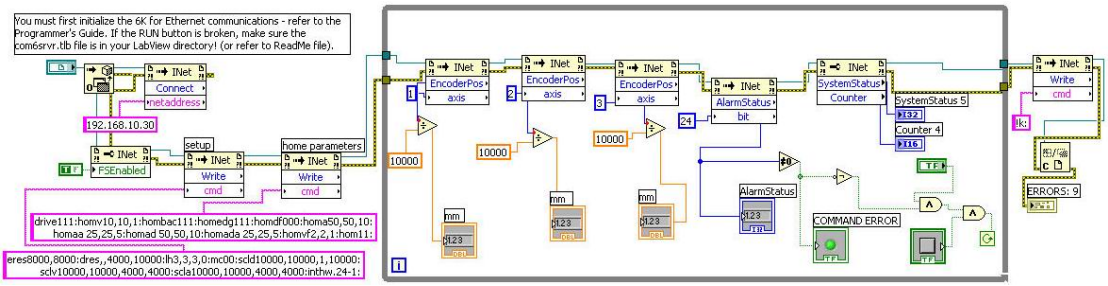

Figure D-1. Block Diagram for the Front Panel named "X Y home".

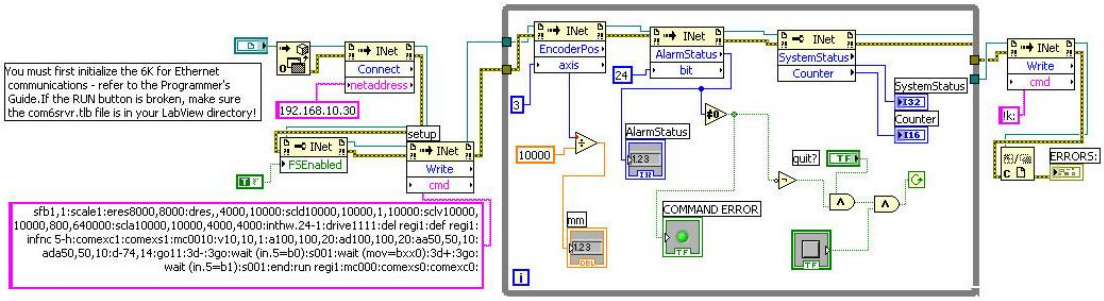

Figure D-2. Block Diagram for the Front Panel named "Z home".

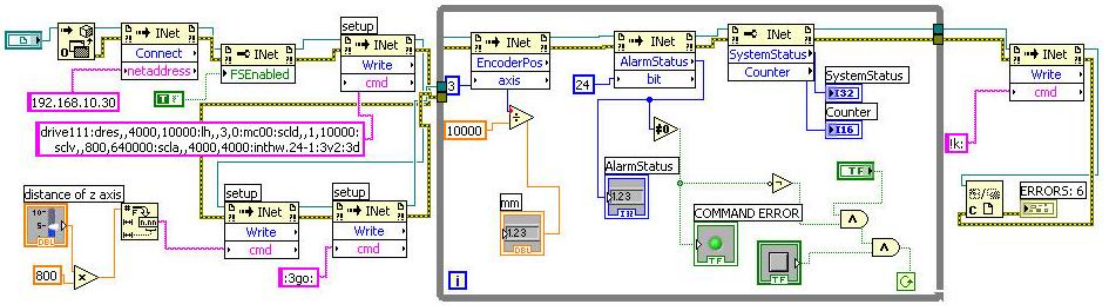

Figure D-3. Block Diagram for the Front Panel named "move Z axis".

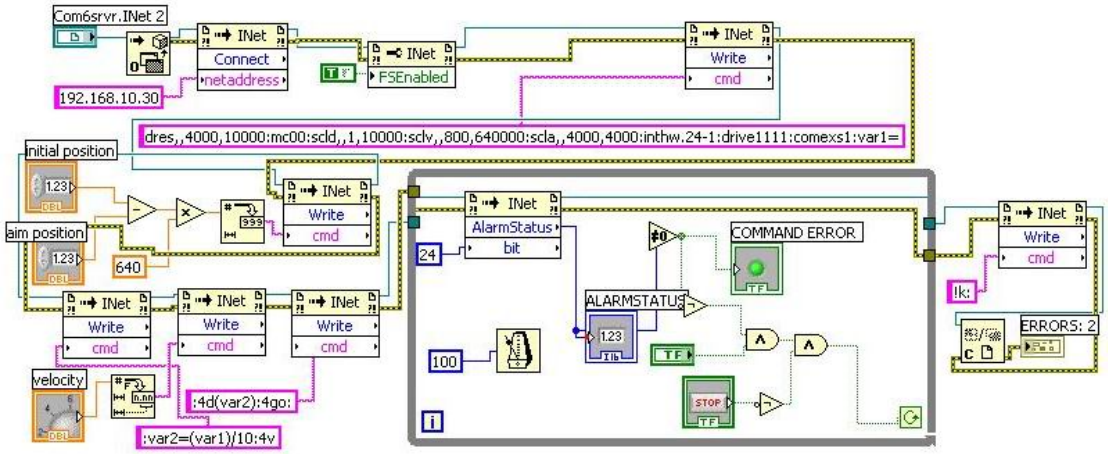

Figure D-4. Block Diagram for the Front Panel named "COARSE for extrusion axis".

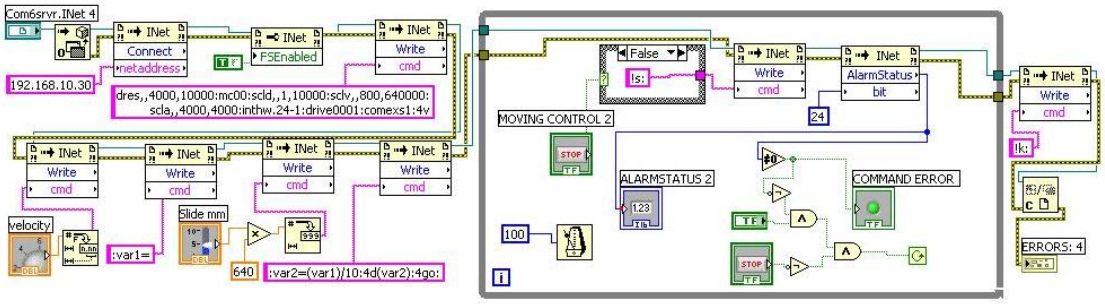

Figure D-5. Block Diagram for the Front Panel named "FINE for extrusion axis"